CYRIC

ANNUAL REPORT

2008

(January 2008 - December 2008)

CYCLOTRON AND RADIOISOTOPE CENTER
TOHOKU UNIVERSITY
http://www.cyric.tohoku.ac.jp/

PREFACE

In this twenty-ninth issue of the CYRIC Annual Report, we summarize the activities in research and development, and in training of radioisotope safe-treatment at the Cyclotron and Radioisotope Center (CYRIC) during the calendar year 2008

Research at CYRIC was carried out in the fields of nuclear physics, nuclear chemistry, material sciences, nuclear medicine using PET (oncology, brain study, pharmacology), radiopharmaceutical chemistry, health physics, nuclear instrumentation, nuclear medical engineering (diagnosis and therapy technology), nuclear engineering and elemental analysis using PIXE.

Developments and improvements on nuclear instruments and techniques have progressed; one of the 2008 highlights is the start of the on-campus service of an ultra high resolution semiconductor small animal PET of which the spatial resolution is 0.78mm FWHM.

Both the K=110 MeV AVF cyclotron and K=12 MeV AVF cyclotron were steady operated in this year. New ECR ion source (10 GHz) was installed for heavier particle acceleration up to Xe ions. First observations of magnetic moments of neutron-rich unstable nuclei along R-process path have been done by the advanced RF ion-guide system. The newly developed thermal ionizer was installed in the 34 course for the production of the ^{210}Fr to search for the electric dipole moment of the electron. The ^{210}Fr, which was produced using the fusion reaction with the ^{18}O beam and ^{197}Au target, were observed for the first time at CYRIC.

In the research program on charged particle therapy at CYRIC, a therapeutic approach to proton therapy combined with the novel vascular disrupting agent targeting the existing tumor blood vessel network has been investigated. The experimental study in the murine fibrosarcoma model demonstrated that the tumor growth was strongly inhibited by this therapeutic strategy, and provided encouraging results leading to enhancement of the efficacies of conventional radiation therapy or monotherapy with vascular targeting agents.

Routine productions of [^{18}F]FDG (31 preparations), [^{18}F]FRP-170 (7), [^{18}F]FACT (9), [^{11}C]methionine (5), [^{11}C]doxepin (22), [^{11}C]raclopride (12), [^{11}C]donepezil (26), [^{11}C]BF-227 (25) and [^{15}O]water (22) for clinical PET studies were carried as in other years. [^{11}C]Galantamine and [^{11}C]interleukin 8 were successfully prepared as a new PET probe and

evaluated for basic biological studies. The radiosynthesis of 2-deoxy-2-[^{18}F]fluoro- D-mannose using a new precursor was developed for future clinical use. The details of these studies will be reported in next issue. The most successful achievement of PET radiochemistry in 2008 was the establishment of electrochemical concentration of aqueous [^{18}F]fluoride using a disposable microchip. Microfluidic preparation of ^{18}F-labeled probes will hopefully be accelerated using this innovative technique.

"Molecular Imaging Program" supported by a JST grant for "research and education in molecular imaging" has been so fruitful and the CYRIC has played an important role as the site of basic and clinical experiments. Clinical PET studies using our new original _-amyloid imaging probe, [^{18}F]FACT, have been almost completed. Our new findings from additional studies using [^{11}C]BF-227 have been published in leading journals. [^{18}F]FDG study is still active, increasing the number of publication, and also new findings on PET imaging of shoulder joint muscles will be published in near future. Using the [^{18}F]FDG, CYRIC has been contributing also to multicenter study projects on diagnosis of early Alzheimer's disease (SEAD-J) and Alzheimer's disease neuroimaging initiative in Japan (J-ADNI). Clinical application of [^{11}C]doxepin and [^{11}C]donepezil has been also fruitful and lead to several publications regarding clinical pharmacology and elucidation of pathophysiological mechanism of anorexia nervosa and Alzheimer's disease.

The research program on PIXE analysis has been carried out by using electrostatic accelerator (4.5 MV Dynamitron) at the Fast Neutron Laboratory, Graduate School of Engineering, Tohoku University, under the scientific tip up between CYRIC and FNL. Research studies using micro-PIXE/RBS analysis, STIM analysis, and Micron-CT are routinely carried out. A total of 1041 hours of beam-time was served to this program without a serious problem.

The beginners training for safe handling of radiation and radioisotopes was carried out as usual. In 2008, a total of 1031 staffs and students of Tohoku University took three courses: 1) Radioisotopes and radiation generators (514 trainees), 2) X-ray machines and electron microscope (396), and 3) Synchrotron Radiation (121). The number of trainees in this year increased by about 4 percents compared with the previous year (988). The English classes for each course were practiced for 82 foreign students and scientists.

In addition to our above reports, we present an invited paper by Emeritus Professor Taiju Matsuzawa in this issue. This year is just the twenty fifth anniversary of the on-campus service of PET for nuclear medicine which was started at 1983 under the leadership of Prof. Taiju Matsuzawa. He introduced a PET scanner (ECAT II) first in national universities in Japan and has led the study on brain and cancer using PET since. In the cancer study, he showed first in the world that FDG was useful for cancer diagnosis, that is,

he is really a pioneer of this field. Since he began a cancer chekup with PET at Yamanaka lake (Himedic Yamanakako : Grand Himedic Co.Ltd.) first in the world and more than 100 PET such centers are now in operation. He organized a first International Symposium on PET in Oncology in 1985 and second one again in 1993, and edited a book of PET oncology("Clinical PET in Oncology", World Scientific Publishing Co. Pte. Ltd.1993). His works on the higher functions of the brain are also remarkable ("Visually understanding Brain and Mind" NHK press, 2003). Thus, Prof. Taiju Matsuzawa played a big part in the field of PET nuclear medicine and he is still active in this field. We invite him here to present his recent work on the brain.

We are most grateful to Tohoku University and to the Ministry of Education, Sports, Culture, Science and Technology for continuous support.

January 2009

Keizo ISHII
Director
Cyclotron and Radioisotope Center, Tohoku University

EDITORS:

Keizo	*ISHII*
Ren	*IWATA*
Hiromichi	*YAMAZAKI*
Yasuhiro	*SAKEMI*
Tsutomu	*SHINOZUKA*
Manabu	*TASHIRO*

WORD PROCESSED BY

Yu-ko YAMASHITA

CONTENTS

SPECIAL CONTRIBUTION

I. NUCLEAR PHYSICS

II. NUCLEAR INSTRUMENTATION

III. NUCLEAR ENGINEERING

SPECIAL CONTRIBUTION

Regenerative Medicine in Alzheimer's Disease

Matsuzawa T.

Department of Nuclear Medicine and Radiology
Institute of Development, Aging and Cancer, Tohoku University, and
Department of Radiology, Tokyo Kyobashi Future Clinic

Introduction

Alois Alzheimer (1834 - 1915), a German psychiatrist, chanced to have a 51-year-old female psychiatric patient who developed strong delusion of persecution that her husband were having a love affair used to shout aloud, and turned violent. Dr. Alzheimer closely observed her and described in detail what he observed. As her diseases progressed, she lost memory at all, confused and disoriented four and half years later.

At autopsy, Dr. Alzheimer observed pronounced pathological changes in the cerebral cortex. He reported the case as a novel disorder in one of the German journals[1] in 1907.

Recently, this Alzheimer's disease (AD) has turned to be one of the most shattering diseases throughout the industrial countries. AD is an intimidating disorder firstly because of its high prevalence as high as 80% of the senile dementia, secondly because of lack of established knowledge of etiology, prevention, and curing treatment, and thirdly because of its relentless progression by destroying humanly personality, and leading to eventual death.

By the way, we have long studies AD with XCT[2-4] for 30 years, and with MRI[5] for 10 years so as to discover the primary focus of AD in the brain.

Brain atrophy in AD is a dilatation of cerebral ventricles, especially when the lateral posterior horn is significantly dilated. Based on this, we have developed a new tomographic technique (Matsuzawa's tomographic method, patented) and finally succeeded in finding the primary focus. This primary focus is a specific destruction (deficit) of the amygdala and hippocampus in the limbic system occurring symmetrically on both sides. In general, there is a mechanism by which wounds of the living human body are healed. This mechanism involves neural stem cells which proliferate and differentiate into glial

cells and neural cells[6,7]. The theory[8] advanced by Cajal that the brain cells in the mature brain are not regenerated, but only reduced, has been the standard belief for as long as 80 years. This has now been proved to be incorrect. Regenerative medicine, in which Alzheimer's disease can be prevented and cured, is realized by inducing the healing capacity of neural stem cells through appropriate treatments.

1. Methods and Subjects

1-1. MRI

Development of Matsuzawa's tomographic method (Japanese patent number 4111826, European patent number 1344491).

The new tomography has been developed for carefully examining the cerebral limbic system of the cerebral parenchyma adjacent to the lateral posterior horn utilizing MRI (Fig. 1A, 1B and 1C).

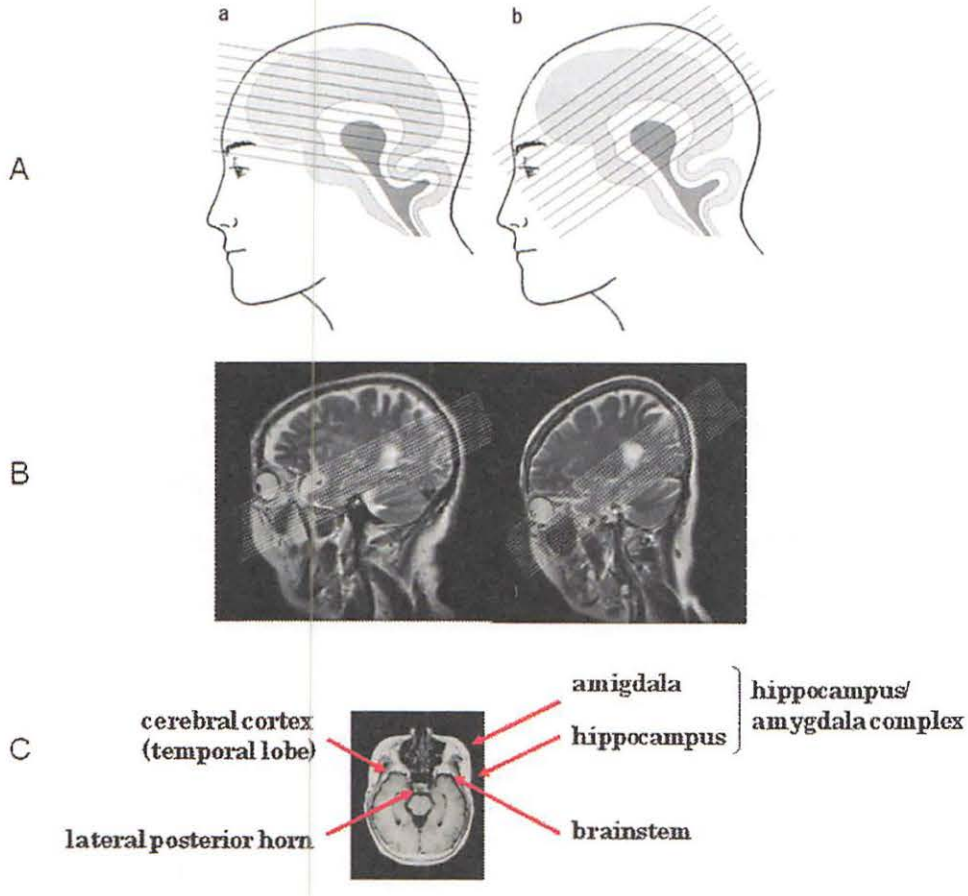

Fugure 1. Matsuzawa's new tomographic method (A, B, C).

Figure 1A shows pattern diagrams of the conventional tomography and Matsuzawa's newly developed tomographic method (b). In the conventional tomography, several parallel sections were obtained above the line connecting the superior orbital margin and ear canal. As shown in Fig. 1B, a scout view is made via a T2-enhanced image for positioning,the lateral posterior horn outlined by the scout view is used as a reference line and several parallel cross-section diagrams are obtained above and below the reference line in the newly developed method. As shown in Fig. 1C, this method is capable of capturing a triple structure of the brain (including the brain stem, amygdala–hippocampal complex in limbic system and cerebral cortex) altogether on the same plane.

1.5 Tesler MRI

MRI Images were obtained with a 1.5 Tesla whole-body imager (Signa EXCITE XL;GE Medical Systems, Japan) by using a 8 channel Brain Array Coil. The Protocol included axial T2-weighted fast spin-echo images (4000/120 [repetition time msec / echo time msec], Echo Train Length; 16, Section Thickness; 5mm, Gap; 0mm, Field of View 24cm, Matrix; 320x320, NEX; 3). T1-weighted T1-Flair images (2400/24 [repetition time msec / echo time msec], Inversion Time; 1000msec, Echo Train Length; 6, GAP; 0mm, Field of View; 24cm, Matrix; 320×256).

3 Tesler MRI

MRI Images were obtained with a 3.0-Tesla whole-body imager (Signa EXCITE HD; GE Medical Systems, Japan) by using a 8 channel Brain Array Coil. The protocol included axial T2-weighted fast spin-echo images (4000/102 [repetition time msec / echo time msec]; Echo Train Length; 16, Section Thickness; 3mm, Gap; 0mm, Field of View; 24cm, Matrix; 512×320). T1-weighted T1-Flair images (2200/9.1 [repetition time msec / echo time msec] Inversion Time, 1000 msec, Section Thickness; 3mm, GAP; 0mm, Field of View; 24cm, Matrix; 320×256). 3D-SPGR (Spoiled Gradient Echo) images (11.8/5.2 [repetition time msec / echo time msec] Flip Angle; 10°, Slice Thickness; 1.4mm, Location per Slab; 60mm, Field of View; 24cm, Matrix; 320×256)

DWI (Diffusion Weighted Image)

Pulse Sequence; Spin Echo EPI; TR=5000msec, TE=75.9msec, Field of View; 24cm, Slice Thickness; 3.0mm (for 3Tesler) or 5.0mm n (for 1.5Tesler), Spacing; 0mm, Matrix; 256×128, NEX; 2 times, Imaging Option; ASSET (Asset Factor; 2.0).

In daily interventions, three types of images, including T1-weighted images (T1WI), T2-weighted images (T2WI) and diffusion-weighted images (DWI) are obtained by this method for each patient.

1-2. PET

a. The subjects were scanned using an ECAT PT931/04-12 scanner (CTI Inc. Knoxville, TN, USA), and further subjects were administered placebo and scanned with the same equipment. The ECAT PT931/04-12 scanner has a spatial resolution of 7-8mm FWHM in the center of the field of view (FOV) and has a 5cm-long axial FOV that is not capable of covering the whole brain.

b. Tracer: ^{18}F-FDG=2-deoxy-2-[^{18}F]fluoro-D-glucose used as a trace[9,10].

1-3. Subjects

Normal volunteers

A total of 16 normal volunteers (males 8 and females 8) their age ranged from 13 to 89 were selected as a control group. Moreover, a total of 14 aged subjects (males 7 and females 7) their age ranged from 65 to 87 were added to the control group for the study on onset and progression of AD.

AD patients

- AD patients were distinguished from normal subjects by MMSE (minimental state examination)[11] and MRI images, number of AD patients male 58 female 99, total 157, their age ranged from 65 to 83.
- Subjects for preventative treatment; patients of mixed type of mental disease depression and schizophrenia with hippocampus atrophy were selected to subjects for preventative treatments. Number of patients is 179 male and 277 female, total of 456, their age ranged from 14 to 85.

1-4. Diagram of regenerative medicine for prevention and treatment of AD (Fig. 2)

1-4-1. Onset

1) Heavy stress lowers the serotonin level, causes destructions of depression and makes a patient go into depression.

2) Total dopamine generates a toxicity that total dopamine originally has due to the decreased serotonin level, resulting in destructions of schizophrenia in the amygdala.

- In the normal state, the amount of total dopamine and serotonin is stable, owing to the negative feedback mechanism. Generated destructions demolish this stability mechanism, resulting in a discharge of total dopamine. The patient develops positive symptoms of schizophrenia. Likewise, serotonin is also discharged and the patient goes into a manic state. Bipolar depression is caused an abnormally high or low serotonin level. In AD, the destructions shown above and progressive atrophies of the hippocampi develop and progress to AD.

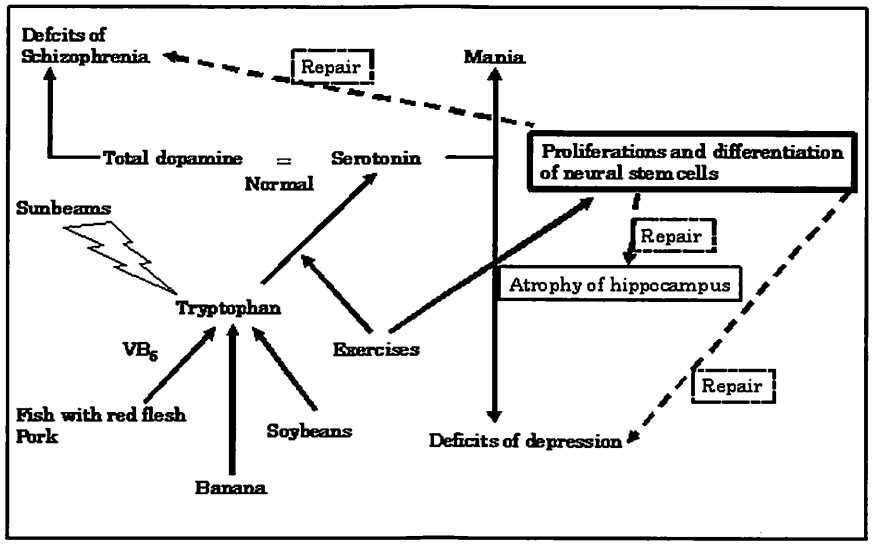

Figure 2. Diagram of regenerative medicine for prevention and treatment of AD.

1-4-2. Treatments

1) Pharmacologic treatment

Antidepressant drugs and antipsychotic drugs should be administered to patients at the same time without fail to normalize the amount of serotonin and total dopamine and stabilize the symptoms of patients. A minimum of necessary drugs should be used.

2) Alimentary therapy

Patients should eat foods that are rich in tryptophan, which is a precursor of serotonin (e.g., soybeans, bananas and lean fish). Patients should be advised to eat pork containing arachidonic acid, which is a component of the cell membrane.

3) Exercise therapy

This is an important therapy indispensable for increasing the serotonin level in the body and accelerating the proliferation and differentiation of neural stem cells.

4) Suggestion and persuasion therapy

It is important to explain the healing status of neural stem cells while showing images and to give an explanation that the disease can be completely healed to patients and family members.

2. Results

2-1. Primary foci of AD

All destructions (deficits) of Fig. 3b, c and d are observed in Alzheimer's disease patients. In other words, all of them are the primary focus of AD. MMSE (Mini Mental State Examination) is a mental test developed by Folstein et al. It is widely used throughout the world to discriminate AD patients from normal persons. AD is diagnosed if the MMSE score is 23 or less and atrophy of the hippocampus were recognized by MRI image.

Among mental disorders which are called by various names such as depression, schizophrenia, bipolar disorder, major depression, obsessional neurosis and social withdrawal, a patient always has both destructions b and c of depression and schizophrenia based on 3000 or more cases. All mental disorders are a mixed mental disorder caused by depression and schizophrenia. In the development of the mixed mental disorder,

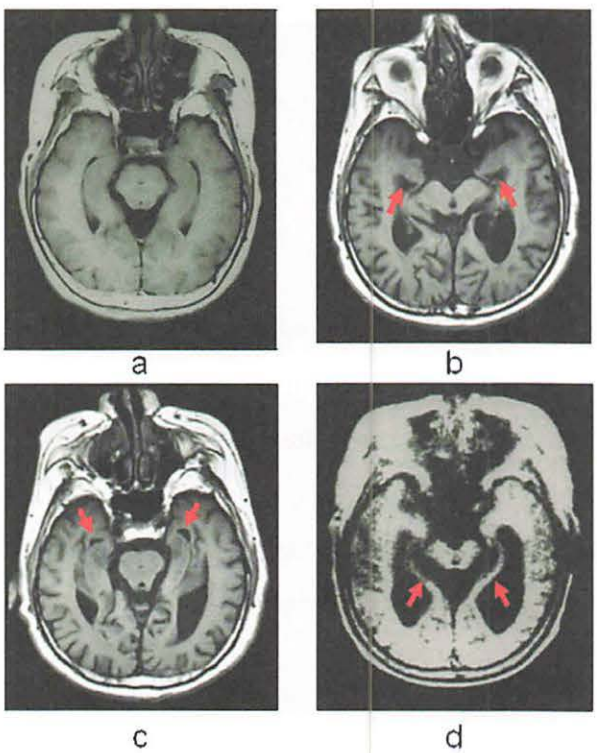

a; normal volunteer, 71 year's old female
b; deficits of depression, 78 year's old male, AD patient
c; deficits of schizophrenia, 78 year's old male, patient
d; atrophy of hippocampi , 66 year's old female, AD patient

Figure 3. Primary foci of AD.

depression develops due to an abnormal reduction of serotonin and schizophrenia develops due to an abnormal increase of total dopamine. It seems that the mixed mental disorder consisting of depression and schizophrenia develops because the reduction and increase occur almost simultaneously.

The mixed mental disorder is roughly divided into the dementia type, social withdrawal type and affective disorder type. The dementia type is accompanied by an atrophied hippocampus. Dementia is sometimes observed in young people (i.e., presenile dementia). AD is dementia of the mixed mental disorder occurring in elderly people (65 years old or more), i.e., atrophied hippocampus type.

2-2. Onset and progression of AD

Figure 4 shows the onset and progression of AD. AD shows various symptoms accompanying its onset and progression. This is because AD is a progressive hippocampus atrophy type of mixed mental disorder consisting of depression and schizophrenia.

Photos on the left side of Fig. 4 show the progression of the atrophy of the hippocampus with MRI (T1WI). Photos on the right side of Fig. 4 show working conditions of the cerebral cortex with PET. Changes in glucose utilization imaged by PET were correlated with the atrophy of the hippocampus imaged by MRI.

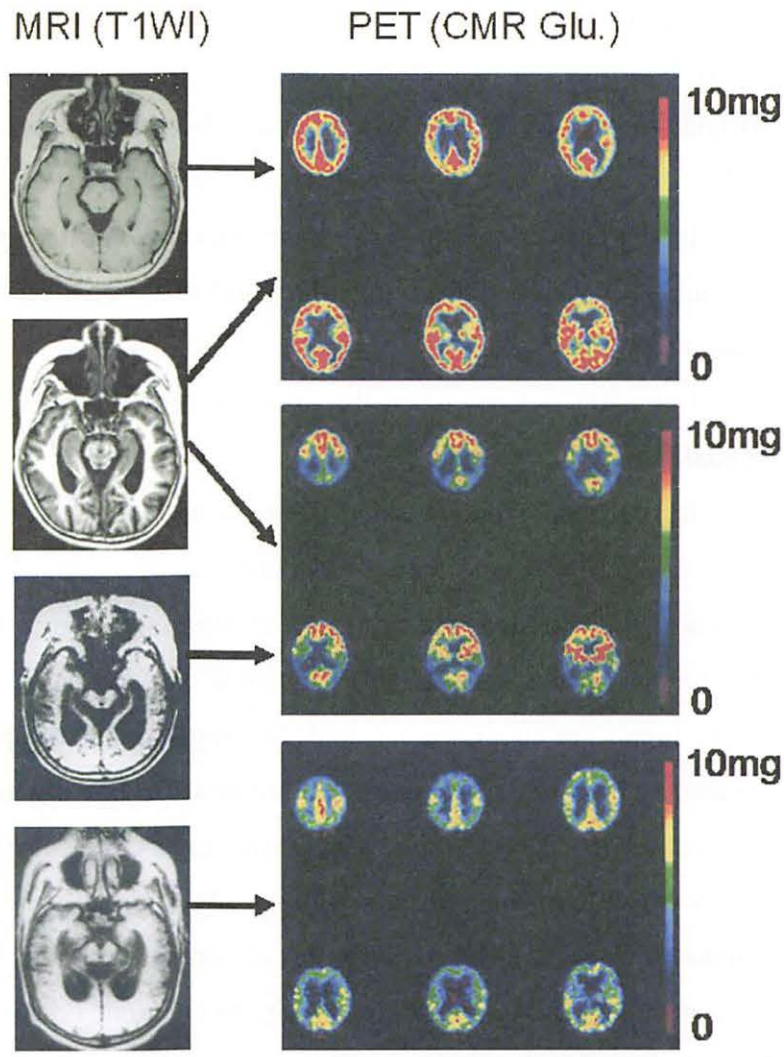

Figure 4. Onset and progression of AD.

The cerebral cortex is roughly divided into left and right hemispheres, and the frontal and occipital lobe. They have different functions respectively. The primary area controlled by the brain stem, the brain of life, which works when humans look, listen and touch, and the association cortices of the higher-order brain function area controlled by the hippocampus, amygdala, ventral striatum, etc., (i.e., the brain of the mind) which works when humans think, are impressed, and have desire are mixed within the cerebral cortex.

Photos in Fig. 4 show the working states of the cerebral cortex sliced into six layers by height. The amount (mg/brain, 100 g/min) of glucose utilized by 100 g of the brain is indicated by color (0-10 mg) using a tracer (^{18}F FDG). The red and yellow show the regions of the brain which are functioning normally. The blue shows the regions of the brain whose function is decreased.

AD is a disease whose symptoms get worse and ultimately lead to death. Atrophy of the hippocampus progresses bilaterally. The destruction progresses to a certain level where both sides of the posterior half, i.e., six association cortices including the temporal, parietal and occipital lobes synchronously become impaired at once. This is the onset of AD.

In the early stage, patients sometimes develop dementia and sometimes return to a normal state, as if a light is turned on and off. This state is called intermittent dementia (early stage).

Dementia is fixed when the bilateral atrophy of the hippocampus further progresses (middle stage).

In the middle stage, patients have a high forgettery and loss faculty of orientation. They do not know who they are, where they are, and what they were doing at that time. Additionally, various symptoms such as depressive symptoms and delusions of persecution develop. In this stage, patients wander at day and night. Furthermore, bilateral atrophy of the hippocampus progresses and the hippocampus disappears. Then, the entire limbic systems in both sides disappears and are replaced by "big holes." At this point in time, the prefrontal cortex and several motor association cortices also become impaired because the lesion expands to the ventral striatum. At this moment, all association cortices become impaired. Consequently, higher-order integrated functions of all association cortices, (e.g. memory, learning, cognition, thinking, motivation, creativity, and emotion) will be lost. Patients lose their humanities. However, the primary functions to sustain life (e.g. optical, auditory and tactile sensations, food appetite and the ability to excrete) remain almost intact

and can survive (Late stage).

2-3 Pathology of AD

Figures 5A and B show findings of autopsies of patients who died from AD and other diseases. Figure 5A shows the brain of a patient who died due to AD (left) and the brain of a patient who died due to a different disease (right) seen from underneath. The author thanks Dr. Toshio Mizuno for his providing the photos.

Bilaterally symmetric holes (deficits) are observed in the left and right limbic system. This coincides with the findings of MRIs showing that AD is a disease causing deficits in the limbic system. Another important finding is that the cerebellum of patients who died of AD is hypertrophied (several times larger than that of patients who died of other diseases). This is supposed to be a compensatory hypertrophy to compensate for the dysfunction of cerebral cortices, suggesting that neural stem cells are proliferating and differentiating. Further research is required in this field.

Figure 5B is a photomicrograph of the remaining amygdala. The figure is a photomicrograph at a magnification of 200. The cells are dyed with a silver impregnation stain. The larger cells with projections are normal neural cells (B). They are gradually reduced in size (C) and fall to pieces. This kind of cell death is called cell suicide or apoptosis[12].

Many cells (D), like small lymphocytes, are observed along with senile pigment flecks (A). Most of them are macrophages (histiocytes). It is likely that they include killer T cells which trigger apoptosis.

2-4. Colony of neural stem cells in presenile dementia and AD

Figure 6A shows images of the brain of a 23-year-old male diagnosed with schizophrenia by a psychiatry shot by T1WI (upper row) and DWI (lower row) using Matsuzawa's tomographic method. Images of continuous sections were created from bottom to top (left to right in the figure) by a 3-Tesla MRI apparatus with slice thicknesses of 3 mm and no gap. T1WI (the first and second photos from the left) shows the destructions of schizophrenia half-healed through, treatments. The rightmost photo shows half-healed destructions of depression.

This patient is a psychiatric patient with schizophrenia mixed with depression. Based on more than 3000 cases diagnosed by Matsuzawa's tomographic method, all patients

Macroscopic findings

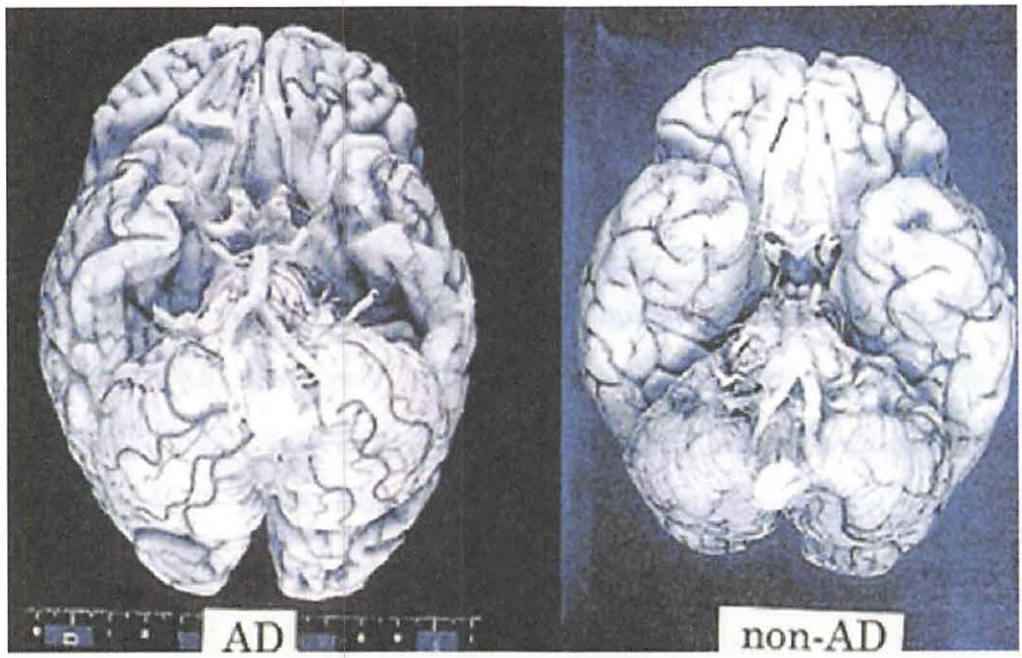

Symmetral destraction of limbic system and enlargement of cerebellum in AD brain. This coincides with the MRI image.

Histological findings of the amygdata(silver stain)

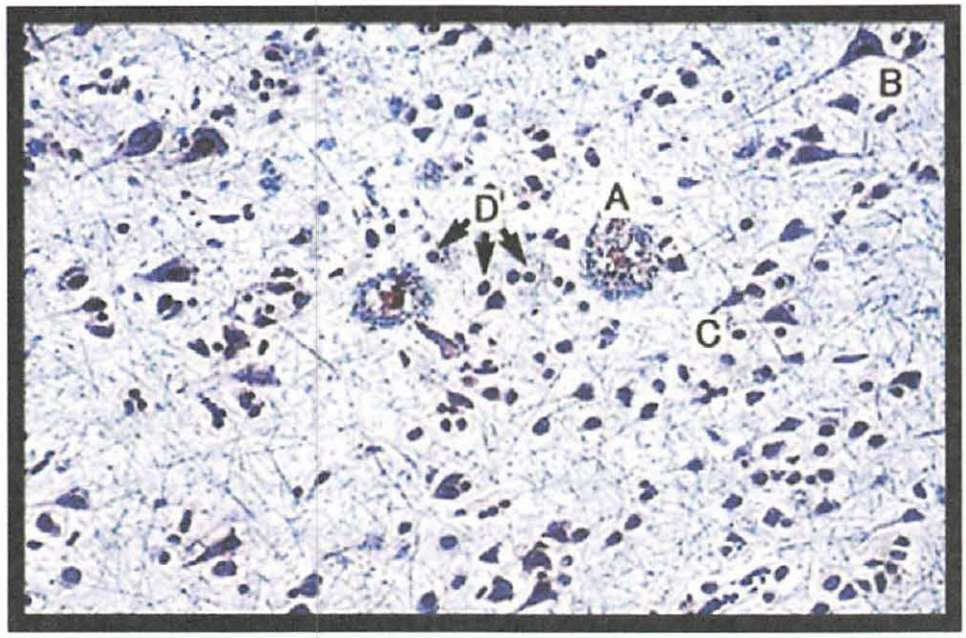

A senile pigment flecks
B neural cell (normal size)
C neural cell dying due to apoptosis
D macrophage + killer T cell

Figure 5. Pathology of Alzheimer's disease.

with "diseases of the mind" are categorized into this mixed type. Not one patient who developed only depression or only schizophrenia has been found. Actually, the disease which has been called by various names such as depression, schizophrenia, major depression, bipolar disorder and obsessional neurosis was actually this depression-schizophrenia mixed mental disorder.

Photos imaged by DWI in the lower row show a colony of neural stem cells (white areas indicated by arrows). Colonies of neural stem cells are observed all over, in areas such as the periphery of cerebral ventricles, hippocampus, amigdala and cerebral cortex. The reason why the author identifies them as colonies of neural stem cells will be explained later in this report.

Figure 6B shows images of a 69-year-old female diagnosed as having AD (MMSE=18). In this report, 65-year-old or older patients with degenerative dementia are called AD. These images are obtained by a 1.5-tesla MRI. T1WI images in the upper row show destructions for schizophrenia (1), destructions created by destructions of schizophrenia combined with atrophies of the hippocampi (2), and destructions of depression (3 and 4). In the DWI images in the lower row, many colonies of neural stem cells are observed all around (arrows) and this case may be cured through appropriate treatments.

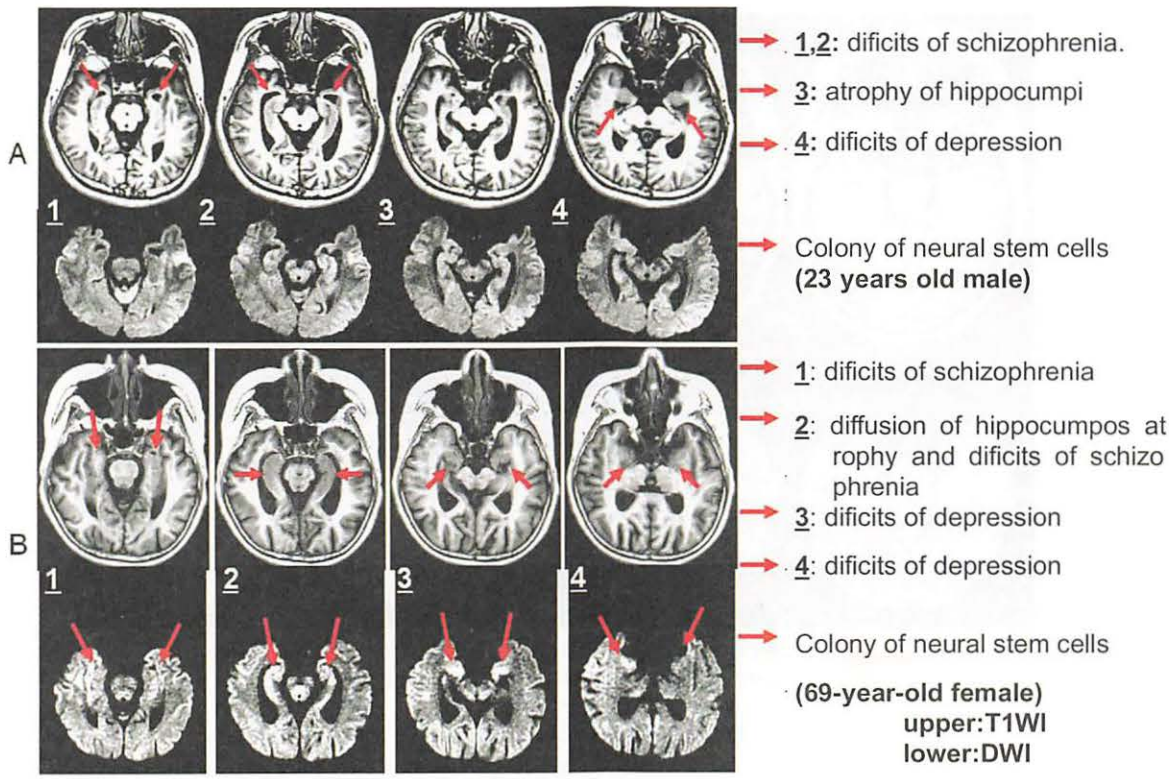

Figure 6. Colony of neural stem cells in senile dementia and AD.

The number of colonies is smaller than the case of the 23-year-old male in Fig. 6A. The blood total dopamine of the patient was abnormally high, at 96 ng/ml (normal value: 0.5-6.2 ng/ml). Meanwhile, the blood serotonin was abnormally low, at 3 ng/ml (normal value: 53-200 ng/ml).

Mixed mental disorders which are "mental diseases" and Alzheimer's disease develop develop due to an imbalance between total dopamine and serotonin. The details will be explained in a separate report.

2-5. Presenile dementia (Fig.7)

24-year-old female with mixed type of mental disorder visited us on October 5, 2005. She had a significant disorder of memory. She forgot things that had happened just recently and that she had eaten food immediately before. She visited us accompanied by her family. Her MMSE score was 19. She recovered significantly through therapies. Symptoms disappeared in October, 2006. She learned to be able to lead an active life and read books. Her MMSE recovered to 26. She is taking no medicine. T1WI and DWI images show that the destructions of schizophrenia and depression have been repaired and atrophies of the hippocampi have been improved completely.

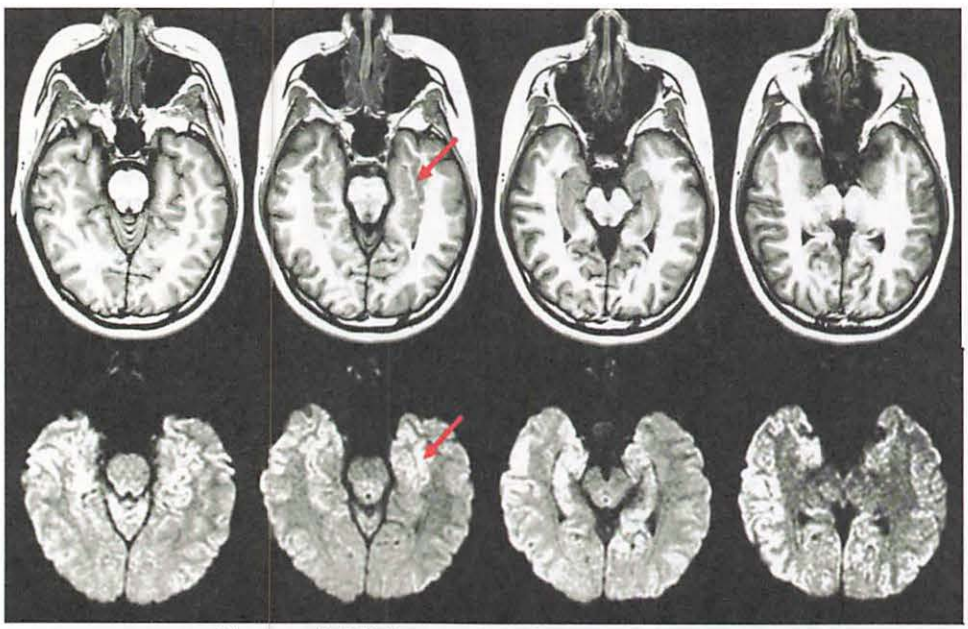

Figure 7. Full cure case of senile dementia (24-year-old female).

2-6. Alzheimer's diseases (AD)

Cure cases of AD

Full cure case (Fig. 8A)

A 78-year-old male visited us on November 22, 2004. He had symptoms in that he forgot things a lot, could not find his way home after going out, and could not read books or watch TV. He visited us accompanied by his wife. He responded relatively well to the treatments. T1WI images show the destructions of schizophrenia and the hippocampi repaired by neural stem cells. To our astonishment, the findings of T1WI on July 23, 2007 showed that colonies of neural stem cells had proliferated from the periphery of the hippocampi and had differentiated into cerebral cortex-like tissues. Neural stem cells are multipotent cells that can differentiate into any kind of cells as long as they are cells in the brain. In this case, MMSE was improved from 18 to 26.

Resistant case (Fig. 8B)

This is a treatment resistant case. A 79-year-old female with symptoms of completely forgetting things and loss of orientation visited us accompanied by her family. She did not respond to the treatments. Instead, she went from bad to worse. T1WI and T2WI images show significant bilateral atrophies of the amygdala and hippocampus. DWI shows few colonies of neural stem cells. MMSE was 10 or less.

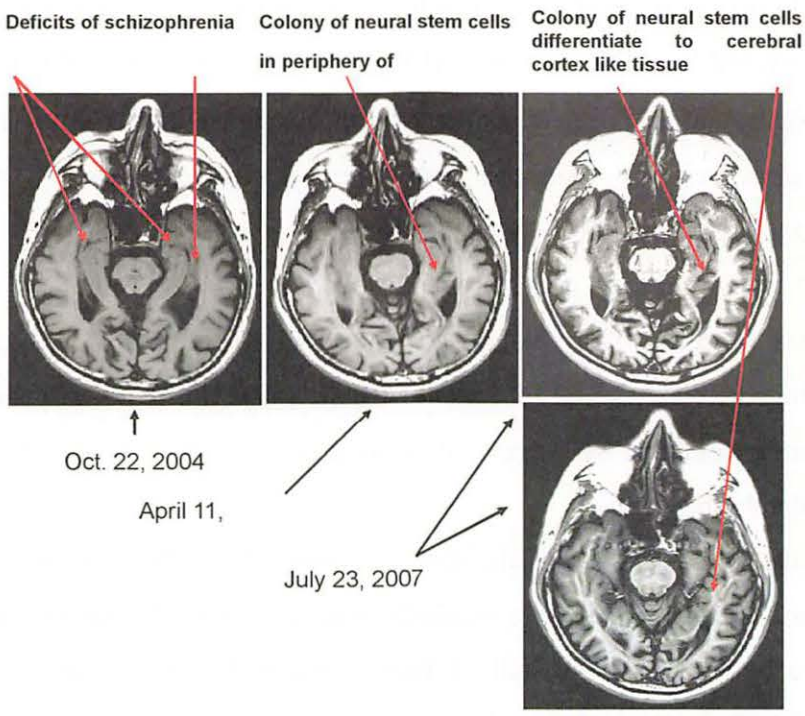

Figure 8A. Full care case of AD (78-year-old male).

Figure 8B. Resistant case of AD (79-year-old female).

2-7. Combined results of regenerative medicine for prevention and treatment of AD

- *Combined results*

Figure 9 shows the combined results. Treatments were performed by dividing subjects into a would-be-AD group and Alzheimer's patients. The Would-be-AD group included 179 male and 277 female patients with atrophied hippocampi (total: 456) and mixed mental disorders who visited us over a period of three years (36 months). This cohort included all age groups from pre-teens to 80's.

The AD patient group patients were referred to our hospital by other medical institutes. They were positively diagnosed with AD by MRI and MMSE at our hospital. The group included 58 males and 99 females (total: 157) who were 65 years old or older. Both groups underwent the AD regenerative medicine treatment. The procedures were basically completely the same.

For results, "cure" and "convalescence" accounted for 89.4% in total of the would-be-AD (preventive care) group. It suggests that this method changes almost 90% of patients for the better and about half of them are cured. "Cure" and "convalescence" accounted for 74.6% in total of the AD group. This percentage is lower than that of the

preventive care group by 10% or more. This difference is caused by the difference in ages between the target groups, and ultimately by the difference in proliferations and differentiation of neural stem cells.

3. Discussion

1. It has become apparent that treatment results of regenerative medicine depend on the proliferation and differentiation potency of neural stem cells.
2. It is expected that iPS cells could be safely and effectively used for regenerative medicine in Alzheimer's disease in the near future.
3. For many ongoing studies on Alzheimer's disease, the following items may be commented on the results of Alzheimer's disease:
   1) Neurofibrillary degeneration (protein tau),
   2) Deposition of β amyloids,
   3) Decrease of acetylcholine, etc.

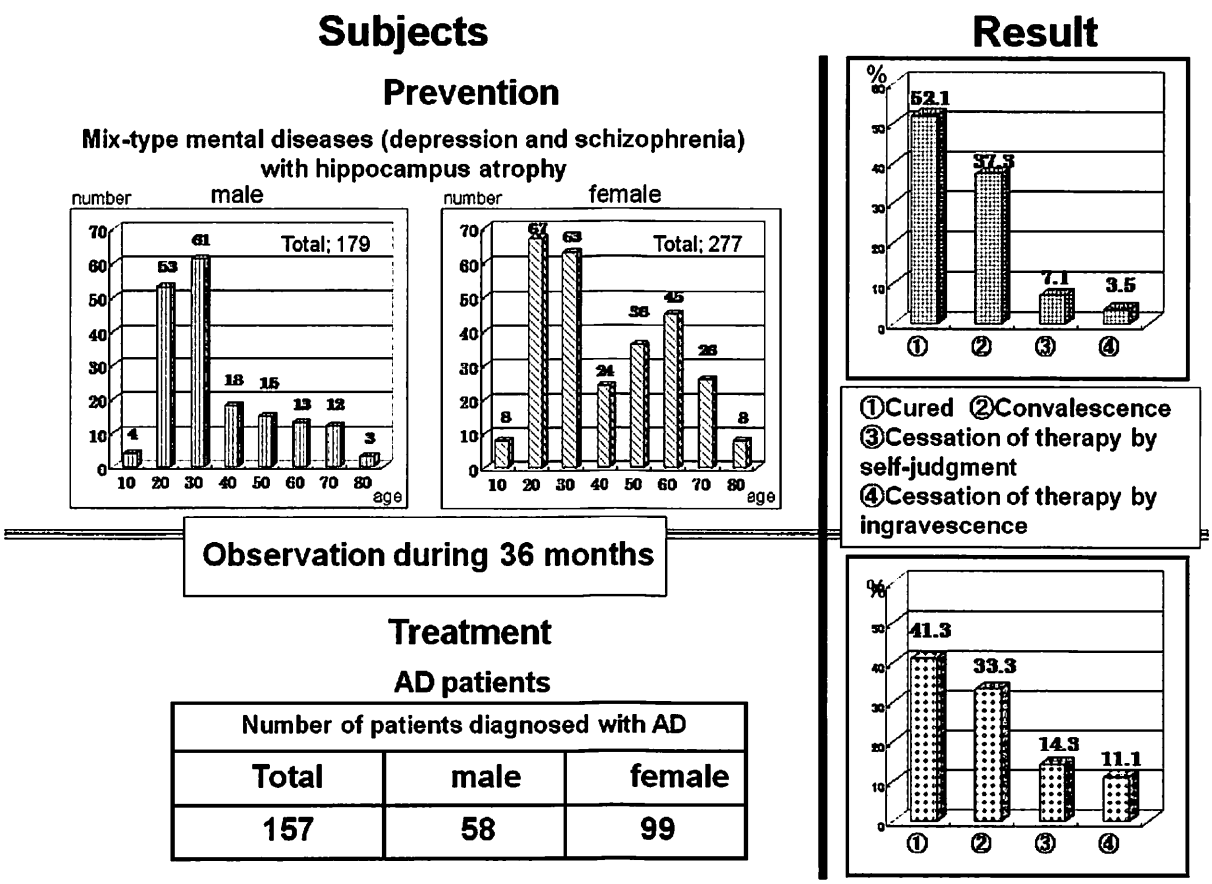

Figure 9. Combined results regenerative medicine in AD.

4. Conclusion

Alzheimer's disease is a disease in which a specific destruction (deficit) occurs both in the hippocampus and the amygdala in the limbic system symmetrically on both sides. In general, there is a mechanism by which wounds of the living human body are healed. This mechanism involves neural stem cells which proliferate and differentiate into glial cells and neural cells. Regenerative medicine, in which Alzheimer's disease can be prevented and cured, is realized by inducing the healing capacity of neural stem cells through appropriate treatments.

References

1) Alzheimer A., Allgemeine Zeitschrift fur Psychiatrie **64** (1907) 146.
2) Yamaura H., Itoh M., Kubota K., Matsuzawa T., J. Gerontrogy **35** (1980) 492.
3) Itoh M., Hatazawa J., Yamaura H., Matsuzawa T., Brit. J. Radiol. **54** (1981) 384.
4) Takeda S., Matsuzawa T., J. Am. Geriatr. Soc. **32** (1984) 520.
5) Matsuzawa T., Bulletin of Tohoku Fukushi University **25** (2000) 139.
6) Altman J., J. Comp. Neurol. **126** (1966) 337.
7) Watts C., J. Anat. Sep., **207** (2005) 197.
8) Ramon Y., Cajal S., Degeneration and regeneration of the nervous system, Hafner, New York, 1928.
9) Sokoloff L., Mongold R., Wichsler R.L., Kennedy C., Kety S.S., J. Clin. Invest. **34** (1955) 1101.
10) Reivich M., Kuhl D., Wolf A., Greenberg J., Phelps M., Ido T., Casella V., Fowler J., Hoffman E., Alavi A., Som P., Sokoloff L., Circ. Res. **44** (1979) 127.
11) Folstein M.F., Folstein S.E., McHuge P.R., J. Psychiatr. Res. **12** (1975) 189.
12) Kerr J.F.R. et al., Br. J. Cancer **26** (1972) 239.

I. NUCLEAR PHYSICS

I. 1. Low Background Beta-ray Spectroscopy Based on a Counter Telescope with Plastic Scintillation Detectors

Orihara H., Yamamoto M., Stoh Y., and Umeda K.

Center for General Education, Tohoku Institute of Technology

Bata-ray spectrometer, consisting of two peaces of plastic scintillator forming a counter-telescope, has been developed for the purpose of compliance with the clearance level for solid materials generated from the decommissioning and operation of the reactors at electric power plants. Due to coincidence measurements, background-free counting for low-level emission of the beta-ray is available. Compliance with the clearance level for solid materials is in the order of 0.01 Bq/gr with the present beta-ray spectrometer.

In the case of clearance compliance, judgment is carried out by measuring specific gamma-rays such as these from ^{59}Co etc, mainly due to the conveniences to detect gamma-ray compare to these to analyze beta-rays. However, counting of gamma ray is not straightforward for judgment of the density of activity in the unit of Bq/g, while that of beta ray is directly connected to the activity in the unit of Bq/g in the clearance object. As such, a compact system to detect beta-ray with low background and high-efficiency specifications is strongly awaited for.

One of the most important points in the system specification is "low-background", since the radiations, concerning clearance level, are more than ten times smaller in magnitudes comparing to those of surrounding natural radiations. For this purpose, the counter telescope type detector has been tested[1]. In Ref. 1, beta energies were measured via a 5 cm diameter ~ 2 cm thick BC-404 plastic scintillator preceded by a single, 100 mm thick, totally depleted, silicon D*E* detector. Photon events in the *E* detector were rejected by requiring a coincidence between the *E* and D*E* detectors. Photon rejection ratios vary from 225:1 at 1.25 MeV (^{60}Co) to 360:1 at 0.36 MeV (^{133}Ba).

Beta-ray Detector and Measuring System

In this report, we discuss another beta-ray detector for clearance level inspection,

where much more simple composition is essentially requested. As such, we used a thin plastic detector, in stead of silicon semi-conductor, for D*E* counter.

Figure 1 illustrates the counter-telescope type beta-ray detector tested in the present experiments.

As shown in Fig. 1, the counter telescope is consists of two detectors. The D*E* counter is made of 50 mm-thick NE-102A plastic scintillator, the size for which are 20×20 mm^2. The counterpart E-counter is made of the same NE-102 plastic scintillator, the size for which are 20×20 mm^2 and 30 mm in its length.

From the technical points of view, light shield was difficult, since a beta ray passes through three times the light-shield losing its energy significantly. In the present detector, 30 mm-thick black-tapes shut out completely lights from outside. These arangements makes a particle identification system. The several hundred keV-energetic electrons are able to go through three by 30 mm-thick black-tapes and one 50 mm thick plastic scintillator, and produce two electric signals, while gamma ray gives us only one signals produced in thicker 20 mm scintillator. Figure 2 shows the electric diagram for beta-ray counting. The system is nothing but ordinary one. Two signals formed by linear amplifiers are analyzed by two-dimensional analog to digital converter (2D-ADC) and (512×512) list data are stored in the computer memories.

Performance Test and Results

Performance tests have been carried out by measuring beta-rays from radioisotopes of ^{90}Sr with the beta-rays (Q_b = 2.28 MeV), ^{137}Cs with a beta-ray (Q_b = 0.51 MeV) and monochromatic electrons with E_e=0.625 MeV, and RaD(^{210}Pb) with a beta-ray (Q_b =1.18 MeV). Figure shows pulse-hight spectrum projected to the axis of thick detector. The single peak due to internal conversion electron is clearly seen.

Further measurements have been carried out for ^{90}Sr and RaD(^{210}Pb). Continuum spectra are illustrated in Fig. 5 together with fitting by phase space calculation: with

$$\frac{dn}{dE_0} = \frac{dw_e dw_\nu}{(2\pi\hbar)^6 c} \cdot (E_0 - E)^2 \cdot \sqrt{E^2 - m_e^2 c^4} \cdot EdE$$

, where E_0 is Q-value of beta decay.

Line shapes of continuum electron spectra have been reproduced successfully by calculations. The energy resolution for the monochromatic 625-keV electrons from ^{137}Cs source is 13.6%. The detection efficiency for the 625-keV electrons from ^{137}Cs source is 53.0%.

Conclusion

A low-background, compact and high-resolution beta ray spectrometer has been constructed. Compliance with the clearance level for solid materials is now in the order of 0.007 Bq/gr in the energy range of ~625 keV with the present beta-ray spectrometer. The size of the spectrometer is 20 mm×20 mm. Further development for larger detector is needed for practical use.

Reference

1) Holowitz Y. S., et al., Nucl. Instrum. And Meth. In Phys. Res., A**338** (1994) 522.

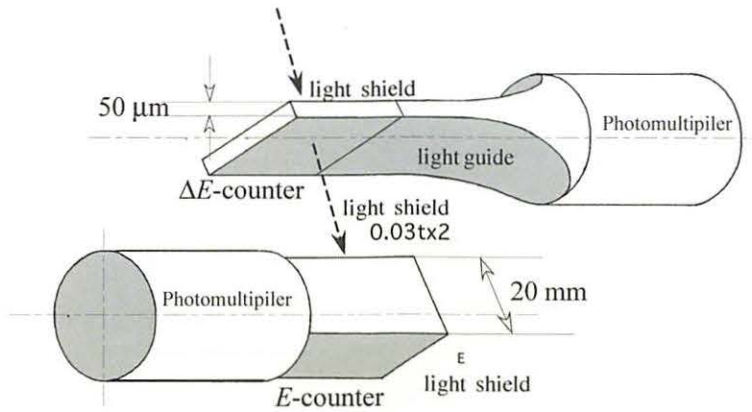

Figure 1. Counter telescope beta-ray spectrometer.

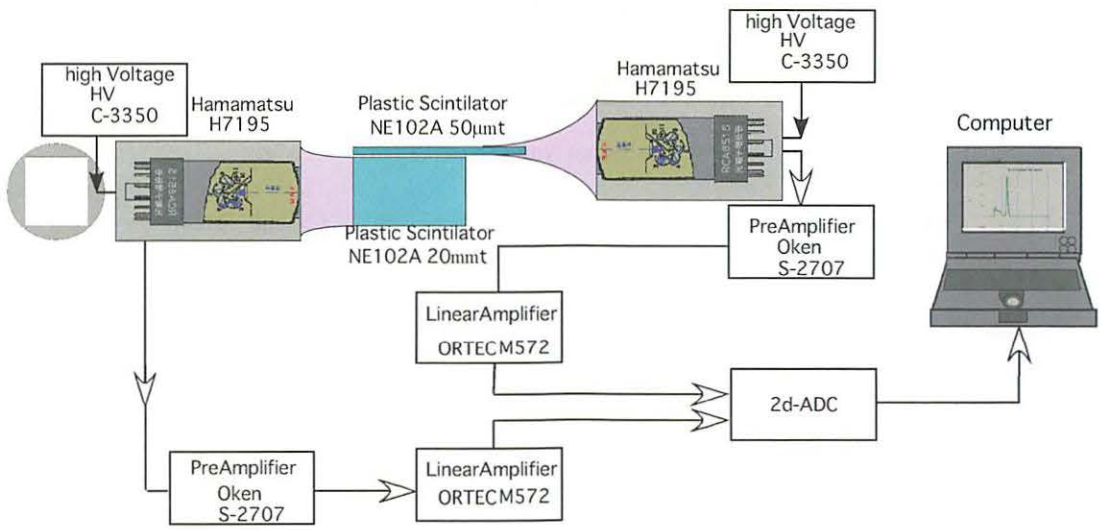

Figure 2. Electric diagram for beta-ray counting.

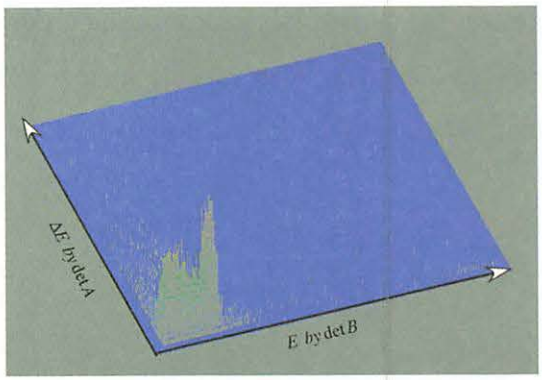

Figure 3. Two dimentional display of two signals from counter telescope system.

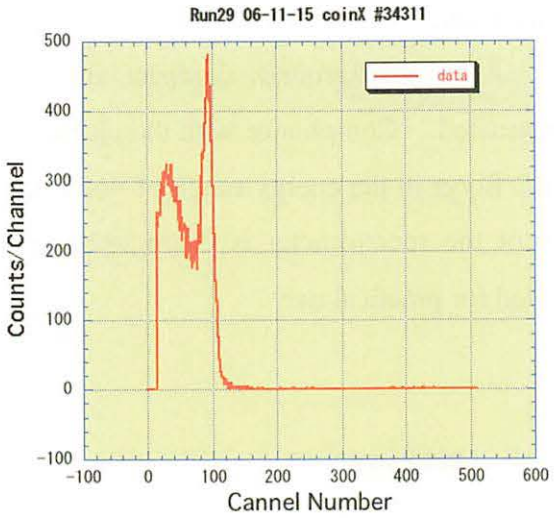

Figure 4. Projected energy spectrum of beta ray from ^{137}Cs projected. Monochromatic peak corresponds to events of 625-keV conversion electrons.

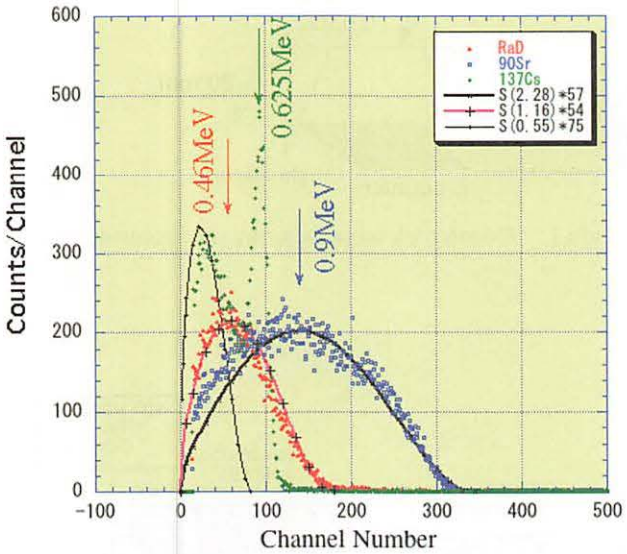

Figure 5. Projected spectra of beta rays from ^{90}Sr, ^{137}Cs and RaD. Lines are fitting by phase space distribution.

I. 2. Half-life and Magnetic Moment of the First Excited State in ^{132}I

Izumi S.[1], Tanigaki M.[2], Ouchi H.[1], Sasaki A.[1], Miyashita Y.[1], Sato N.[1], Hoshino S.[1], Shimada K.[3], Wakui T.[3], Shinozuka T.[3], and Ohkubo Y.[2]

[1]Department of Physics, Tohoku University
[2]Research Reactor Institute, Kyoto University
[3]Cyclotron and Radioisotope Center, Tohoku University

The recent progresses in the shell model calculations[1] enable the detailed discussions on the nuclear structure in the region around ^{132}Sn. In this region, there has been a long time confusion on the half-life measurements of the first excited state in ^{132}I. Several groups performed the lifetime measurements, but the reported values range from 1 ns to 7 ns[2-4]. Therefore, the magnetic moment of this state reported by Singh[5] should not be treated as reliable because they used time-integral perturbed angular correlation (TIPAC) method, where the Larmor frequency was determined as the rotation angle of the nuclear alignment during the lifetime of this state.

On the other hand, iodine, which is one of the elements in the halogen family, plays important roles in the materials with high conductivity. ^{132}I is expected to be a good probe nucleus in the halogen family as far as the half-life of $T_{1/2}$=7.14 ns reported by Yousif[3], which is suitable for perturbed angular correlation (TDPAC) measurements, is true.

Based on these points of view, we report the determination of the half-life and the magnetic moment of this state[6].

The first excited state in ^{132}I was populated by the β-decay of ^{132}Te ($T_{1/2}$ = 3.204 d) obtained as a radioactive beam of A = 132 from the RFIGISOL (Radio Frequency Ion Guide Isotope Separator On-Line system) at Tohoku University[7,8]. This is the first successful extraction of a radioactive beam in the region around ^{132}Sn by RFIGISOL. The radioactive beam, of which intensity is 500~1000 atoms/s in terms of ^{132}Te, is implanted into either aluminum or nickel foil for off-line measurements. The contaminations in the sample were attenuated by cooling the sample down for a few hours. After this cool-down, implanted foil was cut into several pieces, and we used only selected pieces in which ^{132}Te

was dominantly implanted.

The half-life of the first excited state in ^{132}I was determined to be $T_{1/2}$ = 1.120±0.015 ns by observing the cascade of 228.2 and 49.7 keV with a pair of BaF_2 detectors. A sufficient time-resolution of this system was confirmed by the prompt gamma rays. The obtained time spectra are shown in Fig. 1.

TDPAC measurements were performed for the first excited state of ^{132}I implanted into Ni. A strong hyperfine field of B_{hf} = +(26.5 ±0.5) T at the iodine site in nickel was applied and an external field of 0.3 T was applied to produce the alignment of this hyperfine field. We have developed a so-called cage type magnet for suppressing the effect of the fringing field towards the low-energy detection by BaF_2 detectors. Three BaF_2 detectors were placed form ± 135° in a plane perpendicular to the external magnetic field, then the time dependence of the asymmetry is given as follows:

$$R_{\pm}(t) = \frac{N_{\pm}(t,\mp 135) - N_{\pm}(t,\pm 135)}{N_{\pm}(t,\mp 135) + N_{\pm}(t,\pm 135)} = \frac{3}{4} A_{22} \sin(\pm 2\omega_L t), \quad (1)$$

$$\omega_L = -\frac{\mu B}{I\hbar}, \quad (2)$$

where $N_{\pm}(t, \alpha)$ is the number of coincidences between the two γ rays at 0 and α degrees, and the subscript $\pm$ in Eq. (1) stands for the direction of the external magnetic field. μ and I are the magnetic moment and the spin of this state, respectively, and B is the magnetic field at the nucleus. A typical TDPAC spectrum is shown in Fig. 2. The magnetic moment for this state was determined to be μ = +(2.06 ± 0.18)μ_N.

The present magnetic moment result is consistent with the magnetic moment for $(\pi g_{7/2})(\nu d_{3/2})^{-1}$ (μ = +2.40 μ_N) which is calculated by using a simple *jj*-coupling model and the empirical g-factor of neighboring nuclei. The present results are consistent with the half-life value obtained by Gorodetzky *et al.* and the magnetic moment value obtained by Singh *et al.* Then, the transition probability, $B(M1)$ deduced from the present half-life value is 1/50 of Weisskopf unit, and may indicate a large $M1$ retardation for this state.

This is the first successful extraction of a radioactive beam in the region around ^{132}Sn from the RF-IGISOL at Tohoku University. We will extend the magnetic moment measurements in this region with radioactive beams produced by the RF-IGISOL.

References

1) Brown B.A., Stone N.J., Stone J.R., Towner I.S., Hjorth-Jensen M., Phys. Rev. **C71** (2005) 044317.
2) Gorodetzky., Schulz N., Chevallier J., Knipper A.C., J. Phys. (Paris) **27** (1966) 521.
3) Yousif A.A., Hamilton W.D., Michelakakis E., J. Phys. **G7** (1981) 445.
4) Das S.K., Guin R., Saha S.K., Eur. Phys. J. **A4** (1999) 1.
5) Singh V., Tandon P.N., Devare S.H., Devare H.G., Nucl. Phys. **A132** (1969) 221.
6) Tanigaki M., Izumi S., et al., Phys. Rev. **C80** (2009) 034304.
7) Miyashita Y., Wakui T., Sato N., Yamazaki A., Endo T., Fujita M., Goto A., Kinoshita S., Koike T., Ma Y., et al., Nucl. Instrum. Methods **B266** (2008) 4498.
8) Sonoda T., Fujita M., Yamazaki A., Endo T., Shinozuka T., Miyashita Y, Sato N., Goto A., Tanaka E., Suzuki T., et al., Nucl. Instrum. Methods **B254** (2007) 295.
9) Reintsema S.R., Waard H., Drentje S.A., Hyp. Int. **2** (1976) 367.
10) Akai H., Akai M., Bl¨ugel S., Drittler B., Ebert H., Terakura K., Zeller R., Dederichs P., Prog. Theor. Phys. Suppl. **101** (1990) 11.

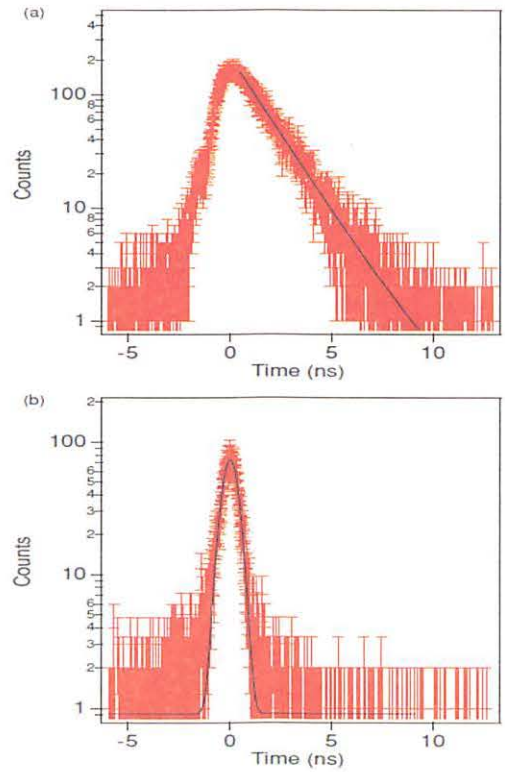

Figure 1. (a) Time spectrum of the 228.2- to 49.7-keV cascade. A single exponential curve with a constant term was applied as a fitting function to the data. (b) Time spectrum taken with the γ-gates shifted slightly above to miss the 228.2- to 49.7-keV cascade. A Gaussian function with a constant term as the fitting function was applied to the data.

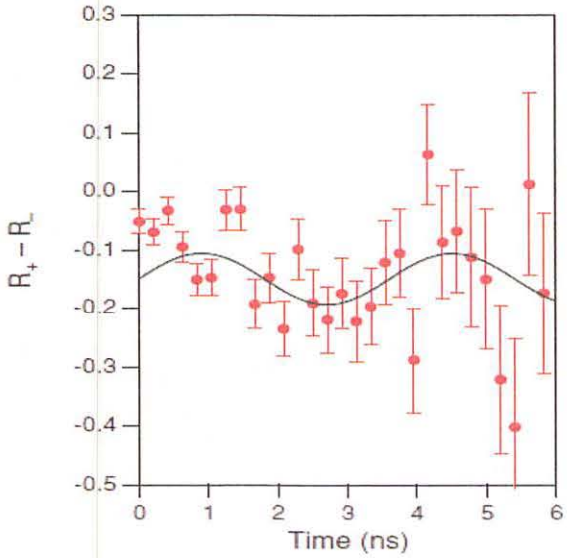

Figure 2. TDPAC spectrum of ^{132}I in nickel. We performed two runs of the TDPAC measurements by inverting the direction of the external magnetic field along with the sample. Then, one obtain the enhanced asymmetry change by subtraction as $R_+(t) - R_-(t) = 2R_+(t) = \frac{3}{2} A_{22} \sin(+2\omega_L t)$

I. 3. G-Factor of the Excited State in ^{109}Rh

Shimada K.[1], Miyashita Y.[2], Ouchi H.[2], Asai M.[3], Hoshino S.[2], Izumi S.[2], Sasaki A.[2], Sato N.[2], Tanigaki M.[4], Tateoka M.[2], Yamazaki A.[1], Wakui T.[1], and Shinozuka T.[1]

[1]Cyclotoron and Radioisotope Center, Tohoku University
[2]Department of Physics, Tohoku University
[3]Japan Atomic Energy Research Institute
[4]Research Reactor Institute, Kyoto University

It is interesting that Rh and Ru isotopes located in a region between Zr and Sn have been predicted shape coexistence. ^{132}Sn is known as spherical-shape because of the double-closed shell, while ^{100}Zr is strongly deformed-shape although a proton number of Zr is smaller by only 10 than that of Sn. It is originated from the fact that a paring or a quadrupole interaction becomes predominant and how many nucleons occupy for each orbit. The paring interaction works between two nucleons on open orbits, and tends to keep spherical-shape, while the quadrupole interaction works between a particle and a hole, and makes the shape to deform.

Many theoretical models have been studied and compared with experimental results, but these models have been constructed for the nuclei around the stable region. In the neutron-rich region a ratio between a number of the proton and that of the neutron is very different, so that interactions between the proton and the neutron which have been ignored would become strong. In the right neutron-rich region, actually, it is reported that disappearances of traditional magic numbers and appearances of new magic numbers, which are not explained by traditional theories. For such studies systematic measurements of excited energies, transition probabilities, masses, nuclear moments and lives are important.

In this report we show the g-factor of a low-lying excited state at 225.98 keV in the ^{109}Rh. This state were populated by the β decay of ^{109}Ru ($T_{1/2}$=34.5 s) and its g-factor was measured using the time-differential perturbed angular correlation method (TDPAC) [1].

The ^{109}Ru beam was provided using proton induced fission reactions and the RF-IGISOL[2,3]. The beam of the proton at 50 MeV with 1 μA bombarded a natural uranium target, which

was a stack of ten 20-mg/cm^2-thick uranium plates and located on the beam with a tilt angle of 6 degrees. Its effective thickness was 190 mg/cm^2. Fission products emitted from the target by the recoil were stopped in the 3-kPa He gas buffer. We applied 70 V for the cylindrical electrodes and RF voltage of 50 V_{pp} at 2.85 MHz for the RF carpet of the RF-IGISOL. The products were accelerated by the 30 kV and mass analyzed by a dipole magnetic field, and then transported to a tape-transport position. Then a yield of the ^{109}Ru was 10^3 particles per second at the tape-transfer position with the proton-beam intensity of 1 μA. The ^{109}Ru was transported to a magnet position at a distance of 900 mm by 1.5 s using the tape-transport system. Measurements were performed with two magnetic fields of 1.09 and 0.34 T. The time dependences of an angular correlation of a γ-ray cascade were measured using two BaF_2 and two HPGe detectors. A setup is shown in Fig. 1.

A γ-ray cascade involving the 225.98-keV level was 116.32-(31.80)-225.98 keV cascade shown in Fig. 2, and an angular correlation of the 116.32- and 225.98-keV γ rays were measured because the 31.80-keV γ ray was under thresholds of the detectors. The angular correlation of the γ-γ-γ cascade is explained in Refs. 4 and 5.

Typical measurements of the time-pattern of the angular-correlation precessing in external magnetic fields are shown in Fig. 3. Therefore the Larmor precession frequency was derived from the time patterns and the g-factor was obtained as $0.78^{+0.17}_{-0.03}$.

The magnetic moments using I^π = 5/2$^+$ and 3/2$^+$ are derived as $1.95^{+0.43}_{-0.08}$ and $1.17^{+0.28}_{-0.07}$ μ_N, respectively. In the single-particle model a configuration of a ground state on the ^{109}Rh is $\pi(0g_{9/2})^5$. The simplest configurations of the low-lying excited states, spins of which are 5/2$^+$ and 3/2$^+$, are $\pi(2d_{5/2})^1$ and $\pi(2d_{3/2})^1$. These Schmidt values are calculated as 4.793 and -0.124 μ_N, respectively, both of which are quiet different from our values. Thus it is suggested that this state is not the single-particle state.

We established the method of the measurement of the magnetic moment of the neutron-rich unstable nuclei using the RF-IGISOL and the TDPAC, and obtained the g-factor of the excited state at the 225.98-keV level in ^{109}Rh as $0.78^{+0.17}_{-0.03}$.

References

1) Miyashita Y., PhD. thesis, Tohoku University (2008).
2) Sonoda T. *et al.*, Nucl. Instr. and Meth. **B 254** (2007) 295.
3) Miyashita Y. *et al.*, Nucl. Instr. and Meth. **B 266** (2008) 4498.
4) Krane K.S. *et al.*, At. Data Nucl. Data Tables **11** (1973) 351.
5) Krane K.S., Nucl. Instr. and Meth. **214** (1983) 321.

Figure 1. Photo of the setup. Two detectors above were BaF2 and two detectors bottom were HPGe. They were placed in each 90 degrees. In the case of the experiment with the 1.09-T magnet only one HPGe detector was used.

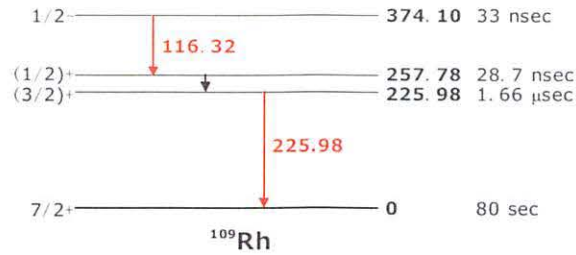

Figure 2. Remarkable part of the decay scheme of ^{109}Rh.

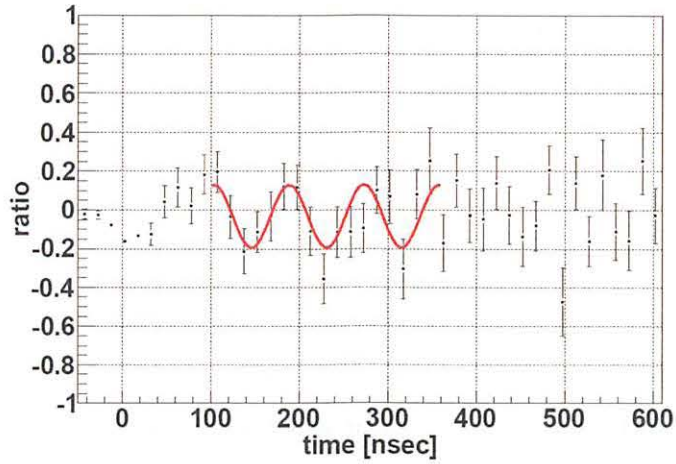

Figure 3. Typical measurements of the time-pattern of the angular-correlation precessing. In this case the external magnetic field applied was 1.09 T. The 116.32-keV γ ray was detected with the HPGe detectors, and 225.98-kV γ rays which emit to 90 and 180 degrees were detected with the BaF_2 detectors.

I. 4. Development of the Surface Ionizer for the Fr Production to Search for the EDM

Sakemi Y., Hayamizu T., Oikawa A., Itoh M., and Yoshida P.H.

Cyclotron and Radioisotope Center, Tohoku University

An Electric Dipole Moment (EDM) of the elementary particle is a good prove to observe the phenomena beyond the Standard Model (SM), since the SM predicts quite small EDM such as less than 10^{-37} e • cm for the electron. A non-zero EDM is considered as a background free signal of CP violation beyond the SM. In paramagnetic atoms an electron EDM results in an atomic EDM enhanced by the factor ~ $Z^3\alpha^2$ [1]. The element which has largest enhancement factor is a heaviest alkali element and the radioactive atom francium (Fr). However the EDM for the Fr have not yet been measured because it is difficult to make a concentrated sample due to a short life time for the standard experiment. Then, we started to construct a high intensity laser cooled Fr factory at CYRIC for the first challenge to perform the search for the unstable atom Fr. The key points of this successful next generation experiment are the high intensity Fr source and the laser cooled/trapped equipments to achieve the small statistical and systematic errors. In this report, the present status of the developments of the thermal ionizer to produce the Fr ions is described.

The Fr is produced by a heavy-ion fusion reaction between an oxygen beam and a gold target ($^{18}O+^{197}Au \rightarrow {}^{210}Fr$ +5n etc.) with the primary beam energy ($E_{^{18}O}$~100 MeV) just above the coulomb barrier. The target consists of a lump of gold melted and flattened onto the end of a nickel rod with a thickness of 50 μm (97 mg/cm^2). The cartridge heater is configured inside the nickel rod for heating the gold target to diffuse Fr ions produced in fusion reaction with surface lionization, but it was found to be not necessary to heat up the target because the target itself could be heated by the primary beam power and the radiation from the oven described below. The embedded Fr in the target diffuses rapidly to the surface and evaporates as the ions with the fraction according to the Langmuir-Saha equation:

$$\frac{n_+}{n_0} = \frac{\omega_+}{\omega_0} \exp\left(\frac{E_{WF} - E_{IP}}{k_T}\right),$$

where n_+/n_0 is the ratio of ions to atoms desorbed, w_+/w_0 is the ratio of the statistical weights and equals 1/2 for alkali atoms, E_{WF} is the work function of the surface, and E_{IP} is the ionization potential of the desorbed atom. The target is surrounded by the high temperature oven to collect all the Fr ions in the limited space. The oven is heated by the 4 cartridge heaters installed in it. The Fr ions are extracted from the extraction electrode placed in the side face of the oven. The shape and size of the extraction electrode is designed and optimized to realize the small Fr beam emittance with ~15π mm–mrad with the Fr ion track simulation using the realistic electric field as shown in the Fig. 2. The structure of the thermal ionizer is shown in the Fig. 1.

We constructed the beam line for the Fr production at the 34 course in the target room 3. The developed thermal ionizer was installed in the end of the beam line with the beam viewer and beam stopper to monitor the primary beam current just before the ionizer. The experiments to observe the Fr production and check the extraction efficiency have been done. We set the SSD detector along with the extracted Fr beam axis with the adjustable distance to measure the alpha decay with the energy 6.5MeV from the produced ^{210}Fr which were stopped on the surface of the detector. The temperature of the detector became high due to the radiation from the ionizer, then it was cooled by the peltier device attached to the bottom of the SSD to keep the high energy resolution. The measured spectrum is shown in the Fig. 3, and it is clearly seen that we have succeeded to extract the Fr from the ionizer without background of other radioisotopes. The detailed analysis to estimate the extraction efficiency is now in progress.

Reference

1) P.G.H. Sandars, Phys. Lett. **14** (1965) 194.

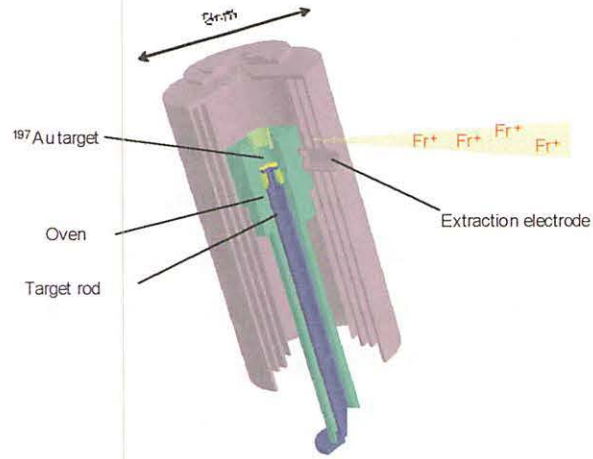

Figure 1. The structure of the thermal ionizer.

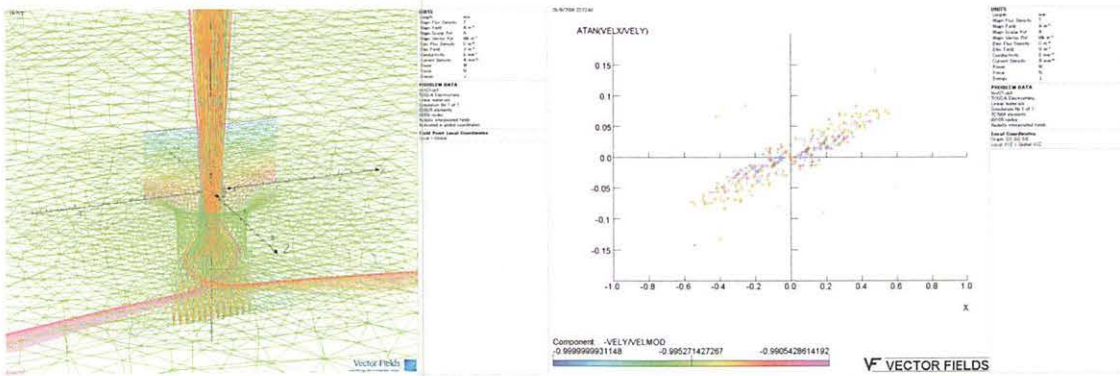

Figure 2. The left figure shows the Fr ion track simulation around the extraction electrode. The right plot shows the distribution of the emittance of the extracted Fr ion beam.

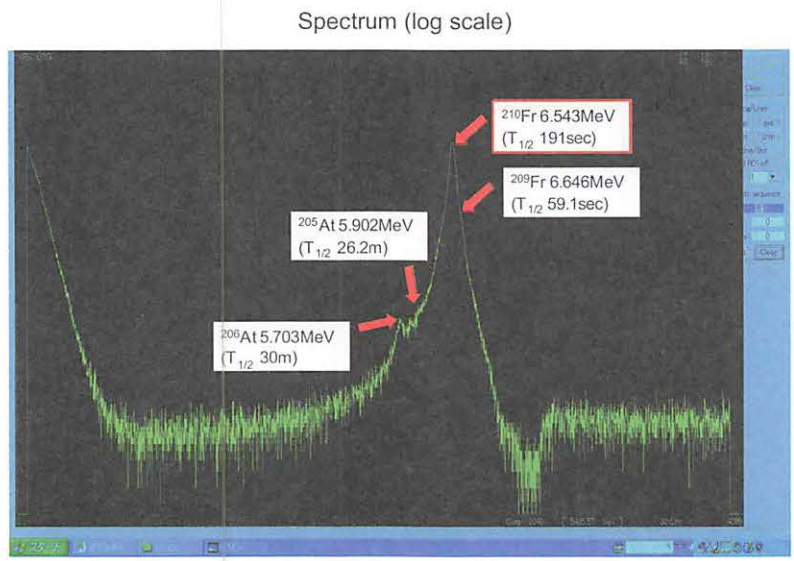

Figure 3. The α decay energy spectrum of the ^{210}Fr extracted from fusion reaction with ^{18}O and ^{197}Au.

II. NUCLEAR INSTRUMENTATION

II. 1. Demagnetization of Nd-Fe-B Magnets by the Fast Neutron Irradiation

Tanigaki M.[1], Shimada K.[2], Izumi S.[3], Ouchi H.[3], Sasaki A.[3], Wakui T.[2], and Shinozuka T.[2]

[1]Researh Reactor Institute, Kyoto University
[2]Cyclotron and Radioisotope Center, Tohoku University
[3]Graduate School of Science, Tohoku University

Rare-earth permanent magnets (REPMs) like NEOMAX are playing a major role in accelerators to realize compact, design-flexible devices for beam optics at no operating cost. One of the most important applications is the undulator in storage rings for light source[1]. But the demagnetization of such REPMs under high radiation environment is a serious problem in such applications because it is directly connected to the lifetime of such components. The degree of demagnetization is correlated with the exposure to neutrons.

Quite interestingly, the number of neutrons for observable demagnetization is ~10^{14} neutrons/cm^2, too few compared to the Avogadro's number. This implies some microscopic change caused by neutrons should be responsible for this demagnetization. Bizen et al. propose the "thermal spike" model[2], i.e., the local heating caused by the recoiled ions produced by the incoming neutron triggers the magnetic disorientation of magnetic domains. Based on this model, the demagnetization should largely depend not only on the fluence, but also on the energy of incoming neutrons. Thus, the demagnetization caused by the neutron with a high intensity and a well-defined monochromatic energy is crucial to the verification of possible models for the demagnetization.

In the study on this demagnetization effect of REPMs, the energy dependence of the demagnetization has not been studied well. Most of demagnetization measurements were performed mainly with thermal neutrons produced by nuclear reactors. Little measurements on the demagnetization caused by the high-energy neutrons, especially in the region of tens MeV. The available measurement is up to 2.2×10^9 n/cm^2 of 65 MeV

neutrons performed by Maréchal[3] at JAEA Takasaki, far below the reported intensity for the demagnetization.

This time, we have performed the demagnetization measurement with a higher intensity of neutron flux available at 32-course at CYRIC, aiming to reach the fluence of ~10^{11} n/cm^2, where the possible demagnetization is expected. A magnetized NMX-S50BH with the dimension of 10 mm×10 mm×2 mm was set on an Al finger with the water-cooling at room temperature and placed 120 mm away from the Li target of 32-course. The direction of the magnetization was set perpendicular to the beam. The magnetization during the irradiation was periodically measured by the induction method with a pick-up coil driven by an air-cylinder. The neutron flux was produced by bombarding the Li target at 32-course with 70 MeV proton beam at 1.5 μA, corresponding to the neutron flux of ~5×10^5 n/cm^2/sec at 65 MeV.

In the present measurement, the neutron fluence was achieved up to 0.7×10^{11} n/cm^2, but no significant demagnetization was observed. Possible demagnetization is expected to be observed above the fluence of 10^{12} n/cm^2[2,3], and ~80% of demagnetization, i.e., 20% remaining magnetization, was achieved at the fluence of 5×10^{13} n/cm^2 in the measurement with thermal neutrons at KURRI[4]. Therefore, the additional irradiation should be employed to achieve the fulence of 10^{12} n/cm^2, which should clarify the role of neutron energy toward the demagnetization.

References

1) Onuki H., Elleaume P., Eds.: "Wigglers, Undulators, and their Applications", Taylor&Francis Pub. England (2002).
2) Bizen T., Asano Y., Maréchal X.M., Kitamura H., in: "SYNCHROTRON RADIATION INSTRUMENTATION: Ninth International Conference on Synchrotron Radiation Instrumentation", (AIP Conference Proceedings, 2007) p. 420.
3) Maréchal X.M., Bizen T., Asano Y., Kitamura H., in: *"Proceedings of EPAC 2006"*, (Edinburgh, Scotland, 2006) p. 3116.
4) Tanigaki M., Takamiya K., Komeno Y., Taniguchi A., Ohkubo Y., Hyperfine Interact. **176** (2007) 125.

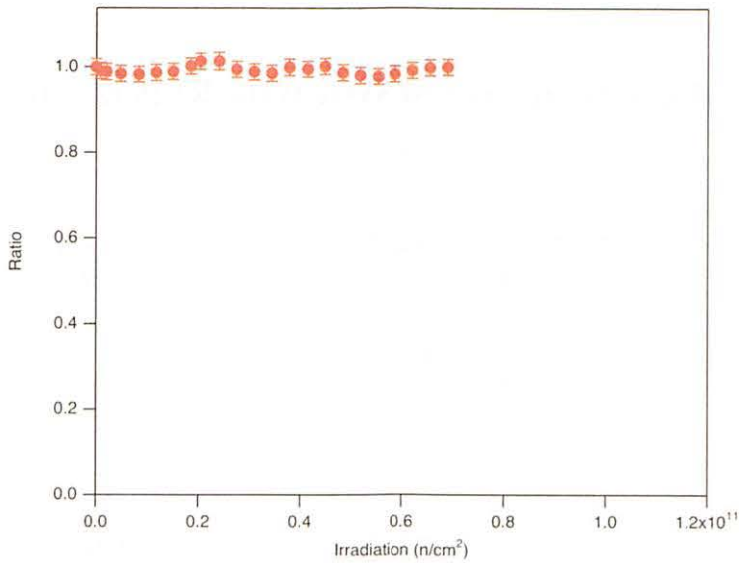

Figure 1. Demagnetization as a function of the neutron fluence.

II. 2. Development of Optical System for RI Polarizing System

Hoshino S.[1], Wakui T.[2], Shimada K.[2], Miyashita Y.[1], Sato N.[1], Sasaki A.[1], Ouchi H.[1], Izumi S.[1], and Shinozuka T.[2]

[1]Department of Physics, Tohoku University
[2]Cyclotron and Radioisotope Center, Tohoku University

We have proposed a new technique to polarize unstable nuclei by a cross polarization method[1]. The aim of this study is to find a possibility to produce a polarization of unstable nuclei better than 10%. The highly polarized unstable nuclei would be useful in the study of nuclear structure as well as material science.

A polarization of unstable nuclei is produced by the following three steps: an optical excitation to produce a population difference in the photo-excited triplet state[2,3], a transfer of the population difference to protons by a cross polarization[4,5] and a polarization transfer from protons to unstable nuclei. To attain a high polarization of unstable nuclei, the population difference and the population on the triplet state should be maximized because the population difference is used as a source of the polarization. For efficient optical excitation, the laser power should be intense as long as stimulated emission is not dominant. Moreover, the pulse width should be longer than the lifetime of the excited singlet state (19.5 ns) and shorter than the lifetime of the triplet state (26 μs).

We use a Nd:YAG laser as a light source for the optical excitation. The laser has a power of 100 mJ/pulse, 5 ns-pulse width and the repetition rate of 20 Hz. The pulse width is thus much shorter than the required pulse width, although the power is sufficiently high. To obtain a longer pulse width, we have designed and constructed an optical system shown in Fig. 1. The laser beam from the Nd:YAG laser is divided by a beam splitter (BS1). A laser beam passes directly to the second beam splitter (BS2), while the other laser beam travels in a delay line (DL1). Each beam is hence travel by different lengths before merge them again at BS2. The laser beam has then twice the pulse width of the original laser beam, if the delay time is adjusted to be almost the same width as the original laser pulse. We used three delay lines to obtain a longer pulse width.

Figure 2 shows a time profile of laser pulses measured with a photodiode seen in Fig. 1. The violet line shows a time profile of an original laser pulse and the blue line shows that of laser pulse after travelling the optical system. By using the optical system, the pulse width has successfully been extended from 4.4 ns to 34 ns. The resultant pulse width is longer than the lifetime of the excited singlet state.

References

1) Tateoka M., Wakui T., Hoshino S., Ishida T., Shimada K., Miyashita Y., Sato N., Nagano T., Ouchi H., Shinozuka T., CYRIC Annual Report 2007 (2008) 9.
2) Kim S.S., Weissman S.I., Rev. Chem. Intermed. **3** (1979) 107.
3) Sloop D.J., Yu H.L., Lin T.S., Weissman S.I., J. Chem. Phys. **75** (1981) 3746.
4) Henstra A., Lin T.S., Schmidt J., Wenckebach W.Th., Chem. Phys. Lett. **165** (1990) 6.
5) Henstra A., Dirksen P., Wenckebach W.Th., Phys. Lett. A **134** (1988) 134.

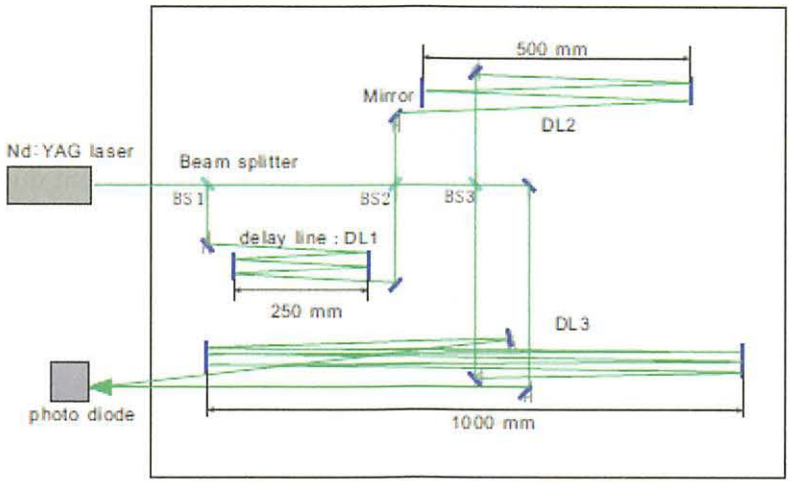

Figure 1. A schematic view of the optical system for extending a laser pulse. The system consists of beam splitters for dividing the laser beam and mirror pairs for delay lines. A time profile of laser pulse is measured with a photodiode.

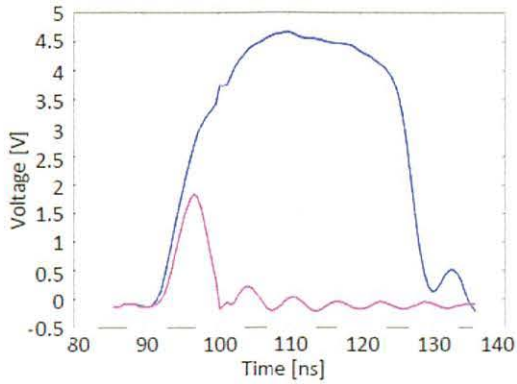

Figure 2. A time profile of laser pulse detected by the photodiode. The gain of the photodiode, i.e. the vertical scale is different for each measurement. The origin of the time axis corresponds to the time that the Q-switch of Nd:YAG laser begin work.

II. 3. Upgrading of the 4.5 MV Dynamitron Accelerator at Tohoku University for Microbeam and Nanobeam Applications

Matsuyama S.[1], Ishii K.[1], Fujisawa M.[1], Kawamura Y.[1], Tsuboi S.[1], Yamanaka K.[1], Watanabe M.[1], Hashimoto Y.[1], Ohkura S.[1], Fujikawa M.[1], Nagaya T.[1], Komatsu K.[1], Yamazaki H.[2], and Kikuchi Y.[1]

[1]*Department of Quantum Science and Energy Engineering, Tohoku University*
[2]*Cyclotron and Radioisotope Center, Tohoku University*

Introduction

A 4.5 MV Dynamitron accelerator was constructed in 1974 for neutron and ion-beam experiments. The Dynamitron accelerator is a single-ended type with a Schenkel type high-voltage power supply. The accelerator was provided with a high-current duoplasmatron ion source, which can generate hydrogen, deuterium, or helium ion beams. The maximum beam current is greater than several hundred microamperes (3 mA recorded). A microbeam line was installed in July 2002[1]; optimization of the system was performed. A beam spot of 0.4×0.4 μm^2 at a beam current of several tens of picoamperes has been produced and smaller beam spots are anticipated in the low-current regime[2].

The analysis system has also been developed and is applicable to simultaneous in-air/in-vacuum PIXE, RBS, SE, and STIM analyses[2-4] and 3D μ-CT[5-7]. These applications demand beam currents of ca. 100 pA, which restricts the spatial resolution to around 1×1 μm^2. In addition, the beam current stability was insufficient. The beam brightness must be increased to improve the resolution to several hundreds of nanometers in the analysis.

In this study, the terminal equipment and an acceleration tube of the Dynamitron accelerator were upgraded to improve the beam brightness and decrease the beam spot size to several tens of nanometers with sufficient beam current for analyses.

System Description

Terminal equipment

The terminal equipment comprises a duoplasmatron ion source along with an extractor,

an Einzel lens, an E×B filter, a pulsing system, and a gap lens. The system configuration is almost identical to the previous one. The ion source, lens system, and their control system are shown in Figure 1. The vacuum products were provided by National Electrostatics Corporation (NEC). The ion source is expected to produce ca. 10 mA H_1^+ beams, with beam emittance of 2.1 mm· mrad· $MeV^{1/2}$ (specification). Both values are better than those of the previous ion source. Moreover, they are estimated to be brighter than other RF ion sources. An uncoated tungsten filament (0.9 mm diameter) was obtained from NEC. The tungsten filament lifetime was too short, only several hours, which is unsuitable for an ion source used in the single-ended accelerator. Therefore, a LaB_6 filament (C2B, Denka Co. Ltd.) was used to achieve a longer lifetime. A 0.1-mm-diameter anode aperture made of iron was also supplied by NEC. The aperture was obstructed within several hours because of the heat load in the source. As the previous ion source, we had used a 0.3-mm-diameter tungsten anode aperture. The aperture can be used for more than 10,000 h without deterioration. Therefore, we used a 0.3 mm diameter anode aperture lined with tungsten. The extracted beams pass through the Einzel lens and the E×B filter. An electrical field E, formed by a deflector and a magnetic field B by permanent magnets, is crossed in the E×B filter. Under the combined influence of E and B, the net force on the particles is cancelled at the specific mass, charge, and velocity conditions. Then the E×B filter provides mass analysis of a monoenergetic beam by selecting a deflection voltage. The Einzel lens focuses the beam on the E×B aperture (1.5 mm diameter). Because the beam spot size on the aperture influences the ability of mass analysis, the Einzel lens performance is important. The duoplasmatron ion source generates more than one ion species. In case of generating hydrogen plasma, the source will produce not only protons, but also diatomic and triatomic molecular hydrogen as well as minor amounts of other ion species. Therefore, the E×B filter reduces the load to the accelerator and improves the accelerator stability. The gap lens focuses the beam to match beam parameters into the acceleration tube[8]. Although the system includes a sweep, a pop, and a buncher for pulsed beam production, their power supplies are not equipped. In this study, the sweep electrodes are used as a steerer by DC voltage application.

The whole control system was developed by our group. The system configuration is presented in Figure 1. These power supplies are driven by 0–10 V signals from digital-to-analog converters (DACs) and are monitored using analog-to-digital converters (ADCs) in programmable logic controllers (PLC, FA-M3; Yokogawa Electric Corp.). The DAC and

ADC modules are standard components of the PLC, but special modifications were undertaken for spark protection. These PLCs in the terminal (sub PLC units) have no CPU and are connected to a main PLC in the ground potential via two plastic fibers. The main PLC module has CPU, receives commands from a personal computer and controls the sub PLC units in the terminal. The main PLC module was used outside an accelerator pressure tank to prevent damage caused by spark-out. In this case, the plastic fibers must traverse the pressure tank. Because the plastic fiber is colored by X-ray irradiation, it must be changed periodically. For easy fiber maintenance, light signals are converted to electric signals, extracted as electric signals through hermetic connectors, then reconverted to light signals using light/signal converters that were specially developed by our group.

The control parameters for operation are stored in the memory space of the main PLC. A personal computer used as the user interface can only refer to these parameters via an Ethernet network. During the start-up process, control software retrieves the parameters for the PLC and can send commands to change the parameters. This framework was adopted to address the situation of a possible computer hang-up. Control software was designed using LabVIEW based on user requirements and requests.

Acceleration tube

The acceleration tube was replaced with a new one obtained from NEC. The acceleration tube comprises 12 sections arranged in compressed geometry. Figure 2 portrays schematic drawings of one section of the tube. The acceleration tube was assembled in one piece compressed with two square flanges and four Lucite tension rods and was shipped in one piece. Each section has 18 live gaps and 3 shorted gaps. The center of the shorted region has an aperture of 25.4 mm diameter and internal electrodes, which resemble those between the sections. The lens effect will be stronger than that of the previous tube, which has larger apertures. The potential grading of the tube is provided with high mega-ohm resisters. The first seven gaps of the tube have lower value resistors (60 MΩ) than the other 209 gaps (100 MΩ). The gradient is lower in the first gaps. For that reason, the strength of the entrance lens effect is reduced, which better matches the available gap lens voltages.

Performance of the system

1. Basic performance

Upgrading of the accelerator started February 2007 and the first beam was obtained August 2007. First, high-voltage spark-out of the accelerator damaged the terminal equipment. By adding filters and shields, damage to the equipment was reduced. Figure 3 shows a typical mass spectrum measured at a 0 deg target by varying the voltage to the ExB filter. The H_1^+, H_2^+, and H_3^+ beams were sufficiently separated and the ExB filter functioned as expected. Because the data were measured at an arc current of 0.5 A, the proton ratio is ca. 0.15, which is rather low. Maximizing the proton ratio necessitates maximizing the arc current and minimizing the source gas pressure. However, a tradeoff pertains between low source gas pressure and source stability. High arc currents are great for a high proton ratio, but take the risk of welding the anode aperture shut. From these conditions, we are running the source for the arc current range of 1–2 A for proton beam production. The gas pressure is used at the lowest level where the source works stably. Even in that condition, the proton ratio is ca. 0.25, which is lower than that from operational experience of the same NEC duoplasmatron ion source[9].

The beam current was measured at the 0 deg target. Proton beam currents of 21 μA, 52 μA, and 75 μA were obtained respectively for arc currents of 1.0, 1.5, and 2 A with a 0.25 A magnet current. Because the source is expected to provide more than 1 mA of H^+ beam, beam currents were lower than expected. By applying the voltage to the sweep and increasing the magnet current, the beam current increased and exceeded 100 μA at an arc current of 2 A. The beam shifts by varying ion source parameters. Misalignments might occur in the ion source and lens system in the terminal. For H_2^+, the beam currents of 100 μA were obtained easily with lower arc current, which might be related to the lower proton ratio. Additional adjustments for ion source geometry and for operational conditions should be made to improve the performance.

The lifetime of a LaB_6 filament in the source is longer 700 h; it is still running. The aperture lined with tungsten has worked for more than 900 h without changing beam properties. The accelerator has been operated routinely for various experiments without a serious problem.

2. Beam brightness

The beam brightness is of primary importance to focus the beam down to micrometer scale with sufficient beam current. The system's beam brightness was measured by measuring the target current in the microbeam system for 2.4 MeV hydrogen beams. The

microbeam system consists of a doublet quadrupole and the slit-system of microslits (MS), divergence-defining slits (DS), and baffle slits (BS)[1,2]. The brightness was measured using various DS slit width in square geometry. The MS widths were set at 82×12 μm^2, which correspond to beam spot size of 1.5×1.5 μm^2.

As described by Liouville's theorem[10], the beam brightness cannot be increased using a subsequent optical system. It can only decrease according to effects such as those of collimation and misalignment. Beam lines to the microbeam system are short and simple in the newly built facilities for nanobeam and microbeam applications. However, our microbeam system is sufficiently long to reduce the beam brightness because the system is connected to the existing beam line and to a high-resolution beam-energy analyzing system[1]. Figure 4 shows the beam line to the microbeam system. Accelerated beams pass through a doublet quadrupole lens (DQ1), a switching magnet, another quadrupole doublet lens (DQ2) and the analyzing system and enter the microbeam system. To define the correct axis with respect to the analyzing magnet and to keep the energy analyzing performance, DQ2 was not used in the normal operation. The highest beam brightness of the previous system was ca. 0.7 $pA \cdot \mu m^{-2} \cdot mrad^{-2} \cdot MeV^{-1}$ at a half divergence of 0.2 mrad. In this study, the brightness was measured for three beam transport conditions. Figure 4 presents the calculated beam envelope after passage through the ExB aperture to the entrance of the energy analyzing system using OPTICSIII code, which is supplied from NEC for three beam transport conditions. The first condition (case 1), higher extraction voltage (ca. 30 kV) and higher gap lens voltage (ca. 55 kV), was applied and DQ1 was used. These voltages and currents of the lens system were adjusted to obtain the highest beam current at the target. Using higher extraction and gap lens voltage, the lens effect of the tube is the weakest. Therefore, the accelerated beams are estimated as parallel beams. For case 2, the standard extraction voltage (20 kV) was applied. The gap lens voltage was arranged such that the waist was formed in the tube exit. Both DQ1 and DQ2 were used in this case. Case 2 is the highest beam transmission in the accelerator and is recommended from NEC. For case 3, the standard extraction voltage (20 kV) and lower gap lens voltage (10 kV) were applied; only DQ1 was used. In this setting, the beam waist is formed in the middle of the tube and the transmission in the accelerator is not good. Figure 5 portrays the measured beam brightness for three beam transport conditions with that obtained using the previous system. The beam brightness in case 2 is 0.7 $pA \cdot \mu m^{-2} \cdot mrad^{-2} \cdot MeV^{-1}$ at a half divergence of 0.1 mrad; it is highest in these cases, but is lower than that of the previous

system. As shown in the beam envelope calculation, the beam spot size at entrance slit of the energy analyzing system (ESS1, slit opening = 0.4 mm) is smallest in case 2; thereby, the beam brightness is highest. As mentioned in this section, chromatic aberration may increase in case 2. Thus the beam transport condition of case 2 is applicable to an experiment with a beam spot size larger than 1×1 μm^2. The beam brightness of case 1 is almost identical to that of case 3. In case 1, the beam brightness increased with the slit opening of ESS1. The slit opening of ESS1 affects the energy resolution. The beam brightness increased by five times, as expected from energy stability of the accelerator when the slit opening is set to 5 mm[1)].

To compare brightness among various systems, a brightness value at 0.07 mrad half divergence is used as a normalized brightness[11-13)]. The highest normalized brightness was reported as 30 $pA \cdot \mu m^{-2} \cdot mrad^{-2} \cdot MeV^{-1}$ [11)]. The value of 74 $pA \cdot \mu m^{-2} \cdot mrad^{-2} \cdot MeV^{-1}$ was reported in a different half divergence[14,15)]. Normalized beam brightness of 0.44 $pA \cdot \mu m^{-2} \cdot mrad^{-2} \cdot MeV^{-1}$ was obtained in case 1, which was obtained under the arc current of 1.8 A and magnet current of 0.3 A. Under these conditions, the source provided 45 μA H^+ beam. For H_2^+ beams, normalized brightness of 2.6 $pA \cdot \mu m^{-2} \cdot mrad^{-2} \cdot MeV^{-1}$ was obtained. This value was obtained under the arc current of 0.6 A and magnet current of 0.3A. The source provided 120 μA H_2^+ beam. As described in the preceding section, adjustment of the ion source is not perfect and the beam current and proton ratio are lower than expected. The brightness is improved with adjustment of the source. Because the anode aperture diameter also affects the brightness, aperture optimization should also be done.

3. High-voltage stability

The beam current of the previous system fluctuated between 0 and its maximum value, which stemmed from the instability of the terminal voltage. The voltage ripple was sometimes larger than 10^{-3} and was larger than the specification. Voltage ripple of this order can be measured easily using the load current change of the resisters, which were connected from the terminal to the ground (high voltage divider, HVD). After replacing the tube, the voltage ripple was measured, but it did not decrease drastically. The voltage ripple came from bad adjustment of the voltage regulation circuit. A proportional integration (PI) regulator is used to stabilize the high voltage. The PI controller acts on the error signal from the comparison of the set reference voltage and the voltage generated on the precise resister by the HVD current. The response time is very important to stabilize the terminal

voltage. The response time was adjusted at installation of the accelerator when rectifier tubes were used for high voltage generation. After changing the rectifier tube into diodes, readjustment was not carried out. Readjustment should be carried out because the response of the diodes is faster than that of the rectifier tubes. Because voltage stability was not important for any application at that time, adjustment was not carried out. After adjusting the response time, the voltage ripple decreased to a level that was within the specification, thereby improving the beam current stability at the microbeam target. The elemental map had an artifact that was attributed to the beam current fluctuation in the previous system. After upgrading the system and adjusting the response, the artifact was greatly reduced. As the next step, we are planning to replace the voltage regulating system and to increase the system performance.

Conclusion

The Dynamitron accelerator at Tohoku University was upgraded to improve the microbeam performance and decrease the beam spot size down to several tens of nanometers with beam currents of ca. 100 pA. The microbeam system has the capability of focusing the beam down to several hundred square micrometers, but beam currents were insufficient for analyses at sub-micrometer resolution.

An ion source and lenses in the terminal and an acceleration tube were replaced with new ones from National Electrostatics Corporation. The control system of the terminal equipment was also developed by our group. Beam brightness of 2.6 and 0.44 $pA \cdot \mu m^{-2} \cdot mrad^{-2} \cdot MeV^{-1}$ was obtained for H_2^+ and H_1^+ beams at a half divergence of 0.07 mrad. The beam brightness is lower than expected and optimization of the ion source and its operational condition should be carried out. The voltage stability of the accelerator was improved by adjusting the voltage stabilizing system. Thereby, the beam current stability is improved and artifact shown in the elemental image was greatly reduced. The Dynamitron accelerator has been operated routinely for various experiments without a serious problem and will be useful for nanobeam and microbeam applications.

Acknowledgements

The authors thank Prof. M. Igashira, Tokyo Institute of Technology, Dr. T. Matsumoto, National Institute of Advanced Industrial Science and Technology, and Dr. M. Kowatari, Japan Atomic Energy Agency for their valuable suggestions and advice from their

experience on their duoplasmatron ion source of the Pelletron accelerator. The authors also acknowledge the assistance of Dr. C. Kobayashi, Dr. T. Yoshida, Mr. S. Takahashi, Mr. M. Anshita, and Mr. T. Saito (Staff of Hakuto Co. Ltd.) in installing the ion source and the acceleration tube.

This study was partly supported by Grants-in-Aid for Scientific Research, (S) No. 13852017, (B) No. 18360450, (C) No. 16560731, and a Grant-in-Aid for Scientific Research in Priority Areas under Grant No. 14048213 from the Ministry of Education, Culture, Sports, Science and Technology, Japan.

References

1) Matsuyama S., Ishii K., Yamazaki H., Sakamoto R., Fujisawa M., Amartaivan Ts., Ohishi Y., Rodriguez M., Suzuki A., Kamiya T., Oikawa M., Arakawa K., Matsumoto N., Nucl. Instr. andMeth. **B210** (2003) 59.
2) Matsuyama S., Ishii K., Yamazaki H., Kikuchi Y., Inomata K., Watanabe Y., Ishizaki A., Oyama R., Kawamura Y., Yamaguchi T., Momose G., Nagakura M., Takahashi M., Kamiya T., Nucl. Instr. Meth. Phys. Res. **B260** (2007) 55.
3) Matsuyama S., Ishii K., Yamazaki H., Barbotteau Y., Amartaivan Ts., Izukawa D., Hotta K., Mizuma K., Abe S., Oishi Y., Rodriguez M., Suzuki A., Sakamoto R., Fujisawa M., Kamiya T., Oikawa M., Arakawa K., Imaseki H., Matsumoto N., Int. J. of PIXE, **14** (1&2) (2004) 1.
4) Matsuyama S., Ishii K., Abe S., Ohtsu H., Yamazaki H., Kikuchi Y., Amartaivan Ts., Inomata K., Watanabe Y., Ishizaki A., Barbotteau Y., Suzuki A., Yamaguchi T., Momose G., Imaseki H., Int. J. of PIXE, **15** (1&2) (2005) 41.
5) Ishii K., Matsuyama S., Yamazaki H., Watanabe Y., Yamaguchi T., Momose G., Amartaivan Ts., Suzuki A., Kikuchi Y., Galster W., Int. J. of PIXE, **15** (3&4) (2005) 111.
6) Ishii K., Matsuyama S., Yamazaki H., Watanabe Y., Kawamura Y., Yamaguchi T., Momose G., Kikuchi Y., Terakawa A., Galster W., Nucl. Instr. and Meth. **B249** (2006) 726.
7) Ishii K., Matsuyama S., Watanabe Y., Kawamura Y., Yamaguchi T., Oyama R., Momose G., Ishizaki A., Yamazaki H., Kikuchi Y., Nucl. Instr. and Meth. **A571** (2007) 64.
8) Elkind M.M., Rev. of Sci. Instr., **24** (1953) 129.
9) Igashira M., private communication.
10) Grime G.W., Watt F., "Beam Optics of Quadrupole Probe-forming Systems," Adam Hilger Ltd, Bristol (1984).
11) Szymanski R., Jamieson D.N., Nucl. Instr Meth. **B130** (1997) 80.
12) Rout B., Greco R., Pastore N., Dymnikov A.D., Glass G.A., Nucl. Instr. Meth. **B241** (2005) 382.
13) Jamieson D.N., Rout B., Szymanski R., Spizzirri P., Sakellarieu A., Belcher W. Ryan C.G., Nucl. Instr. Meth. **B190** (2002) 80.
14) Visser J., Mous D.J.W., Gottdang A., Haitsma R.G., Nucl. Instr. Meth. **B231** (2005) 32.
15) Watt F., van Kan J.A., Rajta I., Bettiol A.A., Choo T.F., Breese M.B.H., Osipowicz T., Nucl. Instr. Meth. **B210** (2003) 14.

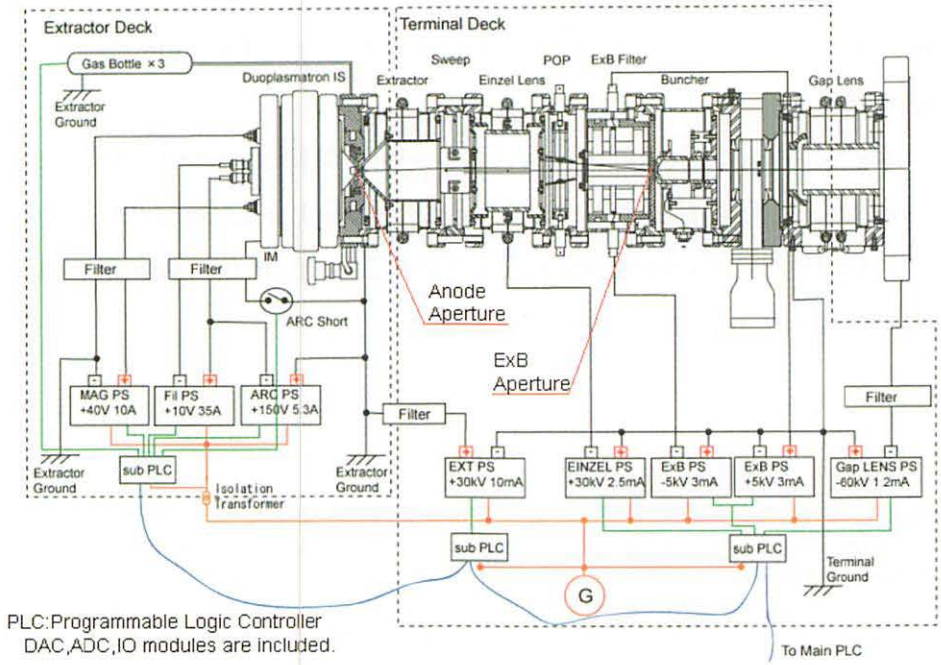

Figure 1. Schematic diagram of the ion source, lens, and control system.

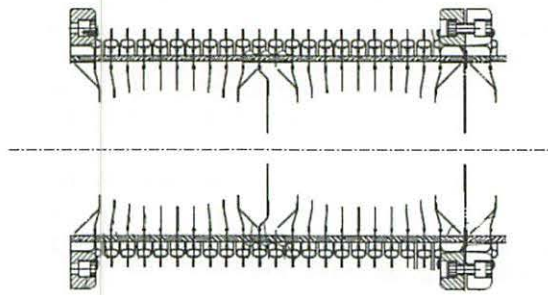

Figure 2. Schematic diagram of the acceleration tube.

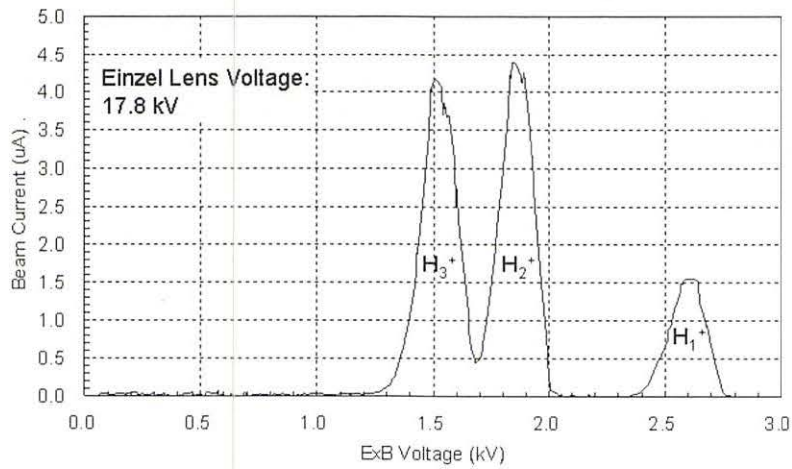

Figure 3. Mass spectrum measured by varying the voltage applied to ExB filter at the 0-deg target.

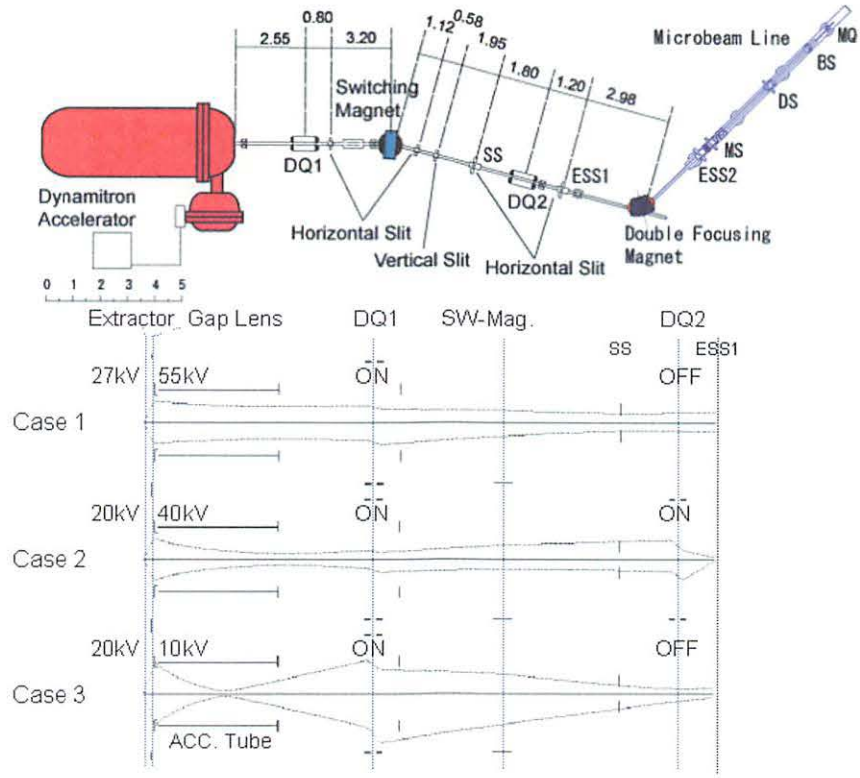

Fig.4

Figure 4. Beam transport system and beam envelope calculated using OPTICSIII from NEC for three transport conditions.

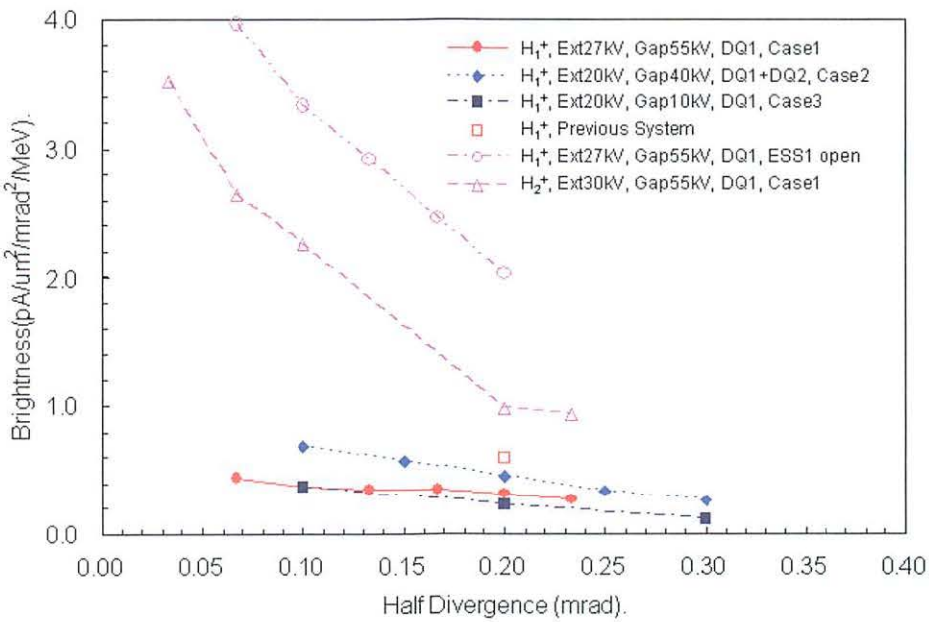

Figure 5. Measured beam brightness for three beam transport conditions.

III. NUCLEAR ENGINEERING

III. 1. Evaluation of Helium Effect on Candidate Structural Materials for Next Generation Long-life Nuclear Plant

Hasegawa A.[1], Nogami S.[1], Satou M.[1], Wakai E.[2], and Aoto K.[2]

[1]Department of Quantum Science and Energy Engineering, Tohoku University
[2]Japan Atomic Energy Agency

Introduction

For development of the next generation long-life nuclear plant, precise prediction of the irradiation damage to reactor vessel and in-core component during operation is necessary. This study focuses on the developing the index for evaluation of the irradiation damage for the candidate structural materials of the next generation long-life nuclear plant such as SUS304 steel, SUS316FR steel and 12Cr steel (HCM12A), which can be applied to reactor design method considering irradiation environment effect. This study also focuses on developing the non-destructive inspection technique for precise understanding of irradiation damage progress during operation based on the index.

The amount of generated helium (He) is recognized as one of the promising index in this study. The database of mechanical property change for those materials due to He implantation should be established in order to verify whether He generation amount is adequate as the index for evaluation of the irradiation damage. Therefore, short time mechanical properties such as the tensile property (tensile strength and yield stress) and the hardness were evaluated in order to clarify the relation between He and their changes.

Experimental

Material in this study is the 316FR steel and the HCM12A steel, which are the candidate structural material for next generation nuclear plants. The chemical composition of these materials is shown in Table 1. The specimen shape was a miniaturized tensile specimen and a rectangular specimen with geometry of 5 mm×16 mm×0.3 mm. The specimen surface was mechanically and electrically polished into mirror state.

The He implantation test was carried out using the AVF Cyclotron accelerator of

Cyclotron and Radioisotope Center of Tohoku University. The implanted particle, implantation temperature and He concentration were 50 MeV He^{2+} ion, about 550°C and about 50 appm, respectively. Helium was uniformly implanted from the specimen surface to about 400 μm in thickness by using a rotating energy degrader consisting of Al foils. Figure 1 shows the depth distribution of He concentration and displacement damage in the specimen calculated by SRIM code.

Tensile test at room temperature for the He implanted miniaturized tensile specimen was performed using an Instron-type multi-purpose testing machine (INTESCO Co., Ltd.) at Radio Isotope Laboratory of Tohoku University. The test environment and strain rate were in-air and about 6.7×10^{-4} s^{-1}, respectively.

Tensile test at about 550°C for the He implanted miniaturized tensile specimen was performed using an Instron-type multi-purpose testing machine (INTESCO Co., Ltd.) at Radio Isotope Laboratory of Tohoku University. The test environment and strain rate were vacuum below 1×10^{-3} Pa and about 6.7×10^{-4} s^{-1}, respectively.

The Vickers hardness measurement at room temperature in air was performed using a Vickers hardness tester (Shimadzu Corp., Micro Hardness Tester type M) at Radio Isotope Laboratory of Tohoku University. The test temperature, indentation load and dwell time was room temperature, 200 gf and 15 sec, respectively.

Results

Figure 2 shows the results of the tensile test ((a) tensile strength, (b) yield stress, (c) uniform elongation, (d) total elongation) at about 550°C in 316FR and HCM12A implanted up to about 50 appm at about 550°C by Cyclotron[1]. About 15% reduction of the tensile strength due to He implantation up to about 1 appm and almost no change of it due to He implantation from 1 to 50 appm were observed in both materials. Almost no change of the yield stress due to He implantation from 1 to 30 appm and slight increase of it due to He implantation up to about 50 appm was observed in 316FR. About 20% reduction of the yield stress due to He implantation up to 1 appm and almost no change of it due to He implantation from 1 to 50 appm was observed in HCM12A.

Figure 3 shows the results of the tensile test ((a) tensile strength, (b) yield stress, (c) uniform elongation, (d) total elongation) at room temperature in 316FR implanted up to about 50 appm and HCM12A implanted up to about 10 appm at about 550°C by Cyclotron[1]. The tensile strength of 316FR gradually decreased with He concentration and about 17%

reduction of it due to He implantation up to about 50 appm was observed. The tensile strength of HCM12A also gradually decreased with He concentration and about 10% reduction of it due to He implantation up to about 10 appm was observed. About 18% reduction of the yield stress due to He implantation up to about 10 appm and almost no change of it due to He implantation from 10 to 50 appm were observed in 316FR. The yield stress of HCM12A also gradually decreased with He concentration and about 23% reduction of it due to He implantation up to about 10 appm was observed.

Figure 4. shows the Vickers hardness in 316FR and HCM12A implanted up to about 50 appm at about 550°C by Cyclotron[1]. Very small change of the hardness in 316FR was observed after He implantation from 1 to 50 appm. While, increment of the hardness by 20~30Hv due to He implantation up to 30 appm and reduction by 20~30Hv due to He implantation up to 50 appm were observed in HCM12A.

Summary

Evaluation of the short time mechanical properties such as the tensile property and the hardness for He implanted materials (316FR and HCM12A steel) using Cyclotron was carried out in order to clarify the relation between He and their changes due to He implantation. Table 2 is the summary of the database of thermal desorption spectrometry, microstructural observation, tensile test and Vickers hardness measurement for 316FR and HCM12A obtained using Cyclotron in 2006 to 2008 for the R&D Project on Irradiation Damage Management Technology for Structural Materials of Long-life Nuclear Plant entrusted to Japan Atomic Energy Agency (JAEA) by the Ministry of Education, Culture, Sports, Science and Technology of Japan (MEXT).

Acknowledgement

Present study is the result of R&D Project on Irradiation Damage Management Technology for Structural Materials of Long-life Nuclear Plant entrusted to Japan Atomic Energy Agency (JAEA) by the Ministry of Education, Culture, Sports, Science and Technology of Japan (MEXT). The authors are grateful to the staffs of CYRIC of Tohoku University relating to the accelerator operation and our irradiation experiments.

References

1) Hasegawa A., Nogami S., Satou M., Wakai E., Aoto K., CYRIC Annual Report (2007) 25.
2) Hasegawa A., Nogami S., Satou M., Wakai E., Aoto K., CYRIC Annual Report (2006) 25.

Table 1. The chemical composition of the 316FR steel and the HCM12A steel..

	Fe	C	Si	Mn	P	S	Cu	Ni	W	Cr	Mo	V	Nb	N
316FR	Bal.	0.01	0.59	0.84	0.026	0.003	0.26	11.19	-	16.87	2.23	0.08	-	0.08
HCM12A	Bal.	0.11	0.27	0.64	0.016	0.002	1.02	0.39	1.89	10.83	0.30	0.19	0.054	0.063

Table 2. Summary of the database of thermal desorption spectrometry, microstructural observation, tensile test and Vickers hardness measurement for 316FR and HCM12A obtained in 2006 to 2008 in the R&D Project on Irradiation Damage Management Technology for Structural Materials of Long-life Nuclear Plant entrusted to Japan Atomic Energy Agency (JAEA) by the Ministry of Education, Culture, Sports, Science and Technology of Japan (MEXT).

Material	He conc. [appm]	TDS	TEM	Mechanical Properties		
				Tensile		Hardness
				550°C	R.T.	
316FR	0	—	2006-2007	2006-2007	2008	2006-2007
	1	2006-2007	2006-2007	2006-2007	—	2006-2007
	10	2006-2007	2006-2007	2006-2007	2008	2006-2007
	30	2006-2007	2006-2007	2006-2007	2008	2006-2007
	50	2008	2008	2008	2008	2008
	100	—	2008	—	—	—
HCM12A	0	—	2006-2007	2006-2007	2008	2006-2007
	1	2006-2007	2006-2007	2006-2007	2008	2006-2007
	10	2006-2007	2006-2007	2006-2007	2008	2006-2007
	30	2006-2007	2006-2007	2006-2007	—	2006-2007
	50	2008	2008	2008	—	2008
	100	—	2008	—	—	—

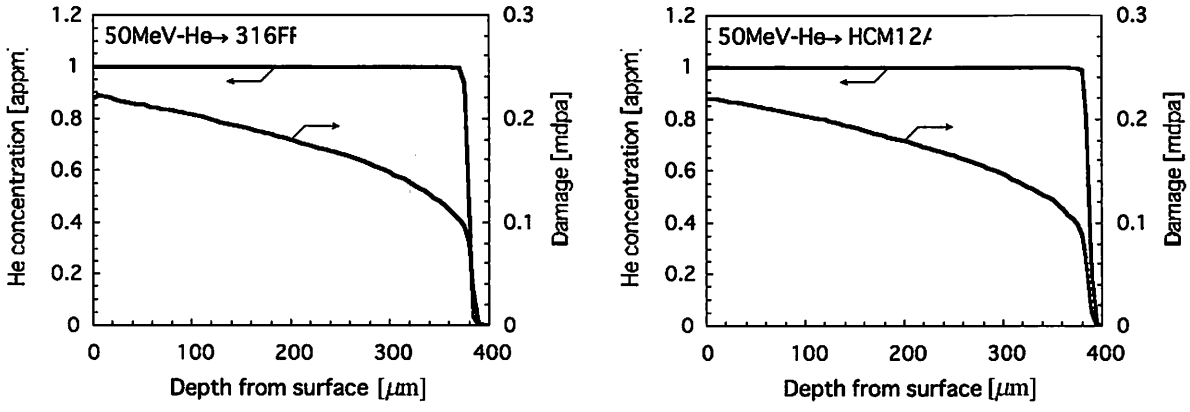

Figure 1. The depth distribution of He concentration and displacement damage in the 316FR steel and the HCM12A steel calculated by SRIM code.

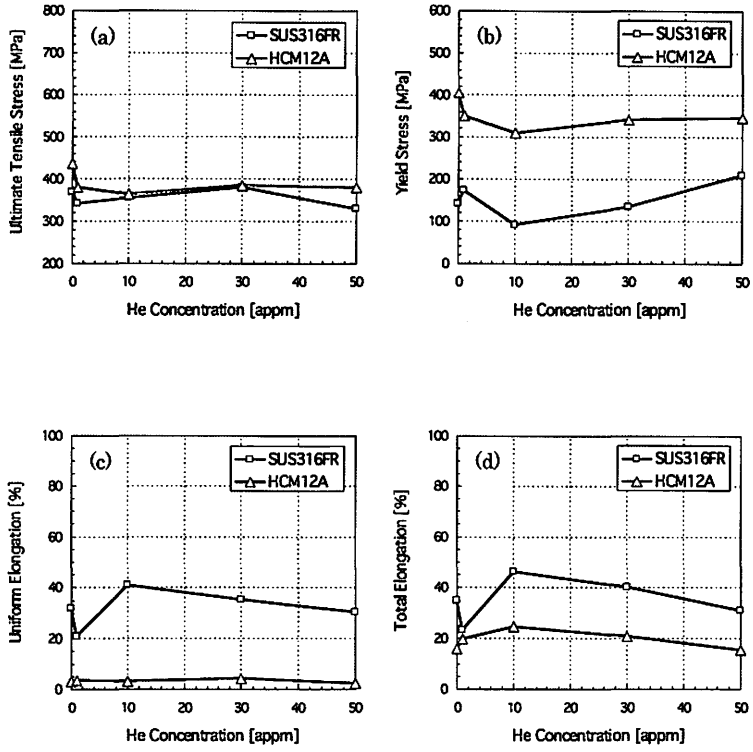

Figure 2. The results of the tensile test ((a) tensile strength, (b) yield stress, (c) uniform elongation, (d) total elongation) at about 550°C in 316FR and HCM12A implanted up to about 50 appm at about 550°C by Cyclotron[1].

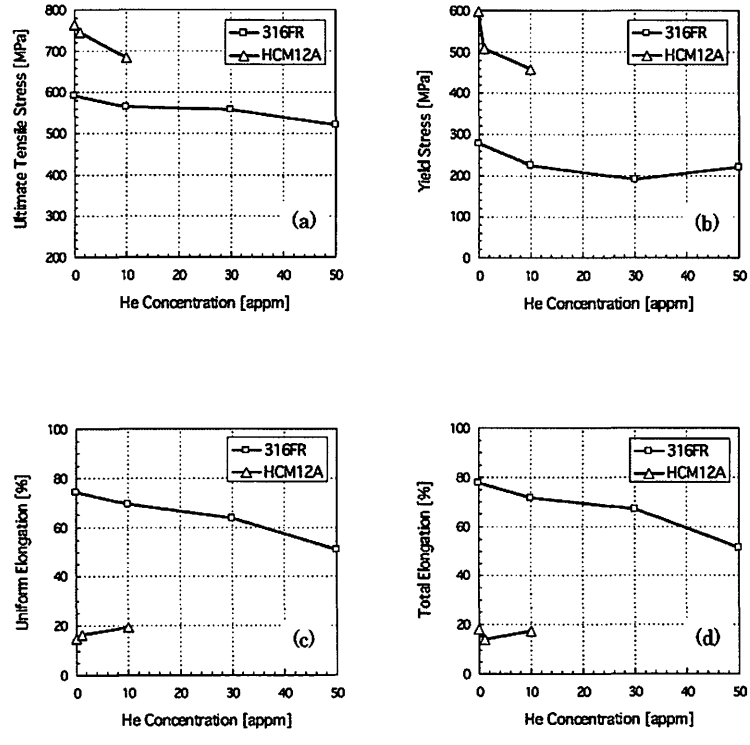

Figure 3. The results of the tensile test ((a) tensile strength, (b) yield stress, (c) uniform elongation, (d) total elongation) at room temperature in 316FR implanted up to about 50 appm and HCM12A implanted up to about 10 appm at about 550°C by Cyclotron[1].

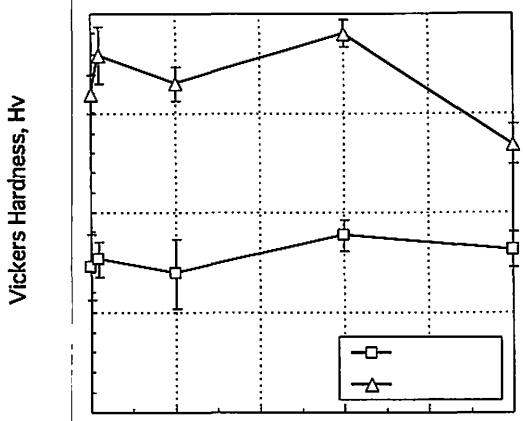

Figure 4. Vickers hardness in 316FR and HCM12A implanted up to about 50 appm at about 550°C by Cyclotron[1].

III. 2. Effective Estimation of Neutron-Induced Soft Error Rate on Advanced DRAMs Beyond 100 nm

Yahagi Y.[1], Saito A.[2], Matsumoto T.[2], Hayakawa T.[2], Ibe E.[1], Itoh M.[3], Yoshida P.H.[3], Sakemi Y.[3], and Baba M.[3]

[1]*Production Engineering Research Laboratory, Hitachi, Ltd.*
[2]*Elpida Memory Inc.*
[3]*Cyclotron and Radioisotope Center, Tohoku University*

Terrestrial neutron-induced soft-error or single event upset (SEU) in semiconductor devices is one of the most crucial reliability-issues in the cutting-edge memory devices, for example, deep-submicron static random access memories (SRAMs)[1-3]. Designers of electronic systems such as high-end servers, therefore, need the soft-error rate (SER) data of the electronic components in order to architecht the system reliability securely. We have intensively developed the SER estimation method for memory devices mainly using monoenergetic and quasi-monoenergetic neutron beams generated by accelerators, which is well reflected also in JEDEC Standard/JESD89A[4] published in Dec. 2006. The essential concept of the method is summarized as follows: the inherent excitation function of a device $\sigma(E)$ is described as the Weibull-type function[1-4],

$$\sigma(E) = \sigma_{\infty}\left[1 - \exp\left\{-\left(\frac{E - E_{th}}{W}\right)^{S}\right\}\right], \quad (1)$$

where σ_{∞} is the saturated value of the SEU cross section, E_{th}, the threshold neutron energy for SEU, W, the scale factor, and S, the shape factor of the Weibull function, respectively. The SER of the device is estimated in the unit of FIT (failure in time; a number of errors in 10^9 hours) by the formula

$$\mathrm{SER\,[FIT]} = 3.6 \times 10^{12} \int_{E_{th}}^{\infty} \sigma(E) \frac{\partial \phi_{\nu}(E)}{\partial E} dE, \quad (2)$$

where $\phi_{\nu}(E)$ means the flux of terrestrial neutrons at a specific place on the ground, for example, at sea level (0 m) in New York city.

Neutron irradiation experiments concerning DRAMs with stacked capacitors from

250-nm to 110-nm process were performed using monoenergetic and quasi-monoenergetic neutron beams of peak energy from 5 to 174 MeV at FNL (Fast Neutron Lab.) and CYRIC of Tohoku Univ. in Japan, and at TSL (The Svedberg Lab.) of Uppsala Univ. in Sweden[5,6]. Typical neutron spectra, which were used in the experiments, are shown in Fig. 1. Neutron energy dependence of SEU cross sections of each device is acquired by using monoenergetic and quasi-monoenergetic neutron beams. Test result of, for example, 220 nm DRAM is shown as solid triangles in Fig. 2. After approximating the energy dependence of SEU cross sections to the Weibull-type function (solid line in Fig. 2), SER of each devices at sea level in New York City was estimated by the self-consistent SER evaluation system, SECIS, by which estimated SERs are consistent with the results of real-time SER (field test) of a SRAM within 35% in accuracy[1-3]. The estimated SER of each device from monoenergetic and quasi-monoenergetic neutron irradiation tests is shown in Fig. 3. This figure shows that the SER of the DRAMs was effectively suppressed as its down-sizing to 150 nm owing to (i) the high storage capacitance, (ii) the shrinking of junction-volumes and (iii) the relatively gradual voltage scaling[1]. The constant SER-trend beyond 150 nm process technology node could be attributed to the difficulty of the design of the stacked-capacitor-type DRAMs at high yield of manufacture because of the high aspect ratio of the capacitor structure. Figure 3 contains also the problem of carrying out irradiation tests. Because of the less susceptibility to neutron-induced soft-errors, it becomes harder to acquire a statistically enough number of error events within an allocated beam time using the neutron beams with a low flux (~1×10^5 n/cm^2/s). A high intensity neutron source with a neutron flux around 1.5×10^6 n/cm^2/s installed in CYRIC[1,7] is very useful for the soft-error testing of devices with relatively higher immunity, and makes it possible to estimate the SER of such devices effectively.

References

1) Nakamura T., Ibe E., Baba M., Yahagi Y., Kameyama H., "Terrestrial Neutron-Induced Soft Errors in Advanced Memory Devices," World Scientific, 2008.
2) Yahagi Y., Ibe E., Saito Y., Eto A., Sato M., Kameyama H., Hidaka M., Terunuma K., Nunomiya T., Nakamura T., Renberg P.U., Prokofiev A., Final Report of IEEE 2002 International Integrated Reliability Workshop (2002) 143.
3) Ibe E., Yahagi Y., Kataoka F., Saito Y., Eto A., Sato M., Kameyama H., Hidaka M., IEEE 1st International Conference on Information Technology & Applications, Paper No.273-21 (2002).
4) JEDEC Standard/JESD89A, 2006.
5) Johansson K., Dyreklev P., Granbom B., Olsson N., Blomgren J., Renberg P.U., IEEE Trans. Nucl. Sci., **45** (1998) 2519.
6) Prokofiev A.V., Pomp S., Blomgren J., Bystrom O., Ekstrom C., Reistad D., Tippawan U., Wessman D., Ziemann V., Osterlund M., Workshop of Radiation Effects on Components and Systems, Data Workshop Paper PW-14 (2005).

7) Baba M., Okamura H., Hagiwara M., Itoga T., Kamada S., Yahagi Y., Ibe E., Radiation Protection Dosimetry, **126** (2007) 13.

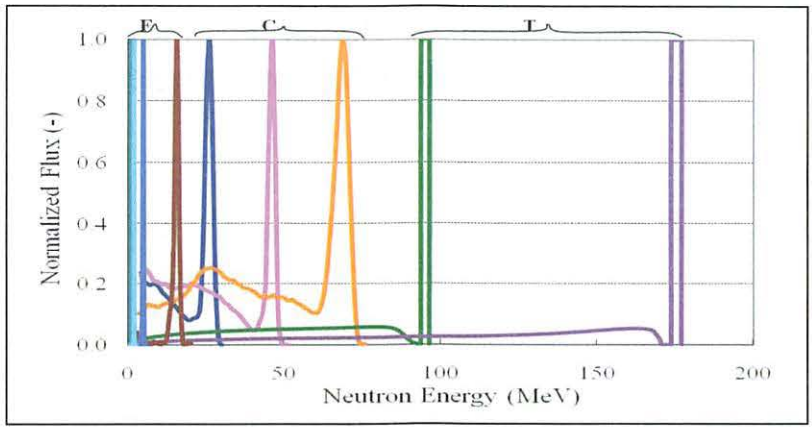

Figure 1. Typical energy spectra of monoenergetic and quasi-monoenergetic neutron sources. F denotes FNL, C, CYRIC and T, TSL.

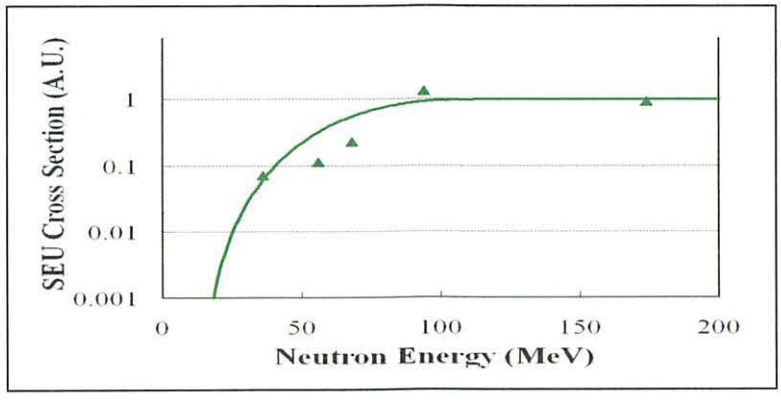

Figure 2. The test and the fitting results for 220-nm DRAM.

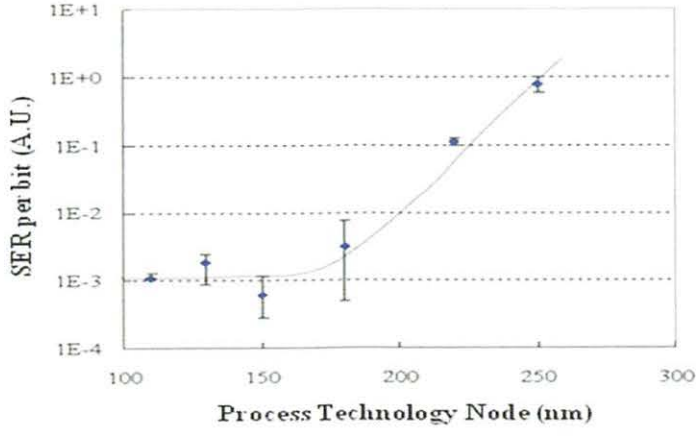

Figure 3. The SER-trend of DRAM with stacked capacitor from 250 to 110 nm rocess technology node. The solid line is an eye-guide for the trend.

III. 3. Evaluation of Radiation Hardness for Nitride Semiconductor Samples

Narita S.[1], Chiba Y.[1], Ichinose D.[1], Hitora T.[2], Yamaguchi E.[2], Sakemi Y.[3], Itoh T.[3], and Yoshida H.[3]

[1]*Department of Electrical Engineering and Computer Science, Iwate University*
[2]*ALGAN K.K.*
[3]*Cycrotron and Radioisotope Center, Tohoku University*

The wide-gap nitride semiconductor has excellent properties in thermal, mechanical and chemical stability, and it has been recently applied to various devices such as light emitting device, UV sensor, high electron mobility transistor (HEMT), and so on[1,2]. Moreover, the nitride semiconductor is known for having lower generation rate of charge carriers and higher atomic displacement energy. Then, the device is expected to have high radiation hardness. We examined the radiation tolerance for GaN Schottky diode, irradiating a high energy electron beam with a fluence up to 10^{16} electrons/cm^2, and found that the performance was not significantly changed[3]. We also evaluated the effects in the electric properties of GaN diode due to intrinsic defects induced by proton beam irradiation. No serious degradation in the diode characteristics was observed even after irradiating 10^{15}~10^{16} protons/cm^2 [4]. In this study, we have irradiated proton beam to GaN Schottky diode to verify the radiation hardness shown in the past experiments and investigated the behavior more precisely. In addition, we have tested another type of nitride device, AlGaN Schottky diode, which we have newly developed.

The Schottky barrier diodes used in this study were fabricated with heterostructure substrate produced by Powdec K.K. growing epitaxial GaN or AlGaN layer on n-type SiC substrate. The chip size of the diode was 0.5×.5 mm^2, and the thickness of the GaN and AlGaN layers were ~900 nm and ~500 nm, respectively. The Schottky Ni/Au electrode was put onto the GaN/AlGaN layer and the Ti/Au Ohmic contact was deposited on the SiC. The diode structure is shown in Fig. 1. The diode chip was mounted on a thin (t=1.2 mm) CEM-3 substrate.

Beam irradiation was carried out at CYRIC, using a 50 MeV proton beam. The beam current was ~100 nA in this experiment. The target diodes were not applied voltage and electrically floated during the irradiation. The degradation of the semiconductor detector, in principle, depends on the energy loss of the particles irradiated in both ionizing (forming electron-hole pair) and non-ionizing processes in the material. Especially, the non-ionizing energy loss possibly makes the atomic displacement in the crystal and it is considered to cause degradation of the device performance which includes increase of noise, lowering charge collection efficiency, and worse signal charge resolution. The non-ionizing energy loss of a 50 MeV proton is estimated to be 4 keVcm^2/g^{-1} [5].

In prior to the irradiation to the sample, an aluminum foil was exposed to the proton beam, then, the radioactivity of meshed area on the foil was measured by imaging plate to obtain the beam profile. Assuming that the beam condition was stable over the experiment periods, the profile measurement was employed just once in. The profiles along X and Y axes obtained with this procedure are shown in Fig. 2. The proton fluences on the diode were determined considering the beam current and these profiles. The fluence on the samples was in the range of 10^{13} to 10^{16} protons/cm^2.

The current-voltage (I-V) characteristics were measured pre- and post-irradiation by the ultra high resistance meter (ADVANTEST R8340) in order to investigate the effect of the incident protons. The samples were kept at room temperature over the experimental term. We performed the measurement after 28 days and 159 days of the irradiation, for study of long-term relaxation of the changes. The I-V curves before and after irradiation for each proton fluence are shown in Fig. 3. With a fluence up to 10^{14} protons/cm^2, the reverse dark currents and the break down voltages were essentially unchanged. In the measurement 28 days after the irradiation, the reverse currents increased by a factor of ~10^3 with a fluence of 6.1×10^{15} protons/cm^2 and a factor of ~10^6 with 2.4×10^{16} protons/cm^2, respectively. The gentle slopes of the forward current were seen in these fluences. Furthermore the reverse current at 6.1×10^{15} protons/cm^2 was fluctuated unstably, while the break down voltages looked unchanged. However, in the measurement 159 days after, some recovery in the dark currents was observed and unstable current behavior of the sample irradiated 6.1×10^{15} protons/cm^2 was not seen any more. Proton irradiation may induce trap states in the material, then, they affect the electric conductivity. This recovery in the dark currents may be associated with the reduction of such trap states.

Figure 4 presents I-V curves of AlGaN diodes before and after irradiating 1.5×10^{15}

protons/cm^2. The irradiation did not induce obvious changes in dark current, break down voltages, and slope of forward current.

Now we have proved the radiation hardness of GaN/AlGaN diodes for irradiating up to 10^{14} protons/cm^2. For GaN sample, we observed increase of dark currents with a fluence above 10^{15} protons/cm^2. The increase in the currents was considerable larger comparing with the results in our previous results. It is possible that the quality of epitaxial GaN substrate and/or the fabrication process might give difference in properties of individual samples. The damage effects depend on various parameters, such as device structure, type and energy of particles irradiated, with/without applying the voltage to the device. Therefore, for ensuring the high radiation hardness of the nitride semiconductor, it is still necessary to repeat the test with various conditions and evaluate the properties quantitatively from various points of view such as changes in carrier density, generation of trap level, and so on.

References

1) Ruterana P., Albrecht M., Neugebauer J., "Nitride Semiconductors" (WILEY-VCH, 2003).
2) Adachi S., "Properties of Group-IV, III-V and II-VI semiconductors" (John Wiley and Sons, Ltd, 2005).
3) Narita S., et al., Research Report of LNS, **40** (2007) 31.
4) Narita S., et al., CYRIC Annual Report (2008) 14.
5) Holmes-Siedle A. and Adams L., "Handbook of Radiation Effects" (Oxford University Press, 2001).

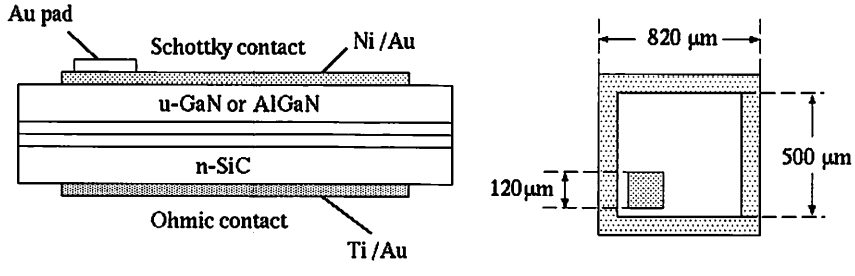

Figure 1. GaN / AlGaN Schottky diode.

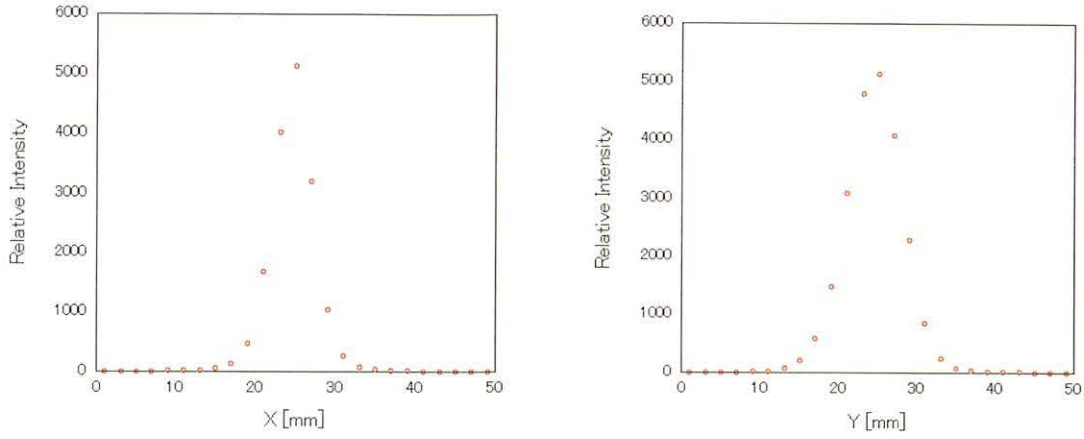

Figure 2. Beam profile. (left:X, right:Y).

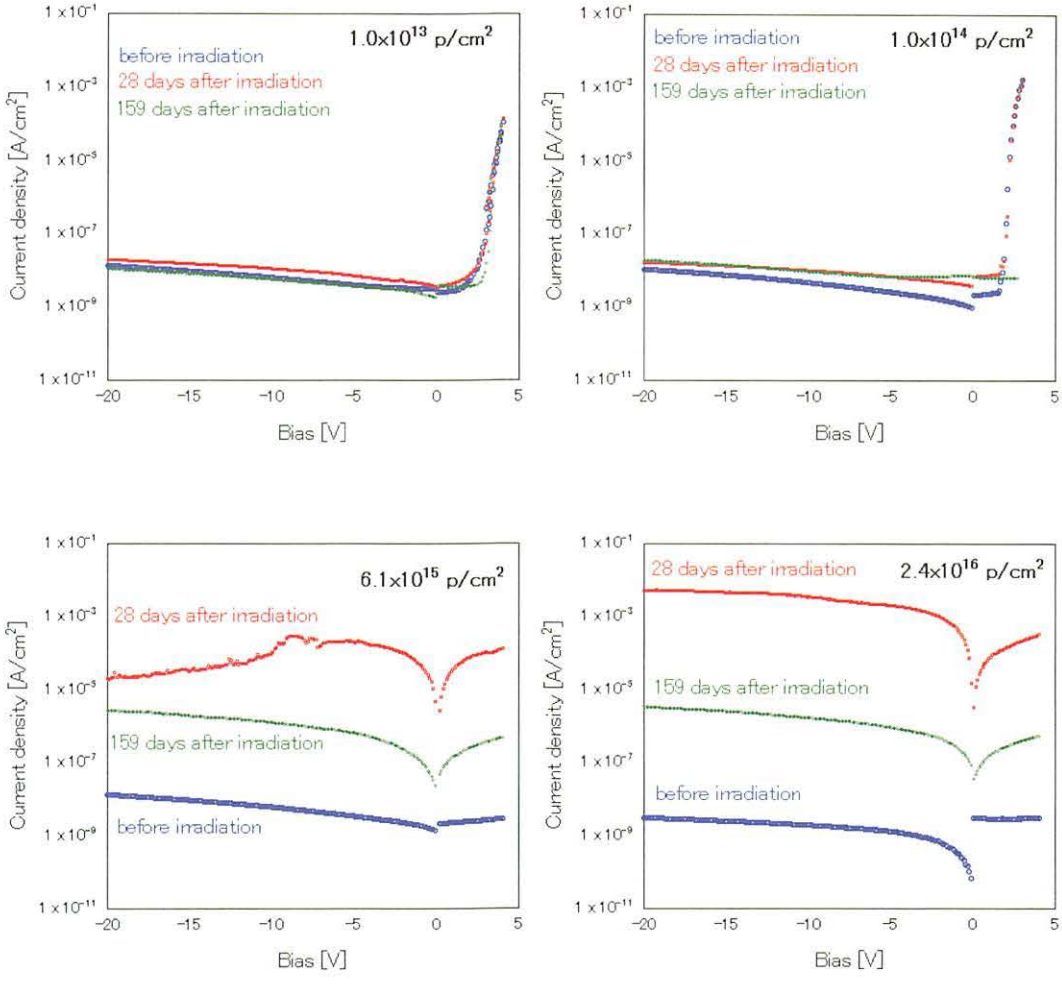

Figure 3. I-V Characteristics of GaN Schottky diode before and after proton beam irradiation.

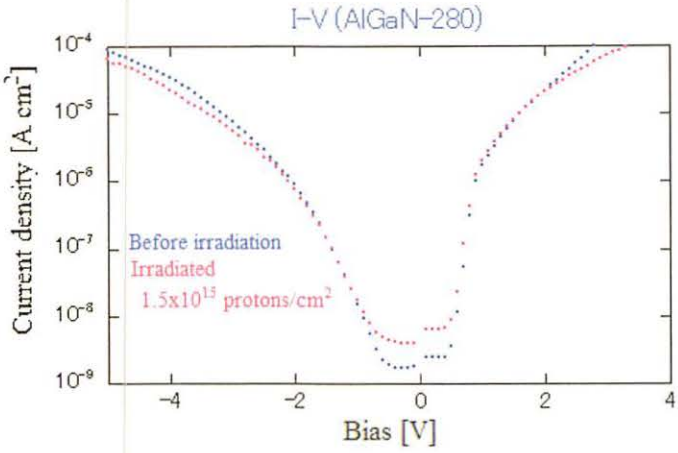

Figure 4. I-V Characteristics of the proton irradiated AlGaN Schottky diode with a fluence of 1.5×10^{15} protons/cm^2, comparing with that of reference sample.

IV. NUCLEAR MEDICAL ENGINEERING

IV. 1 Tumor Growth Delay Caused by Proton Therapy in Combination with the Vascular Disrupting Agent AVE8062

Terakawa A.[1,2], Ishii K.[1,2], Matsuyama S.[1], Kikuchi Y.[1], Akiyama H.[1], Koyata K.[1], Ito Y.[1], Tagawa A.[1], Yasunaga S.[1], Yamazaki H.[3], Tashiro M.[3], Funaki Y.[3], Furumoto S.[4,3], Itoh N.[5], Wada S.[5], and Orihara H.[6]

[1]*Department of Quantum Science and Energy Engineering, Tohoku University*
[2]*Graduate School of Biomedical Engineering, Tohoku University*
[3]*Cyclotron and Radioisotope Center, Tohoku University*
[4]*Tohoku University Graduate School of Medicine*
[5]*School of Veterinary Medicine and Animal Sciences, Kitasato University*
[6]*Department of Intelligent Electronics, Tohoku Institute of Technology*

Vascular disrupting agents (VDAs) are designed to cause a rapid and selective blood flow interruption in tumors leading to extensive tumor necrosis as a result of oxygen and nutrient deprivation. In spite of the fact that VDAs give rise to a catastrophic shutdown in the vascular function of the tumor, the tumor cells at the border between malignant and normal tissue survive treatment with VDAs. It is believed that the tumor cells at the tumor periphery are supported by oxygen and nutrients from the surrounding normal vessels and repopulate the tumor after the VDA treatment alone[1]. Thus, VDAs may fully provide their therapeutic potential when used in combination with radiotherapy or chemotherapy. In the preset study, we aim to evaluate the therapeutic efficacy of proton therapy combined with the vascular disrupting agent AVE8062, which is undergoing clinical assessment, by using the tumor growth delay (TGD) assay in a solid murine tumor.

The proton therapy experiment was performed at the proton therapy facilities[2] of Cyclotron and Radioisotope Center (CYRIC), Tohoku University. NFSa fibrosarcoma cells (5×10^6/50 μL) were transplanted into both hind legs of C3H/HeSlc male mice aged around 12 weeks old. Figure 1 illustrates a beam delivery technique in the present experiment. When each tumor diameter reached about 8 mm, single-dose irradiation was given only to the tumor of the right hind leg. In order to immobilize the mouse during the irradiation, pentobarbital anaesthesia (50 mg/kg) was administered intraperitonealy to each mouse. The tumor was irradiated in the maximum depth dose region, the so-called SOBP

(spread-out Bragg peak) provided with an energy modulation filter, and received a single dose of 15 or 30 Gy at 5 Gy/min. The SOBP width was 10 mm. The normal tissue surrounding the tumor was shielded from the irradiation with patient's collimator and bolus. The tumor of the left hind leg was not irradiated. In addition, AVE8062 was administered intraperitonealy to a part of the mice receiving 15 Gy at a dose of 40 mg/kg 2 hours after irradiation. As a result, we classified the tumors of the right and left hind legs into proton therapy (15 or 30 Gy), AVE8062 treatment (40 mg/kg), combination treatment (15 Gy + 40 mg/kg) and control groups, as shown in Fig. 2. All experimental protocols in this work were reviewed by the Committee on the Ethics of Animal Experiments at Tohoku University, and were performed in accordance with its guidelines.

Figure 3 shows the time-course of tumor volume for each treatment group. The tumor volumes were measured daily after the treatment according to the formula $\pi abc/6$, where a, b and c are three orthogonal diameters of the tumor. In this work, TGD was defined as the difference in tumor growth time in days required for each tumor volume to reach four times the initial volume between the control and the treatment groups[3]. Results of TGD observed for the treated tumors are listed in Table 1. Although TDG for the proton therapy at a single dose of 15 Gy was about 2 days and approximately equal to that for AVE8062 treatment alone, the combination treatment inhibited the tumor growth more strongly and enhanced TGD at levels nearly comparable to that for the proton therapy at a single dose of 30 Gy.

In conclusion, the significant enhancement of tumor growth delay in the proton therapy combined with post-radiotherapy administration of AVE8062 was observed in the present work. A possible explanation for the present result is that the combination treatment may efficiently kill radiation-resistant hypoxic cells in the tumor as well as the tumor cells at the tumor periphery which survive monotherapy with VDAs.

This work was supported by Grants-in-Aid for Scientific Research (B) Nos. 17300169 (A. Terakawa) and 20300174 (A. Terakawa), and by Exploratory Research No. 19650128 (A. Terakawa) of the Ministry of Education, Culture, Science, Sports and Technology.

References

1) Dietmar W. Siemann et al., Cancer, **100** (2004) 2491.
2) Atsuki TERAKAWA et al., Proceedings of the 16th Pacific Basin Nuclear Conference (16PBNC), Oct. 13-18, 2008, Aomori, Japan, PapaerID P16P1378, p1-p6
3) Workman P. et al., Cancer and Metastasis Reviews **8** (1989) 82. UKCCCR Guidelines for the Welfare of Animals in Experimental Neoplasia.

Table 1. Tumor growth delay (TGD) for the treated tumors.

	Proton therapy at 15Gy ($n=4$)	AVE8062 administration (40 mg/kg) ($n=5$)	Proton therapy at 30 Gy ($n=4$)	AVE8062 administration (40mg/kg) 2 h after proton therapy at 15 Gy ($n=5$)
TGD (day)	2.1±1.1	2.8±0.7	9.2±1.1	7.4±0.7

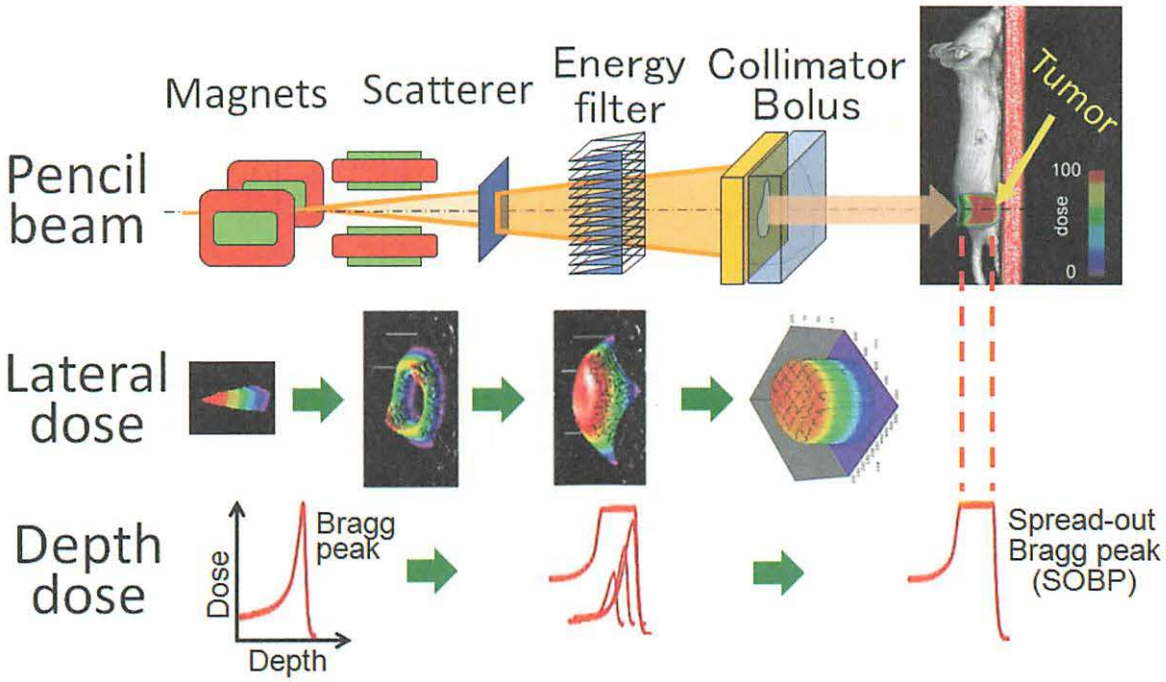

Figure 1. Dose delivery to the tumor in proton therapy.

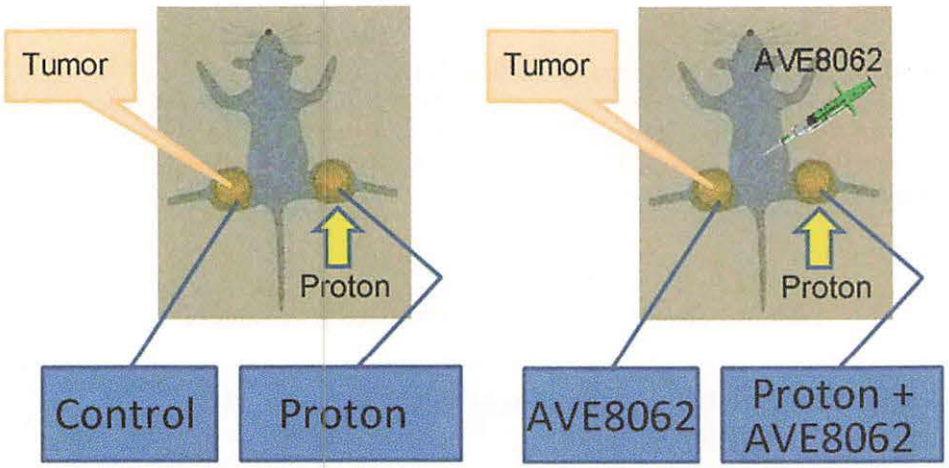

Figure 2. Groups of the treated tumors in the present study.

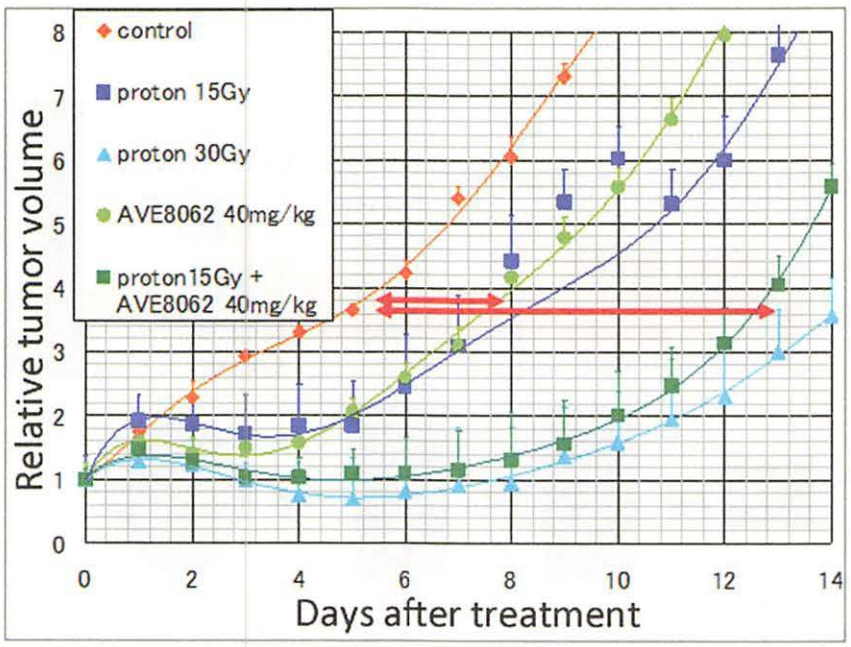

Figure 3. Time course of the relative tumor volumes. Each single-treatment was done at day 0. Arrows indicate the TDGs for the treated tumors.

IV. 2. Development of a Multi-pattern Gas Detector for Beam Monitoring in Proton Therapy

Terakawa A.[1,2], Ishii K.[1,2], Matsuyama S.[1], Kikuchi Y.[1], Togashi T.[1] Arikawa J.[1], Yamashita W.[1], Akiyama H.[1], Koyata K.[1], Ito Y.[1], Tagawa A.[1], Yasunaga S.[1], Sakemi Y.[3], Itoh M.[3], Yamazaki H.[3], and Orihara H.[4]

[1]*Department of Quantum Science and Energy Engineering, Tohoku University*
[2]*Graduate School of Biomedical Engineering, Tohoku University*
[3]*Cyclotron and Radioisotope Center, Tohoku University*
[4]*Department of Intelligent Electronics, Tohoku Institute of Technology*

A pencil beam scanning technique in hadron therapy provides a three-dimensional dose distribution optimized to match the maximum dose distribution to the tumor shape, while the normal tissue in front of the tumor usually receives the same dose as the tumor in a conventional irradiation method using a constant spread-out Bragg peak. Although the scanning irradiation shows therapeutic benefits, its operation requires accurate real-time information about quickly varying characteristics of scanned beams for avoiding under- or over-dosage. Recently, a gas electron multiplier (GEM) technique has been developed[1)] and used in various fields as a new type of a gas detector system. The GEM system has advantages over a multi-wire proportional chamber such as the excellent special resolution and higher counting rate, and can be expected to meet severe requirements for beam monitoring in the scanning irradiation. In this report, we describe a multi-pattern gas detector (MPGD) based on GEM developed at CYRIC as a prototype of a beam monitor for the pencil beam scanning method.

A schematic view of the MPDG system is illustrated in Fig. 1. The MPDG consists of a GEM plate, a cathode plate, a readout and two window foils, and filled with a gas mixture (Ar 90% + CH_4 10%). The GEM plate consists of a 100 μm thick liquid crystal polymer (LCP) sandwiched between 9μm thick cupper electrodes, and has holes in 70μ in diameter with 140 μm distance. Electrons induced by an incident proton beam are multiplied by GEM and detected with the readout plate. It will be possible to evaluate a two-dimensional (2D) intensity distribution of the pencil beam from the readout data. In

the present study we used the GEM plate with an active area of 50×50 mm, and the readout plate having a 2D array of 8×8 channels to verify the fundamental concept of the MPDG based on GEM. The channel pitch is 3 mm for both lateral directions. When obtaining high-resolution 2D distribution of the pencil beam, we have to use a new readout having a large number of channels. Energy loss of the incident beam in the MPDG is about 2.5 MeV for an 85-MeV proton.

In order to evaluate characteristics of the MPDG for beam monitoring, beam tests were performed using an 80-MeV proton beam provided from the K=110-MeV AVF cyclotron at CYRIC. The experimental setup is shown in Fig. 2. The MPDG was placed in the horizontal irradiation system of the CYRIC proton therapy facilities[2], and irradiated with a proton pencil beam. As shown in Fig. 3, lateral intensity distributions measured with the GEM-based MPDG are in good agreement with those measured using an Imaging Plate[3] (IP) located at the same position. In addition, when the pencil beam was deflected using the scanning magnets before the MPGD, the intensity distributions obtained from the MPDG were shifted according to the beam deflection. Thus, we can obtain high-resolution 2D intensity distributions for the scanned beam if the number of the readout channels of the MPDG is increased.

Figure 4 shows typical relationships between current outputs from the MPDG and those from the ionization chamber used for dose monitoring located behind the MPDG (See Fig. 2). Since the current of the MPDG is induced by the incident proton beam, it is likely that the amount of the output current of the MPDG is proportional to that of the dose monitor.

In conclusion, the present experimental results have demonstrated that the MPDG system can be used not only as a beam position and 2D-intensity monitor but also as a dose monitor to obtain real-time information about beam parameters in the pencil beam scanning operation.

This work was supported by Grants-in-Aid for Scientific Research (B) Nos. 17300169 (Terakawa A.) and 20300174 (Terakawa A.), and by Exploratory Research No. 19650128 (Terakawa A.) of the Ministry of Education, Culture, Science, Sports and Technology.

References

1) Sauli F., Nucl. Instrm and meths. **A386** (1997) 531.
2) Terakawa A., et al., Proceedings of the 16th Pacific Basin Nuclear Conference (16PBNC), Oct. 13-18, 2008, Aomori, Japan, PapaerID P16P1378, p1-p6.
3) Fuji Photo Film Co., Ltd.

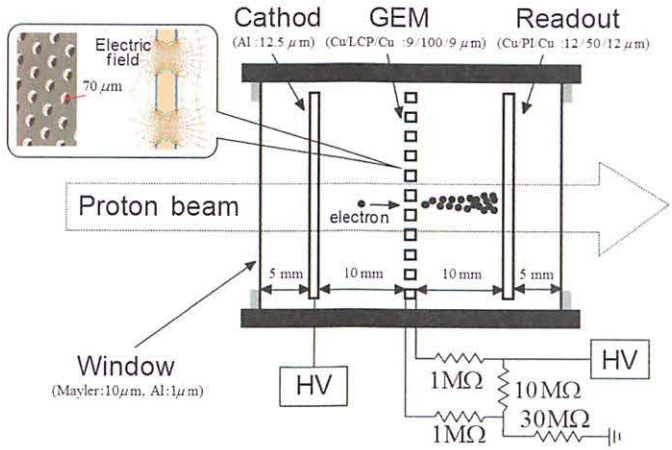

Figure 1. Multi-pattern gas detector based on GEM for measuring a 2D beam-intensity distribution.

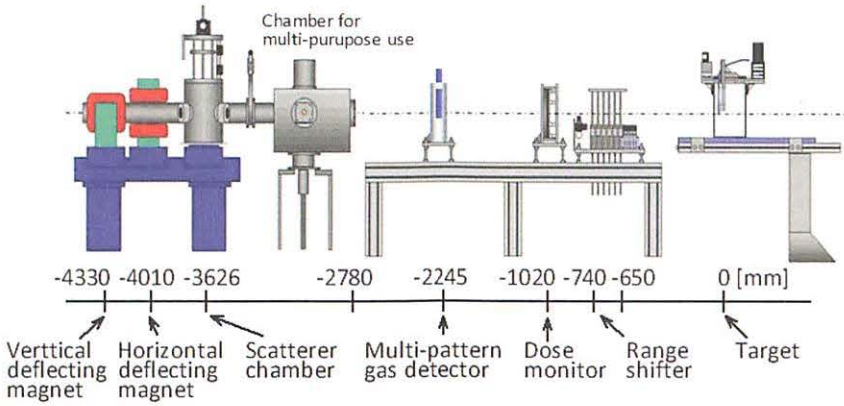

Figure 2. Experimental setup of the multi-pattern gas detector.

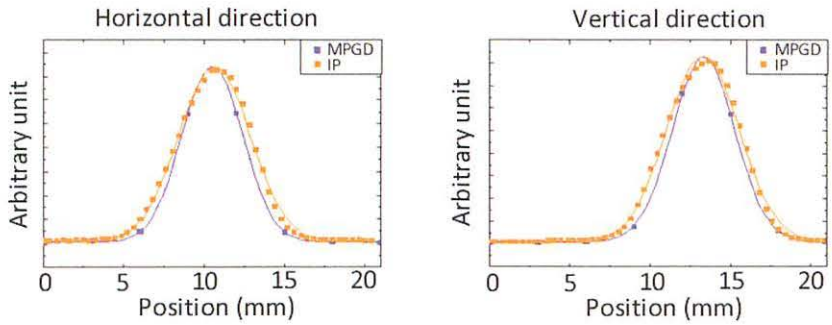

Figure 3. Comparisons of measured lateral intensity-distributions of the incident proton beam between MPDG and IP.

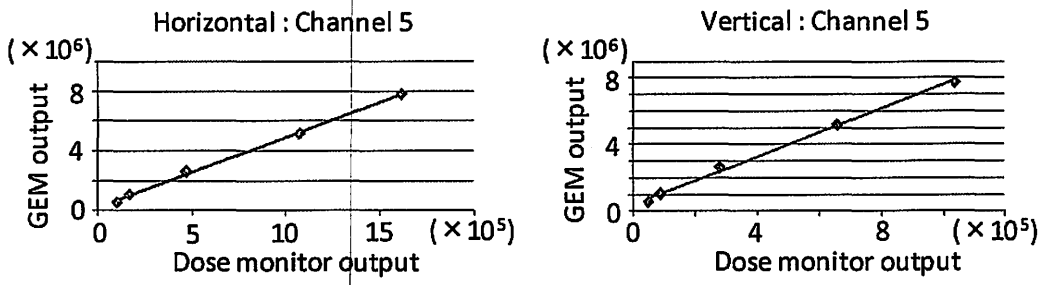

Figure 4. Relationships between the MPDG output current and relative dose measured with the dose monitor placed behind the MPDG.

IV. 3. Computed Tomography Dosimeter Utilizing a Radiochromic Film and an Optical Common-mode Rejection

Ohuchi H.

Graduate School of Pharmaceutical Sciences, Tohoku University

Introduction

Recently the need for novel and precise measurements of calibrated dose distributions in diagnostic CT has been increased. For this purpose, the spatial resolution and ease-of-handling properties of radiochromic films (RCFs) make them ideal candidates. The RCF is a thin, plastic, 2D planar dosimeter offering ease of handling and broadly applied in dosimetry[1-3]. However, its low sensitivity precludes their application to measuring lower doses accurately. Assuming macroscopic and microscopic non-uniformities of film layers, including the thickness variations in the film's active radiochromic layer and coating, were the main causes of light disturbance (noise) against the lights (signal), resulting in a lowering of actual film sensitivities, we developed an optical common-mode rejection (CMR) that can improve the dosimetric sensitivity limit of radiochromic films[4,5]. In the RCF, the R component is highly sensitive to radiation exposure as two absorption peaks, while the G component is less sensitive than R component is, owing to the absence of a clear absorption peak in the green waveband. The ratio of the two components (R:G) is analogous to the 'common-mode rejection' (CMR) in electronics, where the factors common to both numerator and denominator cancel out. In this work, we present a method of measuring reflective mode calibrated radiochromic film response with a flatbed scanner, combined with the conventional analysis way using red component and our new data analysis method of an optical CMR scheme. Then, we investigate the dosimetric characteristics of the film when irradiated with kilovoltage CT X-ray radiation and obtain the radiation dose profiles.

Materials and Methods

The radiochromic film model GafChromic XRCT, produced by ISP (International Specialty Products), was used. In the film, two 25-μm-thick active layers, which are separated by a double 5-μm-thick inert interlayer, are sandwiched between the two substrates of 97-μm polyester, one of which is transparent and the other is opaque (white). The XRCT film is available in a strip of sheet with a metric scale. The scale runs from -50 mm to +50 mm. The dosimetric characteristics of the film were determined by cutting sheets of film into small 2×2 cm squares and the radiation dose profiles were acquired by using the strip of film from an Aquilion 64 CT scanner fabricated by Toshiba Medical Systems Co. The tube voltages of 80, 100, and 120 kV were used to investigate the energy dependence. The dose-response of XRCT films in the range from 0.283 to 119.7 mGy was evaluated in each tube voltage of 80, 100, and 120 kV. The angular dependence of the film response was determined by rotating the CT X-ray tube in the range of -90° to 90° in 30° step. For each exposure, four film samples were irradiated in the lower range less than 1 mGy, two for the delivered dose above 1 mGy and the amount of radiation was measured by using a Radcal 10×5-6 thimble chamber of 6 cm^3 effective volume (Radcal Co.). To obtain radiation dose profiles, the film sample was exposed at 120 kV, 300 mA, and 1.5 s exposure time with 1, 2, 4, and 8 mm beam. The films were scanned before and twenty-four hours after exposure with an Epson ES-10000G flatbed color image scanner (SEIKO EPSON Corporation) with 300 dpi resolution (84.6 μm/pixel) and 16 bits per color of the digital resolution dpi. The scans were performed in reflection mode using a white lid with no color correction factors or filters. The obtained digital data were evaluated using self-written routines in MATLAB 7.3 software (The Mathworks, Natick, MA).

The reflectance is obtained as digitalized output of the R, G, B component, when films are scanned by a color scanner in reflection mode. The relationship between reflectance (Rf) and optical density (OD) used in film dosimetry can be expressed as follows,

$$OD = \log_{10}(2^{16}/Rf),$$

$$\text{net } OD = OD - OD_0 = \log_{10} Rf_0 - \log_{10} Rf = \log_{10} (Rf_0/Rf) \quad (1)$$

where subscripts denote unirradiated background quantities and 'net' stands for the quantities after removing the background.

The conventional analysis way uses only red component, at which net OD_Rd is defined as,

$$\text{net OD\_Rd} = \log_{10}(Rd_0/Rd) \quad (2)$$

In the optical CMR scheme, in which red and green components are used, Rf should be replaced by Rd/Gr, where Rd and Gr are each amount of reflectance lights. Thus, net reduced OD (net ROD_Rd_Gr) in the optical CMR scheme is written as,

$$\text{ROD\_Rd\_Gr} = \log_{10}(Rd/Gr),$$

$$\text{net ROD\_Rd\_Gr} = \log_{10}((Rd_0/Gr_0)/(Rd/Gr)) \quad (3)$$

Results and Discussion

Figure 1 shows the absorption spectra, obtained using a GretagMacbeth SpectroEye reflection spectrometer, for GafChromic XRCT film unirradiated and exposed to 81.25 mGy produced by a 120 kV X-ray beam over the range of 380 - 730 nm in 10 nm steps and an example of filter functions for red, green, and blue wavebands on CCD. The results show the absorption spectra produce two pronounced peaks located around at 630 nm as a main peak and 580 nm as a subpeak, which are lying in the red region of the light spectra.

The two dose-response curves as a function of delivered dose ranging from 1.069 to 119.7 mGy for tube voltages of 80, 100, and 120 kV X-ray beams and from films scanned 24 hrs after exposure are plotted in Fig. 2. Closed marks of triangles, squares, and circles represent the net optical density obtained by using red component in Eq. (2) for tube voltages of 80, 100, and 120 kV, respectively. Open marks of triangles, squares, and circles show the net reduced OD calculated by Rd and Gr components in Eq. (3) for each tube voltage as well. Error bars are shown in the figure as one standard deviation for data of approximately 200×200 pixels. There are no sensitivity variations in the range of 80 - 120 kV for both curves of the net optical densities of OD_Rd (closed marks) and the net reduced OD of ROD_Rd_Gr (open marks), indicating its energy independence from this X-ray energy range. Both figures also indicate that the XRCT film response is nonlinear. The net optical densities of OD_Rd demonstrates a continuous increase in all over the range, however, the curve for the net reduced OD seems to reach its maximum over 50 mGy.

To compare the two dose-response curves as a function of delivered dose between the net optical density of OD_Rd and the net reduced OD of ROD_Rd_Gr under 50 mGy (at which the curve for the doesn't reach its maximum), second-order polynomial fits were applied to each of the two curves and equations without y-intercept were exhibited in Fig. 3 (a). Fig.3 (b) shows the expanded figures for two indices of OD_Rd and ROD_Rd_Gr, respectively, in the low range less than 2 Gy in Fig. 3 (a). In Fig. 3 (b), the measured optical

densities obtained with the optical CMR scheme show a good consistency among four samples and all values show an improved consistency with a second-order polynomial fit. These results indicate that the CMR scheme makes it possible to measure the dose in the lower range less than 1 mGy though the dose of 1 mGy is the lowest detectable dose for product specification.

Figure 4 shows an angular response of optical densities of XRCT films for X-rays with a tube voltage of 120 kV in the range of -90° to 90° in 30° step. The maximum variation among individual readings of XRCT films is 3.0% except -90° and 90°. The result revealed that the XRCT film has an almost isotropic efficiency except -90° and 90°. Relatively low responses of the XRCT film are observed at $\pm 90°$, because large numbers of incidences might not hit the surface of the thin XRCT film and/or X-rays might be attenuated by the XRCT film itself as they traverse the XRCT film.

Figure 5 shows CT radiation profiles collected using the XRCT films with 1, 2, 4, and 8 mm beam and displayed in the net optical density of OD_Rd with an overlay displayed in OD with an overlay of the same profile converted to exposure dose using the experimentally determined relationship between net OD and exposure dose in Fig.3 (a). The both profiles of net OD (closed triangles) and exposure dose (solid lines) show the same shape with 1, 2, 4, and 8 mm beam so that FWHM measured using either OD or exposure results in the same measurement.

This result combined with its energy independence from 80 kV to 120 kV X-ray energy range provides a unique enhancement in dosimetric measurement capabilities such as the acquisition of high-spatial resolution and calibrated radiation dose profiles over currently available dosimetry films for CT applications.

References

1) Cheung J. Y. C., Yu K. N., Ho R. T. K., Yu C. P., Med. Phys. **26** (1999)1252.
2) Fiandra C., Ricardi U., Ragona R., Anglesio S., Giglioli F. R., Calamia E., Lucio F., Med. Phys. **33** (2006)4314.
3) Morris K. N., Weil M. D., Malzbender R., Phys. Med. Biol. **51**(2006)5915.
4) Ohuchi H. and Abe K., Nucl. Instrum. Methods Phys. Res.**A 558**(2006)576.
5) Ohuchi H., Med. Phys. **34(11)** (2007)4207.

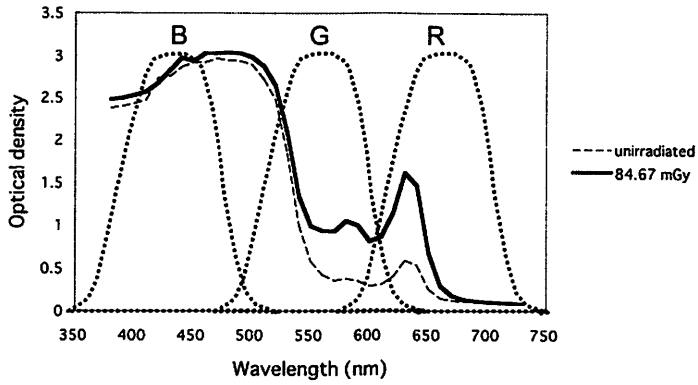

Figure 1. Absorption spectra for GafChromic XRCT film unirradiated and exposed to 81.25 mGy produced by a 120 kV X-ray beam over the range of 380 - 730 nm in 10 nm steps and an example of filter functions for red, green, and blue wavebands on CCD.

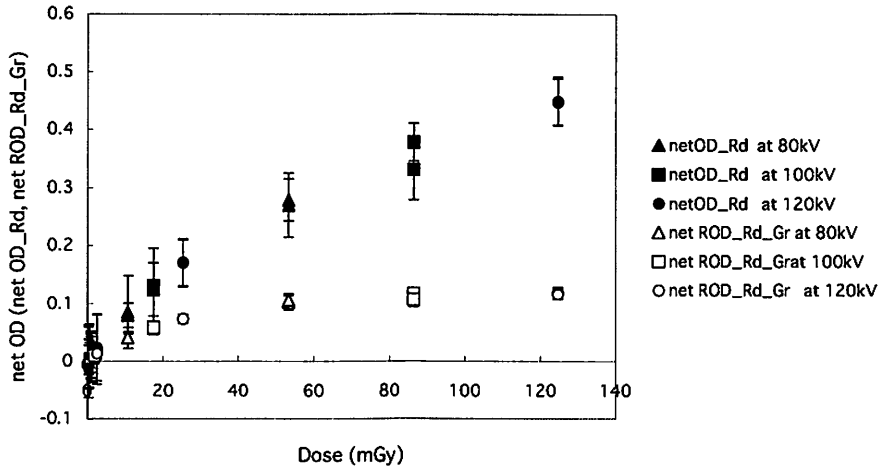

Figure 2. Dose-response curves as a function of delivered dose ranging from 1.069 to 119.7 mGy for tube voltages of 80, 100, and 120 kV X-ray beams and from films scanned 24 hrs after exposure.

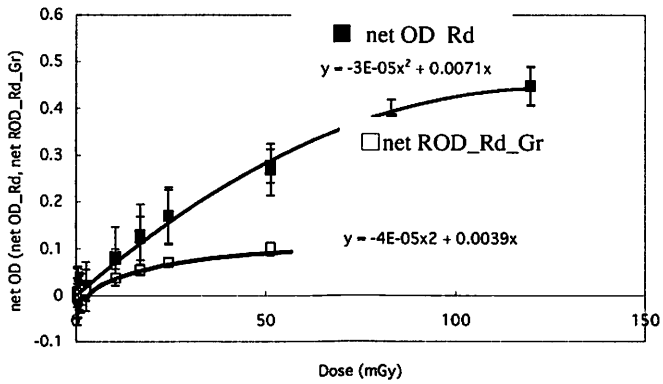

(a)

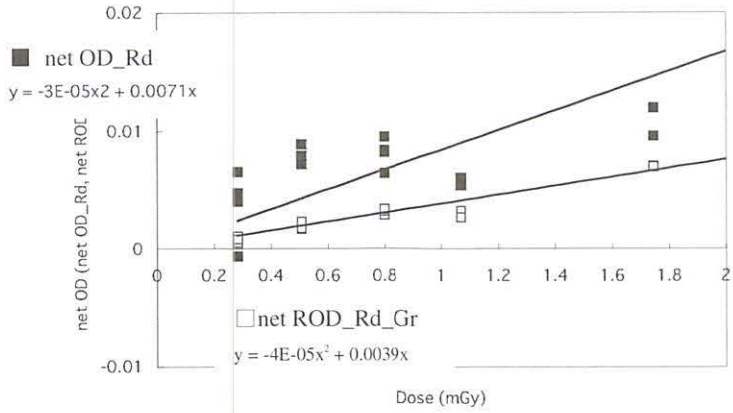

(b)

Figure 3. Net optical density of OD_Rd and the net reduced OD of ROD_Rd_Gr demonstrate each second-order polynomial fit and equation without y-intercept in Fig.3 (a). Fig.3 (b) shows the expanded figures for two indices of OD_Rd and ROD_Rd_Gr. respectively, in the low range less than 2 Gy in Fig.3 (a).

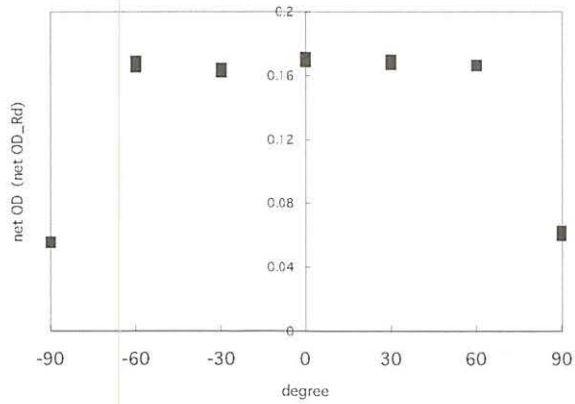

Figure 4. Angular response of optical densities of XRCT films for X-rays with a tube voltage of 120 kV in the range of -90° to 90° in 30° step.

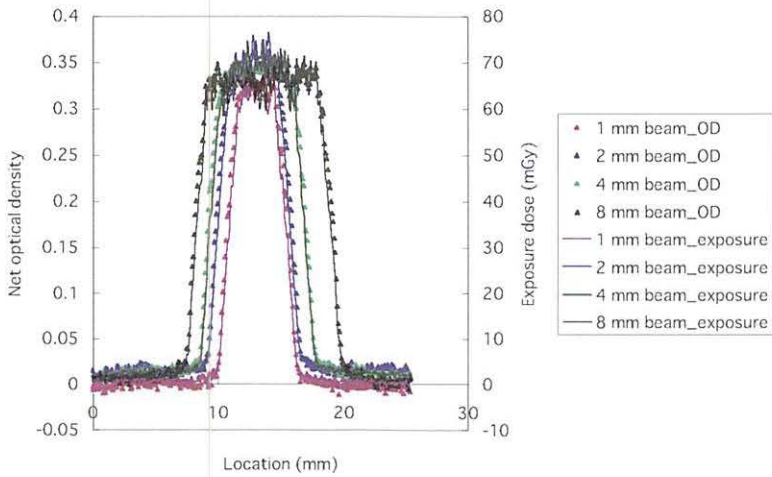

Figure 5. CT radiation profiles with 1, 2, 4, and 8 mm beam measured using the XRCT film. (120 kV, 300 mA, and 1.5 s). Net OD_Rd profiles and their conversion to exposure dose using the relationship between net OD and exposure dose from Fig. 3 (a).

IV. 4. Characteristics of Unerasable and Reappearing Photostimulated Luminescence Signals in Over-irradiated Imaging Plates and a N ew Complete Erasing Method

Ohuchi H.[1] *and Kondo Y.*[2]

[1]*Graduate School of Pharmaceutical Sciences, Tohoku University*
[2]*Ishinomaki Senshu University*

Introduction

An imaging plate (IP) made of europium-doped BaFBr, a photostimulated luminescence (PSL) material, is a two-dimensional radiation sensor[1,2]. It has a wide dynamic range and high spatial resolution, and can be used repeatedly by exposing it to visible light for 20 - 30 min between uses. Through various experiences involving exposure of IPs to X-ray radiation, some unexpected effects have become known, i.e., the phenomena of unerasable and reappearing latent images. In IPs irradiated with X-ray doses exceeding 1 mGy, quite stable latent images remain unerasable after fully erasing with visible light and latent images reappear after a while even when they seem to have been completely erased. It is important to know the detailed characteristics of these effects on applied fields, which typically require establishment confidence, limitations, and a complete erasing. The level scheme of the PSL material is reported by Iwabuchi et al.[3]. In practice, however, the irradiation creates more complexed centers in the material, which may cause unerasable and reappearing PSL signals in over-irradiated IPs. In this study, characteristics of these unerasable and reappearing PSL signals were studied by irradiation with X-rays. Based on the results, a new method to completely erase unerasable latent images has been developed.

Materials and Methods

A PSL sheet lacking a protective surface layer that was developed for ^{3}H detection (type BAS-TR2040: FUJIFILM Co.) was used. Small square pieces with a size of 1.5 - 2.0 cm×1.5 - 2.0 cm were cut from the PSL sheet for use as irradiation samples. The BAS-

TR2040 samples were uniformly exposed to X-ray beams of 100 kV with a 1.0-mm Al filter from an MBR-1520R unit (Hitachi Medico Co.) in the range from 4.6 mGy to 10 Gy. The tube current was varied from 5 mA to 15 mA. The samples were scanned by an imaging plate reader (FLA3000) and a fluorescent eraser (IP Erase 3) was used to erase the samples with visible light. Both are fabricated by FUJIFILM Co..

The irradiated IP samples were fully erased with visible light and then stored under 4°C during the 7, 13, 20, 27, 35 and 42 days prior to reading to study the relationship between reappering PSL signals and storage days. The IP samples were irradiated in the range of 0.3 - 8.1 Gy at a fixed dose rate of 0.815 Gy/min and then stored for 20 day under 0°C to study the delivered dose dependence of the amount of reappering PSL signals. The dose rate dependence of the amount of reappering PSL signals was investigated by irradiating the IP samples with a fixed 0.6 Gy dose of X-ray irradiation at three different dose rates of 0.038, 0.13, and 0.70 Gy/min. The effect of heat on unerasable and reappearing PSL signals was examined by heating the irradiated IP samples at 120°C for periods of 1, 14, and 28 days.

To study the effect of light on unerasable and reappearing PSL signals, each IP sample was exposed to filtered and non-filtered halogen or fluorescent light for a certain period after irradiation with a 10 Gy dose of X-rays and fully erasing with visible light. An IP sample was exposed to the halogen light source for an hour with and without filtered using four different types of sharp cut optical filters: Y-50, R-60, R-72, and U-330 were used. The Y-50, R-60, and R-72 filters cut out light at wavelengths below 500, 600, and 720 nm, respectively. The U-330, which is a band pass filter, passes wavelengths around 330 nm but cuts out those above 400 nm. After the samples were exposed to the halogen light, they were erased with visible light for an hour. An IP sample was exposed to the fluorescent light source for 30 sec and trials were done using the following ultraviolet transmitting optical filters: UV-29, UV-30, UV-31, UV-33, and UV-35. These are lowpass filters and each double figure represents the 50% cutoff wavelength.

Results and Discussion

Figure 1 shows the results for samples with doses varying in the range of 0.0081 - 8.1 Gy and stored at 4°C. The net reappering PSL densities are plotted against the elapsed time, showing a peak between 20 and 30 days on the data of 8.1 Gy (●). The relationship between net reappering PSL density and the delivered dose is shown in Fig. 2. It is clearly

demonstrated that reappering PSL densities become higher in proportion to the dose, showing good linearity, indicating that the amount of reappearing PSL signal are dependent on the dose. Figure 3 shows the net reappearing PSL densities (□) as a function of dose rate in the range of 0.038 - 0.70 Gy/min. Reappearing PSL densities without subtracting a control PSL density (▲) are also potted. The result suggests that reappearing PSL densities are not dependent on dose rate. The relationships between reappearing or unerasable PSL density and storage days (under temperature of 120°C) are exhibited in Fig. 4. The figure shows that a peak appears in reappearing PSL densities (○) at 14 elapsed days among three storage days and signals have essentially disappeared at 28 elapsed days, and that unerasable PSL signals (■) are also negligible at 28 elapsed days. This result indicates that unerasable PSL signals can be erased completely by heating the IP samples. The IP samples at 28 elapsed days showed an obvious discoloration on surface, however, causing deterioration of the IP.

After IP samples were exposed to the halogen light source, with or without filtration, the reappearing PSL signals measured are plotted in Fig. 5. In this figure, regions of interest (ROIs) in the IP sample are denoted A, B, C, D, and E. With the optical filters Y-50, R-60, and R-72, similar tendency was observed in the difference between the filtered light and the non-filtered light. The amount of reappearing PSL signals obtained by the filtered light was generally smaller than that obtained by the non filtered light. This fact suggests that electrons, which are supplied to form F centers and cause reappearing PSL signals, do not exist in the longer wavelength region (500 nm ~). The opposite tendency is seen, however, in the U-330 optical filter, indicating that electrons localize under the shorter wavelength light (around 330 nm). Figure 6 shows the results obtained by exposing the IP samples to filtered and non-filtered fluorescent light. This result clearly shows that the largest amount of reappearing PSL signals is observed when an IP are exposed to the non-filtered fluorescent light. The amount of reappearing signal decreases according to the cutoff wavelength (i.e. as UV-29, UV-30, UV-31, and UV-33, respectively) and PSL signals do not reappear at all with light filtered by the U-35. This indicates that ultraviolet light around 290 nm, which is emitted from the fluorescent light, promotes the occurrence of reappearing PSL signals. PSL signals, reappeared by the exposure to the light, were erased easily by exposure to visible light using the fluorescent eraser.

Based on comprehensive results, new method to erase unerasable PSL signals has been developed. It consists of simultaneously exposing IP samples with an ultraviolet light

and a fluorescent light, i.e., exciting electrons localized in short wavelength region to around 633 nm and causing recombination. To avoid excitation of the Eu ion, we used ultraviolet light filtered by the UV-29 ultraviolet transmitting optical filter to do the erasing.

The effect of the new method on unerasable PSL signals was verified as follows. After irradiation with X-rays at 10 Gy, IP samples were fully erased with visible light. Next, they were exposed simultaneously to an ultraviolet light source filtered with the UV-29 optical filter and fluorescent light source. Exposure to both lights was repeated three times for durations of 8, 6.75, and 6.75 hours, respectively, in one night or one week intervals. After every exposure the samples were erased with visible light for an hour and PSL densities were measured. In Fig. 7, the PSL signals were plotted, showing a large reappering PSL signal peak after the first exposure. However, the signal had been decreased by a factor of two after the second exposure and was essentially absent after the third. The unerasable PSL signals, which were measured after erasing samples with visible light for an hour, also decreased with repeated exposure, falling to the same level as the control IP after the third round of exposure. This result means that the new method was able to erase "unerasable" PSL signals completely.

References

1) Amemiya Y., Wakabayashi K., Tanaka H., Ueno Y., Miyahara J., Science **237** (1987) 164.
2) Amemiya Y., Miyahara J., Nature **336** (1988) 89.
3) Iwabuchi Y., Mori N., Takahashi K., Matsuda T., Shionoya S., Jpn. J. Appl. Phys. **33** (1994) 178.

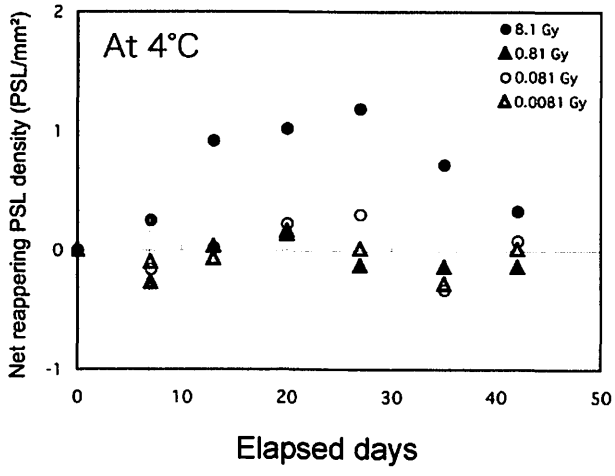

Figure 1. Relationship between reappering PSL signals and storage days for samples with doses varying in the range of 0.0081 - 8.1 Gy and stored at 4°C. The net reappering PSL densities are plotted against the elapsed time, showing a peak between 20 and 30 days on the data of 8.1 Gy (●).

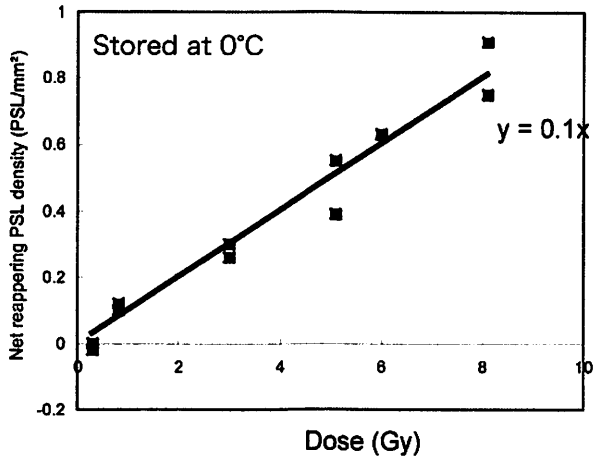

Figure 2. Relationship between net reappering PSL density and the delivered dose, when varied in the range of 0.3 - 8.1 Gy at a fixed dose rate (0.815 Gy/min). The IP samples were stored under 0°C during the experiment. It is clearly demonstrated that reappering PSL densities become higher in proportion to the dose, showing good linearity.

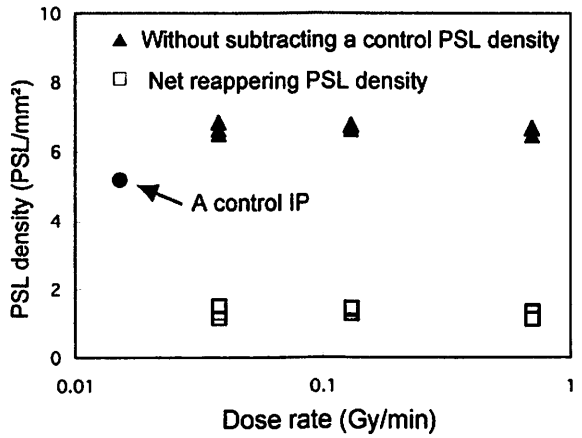

Figure 3. Net reappering PSL densities (□) as a function of dose rate in the range of 0.038 - 0.70 Gy/min, when irradiated with a fixed 0.6 Gy dose and stored at 0°C. The reappering PSL densities without subtracting a control PSL density (▲) are also potted. The result suggests that reappering PSL densities are not dependent on dose rate.

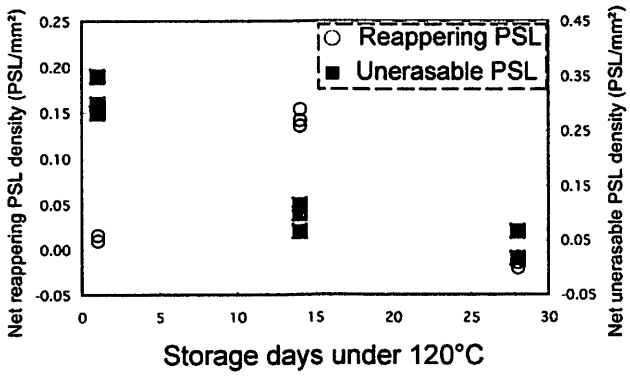

Figure 4. Relationships between reappering or unerasable PSL density and storage days (under temperature of 120°C) are exhibited. A peak appears in reappering PSL densities (○) at 14 elapsed days among three storage days and signals have essentially disappeared at 28 elapsed days. Unerasable PSL signals (■) are also negligible at 28 elapsed days.

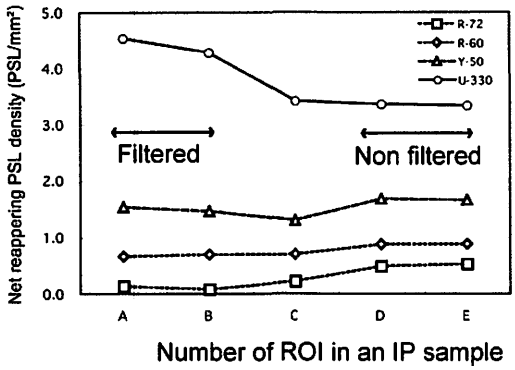

Figure 5. Reappearing PSL signals are plotted when IP samples were exposed to a halogen light source, with or without filtration. Regions of interest (ROIs) in the IP sample are denoted A, B, C, D, and E. The tendency seen in the optical filter of U-330, indicates that electrons localize under the shorter wavelength light (around 330 nm).

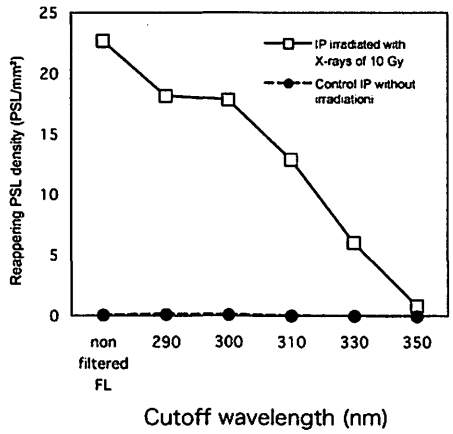

Figure 6. Results obtained by exposing the IP samples to filtered and non-filtered fluorescent light. The largest amount of reappearing PSL signals is observed when an IP are exposed to the non-filtered fluorescent light. The amount of reappearing signal decreases according to the cutoff wavelength and PSL signals do not reappear at all with light filtered by the U-35.

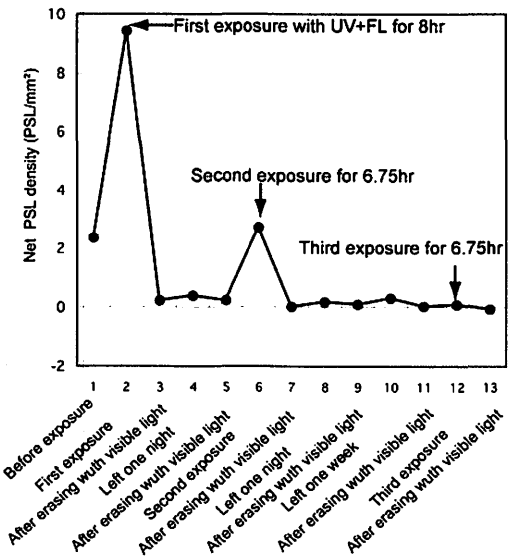

Figure 7. Net PSL density during the repeated treatment of exposure to both lights: a filtered ultraviolet (UV) light with the UV-29 and four fluorescent (FL) lights. After the third round of exposure, the unerasable PSL signals fell to the same level as the control IP.

IV. 5. Development of An Image Reconstruction Method for Planar PEM

Kumagai K., Miyake M., Baba M., and Itoh M.

Division of Cyclotron Nuclear Medicine, Cyclotron and Radioisotope Center, Tohoku University

Positron emission mammography (PEM) with ^{18}F-fluorodeoxyglucose (^{18}F-FDG) is a functional imaging technique optimized for breast cancer detection. The development of dedicated imaging systems with high sensitivity and spatial resolution plays a leading role in early breast cancer diagnosis. A prototype PEM consisting of a dual planar head with 4 detector blocks covering field of view (FOV) of about 20×16×15 cm^3 was constructed by our group to demonstrate the potential of high-resolution breast cancer imaging in 3-D.

Since most of the well known algorithms for 3-D image reconstruction assumes PET system of cylindrical geometry in order to realize the best performance, it is not simply applicable to nor ettificient for planar PEM. The aim of our reconstruction software would be to implement a faster algorithms yet producing fully 3-D resolution which is both homogeneous and isotropic.

Our method is based on ML-EM algorithm which has been widely used for reconstruction of PET images[1,2]. However, straightforward implementation of ML-EM algorithm for 3-D imaging of our PEM would require a system matrix of Terabytes and a computation time of hours. This is mainly because the number of combination of crystal pairs and voxels is too much for a general purpose computer (PC). Among several solutions commonly known in the case of cylindrical PET, concerning 3-D image reconstruction, we used both sparse property and geometrical symmetry of system matrix to reduce its size and to reduce the computationtime.

In planar PEM geometry there exists some symmetries by which we can reduce the size of the system matrix[3]. Assuming x-y plane is parallel to the detector surface, symmetries of $\pi/2$ rotation around z-axis and inversion along x - and y - axis tell us that

every line of response (LOR) always finds 7 other LORs (ignoring the symmetrically identical ones) penetrating vox- els in exactly the same manner, thus we need only LORs whose polar and azimuth angles are both positive and less than or equal to $\pi/2$. LORs with the same polar and azimuth angles can be found to have the same pattern on penetrating the voxels due to translational symmetry, provided that the crystal pitch is multiple of the voxel width.

Recent PCs are commonly equipped with multi-core processors and/or multiprocessors also capable of vector operation. A parallel computing technique was used to running some calculations at the same time as separate threads, which include a certain LOR and its symmetrical partners. In each thread calculations including at most 4 LORs, which are translationally identical, were also processed at the same time by vector operations such as SSE. The vector- ization were further optimized to use as many 128-bit registers as possible by unrolling the loop and coupling some instructions together in assembler codes so that they would be processed in parallel by pipeline architecture of modern CPU.

OS-EM algorithm is commonly known to be effective in reducing computational costs without loss of image quality[4]. It is quite easy to find the best number and order of subsets in the case of cylindrical PET where LORs distribute isotropically. For planar PEM, we found it possible to subsets the projection data according to its parity of index used to identify a crystal pair (indicating x and y coordinates of the crystals) without distorting the reconstruction results. The parity-ordered 4 subsets OS-EM will reduce the number of iteration to 1/4.

The main target of PEM, women breasts are almost homogeneous in its activity and density when seen by annihilation photons and has a relativity simple shape. In particular, it is not difficult to draw a boundary of a volume prior to the reconstruction, which contains most of activities inside and none outside. The fact that in most cases, less than 1/3 of FOV is occupied by such a volume, as shown in Fig. 2 for the case of standard breast size of 565 cc, led us to further reduction of the computation time. In the main loop of the reconstruction algorithm we have incorporated multi-step iterative scheme. In the first step a planar breast image is produced and converted to a 3-D image by simply rotating it, which is used as a initial guess for the next step. Under the ML-EM algorithm, the second and other steps update only a portion of a 3-D image whose voxel value is nonzero, with voxel width gradually decreased beginning from twice to half of the crystal width. The larger voxel size

reduces the number of voxels resulting in the faster convergent at the cost of resolution and which can be fully recovered at the later steps with finer voxels.

The total improvement in computation speed achieved by our method was measured to be faster enough to produce a 3-D image of breast with voxels of 1×1×1 mm^3 in less than 1 min.

In order to investigate the quality of the reconstructed image, we performed a series of Monte Carlo simulations using the GEANT4 software package[5], with various scan time and the tumor size and activity concentration. As shown in Fig. 1, we assumed that the random events from outside the FOV can be completely excluded in principle except that coming through the circular window of the shield. The prototype PEM was equipped with arrays of 2×2×15 mm^3 detector elements made of a new, fast, high-resolution scintillator, Pr:LuAG[6]. Throughout the simulation study time window was set to 5 ns and a energy window of 445-577 keV was applied, assuming energy resolution of 12% at 662 keV. Small spheres were located along $x-$, $y-$ and z–axis to simulate breast cancer. Figure 2 shows the typical simulation result in the case of 3 mm diameter spheres with concentration ratio of 10:1 to background activity and a scan time of 10 min. The spheres are clearly seen separated, however, nonuniformity of the image contrast probably due to the absorption effect are also seen.

Both experimental and simulation study are currently under way to incorporate various modifications, such as absorption and scatter correction and random coincidence rejection, into the reconstruction algorithm.

References

1) Shepp L. A., et al., IEEE Trans. Med. Imaging **1** (1982) 113.
2) Lange K., et al., J. Comput. Assist. Tomogra. **8** (1984) 306.
3) Motta A., et al., Computerized Medical Imaging and Graphics **29** (2005) 587.
4) Hudson H. M., et al., IEEE Trans. Med. Imaging **13** (1994) 601.
5) Agostinelli S., et al., Nucl. Inst. and Meth. A**506** (2003) 250.
6) Kamada K., et al., IEEE Trans. Nucl. Sci. **55** (2008) 1488.

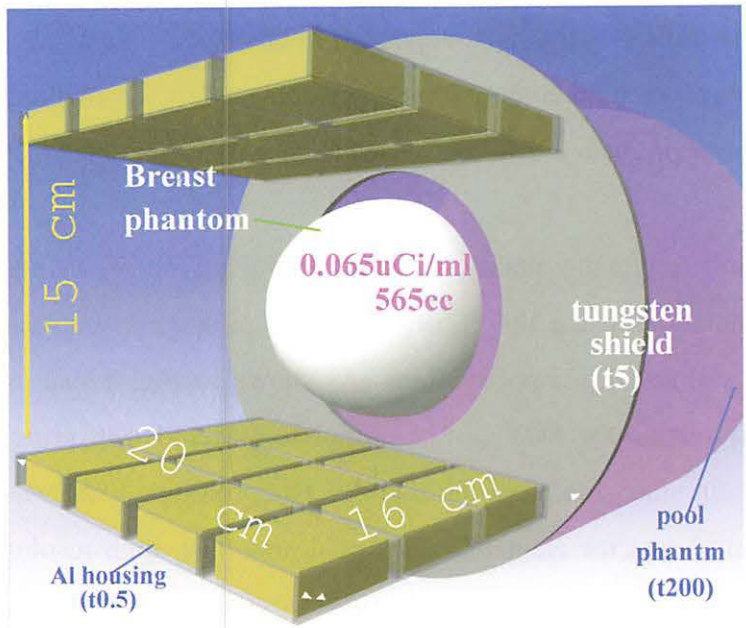

Figure 1. Geometry of the PEM detectors and the breast phantom used in the simulation. Pool phantom was usedto simulate random events coming from the body of the patient.

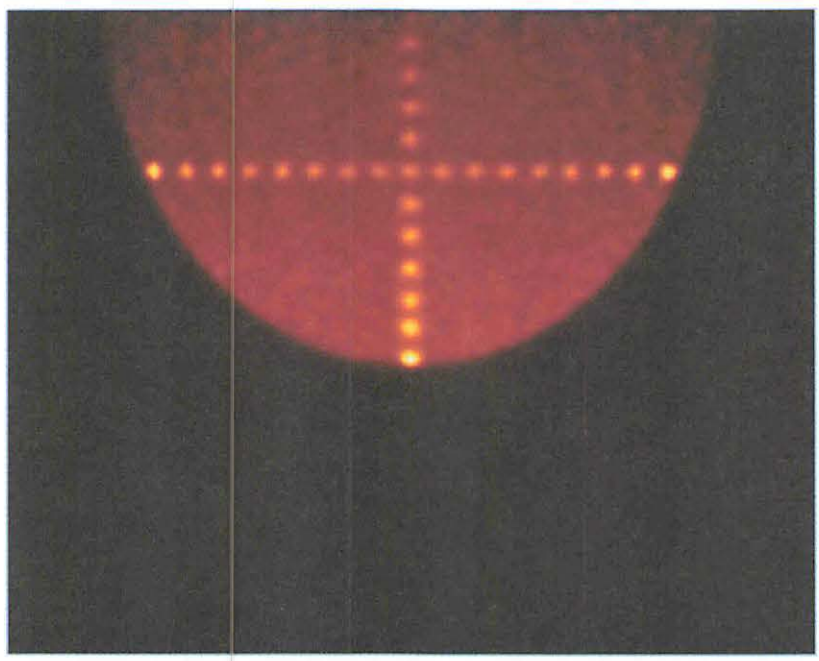

Figure 2. Reconstructed image of simulated breast phantom with tumors of 3 mm diameter sphere and a scan time of 10 min.

IV. 6. Effect of Scatter Correction on the Results of SPM Analysis: PET Phantom Study

Watanuki S.[1], Tashiro M.[1], Ishikawa Y.[1], Shibuya K.[1], and Fujimoto T.[2]

[1]*Cyclotron and Radioisotope Center, Tohoku University*
[2]*Center for the Advancement of Higher Education, Tohoku University*

Introduction

Recently, voxel-by-voxel statistical analysis is widely used in functional brain research using positron emission tomography (PET). Several processes such as attenuation and scatter corrections are applied to PET images for ensuring quantitative accuracy. However, when these processes are applied to PET images, significant differences in activity distribution might occur in these images, which might affect the results of the voxel-by-voxel statistical analysis. Montandon et al. reported that scatter correction changed activity distribution of [^{18}F]FDG in some areas in the cerebral cortex, demonstrated by comparing 2 reconstructed images with and without scatter correction[1]. Their result may suggest that 2 image data sets with and without scatter correction might give different result of statistical analysis. In addition, Aguiar et al. have shown that ideal scatter correction increased detection sensitivity of SPM in simulated brain PET studies[2]. To the best of our knowledge, no study has demonstrated the effect of scatter correction on the result of voxel-by-voxel statistical analysis using actual PET image data sets. The purpose of this study is to evaluate the scatter correction effect on SPM result in activation study by using actual PET phantom studies.

Materials and Methods

1 Phantom data preparation

All PET data were acquired using an SET-2400W PET scanner (Shimadzu, Kyoto, Japan), the characteristic of which were detailed elsewhere[3]. To simulate a human [^{18}F]FDG brain PET study, we used a cylindrical lucite phantom with the diameter and

length of 20 and 21 cm, respectively. The phantom was filled with [^{18}F] solution so that its activity concentration became 6.5 kBq/ml. This is comparable to human brain activity in an actual [^{18}F]FDG activation study. The phantom was placed at the center of field of view and then twenty frames of dynamic emission scans were preformed performed in 3D mode. Each frame time was prolonged to achieve equivalent total number of events, and total scan time length was one hour. Transmission scans of 10 min were performed immediately after emission scans for attenuation correction. Emission data were reconstructed using FORE + OSEM (four iterations and 16 subsets) with (SC) and without scatter correction (NSC) and then post-filtered using a Butterworth + ramp filter (cut-off frequency, 8 mm; order, 2.0). Gaussian scatter correction method was applied for scatter correction in this study[4].

Analysis

Prior to analysis, all reconstructed images were cropped to avoid noise in low statistical image slice in 3D mode acquisition. Thus, medial thirty slices from a total 63 slice were selected for further analysis. As a software package for voxel-by-voxel statistical analysis, we employed Statistical Parametric Mapping (SPM2) (http://www.fil.ion.ucl.ac.uk/spm, Wellcome Department of Imaging Neuroscience of the Wellcome Trust Centre for Neuroimaging at UCL, London, UK). For all data sets, additional Gaussian smoothing with a 12 mm FWHM was performed.

We searched for even single voxels with significantly higher or lower using a height threshold of $p \leq 0.001$ (uncorrected) and an extent threshold of zero voxel minimum. In order to confirm that scatter correction causes statistically significant changes on SC image when compared with NSC image, we analyzed increased and decreased areas using the phantom data. The analysis was done on the BS condition image sets.

Results and Discussion

Figure 1 shows the increased and decreased voxels with significant difference obtained by comparing SC and NSC images. This SPM result indicated that activity distribution tends to increase near the phantom rim and to increase toward the edge. In contrast, activity distribution decreased around center of the phantom and significance increased toward the center. It is assumed that these results were produced because the scatter events estimated here are higher near to the center of the object regardless the

activity distribution. Since overall mean value of SC and NSC images were set to 50 by global normalization, SC image values near the rim become higher than NSC image value and the value near the center become lower compared with NSC. But Motandon ML reported that distribution relatively decreased in the periphery (frontal gyri, middle temporal gyri) and relatively increased in the central area (thalamus, insula and brainstem) in SC with model based scatter correction compared with NSC in human data[1]. This discrepancy was caused probably due to using different scatter correction method, different scanning object and different activity distributions. In the actual human brain FDG PET image, activity tends to distribute mainly in the cerebral cortex, and the skull bone is surrounding it. Model-based scatter correction estimates scatter events with considering activity distribution and non-uniform scattering medium in actual scan. In this situation, it is considered that scatter events will increase in the cerebral cortex. On the other hand, Gaussian scatter correction method does not consider those situations. However, it is not need to consider about activity distribution and non-uniform scattering medium in the phantom study performed here. Therefore, the same result can be expected for model based scatter correction and Gaussian scatter correction method. But, it is necessary to evaluate difference between results with different scatter correction method in future.

References

1) Montandon M.L., Slosman D.O., Zaidi H. NeuroImage **20** (2003) 1848.
2) Aguiar P., Pareto D., Gispert D.J., et al., NeuroImage **39** (2008) 1121.
3) Fujiwara T., Watanuki S., Yamamoto S., et al., Ann. Nucl. Med. **11** (1997) 307.
4) Cherry S.R., Huang S.C., IEEE Trans. NS **42** (1995) 1174.

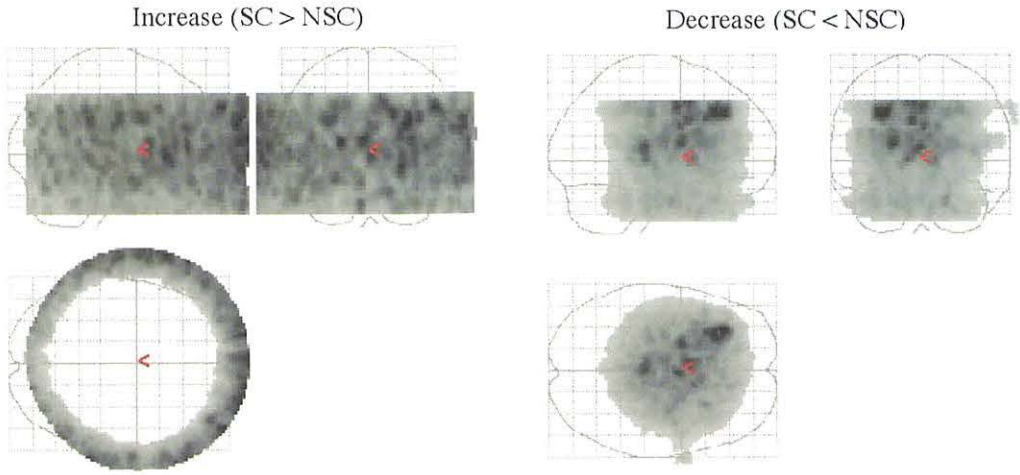

Figure 1. Significant regional increase (left) and decrease (right) in images with scatter correction, as compared with images without scatter correction.

V. PIXE AND ENVIRONMENTAL ANALYSIS

V. 1. Characterization of Aerosol Particles in a Mechanical Workshop Environment

Matsuyama S.[1], Ishii K.[1], Yamazaki H.[1], Kikuchi Y.[1], Fujiwara M.[1], Kawamura Y.[1], Yamanaka K.[1], Watanabe M.[1], Tsuboi S.[1], Pelicon P.[2], and Zitnik M.[2]

[1]*Department of Quantum Science and Energy Engineering, Tohoku University,*
[2]*Jozef Stefan Institute, Slovenia*

Introduction

Atmospheric aerosols are caused, for example by sandy dust, smoke from factories, and autombile exhaust gases[1-3]. Investigation of production mechanisms and aerosol characterization is of utmost importance to form successful global strategies against harmful effects of acid rain and greenhouse screening and also to prevent an excessive pollution of environment from the local sources. On the other hand, the indoor aerosols can have a large impact on human health. In machine workshops and laboratories, where specific materials and chemicals are processed, toxic aerosols can be released into air. Therefore, an aerosol monitoring in working environments is one of the essential prerequisites for an efficient health protection system for the employees.

Aerosol particles are characterized by various physical and chemical factors such as size, density and chemical composition. The elemental analysis of atmospheric aerosols is very important too, since distribution of different elements reflects the sources and their generating processes. Aerosol sampling on thin films and a subsequent PIXE elemental analysis is one of the most effective combinations for studying atmospheric aerosols[1]: many studies in the field has focused onto the bulk analysis of aerosol samples[4-8]. Such an approach is advantageous for aerosol monitoring purposes because the elemental concentrations can be studied with a reasonable time resolution. However, in bulk analysis the data is averaged over the whole sample. Statistical models, such as principal component analysis (PCA) and chemical mass balance (CMB), are necessary to determine the contributions of different aerosol sources[5-8].

As described in previous reports we have developed a multimodal microbeam analysis

system to analyze the elemental composition of single aerosol particles[9,10]. By combining PIXE with RBS, off-axis STIM, and STIM, the method is sensitive to all elements and thereby it is possible to determine chemical composition of single aerosol particles. The method is superior for obtaining source-related information and for understanding the aerosol formation mechanisms[9,10], but it takes considerable time to analyze all the particles in the sample: it is therefore unsuitable for aerosol monitoring.

For this study, the size-resolved aerosols were collected using a cascade impactor set in the machine workshop of Jozef Stefan Institute. The samples were analyzed by a microbeam analysis system at Tohoku University. The use of bulk analysis with wide-area scanning that covers the whole sample area, in combination with microanalysis by microscopic scanning for determination of chemical composition of selected "particles", still provides an efficient aerosol monitoring capability and improves the source identification potential of the method.

Sampling

Aerosol particles were collected inside the machine workshop using a nine-stage cascade impactor (Model 1-1L; PIXE international Co. LTD)[11,12]. In previous studies, only a single-stage impactor was used[9,10]. In that case the particles impacted on the film sometimes congregate and their size information is difficult to obtain. This time, using the cascade impactor, size information of the sub-micrometer fraction is known *a priori* and this knowledge is useful for data evaluation.

The machine workshop has three rooms. The first room, in which the cascade impactor was placed, is used for processing materials such as iron, stainless steel, aluminum, and plastic (workshop room). In that room, machine tools such as lathes and CNC milling machines are installed. On weekdays, about five of the machines are running routinely. The second room is used for welding, drilling, cutting and polishing of metal pieces (preparation room). The third room is used for wood processing (carpentry room).

A non-stop sampling in the workshop room with a cascade impactor was conducted during two time intervals corresponding to weekdays (working regime) and weekend (non-working regime). During the working regime, the sampling started at 9:00 on February 13 and finished at 15:45 on February 15, 2008. The working hours of the machine workshop were from 7:00 - 15:00. For the non-working regime, the sampling period was during the weekend starting at Friday 16:30 on February 15 and stopping on Monday morning at 8:10,

February 18. The average air flow rate through the impactor was 1.2±0.1 *l*/min. The aerosols were impacted on nine impactor stages (7-1, L2 and L1) having the aerodynamic cut-off diameters going from 16 μm - 60 nm. At each stage the aerosol particles were captured on a Mylar film. For the purpose of previous studies, we developed 0.3 μm thick polycarbonate films to reduce the background for low-Z element analysis[9]. Such thin films, however, can be easily damaged by the air streaming through the small holes in the lower impactor stages. The thinnest commercially available Mylar film was therefore used as a substrate for this study. By RBS analysis its thickness was estimated to 2 μm. The film contains uniformly distributed calcium with concentration of ca. 700 ng/cm^2 which is normally lower than Ca signal of the collected aerosol particles.

Experiments

The sample analysis was carried out with the microbeam analysis system at Tohoku University. Technical details of the system were presented in previous papers[13,14]. For multimodal analysis, two X-ray detectors for PIXE analysis and two charged particle detectors for RBS and STIM were mounted to observe the sample simultaneously.

Two X-ray detectors were set in vacuum at 115 degrees with respect to the beam axis. The first detector has a large sensitive area (60 mm^2, LS60148; Princeton Gamma-Tech Instruments Inc.) and is suitable for the trace elemental analysis. A Mylar filter (250 μm) was attached to the front of the detector to reduce pile-up events and deformation of the spectrum by recoil protons. The acceptance solid angle was ca. 0.3 sr. The second detector is used for low-energy X-ray detection: an HPGe detector was newly installed (IGX10119; Princeton Gamma-Tech Instruments Inc.). It has high-energy resolution (119 eV for Mn K X-rays) and an ultra-thin polymer entrance window which does not prevent a detection of carbon and oxygen X-ray lines. For RBS analysis, an ion-implanted Si annular detector was used (ANPD300-19-100RM; Canberra)[15]. Hydrogen content was analyzed by an off-axis STIM method. To the purpose an ion-implanted Si detector (BU-012-050-100) with a sensitive area of 50 mm^2 was placed at the scattering angle of 28 degrees[14,16].

A simultaneous set of PIXE / RBS / off-axis STIM spectra was accumulated upon irradiation of the sample by a 2.4 MeV proton beam with the 1×1 μm^2 beam spot size and 50-100 pA beam current. For analysis of single aerosol particles the beam scanning area was set to 200×200 μm^2. To determine the average total elemental concentration in air

during the sampling, the scanning area was increased to 1×1 mm^2.

Quantitative bulk and individual particle PIXE analysis was performed by GeoPIXEII software[17]. After generating the elemental maps, individual particles were selected from these maps and corresponding PIXE, RBS, and off-axis STIM spectra were extracted. The elemental concentrations for elements heavier than carbon were then deduced from the fit of the extracted PIXE spectra. Concentrations of carbon, oxygen, and hydrogen were derived from peak yields of extracted RBS and STIM spectra, which were calibrated by measuring the peak yields from Mylar films of known thickness[9,10]. The overlap of carbon, nitrogen, and oxygen peak in the RBS spectra was resolved by SIMNRA software[18].

Results

Typical X-ray spectra of impactor stage 3 are shown in Fig. 1. Heavy elements such as Pb, Zn, Cu, and Ba were detected. Surprisingly, higher elemental concentrations were detected during the weekend. The elemental concentrations of stages 1, 2, and 3, collected during the weekdays and during the weekend are shown in Fig. 2 and Fig. 3. The 1,2,3 impactor stages captured mostly a submicron particles (the respective aerodynamic cut-off diameters are 0.25, 0.5 and 1 μm) and were the most loaded with aerosols. The total concentrations of elements were determined from the 1×1 mm^2 X-ray spectral images of the sample considering the microbeam current and the total air volume pumped through the cascade impactor. During the weekend, elemental concentrations of Na, Zn, Ba, and Pb at stage 2 and 3 were more than ten times higher than during the weekdays. The workshop is usually closed on weekends, so that lower elemental concentrations were expected. We found out latter, that an old wooden door was being restored at that time in the vicinity of the sampling point. During that process, an old layer of white paint was removed. It is known that the old white paint often contains Pb and Ba. A single-particle analysis was conducted to determine chemical composition of Pb and Ba containing substances. Although Pb and Ba are mainly distributed uniformly over the sample area at stages 1,2, and 3, some hot spots were also detected. The hot spots, where the elemental concentration was higher, were selected and elemental correlations between concentration levels of various elements were examined. If lead is contained in the old paint that should probably be some form of lead carbonate $PbCO_3$, so that we expected to see the correlations between lead and light elements. We have also looked for Ba-S correlation since $BaSO_4$ is

also a common white paint agent. However, no statistically significant correlation was found for Pb-light elements and Ba-S. It seems that particles are too congregate and information on individual particles is missing. However, in stage 4, which has less accumulated material, a correlation between barium and sulfur is observed but counting statistics is too low to determine precisely the stohiometric ratio of the two elements.

Elemental concentrations of Al, Si, Ca, Ti, Cr, Mn, and Cu at stages 1 and 2 were increased during the weekdays. Their stronger presence in the air is probably related to the movements of the machine and of the workers. Tungsten was detected only during the weekdays. The elemental concentration of S on weekdays was high at stage 1 but lower at stages 2 and 3. Tungsten is contained in high-speed steel (HSS), which is used in the machine parts and cutters. Actually, HSS is also used as a material for drills and power saw blades. It is therefore no surprise that W was found in the aerosols during the working regime. Tungsten shows no correlation with other elements in the microscopic analysis.

During both sampling periods - the weekdays and weekend days- impactor stages 1 and 2 contained features that look like the oil drops. In other stages, no drops were present. We found that the drops contain sulfur and small amount of chlorine and potassium with a fairly constant concentration ratio except near the edges where the potassium concentration is higher than in the central area of the drop, probably due to the self-absorption effect. Figure 4 shows spectral maps of several elements for sample stage 1, collected during the weekend. A large area off-axis STIM density map corresponds to the photographed area of the sample. The spectral maps in Fig. 4 were taken at different sample areas as indicated. Elemental concentrations of S show similar value in the "particle" area and in the "drop" area while the other elements show much lower concentrations in the drop. The drop also contains H, C, and O, as demonstrated by the RBS map. On the other hand, PIXE maps suggest much lower concentration of C and O than is the concentration of both elements in the Mylar foil of the substrate. Since the energy of C and O K-emission lines is relatively low, X-rays from C and O are strongly absorbed in the drop. The areal densities [$\mu g/cm^2$] and mass concentrations [$\mu g/g$] of C and O were extracted from RBS and PIXE maps. The elemental concentrations at the center of the drop were analyzed using RBS and off-axis STIM spectra. Because of the overlap of carbon and oxygen spectral peaks, the composition was determined by a SIMNRA software[18]. The corresponding cross sections for C, N, and O were derived from the refs. 19 and 20. Figure 5 shows a good agreement of the simulated and measured RBS spectra of the drop. The hydrogen

concentration was determined by the analysis of off-axis STIM spectra. The atomic ratios of C, N, O, and H were around 3:1:3:10 and they varied with the position of the drop. The number of S atoms is around 1 % of that of H atoms. The atomic ratio of C is less than that in the 2 μm Mylar and is consistent with the carbon X-ray map. This analysis supports the assumption about the oil origin of the drops. It is possible that during the sampling a partial pressure of the lubricant oil in the workshop was rather high. The air cooled down when it was pumped through small holes of the cascade impactor and the oil was extracted onto filters in the liquid phase. On the other hand, the aerosol particles may have absorbed oil which could explain high S concentration observed at stages 1 and 2 on the weekdays.

Conclusions

Aerosol monitoring in a factory can provide important information about health hazard related to the specific working place and activity. Size-segregated aerosols were collected using a multi-stage cascade impactor set in the machine workshop at Jozef Stefan Institute. The samples were taken during the weekdays and during the weekend and were analyzed afterwards by a microbeam analysis system at Tohoku University. For easy and efficient aerosol monitoring, a bulk PIXE analysis (scan over a whole sample area) was combined with a multimodal microanalysis with microscopic scanning (scan over the selected small "single particle" sample area). Using the bulk analysis, high concentrations of Pb and Ba were detected during the weekend, which is related to an irregular removal of an old white paint layer in course of door restoration. During the weekdays concentration of W and of soil elements increased which is attributed to the workshop activity. At the same time, a sulfur concentration increased too. This is linked to the oil drops detected at stages 1 and 2 of the cascade impactor. It follows from microscopic multimodal analysis that drops are mainly of organic compound with small amount of S, most probably a lubricant oil vapor condensate. A combined use of the bulk and microanalysis is a promising tool for aerosol monitoring and characterization.

Acknowledgement

This study was partly supported by Grants-in-Aid for Scientific Research, (S) No. 13852017, (B) No. 18360450 and (C) No. 16560731 from the Ministry of Education, Culture, Sports, Science and Technology, Japan. This study was also supported by JSPS

and MHEST under the Japan-Slovenia Research Cooperative Program.

The authors would like to acknowledge the assistance of Fujisawa M. for maintenance and operation of the Dynamitron accelerator. The authors would like to thank Mr. Nagaya T.and Komatsu K., for their assistance in constructing the microbeam and target system.

References

1) Johansson S.A.E.and Campbell J.L., PIXE:A Novel Technique for Elemental Analysis, (John Wiley and Sons, 1988).
2) Kasahara M., Park J.H., Yamamoto K., Nucl. Instr. Meth. **B109/110** (1996) 471.
3) Cahill T.A., Nucl. Instr. Meth. **B49** 350 (1990) 345.
4) Ariola V., Campajola L., D'Alessandro A., Del Carmine P., Gagliardi F., Lucarelli F., Mandò P. A., Marcazzan G., Moro R., Nava S., Prati P., Valli G., Vecchi R., Zucchiatti A., Nucl. Instr. Meth. **B190** (2002) 471.
5) Prati P., Zucchiatti A., Lucarelli F., Mandò P.A., Atmospheric Environment **34** (2000) 3149.
6) Bongiovanni S.F., Prati P., Zucchiatti, A. Lucarelli F., Mandò P. A., Ariola V., Bertone C., Nucl. Instr. and Meth., **B161-163**, 786-791 (2000).
7) D.D Cohen, "Characterisation of atmospheric fine particles using IBA techniques", Nucl. Instr. and Meth., **B136-138** (1998) 14.
8) Formenti P., Annegarnand H.J., Piketh S.J., Nucl. Instr. Meth. **B136-138** (1998) 948.
9) Matsuyama S., Ishii K., Yamazaki H., Kikuchi Y., Amartaivan Ts., Abe S., Inomata K., Watanabe Y., Ishizaki A., Oyama R., Kawamura Y., Suzuki A., Momose G., Yamaguchi T., Imaseki H., Int. J. PIXE **15** (2005) 257.
10) Matsuyama S., Ishii K., Yamazaki H., Kikuchi Y., Kawamura Y., Oyama R., Yamanaka K., Yamamoto T., Watanabe M., Tsuboi S., Arao K., X-ray Spectromwtry **37** (2008) 151.
11) PIXE International, P.O.Box 7744, Tallahassee, FL 32316, USA.
12) Bauman S., Houmere P.D., Nelson J.W., Nucl. Inst. Meth. **A181** (1981) 499.
13) Matsuyama S., Ishii K., Yamazaki H., Barbotteau Y., Amartivan Ts., Izukawa D., Hotta K., Mizuma, K. Abe S., Oishi Y., Rodriguez M., Suzuki A., Sakamoto R., Fujisawa M., Kamiya T., Oikawa M., Arakawa K., Imaseki H., Matsumoto N., Int. J. PIXE **14**, (2004) 1.
14) Matsuyama S., Ishii K., Abe S., Ohtsu H., Yamazaki H., Kikuchi Y., Amartaivan Ts., Inomata K., Watanabe Y., Ishizaki A., Barbotteau Y., Suzuki A., Yamaguchi T., Momos G. e, Imaseki H., Int. J. PIXE **15** (2005) 41.
15) Matsuyama S., Ishii K., Yamazaki H., Kikuchi Y., Inomata K., Watanabe Y., Ishizaki A., Oyama R., Kawamura Y., Yamaguchi T., Momose G., Nagakakura M., Takahashi M., Kamiya T., Nucl. Instr. Meth. **B260** (2007) 55.
16) Deves G., Matsuyama S., Barbotteau Y., Ishii K., Ortega R., Rev. of Sci. Instr., **77** (2006) 056102.
17) Ryan C.G., van Achterbergh E., Yeats C.J., Drieberg S.L., Mark G., McInnes B.M., Win T.T., Cripps G., Suter G.F., Nucl. Instr. Meth., **B188** (2002) 18 .
18) Mayer M., SIMNRA Users's Guide, Technical Report IPP 9/113, MPI Plasmaphy.
19) Amirikas R., Jamieson D.N., Dooley S.P., Nucl. Instr. Meth. **B77** (1993) 110.
20) Ramos A.R., Paúl A., Rijniers L., da Silva M. F., Soares, J.C. Nucl. Instr. Meth., **B190** (2002) 95.

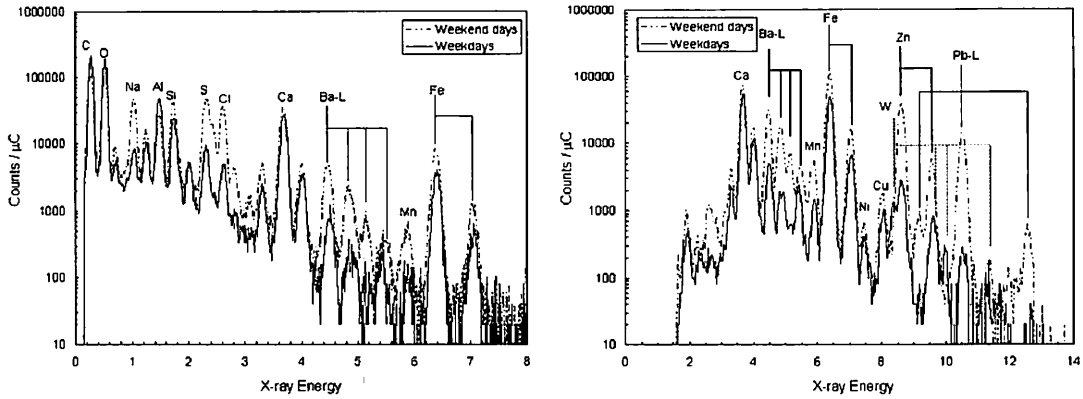

Figure 1. Typical X-ray spectra of impactor stage 3 obtained using the low-energy detector (left) and the high-energy detector (right).

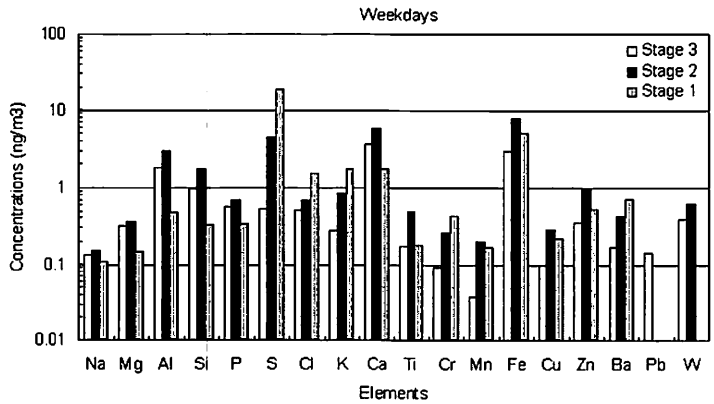

Figure 2. Elemental concentrations in the workshop collected on stages 1, 2, and 3 during the weekdays.

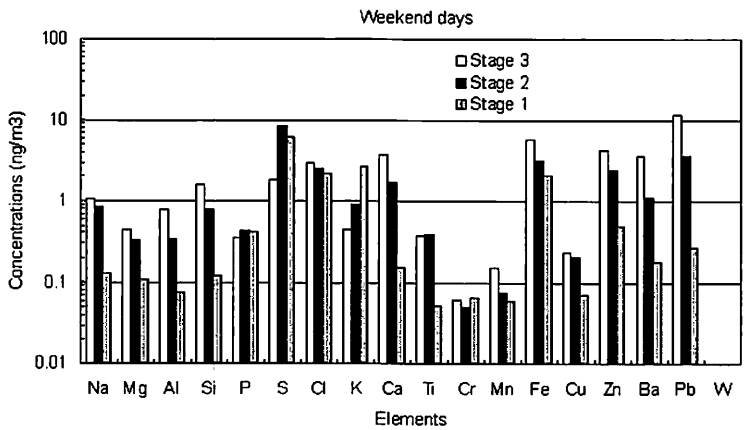

Figure 3. Elemental concentrations in the workshop collected on stages 1, 2, and 3 during the weekend.

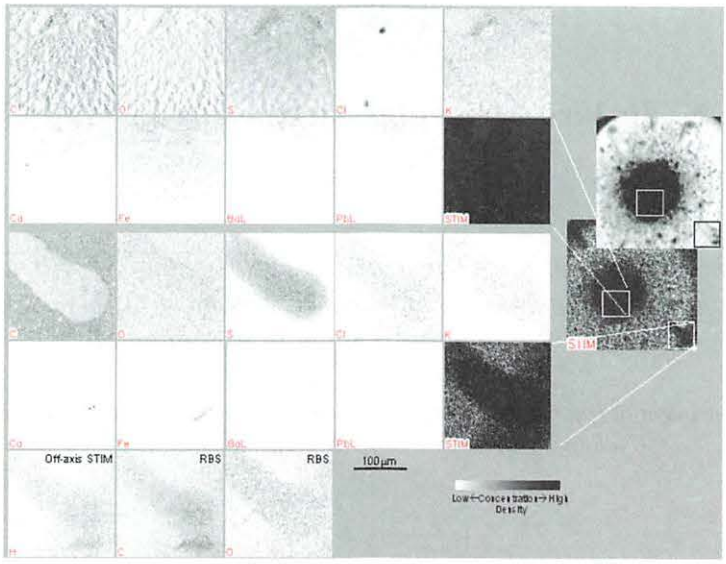

Figure 4. Elemental maps of aerosols on stage 1 collected during the weekend, where Pb concentration shows the highest value.

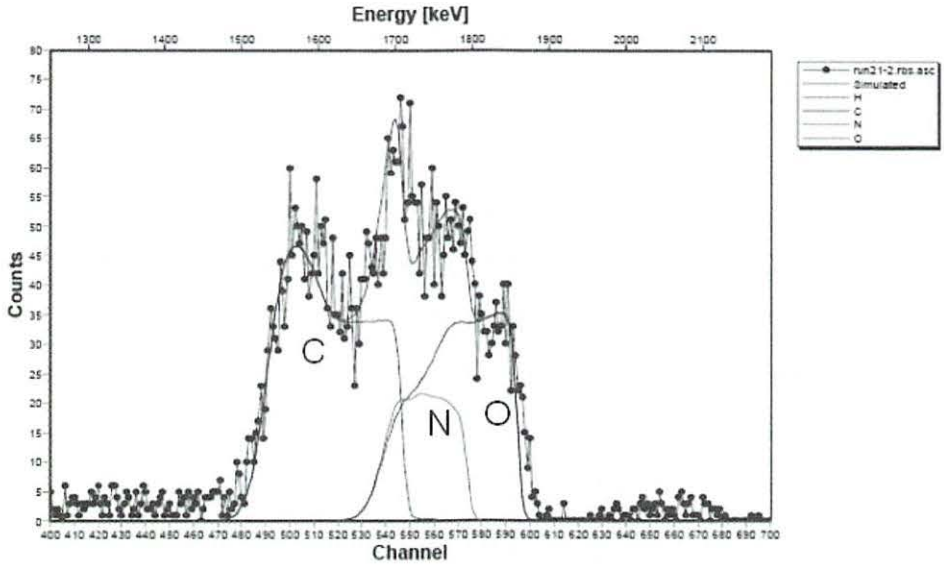

Figure 5. RBS spectrum of the drop with simulation result of SIMNRA.

V. 2. *In-Vivo* Elemental Analysis by PIXE-μ-CT

Kawamura Y.[1], Ishii K.[1,2], Yamazaki H.[2], Matsuyama S.[1], Kikuchi Y.[1], YamaguchiT.[1], Watanabe Y.[1], Oyama R.[1], Momose G.[1], Ishizaki A.[1], Tsuboi S.[1], Yamanaka K.[1], and Watanabe M.[1]

[1)]Department of Quantum Science and Energy Engineering, Tohoku University,
[2]Cyclotron and Radioisotope Center, Tohoku University

Introduction

PIXE (Particle-induced X-ray emission) has been successfully used as a powerful tool of trace element analysis, because the production cross-section of characteristic X-ray is very large in comparison to those of continuous X-ray. This feature is quite different from the case of electron bombardment, where electron bremsstrahlung contributes predominantly to the X-ray spectrum[1,2]. X-rays produced by ion microbeams could be used as a monochromatic and low energy m-X-ray source without using monochrometer. Therefore, the 3D micron-CT can be realized by the use of this monochromatic X-ray-point-source, which provides the 3D structure of small object less than 1 mm with a high spatial resolution and high contrast. On the basis of this idea, we have developed a 3D micron-CT using micro-PIXE for *in-vivo* imaging, which is very useful in biological studies[2~4]. Using a monochromatic X-ray point source produced by bombarding pure metal target by ion microbeam, we could acquire X-ray projection data. 3D images were reconstructed from these 2D projection data by using cone-beam CT reconstruction algorithm[5]. In the CT system, the target can be readily exchanged. Therefore, the image with excellent contrast could be obtained by using an appropriate target according to the object. Figure 1 shows a 3D image of an ant's head acquired by using this CT system. These images were obtained by Ti-X-rays. A strong intensity which corresponds to the Gnathic Glandular could be seen. It is suspected that the Gnathic Glandular contains heavier elements than the other organs. In the biological studies, it is preferable to know elements that are contained in the organs.

In this study, we applied the dual-energy subtraction imaging method[6-8] to the 3D

micron-CT for *in-vivo* elemental imaging. Since the 3D micron-CT can easily change the X-ray energy by changing the X-ray target, the dual-energy subtraction method is suitable for elemental imaging in the system.

The dual-energy subtraction method is one of the tools which enhance the contrast of the specific elements. The method is based on the sharp change of attenuation coefficient at K-absorption edge of contrast media, which is applied to the X-ray radiography in a human angiography by adding iodinated contrast media. The method uses two different energy X-rays of higher and lower energies of I-K-absorption edge and subtract image obtained by the high energy from the one by the lower energy. Thus the subtract image shows enhanced image of iodine[6,7].

We do not use a contrast media for elemental imaging. By changing the X-ray targets, we obtained projection data corresponding to the X-ray energy. By subtracting the image from the other image obtained by an adjoining X-ray energy, we can obtain elemental image corresponding to the absorption edges. We apply the dual-energy subtraction method for elemental imaging of the Gnathic Glandular, where Mn is known to be accumulated. Figure 2 shows the schema of dual energy subtraction method.

Experiment & Result

The 3D micron-CT comprises a high-speed X-ray CCD camera, a monochromatic X-ray point source and a rotating sample stage[3]. In our system, the X-ray point source and the CCD camera are fixed and the sample is rotated by the stage to acquire the projection data. A monochromatic X-ray is produced by proton microbeam bombardment on the pure metal target. The microbeam system was designed to achieve sub-micrometer beam spot sizes and was developed in collaboration with Tokin Machinery Corp[9]. The system is connected to the 4.5 MV Dynamitron accelerator at Tohoku University. The demagnification factors are 9.2 and 35.4 for horizontal and vertical directions, respectively. A beam spot size of 0.4×0.4 μm^2 was obtained using a beam current of several tens of pA. In this study, we adjust the beam spot size to 1.5×1.5 μm^2 in order to increase X-ray intensity[2,9]. Beam currents were around 200 pA. An X-ray producing target is set at 30 degrees with respect to the horizontal axis and produces the X-ray cone beam by microbeam bombardment.

A sample was encapsulated in a polycarbonate tube with micrometer dimension (inside diameter of 1000 μm and wall thickness of 25 μm). Because X-ray attenuation in

the tube is low and clear projection images could be taken. Since composition of the tube is homogeneous contrary to the majority of biological materials, the tube can be used as a reference in the reconstruction procedure. Inside of the tube was kept in atmospheric pressure. Therefore, we can acquire the CT image *in-vivo*. During acquiring the data of living sample, the sample is encapsulated after anaesthetization. The anaesthetized ant lives around two hours[3]. To reduce the ambiguity of obtained data which depends on the ant's condition, we used the ant which was fixed by formalin. In this application it took more than two hours to obtain the images for two or more X-ray energies and it was difficult to keep an ant living for more than two hours.

A high-speed X-ray CCD camera (Hamamatsu, C8800X) was used to detect transmitted X-rays. The pixel size of the CCD is $8\times8\mu m^2$ and the number of pixels is 1000x1000. The CCD is cooled to –50°C by a Peltier cooler to suppress dark currents. The CCD starts to exposure by an outside trigger and it stops when the beam charge has been accumulated to a constant value; readout of data finishes while the sample rotates. A 100 μm Mylar film is placed in front to prevent recoil protons into the CCD[1].

The spatial resolution of this CT system depends strongly on the geometrical condition such as X-ray source to sample and sample to the CCD distances. We set the source-to-sample distance was set to 2100 μm and the sample-to-the CCD was set to 3900 μm. In this condition, the spatial resolution was estimated to be 6 μm[4].

The micron-CT changes the X-ray energy by changing the metal targets. Figure 3 shows the transmittance of X-ray through water and the measured energy spectra of X-rays, which were detected by a Si(Li)-detector for comparison. Transmittance of X-ray for energies higher than 10 keV is too high and not appropriate for biological application. Considering the detection efficiency of the CCD, we use Ti, Fe and Co K-X-rays.

To determine the elements that are contained in the Gnathic Glandular, the dual energy subtraction method was applied. After obtaining the 3D images for Ti-, Fe- and Co-K-X-rays, the CT values are compared. The ML-EM reconstruction method was used for 3D imaging to reduce the background. However, Fe- and Co-K-X-rays are not appropriate for imaging since transmittance is too high compared to Ti-K-X-ray imaging for a small object. Figure 4 shows the cross sectional views obtained by Fe- and Co-K-X-rays. Co-K-X-rays are strongly absorbed in the Gnathic Glandular.

In applying the dual energy subtraction method using these two different data (i.e. Fe and Co), we normalize the data by using the calculated CT values of polycarbonate tube.

Because the X-ray energy of Fe and Co are close, the tube's CT values of Fe and Co are almost equivalent. By this normalization, we could observe the distribution of Mn with less interference of other organs. Figure 4 shows the result of dual energy subtraction using 3D data set. The distribution of Mn clearly observable and we could confirm that the position in which Mn has concentrated corresponds to the position of Gnathic Glandular in the ant's head.

Conclusions

We have developed the micron-CT using micro-PIXE for *in-vivo* imaging. The ion microbeam system is used as a monochromatic m-X-ray source by bombarding a pure metal target. The sample was placed in a tube of a small diameter, and rotated by a stepping motor. The 3D images were reconstructed from the obtained projection data by using cone-beam CT reconstruction algorithm. X-ray spectra produced by heavy charged particle bombardment exhibits a much smaller continuous background compared to that of electron bombardment. Therefore, X-rays produced by ion beam can be used as a monochromatic and low energy X-ray source. The feature is very effective to investigate small insects in micrometer dimension. Moreover we can get elemental distribution image of object by choosing appropriate characteristic X-rays corresponding to the absorption edge. Using this system, we were able to get 3D images of a living ant's head with 6 μm spatial resolution. The Dual energy subtraction method was applied for 3D elemental analysis. By using Fe-K-X-rays (6.40 keV) and Co-K-X-rays (6.93 keV), we can investigate the 3D distribution of Mn (K-absorption edge=6.54 keV) in an ant's head. The 3D micron-CT is useful for 3D elemental imaging of small insect *in-vivo* as well as electron density imaging and will be a powerful tool for biological studies.

Acknowledgements

This study was supported by 21 COE Program "Future Medical Engineering based on Bio-nanotechnology" and a Grant-in-Aid for Scientific Research (S) No. 13852017 (K. Ishii) of the Ministry of Education, Culture, Science, Sports and Technology.

References

1) Ishii K., Morita S., *Int. J. PIXE*, **1** (1990) 1.
2) Ishii K., Matsuyama S., Yamazaki H., Watanabe Y., Yamaguchi T., Momose G., Amarttaivan Ts., Suzuki A., Kikuchi Y., Galster W., *Int. J. PIXE*, **15** (2005) 111.
3) Ishii K., Matsuyama S., Watanabe Y., Kawamura Y., Yamaguchi T., Oyama R., Momose G., Ishizaki A., Yamazaki H., Kikuchi Y., *Nucl. Instr. and Meth.*. **A571** (2007) 64.

4) Ishii K., Matsuyama S., Yamazaki H., Watanabe Y., Kawamura Y., Yamaguchi T., Momose G., Kikuchi Y., Terakawa A., Galster W., *Nucl. Instr. and Meth.*. **B249** (2006) 726.
5) Yamaguchi T., Ishii K., Yamazaki H., Matsuyama S., Watanabe Y., Abe S., Inomata M., Ishizaki A., Oyama O., Kawamura Y., *Int. J. PIXE*, **15** (2005) 195.
6) Oguri Y., Hasegawa J., Ogawa M., *Proceedings of 23rd PIXE Symposium*
7) Umetani K., Ueki H., Ueda K., Hirai T., Takeda T., Doi T., Wu J., Itai Y., Akisada M., *J. Synchrotron Rad.* **3** (1996) 136.
8) Rubenstein E., Hughes E.B., Campbell L.E., Hostadter R., Kirk R.L., Krolicki T.J., Stone J.P., Wilson S., Zeman H.D., Brody W.R., Macovski A., Thompson A.C., *SPIE.* **314** (1981) 42.
9) Matsuyama S., Ishii K., Yamazaki H., Sakamoto R., Fujisawa M., Amarttaivan Ts., Oishi Y., Rodriguez M., Suzuki A., Kamiya T., Oikawa M., Arakawa K.,Matsumoto N., *Nucl. Instr. and Meth.*. **B210** (2003) 59.

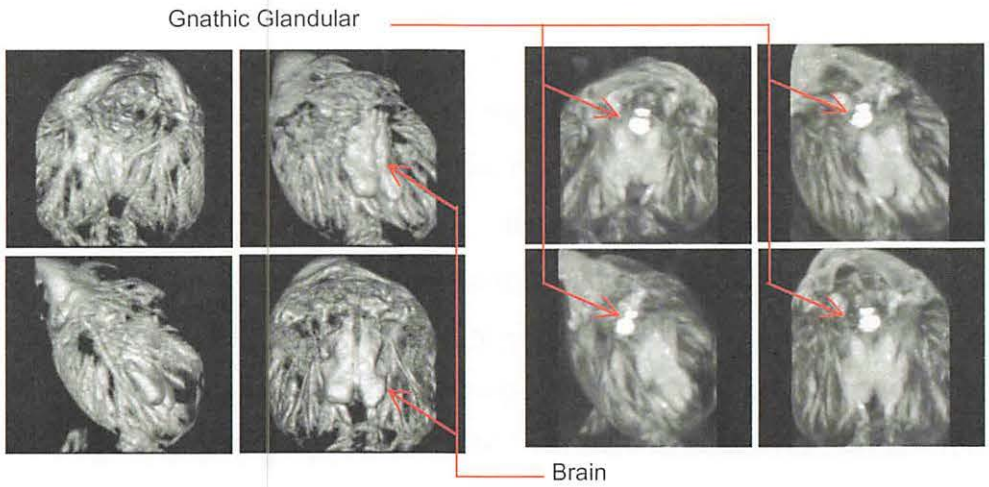

Figure 1. 3D images of ant's head (Volume rendering: left, MIP : right).

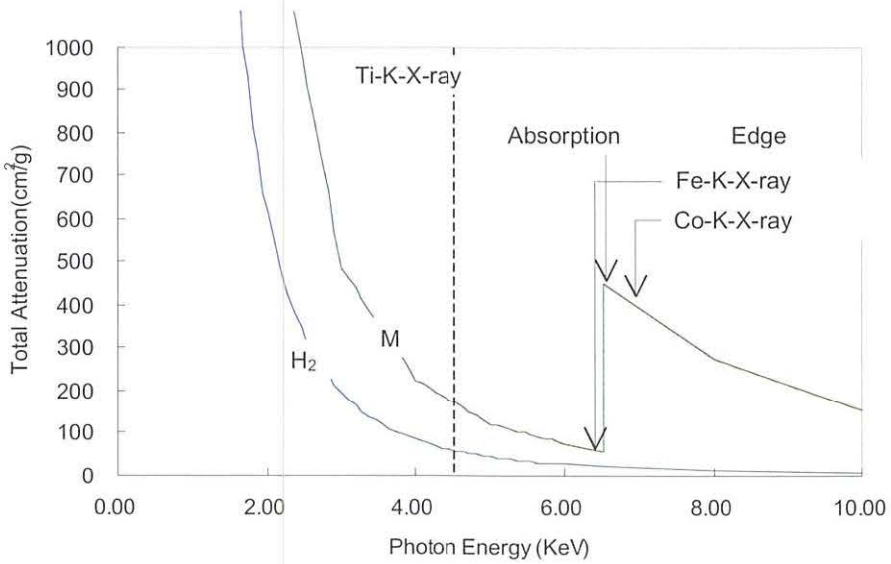

Figure 2. Dual Energy subtraction method.

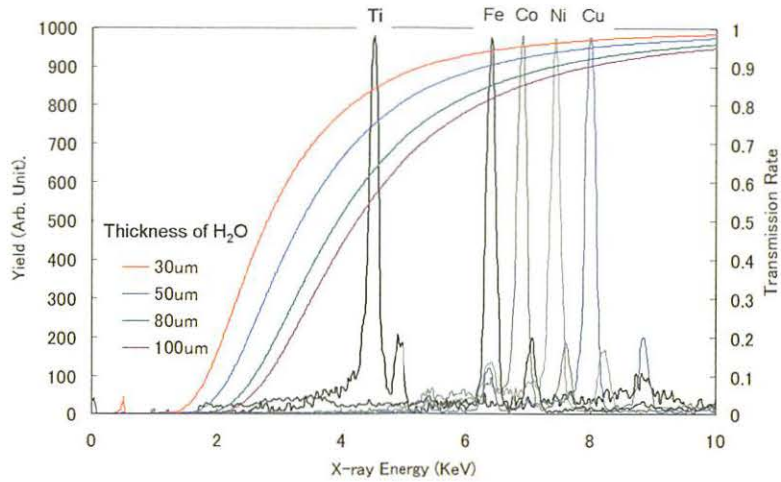

Figure 3. Transmittance of X-ray through water.

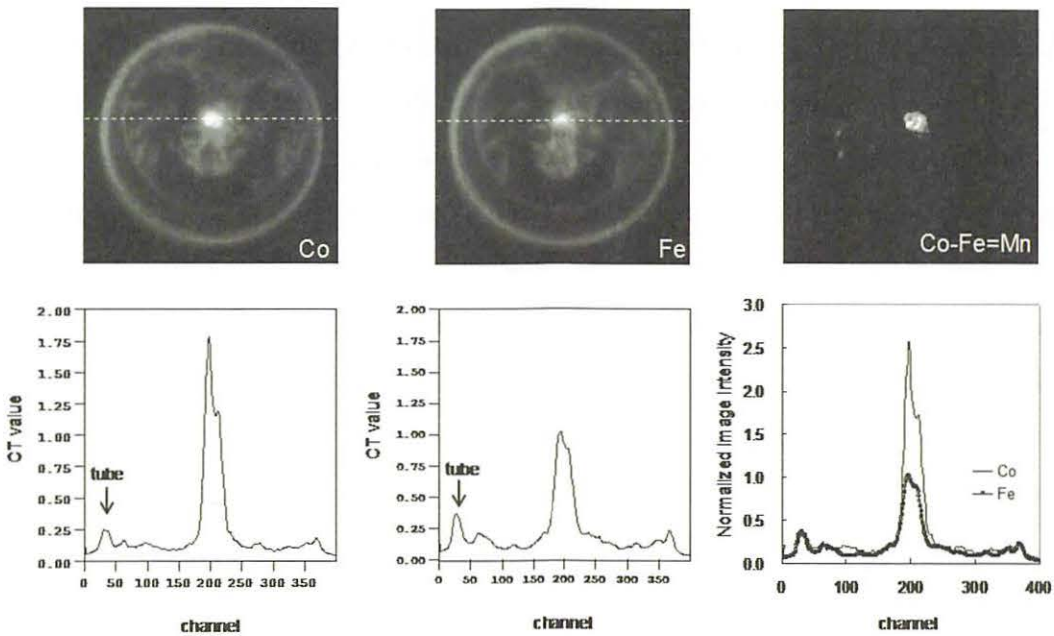

Figure 4. CT images of Gnathic Glandular and line profile of CT value along red broken line.

Figure 5. Dual Energy subtraction 3D MIP image (3D mapping of Mn).

V. 3. Elemental PIXE Analisis of Oolong Tea

Watanabe M.[1], Ishii K.[1,2], Matsuyama S.[1], Terakawa A.[1], Kikuchi Y.[1], Fujiwara M.[1], Kawamura Y.[1], Tusboi K.[1], Yamanaka S.[1], Okura S.[1], Fujikawa M.[1], and Yamazaki H.[2]

[1]*Department of Quantum Science and Energy Engineering, Tohoku University*
[2]*Cyclotron and Radioisotope Center, Tohoku University*

Introduction

At the present time, production volume of coffee drinks and carbonated beverages is about 3 million kl per year, of fruit drinks' one is 2 million kiloliter and isotonic drinks' one is 1.6 million kiloliter in Japan. On the other hand, production volume of tea-based beverages is 6 million kiloliter per year. Oolong tea occupies 20% of the production volume.

Oolong tea is one of the beverages which are mainly consumed in Asian area. Generally, oolong tea contains catechin, zinc, caffeine, carotene, saponin, selenium, vitamin C, vitamin E, fluorine, flavonoid, manganese, and oolong tea polymerized polyphenols (OTPP). The later, OTPP prevents the absorption of neutral fat, so it has attracted our attention for several years. For this reason oolong tea became a popular drink as a healthy drink. This indicates Japanese people daily drink oolong tea. Almost all the oolong tea leaves are producted in China. Recently, soil pollution has become serious problem in China. Harmful substances accumulate in crops and, via the food chain, find their way into our bodies, where they can cause a variety of illnesses. Especially, heavy-metal contamination such as As, Cd, Hg, Pb is harmful to human health. In this study, we analyzed elemental concentration of oolong tea which is producted in China and researched concentration of heavy metal in oolong tea.

Sample Preparation

Six oolong teas which are popular in Japan were chosen as samples in this study. Two of these (BO and SABO) were black oolong tea. They were fermented and toasted

for a longer time than ordinary oolong tea. All of these oolong tea leaves were cultivated in China. We also chose green tea (IC) which was cultivated in Japan.

A very simple sample preparation is useful for an examination of a large number of samples. In this study, we applied an internal standard method using Ga as an internal standard element[1]. 0.03 ml of sample was pipetted onto 2 μm thickness polycarbonate films and then was dried. Concentration of Ga was 5 ppm. Here, we check the sensitivity of this simple method for toxic elements.

Analysis System

Analysis was carried out using the proton beam at Tohoku University[2]. For elemental analysis, two X-ray detectors for PIXE analysis were used.

Two X-ray detectors were set in air at 135 degree with respect to the beam axis[3]. The first one has a large sensitive area (60 mm^2, LS60148 ; Princeton Gamma-Tech). To reduce pile-up events or deformation of the spectrum by recoil protons, a Mylar filter (500 μm) was attached to the front of the detector. Maximum solid angle is ~0.13 sr. The second detector (LS10129 ; Princeton Gamma-Tech) with a high energy resolution (~129 eV) , a thin Be entrance window (7.5 mm) and small solid angle of ~0.02 was used to detect X-rays lower than 5 keV. To reduce pile-up events or deformation of the spectrum by recoil protons, a Mylar filter (500 μm thickness and holed 0.4 mm pinhole at the center) was attached to the front of the detector. The system enables to detect X-ray ranging from 1.48 to 30 keV with a high energy resolution. The samples are analyzed by using a beam of 2.39 MeV protons focused to a 2 mm diameter spot.

Results and Discussion

As shown in Fig. 1 and 2, the heavy metals of As, Cd, Hg, Pb were not observed. The detection limits of those elements were [As]<2.35×10^{-2} ppm, [Cd]<5.29×10^{-1} ppm, [Hg]<3.90×10^{-1} ppm, [Pb]<5.71×10^{-1} ppm. The limit of quality of water to drink which based on food hygiene law in Japan was given as follows; [As]<5.0×10^{-2} ppm, [Cd]< 1.0×10^{-2} ppm, [Hg]<5.0×10^{-4} ppm, [Pb]<5.0×10^{-2} ppm. This indicates oolong tea is safety for As, however we can not mention it for Cd, Hg, Pb with the present sensitivity of PIXE.

Trace elements detected from oolong tea were Al, Si, P, S, Cl, K, Ca, Cr, Mn, Fe, Co, Ni, Cu, Zn, Br, Rb, Sr, Zr, and Ba. Concentration of several elements are shown in Table.1. Elemental concentrations are almost same among six samples, but concentration of Rb in

green tea is different from in oolong tea. In previous study[4], some kinds of elements were detected in drinking water; [Mn]<50 ppb, [Fe]<300 ppb, [Ni]<10 ppb, [Cu] and [Zn]<1000 ppb, and [Pb]<50 ppb. Concentrations of these elements in oolong tea are higher than those in water. Mn was detected by 0.99 ppm on average of all samples. Mn has antioxidant action, so it increases amount of oxygen in human body and improve immunity. Zn was also detected oolong tea and green tea, it prevents from disturbance in taste, dermatitis, namely, Zn has an effect to accelerate curing of wound. Cu was not detected and its detection limit was [Cu]< 1.06×10^{-2} ppm.

The concentration of Rb in green tea is smaller than in oolong tea. Green tea contains 0.1 ppm of Rb. On the other hand oolong tea contains 0.5~1.5 ppm. The concentration of Rb in soil is small but Rb tends to be accumulated in plants. All of oolong tea leaves which were analyzed in this study were cultivated in China, of green tea was cultivated in Japan.

The difference of Rb concentration for each tea is caused by the concentration of Rb in the area where oolong tea leaves were cultivated. Therefore analysis of Rb concentration can be used to specify where tea was cultivated.

Conclusion

As a result, we can check easily the concentration of a toxic element, As in oolong tea by PIXE analysis. On the other hand, safety for Hg, Cd can not examined by present very simple sample preparation.

References

1) Futatsugawa S., Hatakeyama S., Saitou Y., Sera K. Nucl. Instrm. Methods B**109** (1996) 113.
2) Matsuyama S., Gotoh K., Ishii K., Yamazaki H., Satoh T., Yamamoto K., Sugimoto A., Tokai Y., Endoh H., and Orihara H., Int. J. PIXE, **8** (1998) 209.
3) Inoue J., Iwasaki S., Murozono K., Ishii K., Matsuyama S., Int. J. PIXE, **6** (1996) 147.
4) Yamazaki H., Tanaka M., Tsutsumi K., Ishii K., Iwasaki S., Matsuyama S., Inoue J., Murozono K., Int. J. PIXE, **7** (1997) 31.

Table 1. Elemental concentrations of oolong tea and green tea.

(ppm)

Sample	Al	Si	P	S	Cl	K	Ca	Mn	Fe	Zn	Rb	Ba
BO	10.37	12.47	7.07	4.37	0.44	8.19	0.66	1.46	0.28	0.22	1.51	0.96
SABO	14.06	18.23	9.12	6.97	0.71	4.61	0.98	1.32	0.28	0.44	1.20	0.97
SVO	8.11	9.28	3.08	2.68	0.44	1.15	0.65	1.01	0.18	0.27	0.50	1.04
SO	11.07	16.82	9.16	6.12	0.53	4.09	0.90	1.14	0.27	0.14	0.79	1.04
YO	15.37	21.27	11.08	6.14	0.74	2.81	0.84	0.62	0.23	0.33	0.43	1.14
ASO	12.80	20.08	9.57	5.39	0.67	3.09	0.79	0.63	0.13	0.32	0.51	1.02
IC	15.71	21.30	11.47	6.77	0.82	4.52	0.96	0.72	0.18	0.41	0.10	1.10

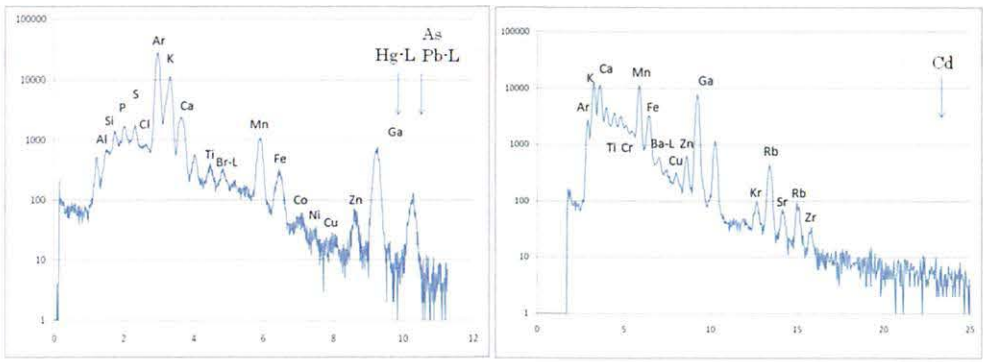

Figure 1. Typical oolong tea (BO) Spectra of the in-air PIXE analysis Using Ga as an internal standard (LS10129 Low energy / LS60148 High energy).

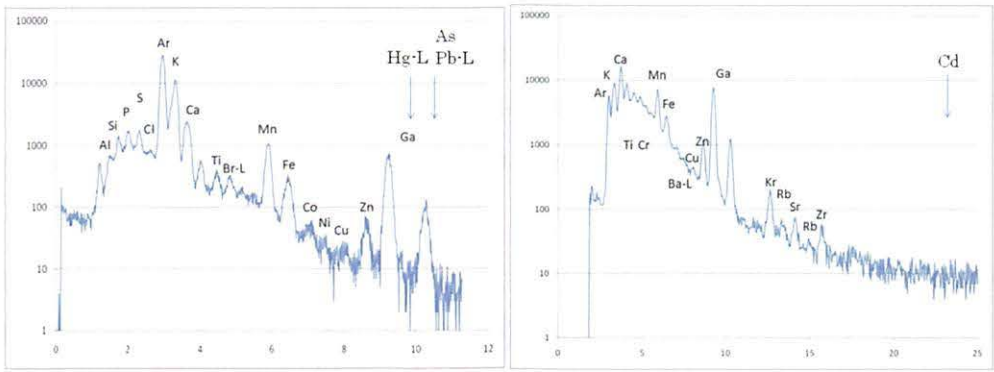

Figure 2. Typical of Green tea (IC) Spectra the in-air PIXE analysis Using Ga as an internal standard (LS10129 Low energy / LS60148 High energy).

V. 4. PIXE Analysis of Atmospheric Aerosols from Asian Continent

Yamanaka K.[1], Ishii K.[1], Matsuyama S.[1], Terakawa A.[1], Kikuchi Y.[1], Fujiwara M.[1], Kawamura Y.[1], Oyama R.[1], Yamamoto T.[1], Watanabe M.[1], Tsuboi S.[1], Okura S.[1], Fujikawa M.[1], Yamazaki H.[2], and Arao K.[3]

[1]Department of Quantum Science and Energy Engineering, Tohoku University
[2]Cyclotron and Radioisotope Center, Tohoku University
[3]Faculty of Environmental Studies, Nagasaki University

Introduction

A large amount of yellow sand dust particles is transported from Asian continent, especially in spring season. It is known as the Kosa. Yellow sand dust is common interest for North East Asia including Japan, China and Korea, as these particles sometimes affect traffic, climate and human health. Yellow sand dust is known as a natural phenomenon, but is considered as an environmental problem, as these particles are mixed with anthropogenic aerosols over the industrial area in East Asia and cause environmental pollution.

In addition to the Kosa events, atmospheric turbid phenomena (like fumes or mists) were occasionally observed in spring in recent years over western part of Japan, characterized by a significant increase in the amount of fine particles (0.3μm~1μm in diameter). These fine particles, which are suspected to cause those turbid phenomena, are not the main components of yellow sand dust, since yellow sand dust particles are composed of 4 μm diameter minerals.

To investigate the origin of these turbid phenomena and the relation between turbid phenomena and Kosa events, we collected atmospheric aerosols every 2-3 hours by using a mini step-sampler from March to June, 2005 in Nagasaki, and analyzed them by PIXE. We also used an optical particle counter to determine the size distribution of aerosols. Time series of elemental concentration and particle number concentration was observed.

Experimental

Sampling

Aerosol particles were collected at the campus of Nagasaki University (32.78°N, 129.87°E; 20 m) from March 16 to June 3, 2005, on Kyushu Island in western Japan, where the aerosols affect daily life. A mini step-sampler, of which details were presented in previous paper[1], was used for aerosol collection. Aerosol particles were collected on a 1μm pore size Nuclepore filter[2] with the constant face velocity of 80m/min. The effective 50% cutoff diameter of the sampler was less than 0.2 μm[3] and was sufficient for collecting fine particles. During those 3 months, and with a sampling resolution of 2 or 3 hours, the mini step-sampler collected more than 900 aerosol samples on Nucrepore filter of 200×200 mm^2. Since the mini step-sampler is single stage, an optical particle counter (OPC) was used together with the mini step-sampler.

Analysis

We performed elemental analysis of each aerosol particles using an in-air PIXE analysis system at Tohoku University[4,5]. The system consists of a beam exit assembly[2], two Si(Li) detectors and X-Y sample stages. Proton beams were extracted from a Kapton exit window of 12.5 μm. The samples were placed at 1 cm from the exit window and on the X-Y stage in air.

Two X-ray detectors were set at the left side and right side with respect to the beam axis respectively, and their observation angle was 135 degrees with respect to incident beam direction and their observation position was 16mm away from the sample. The first detector (LS60148, Princeton Gamma-Tech) has a large sensitive area and is suitable for trace elemental analysis. To reduce the deformation of the spectrum by recoil protons and pile-up events, a 300 μm thick Mylar filter was used. This detector is used to detect X-ray of energy higher than 5 KeV. The second detector (LS10138, Princeton Gamma-Tech) has a higher energy resolution (138 eV), a thin Be entrance window and a small sensitive area of $10mm^2$, and it is suited for the detection of elements of low atomic number ($Z < 25$). Since the intensity of low energy X-ray is too high in this application, a 500 μm thick Mylar filter with a pin-hole of 0.7 mm in diameter was attached to the front of the detector to reduce X-ray counting rate and recoil protons.

Typical X-ray spectra obtained by the detectors are shown in Fig. 1. The system is capable of detecting X-rays ranging from 1.4 to 30 keV with good energy resolution and

detection efficiency. Since elemental concentrations of aerosol samples strongly depend on samples, beam currents in a conventional detector system have to be controlled in correspondence with X-ray counting rate. The present system allowed us to obtain data without changing the beam currents.

The total number of collected aerosol samples was more than 900. Since aerosols were continuously collected under various kinds of atmospheric conditions, analyses of all these samples would have taken too much time. We consequently used the OPC to select the samples to be analyzed, according to their particles number concentrations (exceeding 50 million/L for fine particles and 100/L for coarse particles). The days of March 22, 31, April 3, 15, 16, 21, 22, May 3, 12, 23 and June 2 were selected, representing a total of 140 samples that we analyzed afterwards. For quicker analyzes, we introduced an automatic measurement system which collects data until a fixed charge, saves data and changes the sample in a definite order.

Energy of the proton beam is 3 MeV and beam spot size is 1.5 mm in diameter with a beam current of $\sim$1.5 nA, for a total accumulated charge of 0.4 μC. Quantitative PIXE analysis was performed using external standard method[6]. A program based on pattern analysis was them usud to analyze PIXE spectra.

Result and Discussion

Aluminum, silicon, sulfur, calcium, iron, zinc, lead, mercury and bromine were detected, where bromine is a component of the Nuclepore filter. Concentrations for fine (0.3 and 0.5 μm) and coarse (1, 2 and 5 μm) particles are shown in Figs. 2 and 3, respectively with daily average elemental concentrations. Concentrations of fine and coarse particles show different trends. Fumes and mists were observed on 2 April, 12 and 23 May, when fine particles reached its highest concentrations. On 15, 16, 21, 22 April and 12 May, Kosa events occurred, meaning that fine particles are not correlated with yellow sand dust particles. Elemental concentrations of Si, Ca, Fe, Pb and Hg show similar trends to that of coarse particles, whereas variations of elemental concentrations of S and Zn and fine particles are almost same. It is consequently apparent that coarse particles contain Si, Ca, Fe, Pb and Hg and fine particles contain S and Zn. Figure 4 shows time variations of elemental concentrations and concentrations of fine and coarse particles on April 21 when both fine and coarse particles showed their highest concentrations. It is apparent that the time variations of fine particles are different from that of coarse particles. It also shows

that Aluminum, silicon, calcium, iron, lead and mercury are related to coarse particles, whereas sulfur and zinc are well correlated with fine particles. On April 22, coarse particles presented higher concentrations but fine particles showed lower concentrations. In this case, no correlation was seen between elemental concentrations of sulfur and zinc with number of concentrations of fine particles. On the other hand, on May 23, coarse particles and fine particles showed lower and higher concentrations, respectively. In this case, there was no correlation between coarse and elemental concentrations. Backward trajectory analysis using NOAA HYSPRIT[7] indicated that the particles collected on these days came from the Chinese coastal area to Nagasaki. This therefore proves that fine particles are composed of anthropogenic sulfate aerosols and caused fumes and mists in Nagasaki. Zinc is also an anthropogenic aerosol related to industry, whereas silicon, aluminum, calcon and iron are minerals and components of yellow sand dusts and thus were contained in coarse particles. The coarse particles were also transported from Asian continent over the Chinese industrial area to Nagasaki. Therefore lead and mercury were also contained in coarse particles and are inferred to have been adsorbed through mixture with coarse particles during transportation.

Conclusion

We collected aerosol particles with a mini step sampler for more than two months. We selected some samples using OPC observation data and analyzed them using our automatic PIXE measurement system, which is very useful for numerous samples analyses. As a result, Aluminum, silicon, sulfur, calcium, iron, zinc, lead and mercury were detected in aerosol samples. Moreover, concentrations of fine and coarse particles showed different trends: Kosa events occurred when coarse particles reached high concentrations, and elemental concentrations of Si, Ca, Fe, Pb and Hg showed similar variations along with that of coarse particles. Si, Ca and Fe are main components of yellow sand dusts whereas Pb and Hg are inferred to have been adsorbed through mixture with coarse particles during transportation. Concentrations of fine particles were also correlated with concentrations of S and Zn, showing us that sulfate aerosols cause turbid phenomena in western Japan. In addition, we also showed that PIXE analysis of aerosol particles collected with the mini step sampler is very effective for a better understanding of such turbid phenomena.

Reference

1) Matsuyama S., et al., Int. J. PIXE, **13** (2003) 65.
2) Spurny K.R., et al., Environmental Science and Technology, **3** (1969) 453.
3) Loi B.Y.H., Lee K.W., Environmental Science and Technology, **10** (1976) 345.
4) Iwasaki S., et al., Int. J. PIXE, **6** (1996) 117.
5) Matsuyama S., et al., Int. J. PIXE, **9** (1999) 51.
6) Yamazaki H., et al., Int. J. PIXE, **14** (2004) 57.
7) Draxler R.R., Rolph G.D., 2003. HYSPLIT (HYbrid Single-Particle Lagrangian Integrated Trajectory) Model access via NOAA ARL READY Website (http://www.arl.noaa.gov/ready/hysplit4.html). NOAA Air Resources Laboratory, Silver Spring, MD

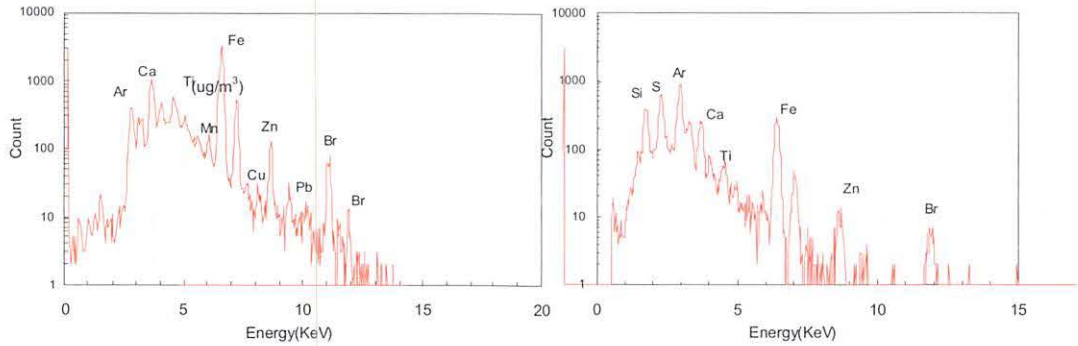

Figure 1. PIXE spectra of aerosol sample collected on 21 April, 2005.

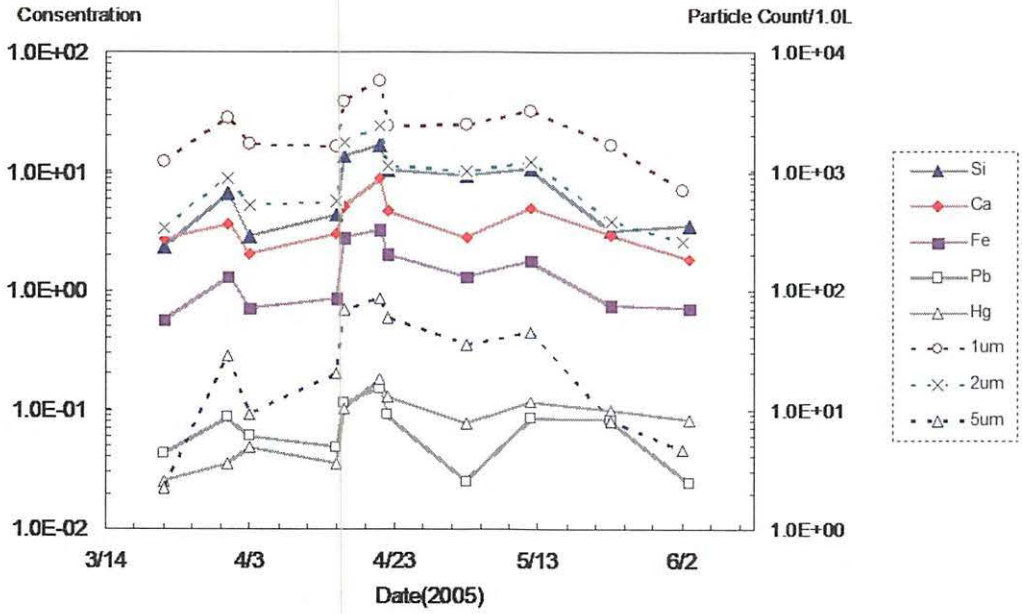

Figure 2. Elemental concentrations related to coarse particles.

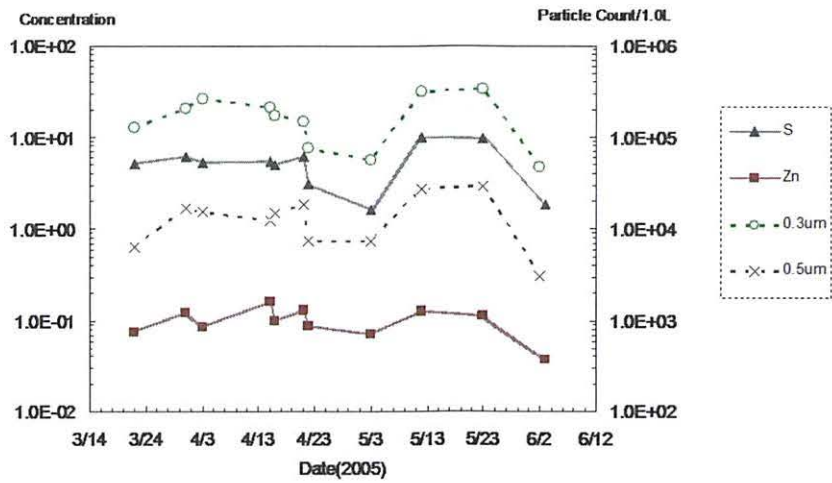

Figure 3. Elemental concentrations related to fine particles.

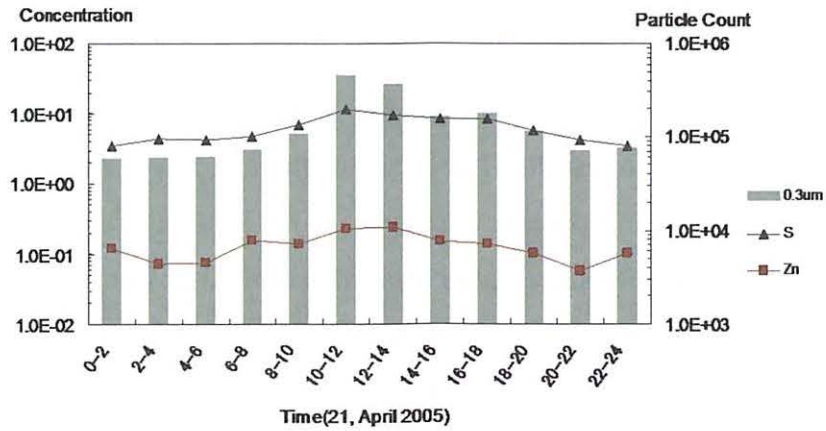

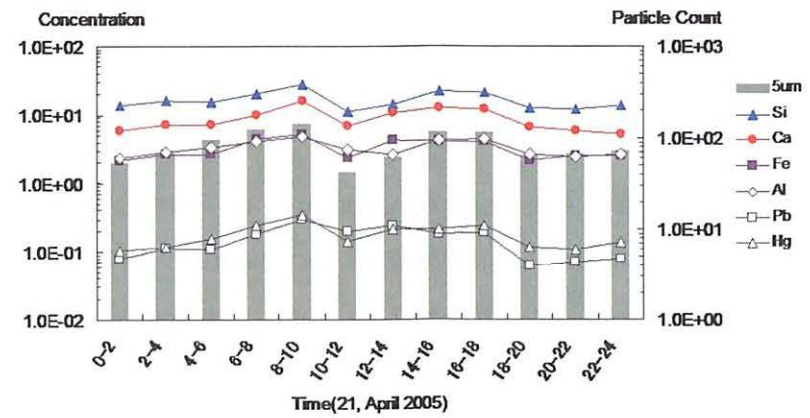

Figure 4. Changes of elemental concentrations and number of concentrations of fine and coarse particles on 21 April.

V. 5. PIXE Analisis of Umeboshi (Dried Plum)

Tsuboi S.[1], Ishii K.[1], Matsuyama S.[1], Terakawa A.[1], Kikuchi Y.[1], Fujiwara M.[1], Kawamura Y.[1], Watanabe M.[1], Yamanaka K.[1], Arikawa J.[1], Okura S.[1], Fujikawa M.[1], and Yamazaki H.[2]

[1]Department of Quantum Science and Energy
[2]Cyclotron and Radioisotope Center, Tohoku University

Introduction

The self-efficiency ratio of food in major advanced country such as USA, France and Germany is 128%, 122% and 84%, respectively, whereas that in Japan is less than 40 %. It means that Japanese people rely strongly upon imported food and should take care of their safety. The Ministry of Health, Labor and Welfare reports of the total 2.0 million imported foods in 2007, only 10 percent were inspected. Under these conditions, imported foods whose concentration of contamination exceeds standard level based on food hygiene law are detected and food-poisoning cases arising from imported food also occurs. Heavy-metal contamination such as As, Cd, Hg, and Pb is especially important. These heavy-metal contaminations harm our health by mediating animals and plants grown in the polluted environment. In recent years, water and soil pollution are becoming more serious in China. On the other hand, Chinese-grown foods increase fourfold in two decades and Chinese agricultural products have a 50% share of the pie. Therefore, importance of Chinese-grown foods for Japanese has been increasing and its safety is a growing concern for Japanese.

In this study, we analyzed elemental concentration of *umeboshi* which is one of the traditional pickled foods in Japan. *Umeboshi* is very popular in Japan. Traditionally, many Japanese have *umeboshi* for breakfast or lunch. Recently, many Japanese eat *umeboshi* as a confectionery. *Umeboshi* is pickled *ume* fruits. *Ume* is a species of fruit-bearing tree in the genus *Prunus*, which is often called a plum, but is actually more closely related to the apricot. Almost all of *ume* for *umeboshi* are imported from China and its consumption per household has been increasing due to inexpensive price. Since *ume* is pickled without peeling, its contamination will directly affect our health. From these

viewpoints, we analyzed *umeboshi* which was pickled using Chinese *ume* and domestic *ume* by PIXE.

Experimental

We analyzed seasoned *umeboshi* sold in convenience stores. Table 1 summarized the samples. KUr and USr are colored by new coccine ($C_{20}H_{11}N_2Na_3O_{10}S_3 \bullet 11/2H_2O$), and the other two are not colored by a food coloring. Seasoned *umeboshi* was divided into 3 parts for PIXE analyses as shown in Fig. 1. A wet ashing method was carried out to conventional PIXE analysis to know averaged elemental concentrations[1]. Direct analysis using submilli-PIXE camera was also carried out to know elemental distribution in surface and cross section.

A dried mass of about 45 mg of *umeboshi* was heated with nitric acid by a microwave oven. 10 μ*l* dissolution was deposited on a backing film (Mylar, 2 μm) after adding indium (2000 ppm for a dried mass of *umeboshi*) as an internal standard. PIXE analysis was carried out by using an in-air PIXE system at Tohoku University. Proton beams of 2.4 MeV were extracted into air through a kapton film of 12.5 μm and irradiated on the target[2]. Prepared samples were fixed to the target holder, and set just after the beam exit window. X-rays were detected two Si(Li) detectors. The one has a large sensitive area of 60 mm^2 and used for a high energy X-rays detection. To prevent piling up of high intensity low energy X-rays, a 500 μm Mylar absorber was used. The other detector has a thin Be window for low energy X-rays. A Mylar foil of 500 μm with a pin-hole of 0.7 mm in diameter was attached. In this set up, elements heavier than Al could be detected.

To know elemental distribution inside and skin of *umeboshi*, cross section and skin of *umeboshi* were directly analyzed by using an in-air submili-PIXE camera. These samples were sliced into thin sections (~1.5mm), fixed on the sample holder (500 μm thick Mylar) using epoxy resin, and set up just after the beam exit window of the in-air submili-PIXE camera[3]. Two Si(Li) detectors were also used to cover wide range of X-ray energy.

Results and Discussion

Figure 2 and 3 show characteristic X-ray spectrum of *umeboshi* and elemental concentrations of *umeboshi*, respectively. Major constituent elements of *umeboshi* are Al, Si, P, S, K, Ca, and Fe. Since Al, Si, Ca, and Fe are major components of soil, *ume* sucked these elements in through their roots and accumulated. Calcium shows the highest concentration,

which stems from the pickled process. During the process in making *umeboshi*, *ume* is dipped in Ca solution for several days and absorbs Ca. Phosphorus, sulfur, and calcium elements are major minerals in plants and play an important role in human health. Table 1 shows concentrations of toxic heavy metals, namely As, Cd, Hg and Pb. These concentrations were estimated by the detection limit of PIXE and were lower than standard values given by a food hygiene law in Japan. Thus, *umeboshi* analyzed in this experiment is safety for As, Cd, Hg and Pb.

Concentrations of elements heavier than Ca show similar trend. On the other hand, lighter elements than Ca show large difference. Elemental concentrations of CFT and US are 2 to 10 times higher than those of KUr and USr, which is related to food coloring. Although samples of US and USr are produced by the same company using *ume* which was cropped in the same area, there are large differences in elemental concentrations of P and S. On the other hand, elemental concentrations of KUr and USr are very similar and lower than other two ones. It means that these differences are related to the process of *umeboshi* and not to *ume* itself.

Elemental concentrations of Sr in US and USr were lower than that of CFT and KUr. MAFF (Ministry of Agriculture, Forestry and Fisheries) of Japan reported that concentration of Sr in Chinese soil is higher than that in Japanese soil[4]. Elemental concentration of Sr in *umeboshi* may indicate the area where *ume* is cropped.

Figure 4 and 5 show elemental distribution images of cross-sectional area and surface of *umeboshi*, respectively. Scanning area was 10×15 mm^2 for cross sectional and was 10×10 mm^2 for surface analyses. It is apparent that Fe is concentrated in hull. Chlorine is uniformly distributed around hull. Ca is concentrated in skin, which is related to the absorption of Ca solution. In Fig. 5, Ca is not uniformly distributed and will be deposition from a solution.

Conclusion

We analyzed *umeboshi* which uses Chinese and Japanese *ume* by using an in-Air PIXE system and an in-air submili PIXE camera at Tohoku University. Major constituent elements are Al, Si, P, S, K, Ca, and Fe. Concentrations of heavy metals such as As, Cd, Hg and Pb were lower than standard values given by a food hygiene law and *umeboshi* analyzed in this experiment is safety for these elements. Calcium shows the highest concentration, which stems from the pickled process. During the process in making *umeboshi*, *ume* is dipped in Ca solution for several days and absorbs Ca. Concentrations of elements heavier than Ca

show similar trend. On the other hand, lighter elements than Ca show large difference, which is related to food coloring or processing technique. Even using *ume* which was cropped in the same area by the same supplier, there are large differences in elemental concentrations of P and S. On the other hand, elemental concentrations of colored *umeboshi* are very similar. It means that these differences are related to the process of *umeboshi* and not to *ume* itself.

References

1) Futatsugawa S., Hatakeyama S., Saitoh Y., Sera K., International Journal of PIXE **4** (1993) 319.
2) Iwasaki S., Ishii K., Matsuyama S., Murozono K., Inoue J., Tanaka M., Yamazaki H., Orihara H., International Journal of PIXE **6** (1996) 117.
3) Matsuyama S., Gotoh K., Ishii K., Yamazaki H., Satoh T., Yamamoto K., Sugimoto A., Tokai Y, Endoh H., Orihara H., International Journal of PIXE **8** (1998) 209.
4) Tsukada M., Fujihara M., Yamasaki Y., Miyatake M., Kobayashi T., http://www.famic.go.jp/technical information/investigation research report/pdf/2802.pdf.

Table 1. Sample Informations.

Sample name	CFT	KUr	US	USr
Food Coloring	-	_	-	_
supplier	A	B	C	
Production Area	China	China	Gunma, Japan	

Table 2. Concentrations of toxic heavy metals.

	Concentrations[ppm]	Standard values[ppm]
As	<0.04	1.5-3.5
Cd	<0.84	1.0
Hg	<0.72	0.4
Pb	<0.90	1.0-5.0

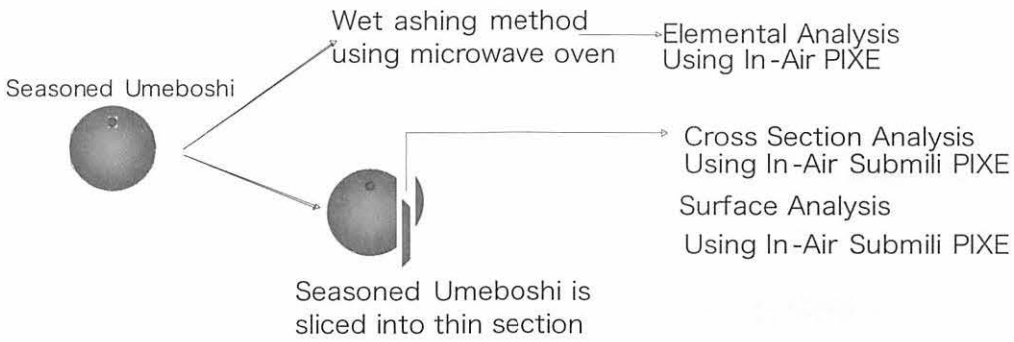

Figure 1. Flow of sample preparation.

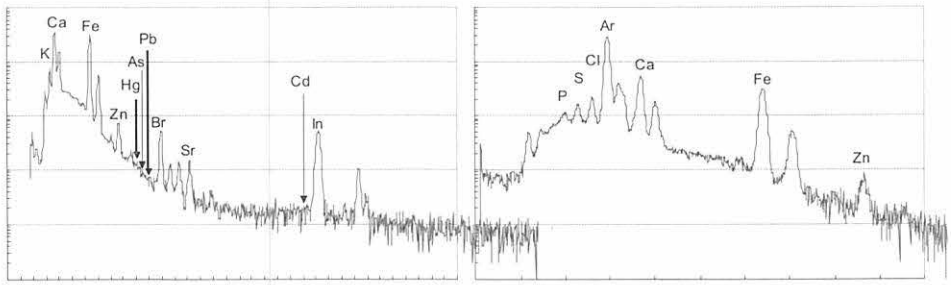

Figure 2. Characteristic X-ray spectrum of *umeboshi.*

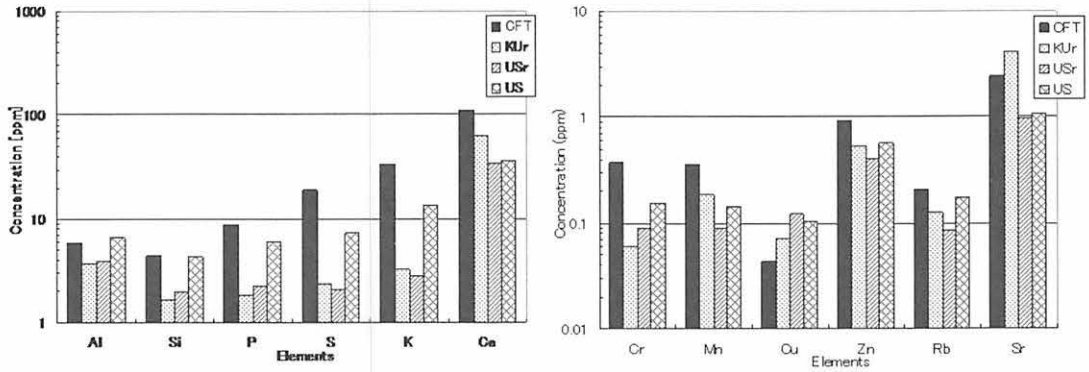

Figure 3. [left] Elemental concentration of *umeboshi.*(Al to Ca), [right] (Cr to Sr).

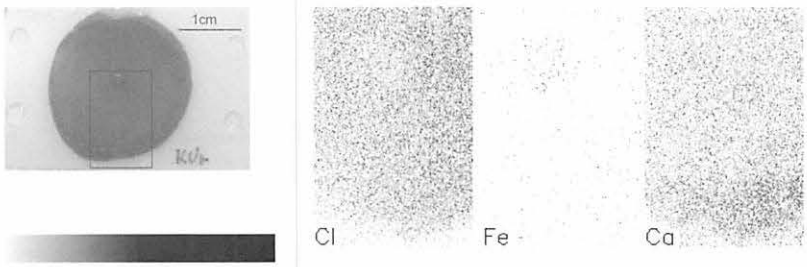

Figure 4. Elemental distribution of Cl, Fe and Ca in a cross sectional area.

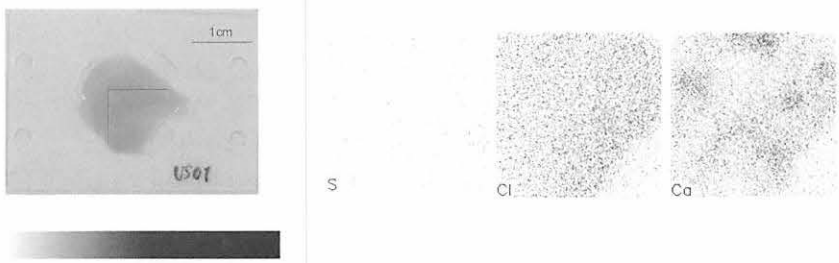

Figure 5. Elemental distribution of S, Cl and C on a surface of *umeboshi.*

V. 6. PIXE Study on Absorption of Arsenate and Arsenite by Arsenic Hyperaccumulating Fern *(Pteris vittata)*

Yamazaki H.[1], Ishii K.[2], Matsuyama S.[2], Kikuchi Y.[2], Takahashi Y.[2], Terakawa Y.[2], Kawamura Y.[2], Yamanaka K.[2], Watanabe M.[2], Tuboi S.[2], Satoh T.[3], and Inoue C.[3]

[1]*Cyclotoron and Radioisotope Center, Tohoku University*
[2]*Graduate School of Engineering, Tohoku University*
[3]*Graduate School of Environmental Studies, Tohoku University*

Introduction

Arsenic contamination of soils and groundwater from various sources such as mines and urban wastes and wood preservatives is of serious environmental problem. A number of technologies for cleaning up arsenic-contaminated soils have been proposed[1-3] Recently, environmentally friendly and low-input phytoremediation of several kinds of phytoextraction, rhizofiltration, phytovolatilization and phytostimulation has been proposed for remediation of soils contaminated with heavy metals and metalloids[4]. Phytoextraction using an arsenic hyper-accumulator, *Pteris vittata* L., has generated increasing interest worldwide due to its both environmentally sound and cost effectiveness[5]. Although many studies have been conducted about the arsenic hyper-accumulator fern[6-8], the entry system of arsenic to *Pteris vittata* is not well understood and the mechanism of arsenic accumulation by this plant is not clear at this time. To develop practical application of the arsenic accumulator fern, it is necessary to explicate the accumulation mechanism based on elemental translocation using an in-vivo analysis of representative parts of the fern cultivated under various conditions of different arsenic oxidation states and different. This study shows the *in-vivo* uptake of arsenate (As(V)) and arsenite (As(III)) by a hydroponic culture of *Pteris vittata* using both an in-air submilli-PIXE for different parts of the fern and an in-air micro-PIXE

Material and Methods

P. vittata L., a perennial and pinnate fern which grows worldwide in a dried area with long sunshine duration, was used throughout the experiment. In our experiments, fern seedlings were used three months after spore germination. In this stage of growth, a rootstock of fern was in several fronds which have not opened completely. The roots were washed carefully in tap water to remove soil particles. The seedlings were then transferred to hydroponic water containing nutrients in concentrations of 8.10 mg/dm^3 KNO_3, 9.50 mg/dm^3 $Ca(NO_3)_2 \cdot 4H_2O$, 5.00 mg/dm^3 $MgSO_4 \cdot 7H_2O$, 1.15 mg/dm^3 $NH_4H_2PO_4$, 15 μg/dm^3 NaFe-EDTA, 3.0 μg/dm^3 H_3BO_3, 1.8 μg/dm^3 $MnCl_2 \cdot 4H_2O$, 0.2 μg/dm^3 $ZnSO_4 \cdot 7H_2O$, 0.05 μg/dm^3 $CuSO_4 \cdot 5H_2O$ and 0.02 μg/dm^3 $Na_2MoO_4 \cdot 2H_2O$. The nutrient solution was aerated continuously. The seedlings were grown on the hydroponic solution for different periods more than one month in a growth camber with a 16 hours light period, 25°C/20°C of day/night temperature and 70% relative humidity.

After a desired period of cultivation on hydroponic solutions, the roots were washed well in tap water. The fern frond of selected growth stage was placed in 100 ml conical beaker filled with 100 ml uptake solution of the same nutrient concentration as culture solution. Then arsenic in the form either As(V) as sodium arsenate (Na_2HAsO_4) or As(III) as sodium arsenite ($NaAsO_2$) was added to the uptake solution to be the final concentration of 23 to 50 mg-As per liter. In order to compare the effect of phosphate, $NH_4H_2PO_4$-free nutrient solution was also used for several arsenic-uptake experiments. The treated ferns were incubated in the growth camber at the same operating condition as above for one day. After 24 hours incubation, total weight of the beaker was measured to determine the amount of transpiration by the fern. Then the roots were washed and the fern sample was placed in 100 ml of fresh solution with the same concentrations of nutrients and arsenic as above. This cycle was repeated for more than 5 days. Arsenic concentrations of the uptake solutions were determined by ICP-MS (Hewlett Packard, HP-4500).

Tow kinds of in-air PIXE measurements of several tens mm^2 and several hundreds μm^2 sized areas were performed by using the in-air submilli-PIXE camera and the in-air micro-PIXE camera at Tohoku University, Japan[9-11]. A part of lamia of *P. vittata* was plucked at three different growth stages; an early active stage at which all leaves have just opened, although the leaves are not opened completely at the beginning stage of growth, a middle active stage at which the area of an apex has served as maximum, and the mature

growth stage at which all pinnas have grown most. In the in-air submilli-PIXE analysis, 3 MeV proton beams of beam current ~800 pA and <0.5 mm beam spot were scanned on a surface area of 10×20 mm^2 of a selected fern frond which was fixed to a target frame just after the beam exit window of 12.5 μm thick Kapton film. The plant sample was kept alive by dipping the stalk part into a hydroponic solution. The distance from the beam exit window and a sample is around 5 mm. The X-ray energy and the beam position were simultaneously measured in order to obtain spatial distribution of elements. For elemental mapping on cells of different plant tissues by the in-air micro-PIXE camera, a sliced fern section with moisture was mounted between two polycarbonate films of 5 μm thickness which were glued to sample holder, and 50×50 ~ 400×300 μm^2 sized areas were analyzed by a proton beam with a diameter of typically 1.5×1.5 μm^2 and energy of 3 MeV at beam currents of approximately 100 pA . In both submilli- and micro-PIXE analyses, X-rays from targets were measured with two Si(Li) detectors; No.1 detector (7.5 μm thick Be window, 10 mm^2 active area) with a low geometric efficiency is well suited for detection of an element of low atomic number, and No.2 detector (12.5 μm thick Be window, 60 mm^2 active area) with a 100-μm Mylar absorber allows detection of X rays > 4 keV and the removal of recoil protons. The list mode data acquisition system can sort the data for a selected element / energy region and generate an elemental image even while the data are accumulated. This resulted in a decrease of the dead time of signal processing. Quantitative PIXE analysis was performed using the GeoPIXEII software[12].

Results and Discussion

Many plants living on a soil contaminated by harmful elements usually maintain the vital activity in such a way that the absorption of harmful elements is blocked on the roots and the epigeal leaves remain free from harmful effects. On the other hand, *P. vittata* fern accumulate arsenic in a very high concentration harmful to the vital activity of the epigeal fronds without blocking arsenic on the roots, indicating a detoxication mechanism of arsenic in the lamina part of ferns[13]. Because of the similarity in chemical forms between orthophosphate and arsenate, the transportation route of phosphorus can be utilized for absorbing arsenate by the fern.

Figure 1 shows a time course of arsenic concentration in hydroponic culture solution with addition of 23 mg/dm^3 arsenic. In this experiment, ferns of the beginning growth stage were treated for two weeks using hydroponics of 1/10 or 1/100 of the ordinary

phosphate concentration (1 mM) in the hydroponic culture solution. The ferns under different phosphorus deficiency conditions and the fern under ordinary phosphorus concentration were moved to phosphorus-free hydroponic solutions with the same concentration of arsenic. Arsenate in similar chemical form to orthophosphate was more rapidly transferred into the plants under heavyer phosphorus deficiency. The genetic expression of phosphorus transportation is reported for the roots of *Capsella bursapastoris* and *Lycopersicon esculentum* corresponding to a phosphate deficiency condition in cultivation. It is considered that a transportation route of phosphorus in *P. vittata* participates in absorption of arsenate. On the other hand, uptake of arsenite for initial 15 min was very quick regardless of phosphate concentrations, indicating different absorption path of arsenite from phosphorus transportation in the fern. After two hours, arsenite was oxidized to arsenate, which was confirmed using liquid chromatography, and the arsenic uptake rate changed greatly with the phosphorus deficiency states of ferns. It is inferred that arsenite influx into the roots of *P. vittata* is much greater than arsenate influx. In addition to this, the oxidation state of arsenic in the fern at early active stage of growth was determined using X-ray absorption near edge structure (XANES) analyzer (Rigaku, R-XAS Looper) with the X-ray tube worked at 23 kV-80 mA and the analyzing crystal of Si (620). These measurements indicated that arsenate ions in hydroponic solution directly entered from the roots of *P. vittata* and were quickly translocated to the epigeal fronds. Moreover, this transported arsenate was reduced to trivalent state and accumulated in the lamina part of the fern.

Three kinds of fern samples of which the growth stage differs were moved to a culture solution included by arsenic 50 mg/dm^3, the absorption experiment of arsenic was conducted for five days, and the element distribution on each terminal pinna was measured by the submilli-PIXE camera. Figure 2-1 shows the elemental mapping for a fern apex in early stage of growth under the arsenite treatment, and Fig. 2-2 shows the results under the arsenate treatment. A measurement domain was 10×20 mm^2, and elemental concentrations were displayed as a function of the position in the rectangular portion of a 4 mm width on the leaf. The concentrations were derived from the relevant X-ray yields integrated on the rectangle segments on a leaf based on the assumption of the leaf matrix of 100 μm thickness in composition of 80% H_2O and 20% $C_4H_6O_3$ with the density of 1 g/cm^3 [13].

Since 1 mM orthophosphate was contained in the culture solutions, a slow uptake rate of arsenate resulted in low arsenic concentration profile on the apex of fern exposed to

arsenate contamination. However, there was no difference in the elemental distribution for two ferns on culture solutions containing different chemical forms of arsenic. That is, potassium and calcium were almost uniformly distributed over whole stenophyllous apex, except for disordered leaf matrix of the venation in the middle of the apex. Arsenic, irrespective of the oxidation states, was transported to the leaf edge distant from the vascular bundle acting as a conducting tissue of elements. Although the results are not shown due to the lack of space, the distribution of K and As did not change when the fern progressed to more mature stage. However, calcium was accumulated in some parts of the vein and some spots on an apex at high concentration.

Figure 3 shows the concentrations of K, Ca and As analyzed at the measurement domains of 10×20 mm^2 on the apexes in three growth steps; the early active stage of growth, the middle one and the mature stage. The five-day uptake of arsenate increased remarkably, when orthophosphate was not contained in the culture solution, and arsenite was absorbed by the fern without the influence of orthophosphate. Although the result was not shown here, arsenic of pentavalent was extremely distributed in the edge of apexes under the phosphorous deficiency state. This finding indicates that a growth function of fern leaf changes under the condition of a phosphorous deficiency and it influences the arsenic transportation to the growth part. Although K concentration was uniformly high in the leaves at the early active and the middle active stages of growth, it decreased 1/7 to 1/5 in the mature stage of growth. Moreover, very high-concentration spots over 10,000 μg/g were detected for Ca on the vein portion and the arsenic-accumulated edge position of the leaf in the mature stage of growth.

Although a plant of active metabolism of growth requires much potassium to prepare the metabolic pathway of cells, this element is not needed so much in the mature stage of the growth to which metabolic activity decreases. Calcium is also largely required for the maintenance of a structure and a function of cell walls at the intense growth phase of cell division. In a low metabolic activity of mature plant, calcium ions combine with carbonate or oxalate ions and then are condensed in a vacuolar part. Especially when harmful organic acid exists superfluously, calcium is taken in high concentration by a plant mostly due to the antidotal effect. The knowledge about elements needed for keeping the metabolism activity of plants put an interpretation on change of elemental concentrations in the fern leaf shown in Fig. 3. That is, arsenic is taken into cells in the fern leaf of an active metabolism requiring a lot of potassium, and it is transported mainly to a perimeter part of

low metabolism. In the grown-up leaf at which cell growth stopped, calcium is conveyed and utilized for detoxification of absorbed arsenic and conservation of a cell wall, but an excessive transported calcium is segregated in a part of venation and pinna of a fern.

Hydroponics of the fern in early stages of growth was carried out for one month on culture solutions which contained arsenate in the concentration of 25mg per liter and the nutritional elements except phosphorous. The in-air micro-PIXE analysis was carried out for a sliced vascular bundle of fern lamina in 50×50 μm^2 area (Fig. 5) and for a sliced mesophyll of fern pinna in 300×400 μm^2 area (Fig. 6). The distribution of essential elements such as K and Ca revealed that the vascular bundle of the fern was formed in many small cells of only a size of 10 to 20 μm. Arsenic was also distributed over the vascular bundle cells along with Mn, Fe, Cu and Zn added as a nutrient to the culture solution. These results suggest that arsenic, like other ingredients, is originally conveyed with water and passes through a conductive tissue of the fern pinna. The elemental mapping of a sliced mesophyll showed that arsenic and potassium were highly distributed over the front part of a pinna in the sun light and on the contrary sulfur and calcium were distributed over the back side of the leaf at rather high concentrations. It is probable that a high concentration of potassium is required to adjust the metabolism of cells in the mesophyll of pinna which actively uptakes arsenic unnecessary for vital activity of a leaf. On the other hand, it is considered that the high concentration of arsenic results in change to the function of a cell wall, and then calcium diffuses out from those cells. In the conductive tissue in a vascular bundle and the mesophyll cells of a pinna of the fern, arsenic is not condensed into a certain specific tissue, but is uniformly distributed over the cells in each tissue. Therefore, the specific organization which detoxifies arsenic does not exist in *P. vittata* fern, but arsenic is accumulated in the vacuole which accounts for a big volume fraction in a plant cell and then arsenic distribution becomes uniform in the tissue of fern fronds.

Conclusion

The centimeter-scale area mapping of elements using the in-air submilli-PIXE camera reveals elemental distribution of living fronds of *P. vittata* fern, and the maicometer-scale area mapping using the in-air micro-PIXE camera indicates the translocation of elements in living tissue of the fern. Hence, the in-air PIXE analysis is an effective measure for under- taking phytremediation research. Since *Pteris vittata* absorbs

a lot of arsenic into the fronds, it is most effective in arsenic phytoextraction to mow the fronds of well growth stage on a polluted soil. The perennial fern is repeatedly applicable to the decontamination of an arsenic polluted land and is effective irrespective of the valence state of arsenic. However, the rate of absorption of arsenate (pentavalent) from a polluted medium with sufficient concentration of phosphorus becomes slow compared with the rate of absorption of the arsenite (trivalent). The translocation of essential elements for plants like potassium and calcium occur in the fern fronds which absorbed a lot of arsenic, and then the vital activity of the fern is maintained. The tissue morphology of the fern fronds is also kept in satisfactory condition, and arsenic is distributed in the lamina cells of *P. vittata* ferns at all growth stages.

Refrences

1) Smith E., et al., Adv. Agron **64** (1998) 149.
2) Tu C., Ma Q.L., J. Environ. Qual. **31** (2002) 641.
3) Lombi E., et al., New Phytologist, **156** (2002) 195.
4) McGrath S.P., Zhao F.J., Lombi E., Advances in Agronomy, **75** (2002) 1.
5) Ma L.Q., et al., Nature, **409** (2001) 579.
6) Poynton C.Y., et al., Planta., **219** (2004) 1080.
7) Zhang W., et al., Sci. Total Environ., **300** (2002) 167.
8) Gumaelius L., et al., Plant Physiol., **136** (2004) 3198.
9) Matsuyama S., et al., International Journal of PIXE, **8** (1998) 209.
10) Matsuyama S., et al., International Journal of PIXE, **8** (1998) 203.
11) Inomata K., et al., International Journal of PIXE, **16** (2006) 149.
12) Ryan C.G., et al., Nucl. Instr. and Meth. **B188** (2002) 18.
13) Yamazaki H., et al., X-Ray spectrometry, **37** (2008) 184.

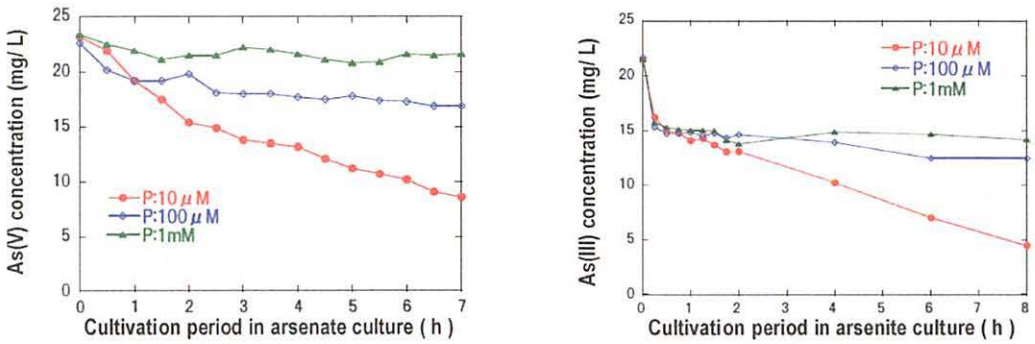

Figure 1. Influence of phosphate deficiency in cultivation on arsenic absorption rates by the fern.

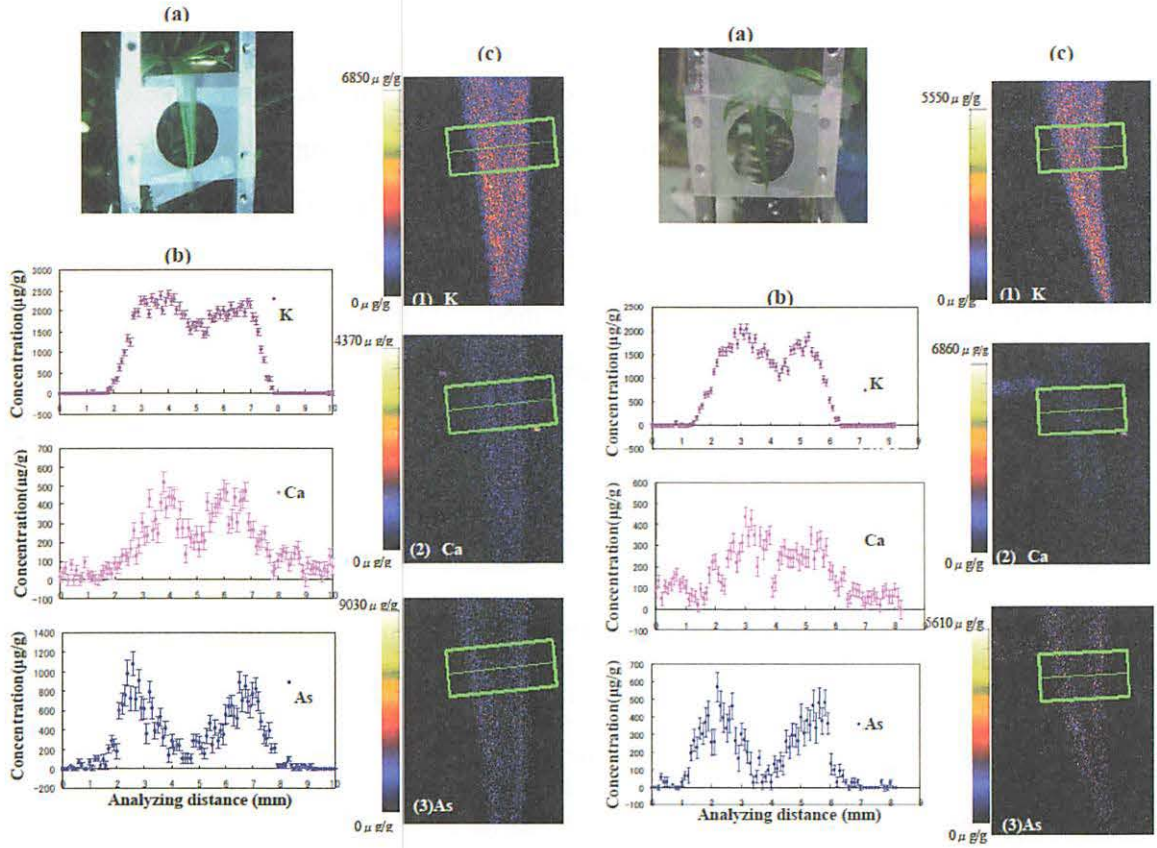

Figure 2-1 (left). Photograph (a), elemental concentration profiles (b) and maps (c) of an apex of *P. vittata* in an early active growth stage for five-day uptake of As(III) using hydropotonic culture solution with 1mM phosphate.

Figure 2-2 (right). Photograph (a), elemental concentration profiles (b) and maps (c) of an apex of *P. vittata* in an early active growth stage for five-day uptake of As(v) using hydropotonic culture solution with 1 mM phosphate.

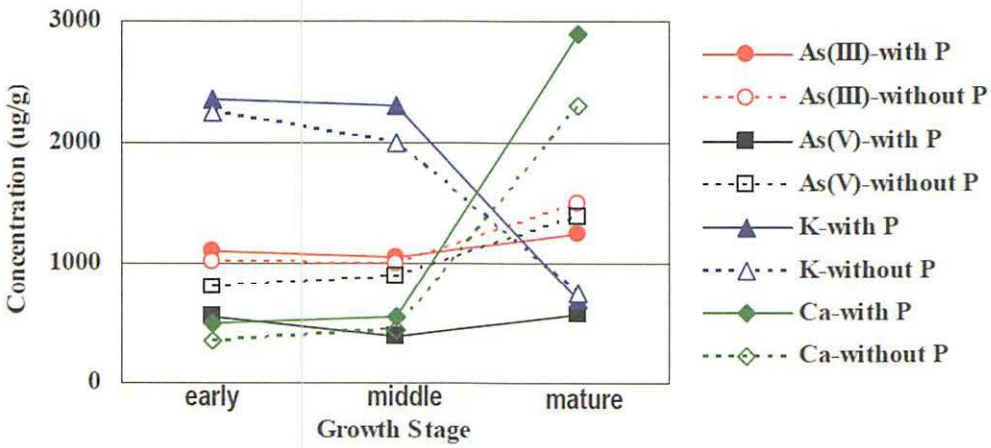

Figure3. Change in concentrations of K, Ca and $As^{III\ or\ V}$ at three different growth stages of apexes of *P. vittata* on hydroponic solutions with or without addition of 1 mM phosphorus nutrient.

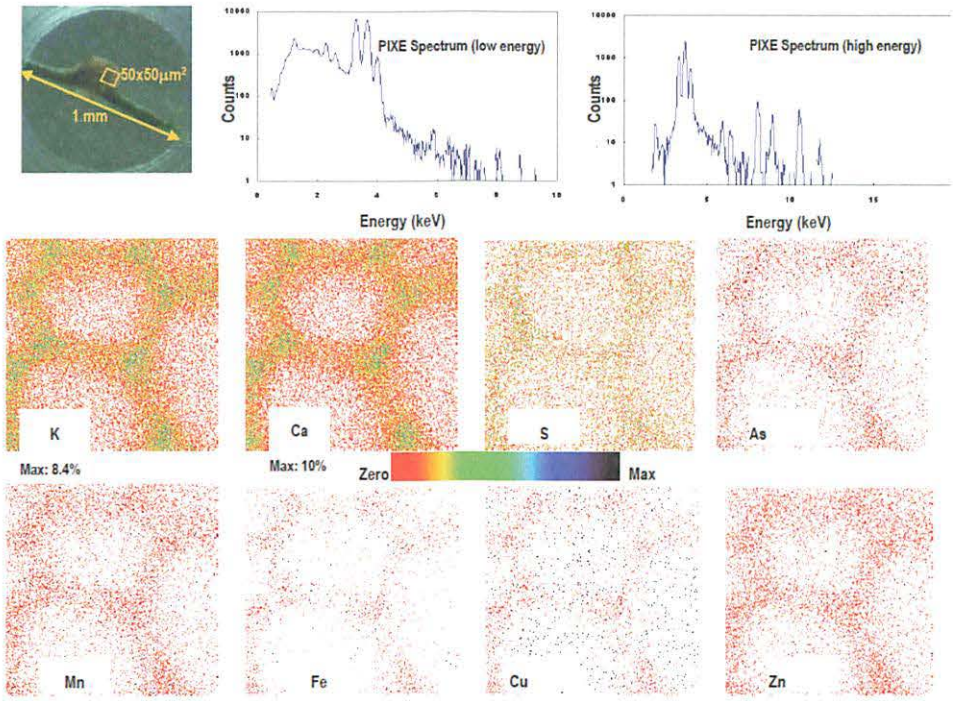

Figure 4. Photograph, PIXE spectra and elemental maps for a sliced vascular bundle of an apex of *P. vittata* under arsenate treatment.

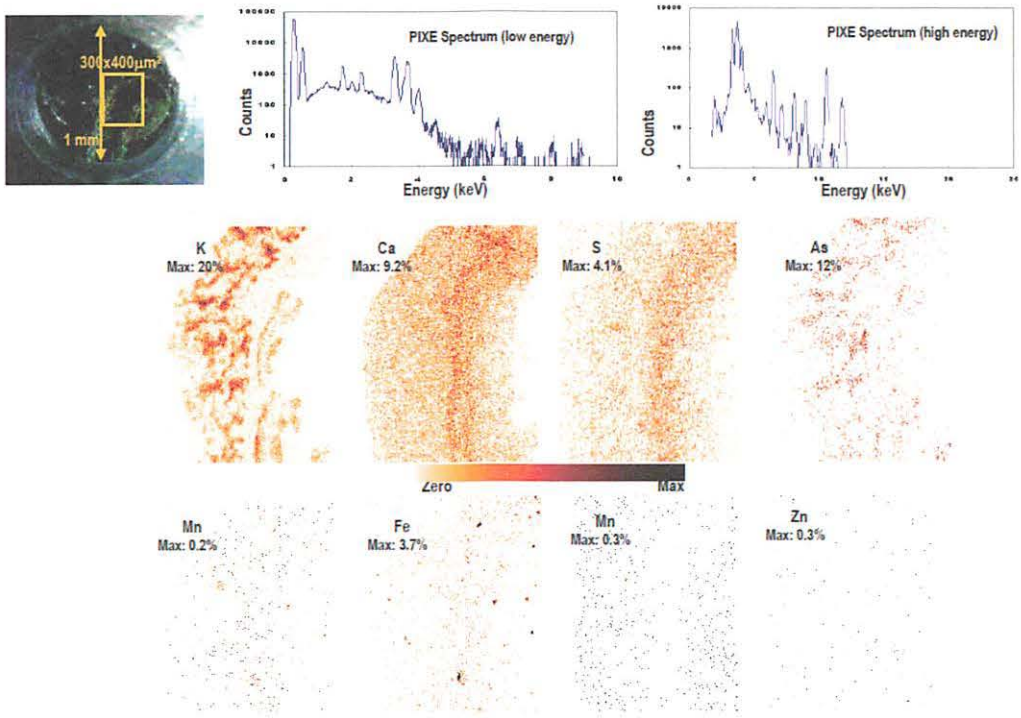

Figure 5. Photograph, PIXE spectra and elemental maps for a sliced mesophyll of an apex of *P. vittata* under arsenate treatment.

VI. RADIOCHEMISRTY AND NUCLEAR CHEMISTRY

VI. 1. Development of a Simplified MA Separation Process Using Novel R-BTP Adsorbents

Kuraoka E., Usuda S., Liu R., Xu Y., Yamazaki H., and Ishii K.

Cyclotron and Radioisotope Center, Tohoku University

Introduction

In recent years, many soft-donor ligands have been developed for liquid-liquid solvent extraction separation of minor actinides (MA: Am and Cm) and/or lanthanides (Ln) from fission products (FP) in the high level radioactive liquid waste (HLLW), which is generated by spent fuel reprocessing. Especially, a new type of nitrogen-donor ligand, R-BTP (BTP: 2,6-Bis-(5,6-Dialkyl-1,2,4-Triazine-3-yl)-Pyridine, R: alkyl group [C_nH_{2n+1}]), which was discovered by Kolarik *et al.*[1,2], shows high extraction selectivity for Am(III) over Ln(III) and is widely noticed because its constituent elements are C, H, O and N which are combustible after use up. Figure 1 shows the chemical structure of the R-BTP.

On the other hand, to overcome the demerits of solvent extraction method and to advantage the merits of R-BTP, another technology of extraction chromatography for separation of MA(III) has been proposed, which combines the selectivity of solvent extraction with the ease of operation of column chromatography. Kuraoka *et al.* have synthesized several R-BTP adsorbents with different alkyl groups for the extraction chromatography and investigated their fundamental properties such as adsorbability and stability[3-9].

In this work, *i)* novel R-BTP adsorbents (*i.e.* extraction resins) were prepared for developing a simplified MA direct separation process (see Fig. 2), then, *ii)* adsorption properties of typical FP elements including Ln(III) with HNO_3 solution onto the resin, and *iii)* chemical and thermal stabilities of the resins were examined.

Experimental

As the R-BTP adsorbents, *iso*hexyl-BTP [C=6] and *iso*heptyl-BTP [C=7]) extraction

resins were prepared by impregnating the R-BTP ligands into the porous silica/polymer composite support (SiO_2-P particles) with a mean diameter of 60 μm, according to the reported procedures[9].

For evaluating adsorption properties, distribution coefficient, K_d, was measured by batch experiment and calculated by the following equation:

$$K_d(\text{mL/g}) = (C_o\text{-}C_s)/C_s\_(V_s/W_R)$$
$$= (A_o\text{-}A_s)/A_s\_(V_s/W_R)$$

where $C_0(A_0)$ and $C_S(A_S)$ denote the element or nuclide concentration (activity) in the aqueous phase before and after adsorption, respectively. W_R indicates the weight of the dry extraction resin (g) and V_s the volume of the aqueous phase (mL).

The concentration of simulated FP (Cs, Sr, Zr, Mo, Pa, *etc.*) including Ln (La, Ce, Nd, Eu, Gd, Dy, Y, *etc.*) in solution was analyzed by ICP-AES (Inductively coupled plasma–atomic emission spectrometer). The radioactivity of ^{99}Tc was determined by liquid scintillation counter.

Physical and chemical properties and thermal stability were examined by use of electron microscope, FT-IR (Fourier transform infrared spectrophotometer), TG-DTA (Thermogravimetry-differential thermal analyzer), *etc.*

Results and Discussion

Figure 3 shows appearance by photograph and microscopic image of the prepared R-BTP extraction resins. The chemical structure of the both resins was verified by analyzing the R-BTP ligands, SiO_2-P particles and R-BTP resins with FT-IR, *etc.*

(1) Adsorption properties

The adsorption performance of the simulated FP from 0.1-4 M HNO_3 solution onto the *iso*hexyl-BTP resin at 25 and 50°C was evaluated by K_d. Elution of the adsorbed metal ions was also attempted with H_2O, dilute HNO_3 and complex agent solutions.

As an example, Fig. 4 shows the dependence of K_d on HNO_3 concentration by batch adsorption experiment at 50°C. The K_d of Dy(III), which is probably similar to the MA in adsorption behavior[10], was much higher than the other Ln in 2-4 M HNO_3. On the other hand, ^{99}Tc, Zr and Mo were adsorbed weekly and their behavior was complicated.

(2) Chemical and thermal stabilities

The chemical stability of the isohexyl-BTP resin was evaluated by observing the deterioration in adsorbability and by analyzing decomposed products after contacting with various concentrations of HNO_3 solution. It was found that the resin was stable in 0.1-5 M HNO_3 solutions by being washed with H_2O at the final stage of the performance.

The thermal stability of the both resins was checked by TG-DTA. Figure 5 shows weight loss of SiO_2-P support, *iso*hexyl- and *iso*heptyl-BTP resins. The weight loss of both resins started at 190°C and was over 550°C, being accompanied by decomposition of the resins at 190°C and 250°C and decomposition of the SiO_2-P support at 480-490°C.

Conclusions

With the aim of developing a simplified MA direct separation process, novel silica-based R-BTP resins were synthesized by impregnating *iso*hexyl- and *iso*heptyl-BTP extractants into the pores of SiO_2-P support. The fundamental properties such as adsorbability of FP including Ln(III) from HNO_3 solution onto *iso*hexyl-BTP resin and the chemical and thermal stabilities of the both resins were investigated. The MA(III) may be possibly separated from FP including Ln(III) because the K_d of Dy(III), similar to that of MA(III), was much higher than the other Ln in 2-4 M HNO_3 at 50°C. The isohexyl-BTP resin was stable in 0.1-5 M HNO_3 by being washed with H_2O.

This work has just started from October, 2008. More detailed adsorption and elution properties and hydrolytic and radiolytic stabilities will be examined.

Acknowledgments

This study is the result of "Development of a Simplified MA Separation Process Using Novel R-BTP Adsorbents" carried out under the Strategic Promotion Program for Basic Nuclear Research by the Ministry of Education, Culture, Sports, Science and Technology of Japan.

References

1) Kolarik Z. et al., Solv. Extr. Ion Exch., **17** (1999) 23,
2) Kolarik Z. et al., Solv. Extr. Ion Exch., **17** (1999) 1155.
3) Wei, Y.-Z. et al., Proceedings of 16th Pacific Basin Nuclear Conference (16PBNC), Aomori, Japan, Oct. 13-18, 2008, Paper ID P16P 1033.
4) Zhang A., et al., J. Radioanal. Nucl. Chem., **274** (2007) 455.
5) Hoshi H., et al., J. Alloys Comp., **408-412** (2006) 1274.
6) Wei, Y.-Z. et al., J. Alloys Comp., **374** (2004) 447.

7) Wei, Y.-Z. et al., J. Nucl. Sci. Technol., **Suppl. 3** (2002) 761.
8) Wei, Y.-Z. et al., J. Nucl. Sci. Technol., **37** (2000) 1108.
9) Wei, Y.-Z. et al., Nucl. Technol., **132** (2000) 413.
10) Geist A., et al., Solv. Extr. Ion Exch., **24** (2006) 463.

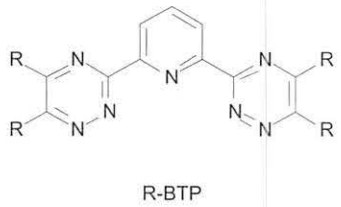

Figure 1. Chemical structure of R-BTP (**BTP**: 2,6-bis-(5,6-dialkyl-1,2,4-triazine-3-yl)-pyridine, **R**: alkyl group [C_nH_{2n+1}]).

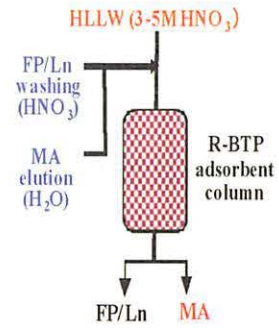

Figure 2. Simplified MA direct separation process by use of novel R-BTP extraction resin column (**MA**: Am, Cm, **Ln**: La, Nd, Eu, etc., **FP**: Cs, Zr, Mo, Tc, Ru, Rh, Ln, etc.).

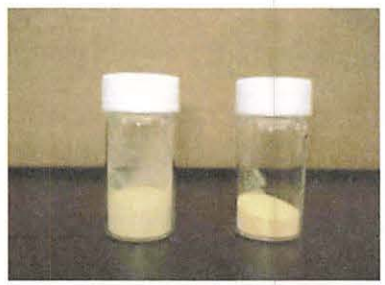

a) Photograph of the R-BTP resins in vials *iso*hexyl-BTP (left) and *iso*heptyl-BTP (right).

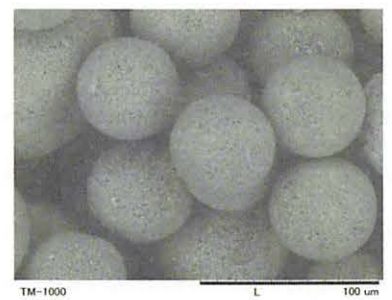

b) Microscopic image of *iso*heptyl-BTP resins (magnification: 800).

Figure 3. Appearance by a)photograph and b)microscopic image of the R-BTP extraction resins prepared by impregnating the R-BTP ligands into the porous SiO_2-P support.

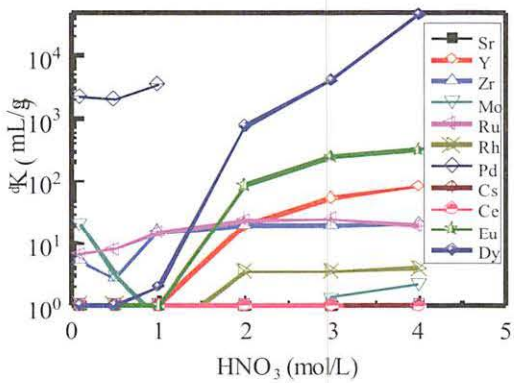

Figure 4. Dependence of HNO_3 concentration on K_d by batch adsorption experiment at 50 °C (Resin: *iso*hexyl-BTP/SiO_2-P, metal ions: 1 mmol/L, contact time: 3 h).

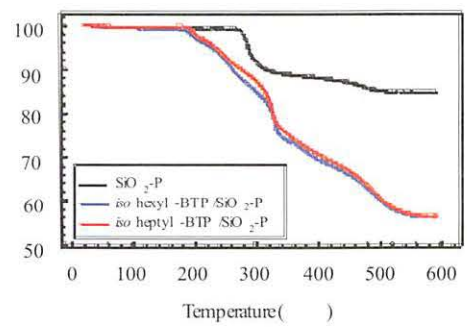

Figure 5. Weight loss of SiO_2-P support and R-BTP/SiO_2-P resins by TG-DTA.

VII. RADIOPHARMACEUTICAL CHEMISTRY AND BIOLOGY

VII. 1. Electrochemical Concentration of Aqueous [^{18}F]Fluoride into an Aprotic Solvent in a Disposable Microfluidic Cell

Saiki H.[1], Iwata R.[2], Wong R.[2], Furumoto S.[3], Ishikawa Y.[2], Nakanishi H.[1], and Ozeki E.[1]

[1]*Technology Research Laboratory, Shimadzu Corporation,*
[2]*Cyclotron and Radioisotope Center, Tohoku University*
[3]*Graduate School of Medicine, Tohoku University*

Microfluidic technology is an attractive strategy found viable in PET radiochemistry. As PET probes demand high specific activities, this technology is predicted to find wide applications in PET radiosynthesis due to the rapid and efficient nature of its reactions. Although several microreactor systems have been developed to date, these were merely proof-of-concept studies limited from the lack of interfacing techniques in introducing target products into a microreactor[1,2]. We present a novel and practical approach of transferring [^{18}F]fluoride from the target water into an aprotic solvent by means of electrochemical separation in a micro-flow cell.

The present method was developed based on the principle of electrochemical separation of nca [^{18}F]fluoride from [^{18}O]water[3,4]. A conceptual design of a disposable flow-cell with the aftermentioned method for electrochemical concentration of aqueous [^{18}F]fluoride is as illustrated in Fig. 1. The volume capacity of the utilized flow-cell is 16 μL (40 x 4.0 x 0.1 mm). Water (*ca.* 1.5 mL) containing no-carrier-added [^{18}F]fluoride was first flowed through the cell (0.1~1.0 mL/min) under a constant electric potential of 1 ~ 10 V applied between the Pt cathode and glassy carbon anode. The cell was then flushed with anhydrous CH_3CN (1.0 mL/min for 2 min) under the same electric potential. Voltage was then disconnected and an aprotic solvent (CH_3CN, DMSO or DMF) containing the K.222-$KHCO_3$ complex (ca. 40 mM) was introduced into the cell and left stagnant. This was followed by heating up of the cell to a preset temperature. Accordingly, a reversed electric potential (1 ~ 10 V) was applied and cell flow was allowed to resume. A radiation sensor was used to detect the released [^{18}F]fluoride, which was then either collected in a vial or sent to a subsequent chip to be used as a labeling agent. The above procedure was

fully automated using syringe pump modules (Hamilton PSD/3) as shown in Fig. 2.

The deposition of [^{18}F]fluoride within the cell clearly depended on the flow rate and the voltage. It was rapidly increased up to 80% between 1 and 4 V followed by a gradual increase to over 90% at 10 V (Fig. 3a), while linear decrease was observed with increasing the flow rate (Fig. 3b). The optimized parameters of 10 V and 0.7 mL/min gave 90% deposition within 3 min. Efficient release of [^{18}F]fluoride from the GC surface required heating at >80°C (Fig. 4a). With a reversed voltage of 2 V and a flow rate of 0.7 mL/min, more than 70% in the trapped [^{18}F]fluoride was recovered in ca. 60 within 2 min (Fig. 4b, Fig. 5). The variation of the overall recovery efficiency in successive use of the same chip was evaluated and it was decided to be usable up to several times without notable decrease in recovery efficiency (Fig. 6). The reactivity of [^{18}F]fluoride thus obtained was exemplified by radiosynthesis of [^{18}F]FDG. High [^{18}F]Fluorination yields of over 80% with mannose triflate were observed in short-time reactions of over 3 sec at 80°C.

In conclusion, the present microfluidic method demonstrated that aqueous [^{18}F]fluoride was electrochemically concentrated in 60 μL within 6 min. The recovered [^{18}F]fluoride showed high reactivity in the synthesis of [^{18}F]FDG in a microreactor.

References

1) Gillies J.M., Prenant C., Chimon G.N., Smethurst G.J., Perrie W., Hamblett I., Dekker B., Zweit J., Appl. Radiat. Isot. **64** (2006) 325.
2) Lee C-C., Sui G., Elizarov A., Shu C.J., Shin Y-S., Dooley A.N., Huang J., Daridon A., Wyatt P., Stout D., Kolb H.C., Witte O.N., Satyamurthy N., Heath J.R., Phelps M.E., Quake S.R., Tseng H-R., Science **310** (2005) 1793.
   L. Liu, CA. Huh, Earth and Planetary Sci. Lett. **180** (2000) 163.
3) Alexoff D., Schlyer D.J., Wolf A.P., Appl. Radiat. Isot. **40** (1989) 1.
4) Hamacher K., Hirschfelder T., Coenen H.H., Appl. Radiat. Isot. **56** (2002) 519.

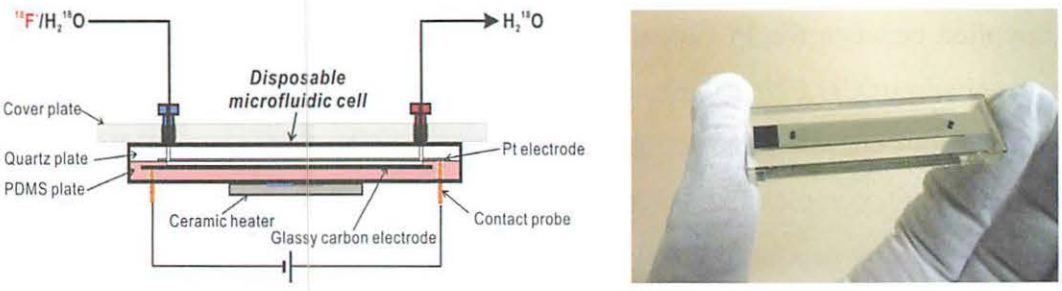

Figure 1. Disposable flow cell.

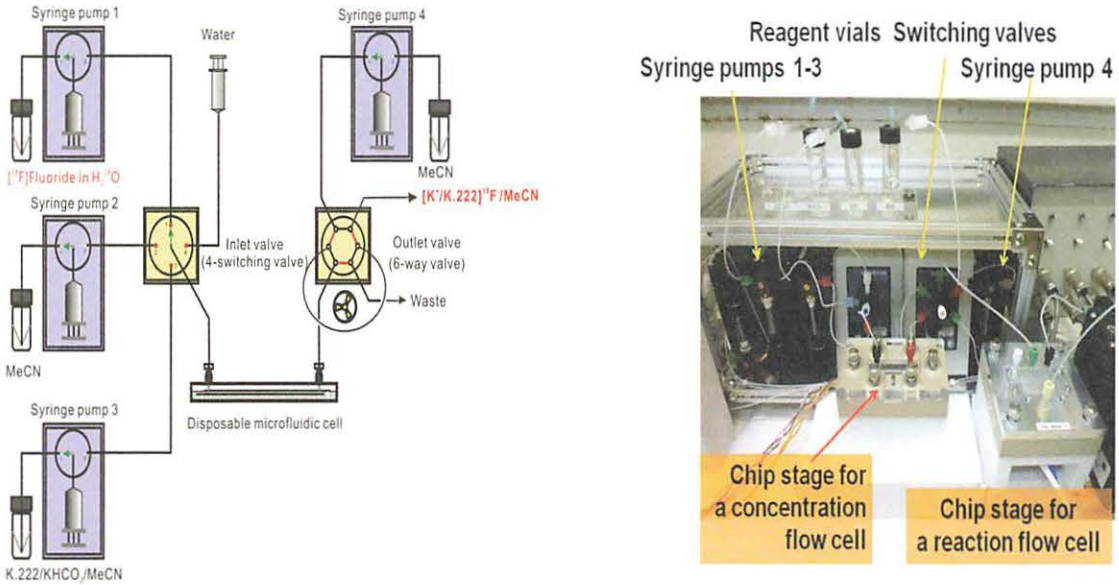

Figure 2. Automated module.

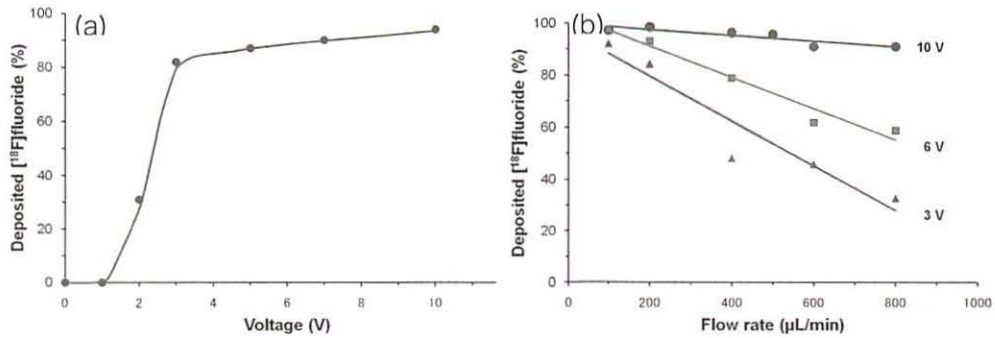

Figure 3. Dependences of the deposition of [^{18}F]fluoride on voltage (a) and flow rate (b).

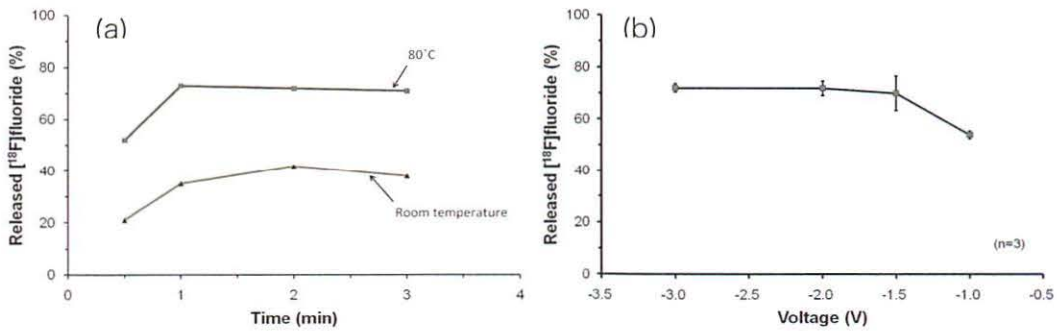

Figure 4. Dependences of the release of [^{18}F]fluoride on time (a) and voltage (b).

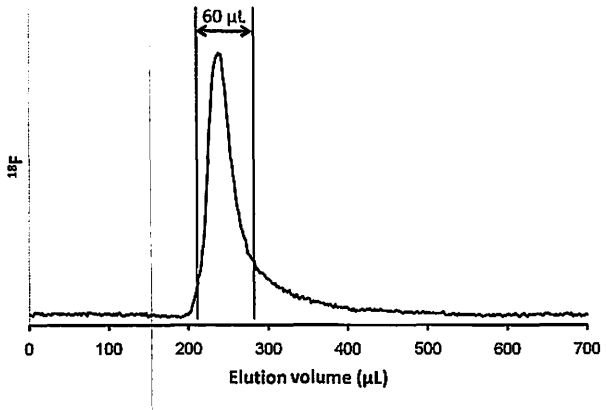

Figure 5. Elution profile of [^{18}F]fluoride.

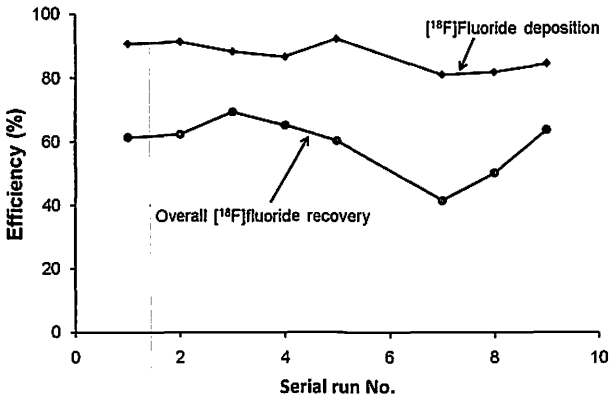

Figure 6. Variation in the recovery yield of [^{18}F]fluoride in successive use.

VII. 2. Radiosynthesis of [^{124}I]Iomazenil and Imaging of Rat Brain by Means of Semiconductor High Resolution Animal PET Scanner

Kanai Y.[1], Yamazaki H.[2], Funaki Y.[2], Matsuyama S.[3], Kikuchi Y.[3], Sakamaki M.[3], Shimosegawa E.[1], Ishii K.[2,3], and Hatazawa J.[1]

[1]*Department of Nuclear Medicine and Tracer Kinetics, Osaka University Graduate School of Medicine*
[2]*Cyclotron and Radioisotope Center, Tohoku University*
[3]*Department of Quantum Science and Energy Engineering, Graduate School of Engineering, Tohoku University*

Introduction

Iodine-124 (^{124}I) is one of the long-lived positron-emitting nuclides which have lately been interested. It has a long physical half-life (4.15 days) in comparison with the other positron-emitting nuclides (^{18}F, ^{11}C, ^{13}N and ^{15}O) conventionally used for clinical PET studies. It is a potential substitute for ^{125}I- or ^{123}I-labeled biologically functional compounds. Moreover, ^{124}I is suitable for labeling large molecules for functional imaging such as proteins, peptides, nucleic acids, and glycoproteins. Using ^{124}I, some researches in oncology have been carried out[1], but there are few studies in neurology because of a disadvantage for PET imaging with ^{124}I. Its low positron abundance (only 22.9% of the disintegration), and prompt γ-rays were anticipated to degrade the image resolution and to increase the noise.

Recently, Ishii et al. developed an ultra high resolution semiconductor PET (Fine-PET)[2]. The trans-axial resolution (full width at half maximum:FWHM) of this PET scanner is less than 1 mm. To perform the rat brain receptor imaging with ^{124}I using this scanner, we chose iomazenil (IMZ) as a ^{124}I labeling compound, because it was used as a clinical tracer for central benzodiazepine receptor imaging.

In this study, we evaluated the feasibility of ^{124}I as a potential nuclide for neurological PET studies by imaging rat brain using the ultra-high resolution semiconductor animal PET.

Materials and Method

^{124}I production

Production of ^{124}I was carried out as described in our previous paper[3]. Briefly, It was produced by the $^{124}Te(p,n)^{124}I$ reaction. The target was $^{124}TeO_2$/6 wt% Al_2O_3 solid solution and it was bombarded with 14 MeV proton beams.

Radiolabeling of IMZ with ^{125}I

We selected iododestannylation reaction with the corresponding tributylstannyl precursor for radiolabeling iomazenil (Scheme 1). Aqueous hydrogen peroxide was added to a mixture of precursor in methanol (1 mg/ml, 0.3 ml), diluted HCl, and 0.1 M NaOH solution of ^{125}I in a sealed vial. The reaction was allowed to proceed for 20 min at room temperature, after which it was terminated by the addition of sodium thiosulfite. After the reaction, radiochemical yield was determined by thin-layer chromatography (TLC). Normal phase TLC plate (Silica gel F_{254}) with an eluent of ethyl acetate/ acetone/ ammonia solution (90 vol%/10 vol%/1 vol%) was used. A 2 μL portion of reaction mixture was spotted 2 cm from the bottom of normal phase TLC plate. After developing 15cm from the spotting position, the TLC plate was contacted to the BAS-SR2025 imaging plate (Fuji Photo Film Co. Ltd.) and exposed for 10 minutes. The intensities on the imaging plate were calculated with the image analysis system (BAS-2000, Fuji Photo Film Co. Ltd., Tokyo, Japan).

[^{124}I]IMZ radiolabeling

[^{124}I]IMZ was radio-synthesized under the best conditions obtained from the results of [^{125}I]IMZ radiosynthesis (Scheme 1). The radiochemical yield of [^{124}I]IMZ was calculated from the $Na^{124}I$ radioactivity added in the reaction vial and [^{124}I]IMZ radioactivity.

PET imaging of [^{124}I] IMZ using ultra high resolution semiconductor PET scanner

[^{124}I]IMZ (97 MBq) was administered from tail vein of male rat (250 g, 8-week old) under the ketamine and xylazine anesthesia. The scan was commenced from 1 hour after tracer injection with Fine-PET[2].

All data were acquired using a Fine-PET in three-dimensional mode (pixel size, 0.6×0.6×0.6 mm) and reconstructed by the method of FORE + ML-EM (30 iterations).

Data acquisition time was 1-2 hours.

Result & Discussion

Radiolabeling condition of IMZ with ^{125}I and Radiosynthesis of [^{124}I]IMZ

To confirm whether the radiochemical yield of IMZ with radioiodine would be sensitive for HCl and hydrogen peroxide concentration, ^{125}I was used for radio-synthesis of IMZ instead of ^{124}I. The radiochemical yield of [^{125}I]IMZ with iododestannylation reaction was strongly affected by the concentration of hydrochloric acid. HCl concentration ranging from 0.5 to 5 mol/L resulted in good radiochemical yield. The radiochemical yields were 2.5 ± 2.7, 9.2 ± 3.6, 49.8 ± 18.4, 75.7 ± 5.6, 46.8 ± 23.2 and 1.7 ± 1.6%, when we used HCl of 0.01, 0.1, 0.5, 1.0, 5.0 and 10.0 mol/L respectively (Fig. 1). Radiochemical yield of [^{125}I]IMZ was also affected by the concentration of hydrogen peroxide. When we used 30% or 3% of hydrogen peroxide for reaction, radiochemical yield was higher than that of 0.3%. The radiochemical yields were 6.98 ± 2.5, 63.75 ± 10.1 and 75.7 ± 5.6%, when we used 0.3, 3 and 30% of hydrogen peroxide respectively (Fig. 2). The differences in yield may be affected by pH of the reaction solution. Therefore, it may be considered that hydrogen peroxide needs suitable pH as an oxidizing agent. However, high HCl concentration (over the 5.0 M) caused low yield. For this reason, it may be suggested that iodine was oxidized to I_2 and became an inactive form. When a chrolamine-T was used as an oxidizing agent, a similar chemical tendency was observed (data is not shown). From these results, the conditions of 1 M HCl and 30% of hydrogen peroxide were used for radio-synthesis of [^{124}I]IMZ. The radiochemical yield of [^{124}I]IMZ was 73% and radiochemical purity was over 98%. This yield of [^{124}I]IMZ was almost the same as that of [^{125}I]IMZ. Consequently, it may be suggested that ^{124}I labeled compounds were synthesized with the same methods of ^{125}I labeled compound such as proteins, peptides, nucleic acids, and glycoproteins in similar radiochemical yield.

PET imaging of [^{124}I]IMZ using ultra high resolution semiconductor PET scanner

The PET images with ^{124}I are suitable for tumor detection but not for brain because low positron abundance (only 22.9% of the disintegration) and high positron energy (maximum energy was 2.135 MeV) of ^{124}I could not visualize brain structures. Using Fine-PET, however, the [^{124}I]IMZ radioactivity was observed in the cerebral cortices of the rat brain and the [^{124}I]IMZ accumulations of the white matter, basal ganglia, and cerebellum

were lower than those of cerebral cortices. The autoradiogram of [^{124}I]IMZ proved the PET image (Fig. 3). As a result, it could become clear that even when ^{124}I is used, the PET image of the brain was obtained using the ultra high resolution semiconductor PET (Fine-PET). This finding could facilitate the use of ^{124}I-labeled compounds for *in vivo* brain PET imaging.

In conclusion, we synthesized [^{124}I]IMZ in good radiochemical yield with the same method of ^{125}I, and [^{124}I]IMZ imaging of rat brain was obtained using the ultra high resolution semiconductor PET. It may be considered that this result expands the possibility to the use of ^{124}I.

References

1) Pal A, et al. Mol Imaging Biol., **5** (2006), 262.
2) Ishii K, et al. Nucl. Inst. and Methd. in Physics Research A., **576** (2007), 435.
3) Yamazaki H., Funaki Y., Horiuchi Y., et al., CYRIC Annual Report 2006.

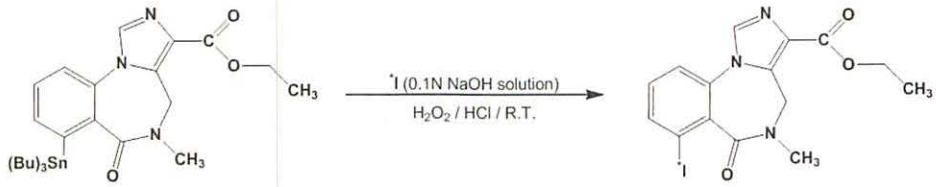

Scheme 1. Radiolabeling scheme of iomazenil.

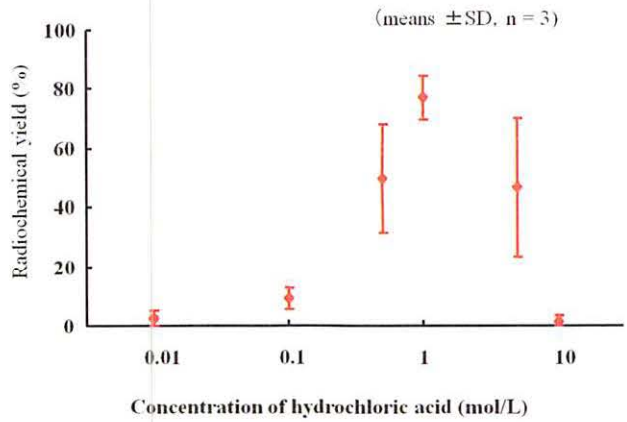

Figure 1. The relationship of radiochemical yield of [^{125}I]iomazenil and hydrochloric acid concentration.

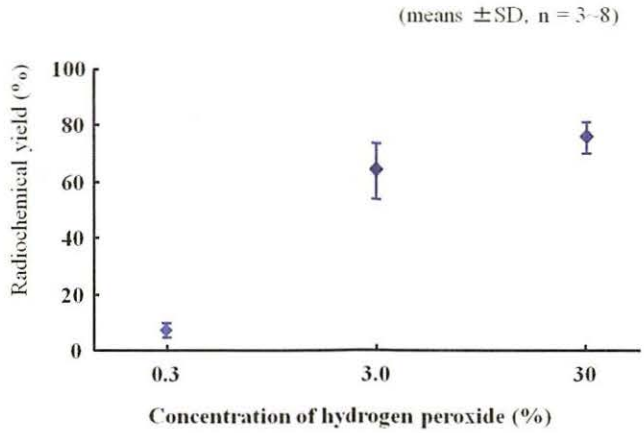

Figure 2. The relationship of radiochemical yield of [^{125}I]iomazenil and hydrochloric acid concentration.

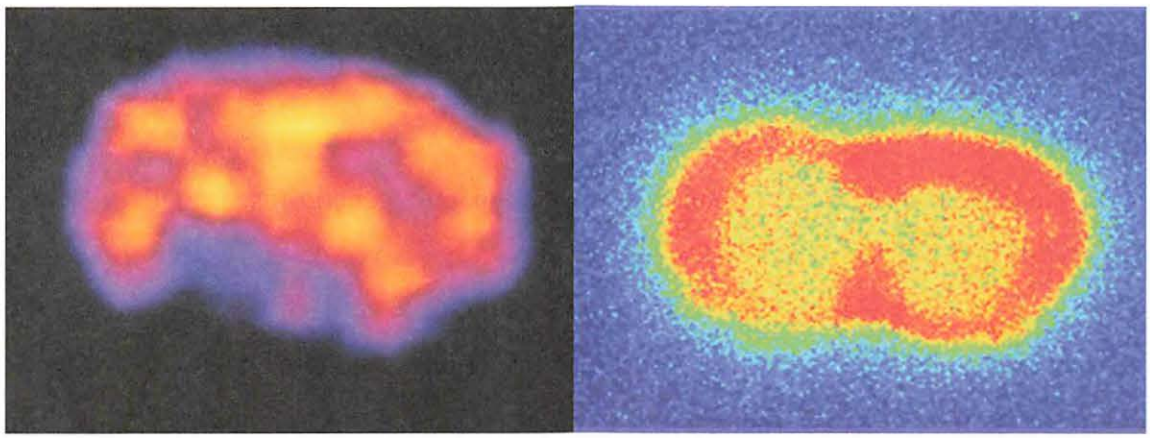

Figure 3. PET image (left) and ARG image (right) of rat brain with ^{124}I-IMZ PET scanner : Ultra-High Resolution Semiconductor PET [CdTe detector: 1.1 mm×1.0 mm×5 mm, FOV: 64 mm in diameter, 26 mm in axis] Animal : Rat (wistar male, 8 weeks, 187 g), Injection dose: 97 MBq (i.v.). Data acquisition: 1 hours (1-2 hours after injection).

VII. 3. Delivery of Na/I Symporter Gene into Skeletal Muscle by Using Nanobubbles and Ultrasound: Visualization of Gene Expression with PET

Watanabe Y.[1], Horie S.[1], Funaki Y.[2], Kikuchi Y.[3], Yamazaki H.[2], Ishii K.[2,3], Vassaux G.[4,5], Mori S.[6], and Kodama T.[1]

[1]*Graduate School of Biomedical Engineering, Tohoku University*
[2]*Cyclotron and Radioisotope Center, Tohoku University*
[3]*Department of Quantum Science and Energy Engineering, Graduate School of Engineering*
[4]*INSERM U948, Nantes, France*
[5]*Institut des Maladies de l'Appareil Digestif, CHU Hôtel Dieu, Nantes, France*
[6]*Tohoku University Hospital*

Introduction

Gene therapy has been applied to many types of genetic disease such as cancer, muscular dystrophy, and vascular disease. Although virus vectors have been used in gene therapy, various side effects and lower tissue specificity have been reported. Thus, non-virus methods are required to be developed to reduce immunogenicity. In addition, clinical endpoints of gene therapy have to be indicated by monitoring the location, magnitude, and kinetics of transgene and by guiding improvements in the design of efficient formulations in patients[1].

The molecular delivery method using nanobubble (NB) and ultrasound (US) is one of non-virus methods. This method is non-invasive and tissue-specific. In the previous study, we demonstrated that the method using US/NB could be used as a potential molecular delivery method for gene therapy[2].

Fluorescent and luminescent imaging methods have been used as monitoring of gene expression for animal models. These methods are easy to use; however, they are hardly applied to deep tissues and to clinical trials. Thus it is required to develop human reporter genes for monitoring gene expression to indicate clinical endpoints. The Na/I symporter (NIS) gene are known as radionuclide human reporter genes. It is able to inhibit immune response compared to other reporter genes due to endogenously expression, and accumulates radioiodide because it is a mediator of I^- transport into the cells. The ^{124}I is

one of radiotracers with a longer half-life (4.2 days) comparing to other positron emitting radionuclide. PET is probably the only noninvasive imaging method that currently can be applied in humans for monitoring of gene expression. Recently, Ishii et. al.[3] have developed a practical semiconductor animal PET with CdTe detector (Fine-PET). The Fine-PET achieves a high spatial resolution of less than 1mm FWHM.

In the present study, we delivered the human NIS gene into the skeletal muscle of three types of mice by the US/NB method, and visualized hNIS gene expression using ^{124}I and the Fine-PET. We demonstrated the methodology could be applicable to human gene therapy.

Materials and Methods

Animal studies were performed in accordance with the ethical guidelines approved by Tohoku University. Three types of mice were used; BALB/c (6-8 weeks, 21-25 g), McH/lpr-RA1 mice (16 weeks, 32-34 g) showing vascular disease[4], and C57BL/10-mdx Jic mice (5 weeks, 14-15 g) showing muscular dystrophy. Two types of plasmid DNA were used: the luciferase reporter vector, pGL3, which expresses luciferase, and the phNIS vector in which expresses human NIS[5]. Acoustic liposomes (ALs) were lipid-based perfluoropropane (C_3F_8) filled bubbles (size: 198 ± 30 nm (n = 3), zeta potential: –4.1 ± 0.85 mV (n = 3)). ^{124}I was produced by the $^{124}Te(p, n)^{124}I$ reaction, using irradiation of a $^{124}TeO_2$ target with 14 MeV protons of a 1-4 μA beam current depending on the target production yield of ^{124}I[6]. Ultrasound exposure conditions were the intensity was 3.0 W/cm^2; the duty cycle, 20%; the number of pulses, 200; the PRF, 1000 Hz; and the exposure time, 60 s[7]. In order to confirm that hNIS gene was definitely expressed in the tibialis anterior (TA) muscle by the US/NB method, phNIS and pGL3 were cotransfected into the TA muscle. Luciferase activity was measured with *in vivo* imaging system. For the biodistribution, the left TA muscle of BALB/c (n = 14) was cotransfected with pGL3 and phNIS by the US/NB method. Mice were i.v. injected with 370 kBq of $Na^{124}I$ (theoretical specific activity, 8.78 TBq/μmol) dissolved in 100 μL of PBS, and scarified after 30, 60, and 180 min. Immediately after scarification, organs of mice were removed. The radioactivity of each sample was measured by a γ-counter, expressed as the percentage of the injected dose per gram (%ID/g). For the blocking study, cotransfected mice were divided into two groups. One group was i.v. injected with $Na^{124}I$ (1.85 MBq), scarified two hours later. The other was i.p. injected with NaI (57 mM), whose concentration was one fifth of LD_{50}. After 15 min, $Na^{124}I$ (1.85 MBq) was i.v. injected, and the TA muscle

was removed from both groups for autoradiography (ARG) images. For the PET imaging study, two mice were selected from each 3 types of mice. The mouse was i.v. injected with $Na^{124}I$ (74 MBq). Data were acquired in list mode format and binned into 0.6 mm sinograms for image reconstruction. PET images of three types of mice were summed 30-150 min. All measurements are expressed as mean ± S.E.M. (standard error of the mean). An overall difference between the groups was determined by one-way analysis of variance (one-way ANOVA). Simple comparisons of the mean and S.E.M. of the data were performed using Student's *t*-test. The differences were considered to be significant at $P < 0.05$.

Results

In the previous study, we found that a peak of gene expression in muscle of a mouse was 4 days after transfection (data not shown). To obtain guaranteed PET images, we cotransfected the TA muscle with pGL3 and phNIS, selected mice which showed enhanced luciferase activity on day 3, and captured their PET images on day 4 after transfection.

For most tissues, the uptake of the ^{124}I reached its maximum value at 60 min, and decreased at 180 min (Fig. 1). The TA where transfected NIS showed significant uptake of the radioactive tracer at 60 min ($P < 0.05$) and 180 min ($P < 0.01$), were compared to the control TA (saline injection alone). To confirm that ^{124}I actually entered the TA muscle due to the expression of NIS, we blocked the uptake of ^{124}I into the TA muscle by injecting NaI. Figure 2 shows ARG images (A) without and (B) with injection of NaI. The uptake of the radioactive tracer by the TA muscle was indeed blocked by the injection of NaI.

Figure 3 shows bioluminescence, PET and ARG imaging of three types of mice. L is the left TA muscle that was cotransfected with pGL3 and phNIS, and R is the right TA muscle that was injected with saline, as a negative control. Gene expression was shown the same tendency in all mice. All mice were showed same results. Bioluminescence was specifically located at the left TA muscle. The uptake of ^{124}I in the left TA muscle by NIS was clearly detected in PET imaging compared to that of right TA muscle. The ^{124}I uptake was confirmed with ARG which shows the same tendency as PET.

Discussion

We cotransfected pGL3 and phNIS into the TA muscle using the US/NB method to ensure the hNIS gene expression with the Fine-PET. At day 3 after cotransfection, one

mouse showing an average luciferase activity was selected for each experimental condition. At day 4, the hNIS gene expression in the TA muscle of the selected mice was visualized using the Fine-PET (Fig. 3) successfully.

For biodistribution studies, activity was analyzed in the major organs 30, 60, and 180 min after ^{124}I i.v. injection (Fig. 1). The thyroid gland and stomach have the underlying NIS gene, and the bladder drains iodide. At 60 and 180 min after ^{124}I injection, the TA muscles transfected with the hNIS gene showed accumulation values doubled compared to the control TA. In addition, the uptake of ^{124}I was blocked by i.p. injecting of NaI, indicating that hNIS was actually transfected in the TA muscle (Fig. 2). These results showed that the hNIS gene was transfected to the TA muscle by the US/NB method and the accumulation of ^{124}I was due to its expression.

The intravenous injected activity (74 MBq) of ^{124}I in this study is similar to that of a clinical study[8]. It is the necessary activity to visualize the NIS gene expression. However, with the activity, acute radiation injury from internal exposure is not avoidable in longitudinal studies. In fact, mice injected with ^{124}I (111 MBq) died 1.5 h after the injection (data not shown). Therefore, it is necessary to reduce the injected dose. There are some strategies to reduce injected dose of ^{124}I including 1) development of a new plasmid with a high gene expression efficiency and 2) development of a transfection method to improve the efficiency using NB/US. In addition, improvement of advanced CdTe detectors that can block complex decay scheme of ^{124}I, resulting in a better PET picture quality, is also an option to reduce the injected dose.

Conclusion

This study provides a new method consisting in non-invasive gene delivery system using the NB/US-hNIS/PET system (to indicate clinical endpoints) for genetic disorders (i.e. vascular disease and muscular dystrophy). These results suggest that the system can be used in clinical studies. In this perspective, we are developing a new plasmid DNA combining therapeutic gene and hNIS gene for visualization of therapeutic effect, and improving the NB/US-hNIS/PET system for advancement of transfection and expression effect.

References

1) Vassaux G., Groot-Wassink T., J Biomed Biotechnol, (2003) 92.
2) Aoi A., Watanabe Y., Mori S., Takahashi M., Vassaux G., Kodama T., Ultrasound in Medicine and Biology, **34** (2008) 425.
3) Ishii K., Kikuchi Y., Matsuyama S., Kanai Y., Kotani K., Ito T., Yamazaki H., Funaki Y., Iwata R., Itoh M., Yanai K., Hatazawa J., Itoh N., Tanizaki N., Amano D., Yamada M., Yamaguchi T., Nuclear Instruments and Methods in Physics Research Section A: Accelerators, Spectrometers, Detectors and Associated Equipment, **576** (2007) 435.
4) Mori S., Tanda N., Ito M.R., Oishi H., Tsubaki T., Komori H., Zhang M.C., Ono M., Nishimura M., Nose M., Pathology International, **58** (2008) 407.
5) Groot-Wassink T., Aboagye E.O., Glaser M., Lemoine N.R., Vassaux G., Hum Gene Ther, **13** (2002) 1723.
6) Yamazaki H., Funaki Y., Horiuchi Y., Ishii K., Kanai Y., Kikuchi Y., Matsuyama S., CYRIC ANNUAL Report, (2006) 90.
7) Watanabe Y., Aoi A., Horie S., Tomita N., Mori S., Morikawa H., Matsumura Y., Vassaux G., Kodama T., Cancer Sci, **99** (2008) 2525.
8) Phan H.T., Jager P.L., Paans A.M., Plukker J.T., Sturkenboom M.G., Sluiter W.J., Wolffenbuttel B.H., Dierckx R.A., Links T.P., Eur J Nucl Med Mol Imaging, **35** (2008) 958.

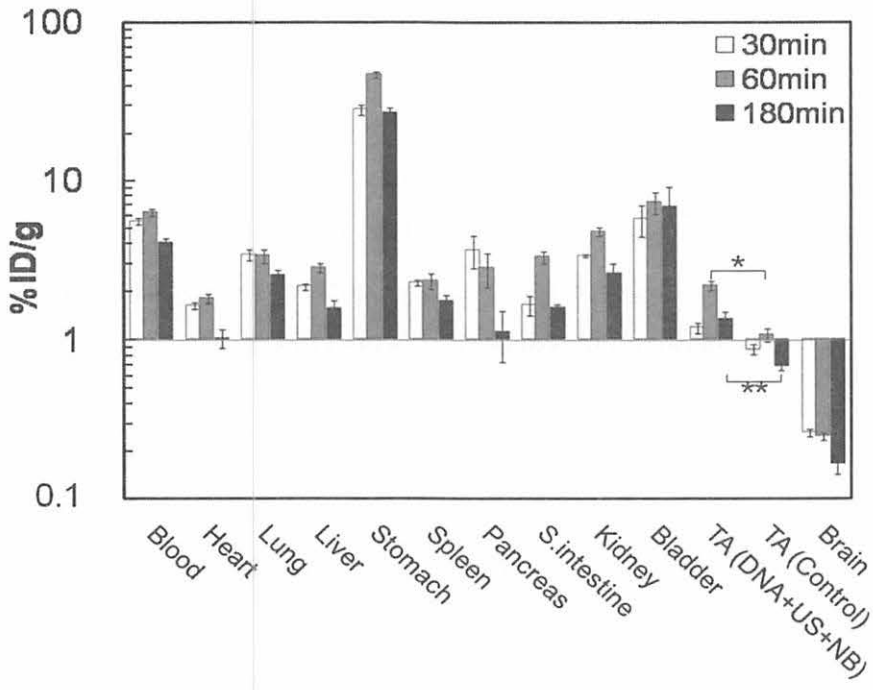

Figure 1. Biodistribution of ^{124}I into TA muscle.
The radioactivity of tissues was expressed as the percentage of the injected dose per gram (%ID/g). The bars represent mean ± S.E.M. $P < 0.01$ (**) and $P < 0.05$ (*).

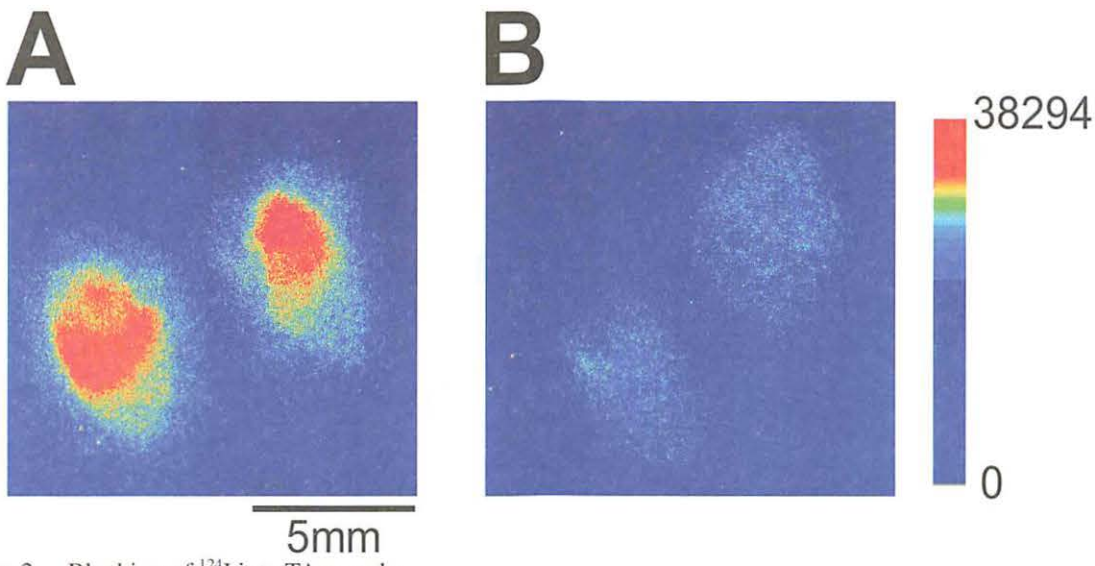

Figure 2. Blocking of ^{124}I into TA muscle.

(A) One group was i.v. injected with $Na^{124}I$ (1.85 MBq), scarified two hours later. (B) The other was i.p. injected with NaI (57 mM). After 15 min, $Na^{124}I$ (1.85 MBq) was i.v. injected, and the group was scarified two hours later.

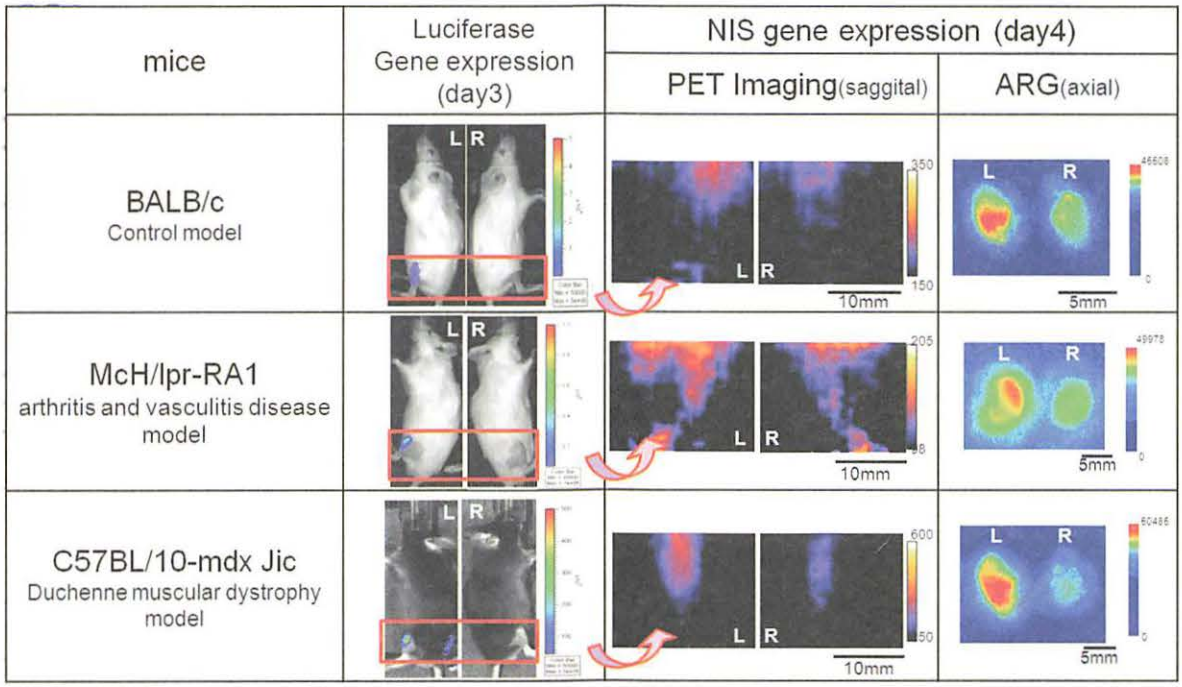

Figure 3. Bioluminescence, PET and ARG images.

VIII. NUCLEAR MEDICINE

VIII. 1. Increased Histamine H1 Receptor Ooccupancy Following Treatment with an Exceeded Dose of Cetirizine Hydrochloride, a Mildly-sedative Antihistamine

Tashiro M.[1], Kato M.[2], Miyake M.[1], Watanuki S.[1], Funaki Y.[3], Ishikawa Y.[3], Iwata R.[3], and Yanai K.[2]

[1]Division of Cyclotron Nuclear Medicine, Cyclotron and Radioisotope Center, Tohoku University,
[2]Department of Pharmacology, Tohoku University School of Medicine,
[3]Division of Radiopharmaceutical Chemistry, Cyclotron and Radioisotope Center, Tohoku University,

Introduction

Antihistamines are often used for the treatment of allergic disorders such as seasonal rhinitis. Antihistamines act mainly on the peripheral tissues but can also induce sedation as a central side effect. This undesirable side effect is caused by blockade of nerve transmission in the histaminergic neuronal system. First-generation (sedative) antihistamines that can easily penetrate the blood-brain barrier (BBB), such as d-chlorpheniramine and hydroxyzine, tend to occupy a large proportion of post-synaptic histamine H1 receptors (H1Rs) (more than 50%)[1,2]. Mildly-sedative antihistamines, such as cetirizine and terfenadine, slightly penetrate the BBB and mildly occupy H1Rs in the brain (usually not more than 20%), and they tend to induce slight sedation at low or recommended doses, but cause dose-related cognitive impairment at higher doses. Non-sedative antihistamines (e.g., fexofenadine) can hardly penetrate the BBB and sparingly occupy H1Rs. Since they do not penetrate the BBB easily, they induce no sedation even at exceeded doses[3]. We previously demonstrated the difference in BBB permeability between mildly-sedative and non-sedative antihistamines using positron emission tomography (PET) and [^{11}C]doxepin following oral administration of double doses of cetirizine (20 mg) and fexofenadine (120 mg)[4]. Thus, variation in cerebral H1R occupancy (H1RO) of antihistamines can be evaluated in terms of "BBB permeability" using PET and [^{11}C]doxepin.

Materials and Methods

Fifteen male Japanese volunteers (age range, 20-35 years), recruited through an advertisement as study subjects, were provided with a clear description of the study, and their written informed consents were obtained. This study was conducted after getting permission from the ethic committee of Tohoku University Graduate School of Medicine and University hospital. All the subjects were in good health with no clinical history of major physical or mental illnesses, and were also not receiving any concomitant medication likely to interfere with the study results. There were no abusers of alcohol, caffeine or nicotine. Alcohol, nicotine, caffeine, grapefruit and grapefruit juice were forbidden during the study period, and food intake was controlled on the test day and the day before PET measurement. The volunteers were requested to finish a light meal at least 3 hours before the start of the study.

Out of the 15 subjects, each of 5 subjects was administered cetirizine at 10 mg (CET10 group: mean age +/- S.D.= 21.6 +/- 1.5 y.o.), cetirizine at 20 mg (CET20 group: mean age +/- S.D.= 23.2 +/- 1.1 y.o.), and hydroxyzine at 30 mg (HYD group: mean age +/- S.D.= 23.2 +/- 0.8 y.o.). Each subject underwent PET measurements after single oral administration of one of the above antihistamines or placebo (i.e., lactobacteria preparation, 6 mg), with minimum washout intervals of 7 days between treatments. Active and placebo conditions were cross-randomized in the present study.

Shortly before [^{11}C]doxepin injection, the subjects were positioned on the coach of the PET scanner so that the transaxial slices were parallel to the orbitomeatal line. Following transmission scan using the ^{68}Ge/^{68}Ga line source for tissue attenuation correction, the subjects were then scanned to detect emission of high-energy photons (511 keV). After tissue attenuation correction and reconstruction with a filtered back-projection algorithm, the brain images were processed by applying graphical analysis to obtain binding potential (BP) images using the time–activity curve in the cerebellum based on region of interest (ROI) analysis[5]. His method was previously validated and described in detail[6]. Finally, H1RO was calculated based on the BP values of the frontal cortex and cingulate gyrus, where the H1R density was the highest and the most suitable for H1RO calculation. The H1ROs of antihistamines were calculated based on the following equation: H1RO = [(BP with placebo – BP with given antihistamine) / BP with placebo] × 100.

Results

BP values in H1R-rich regions such as the frontal and cingulate cortices were evaluated based on ROI analysis (Table 1 and Fig. 1). BP values following treatment with cetirizine 10 mg were only slightly lower than that following placebo treatment in the same subjects. However, BP values following treatment with hydroxyzine 30 mg were considerably low compared with those following placebo treatments. BP values after treatment with cetirizine 20 mg were between those following treatments with cetirizine 10 mg and hydroxyzine 30 mg (Table 1). H1ROs following treatment with cetirizine (10 mg and 20 mg) and hydroxyzine (30 mg) were also calculated using the BP following antihistamine treatment in each subject and utilizing the BP data following placebo treatment in each subject as baseline (0%) (Table 1 and Fig. 1). The mean H1ROs of the frontal and cingulate cortices following treatment with cetirizine 10 mg were 11.6% and 13.6%, respectively (average, 12.6%). Those following treatment with cetirizine 20 mg were 25.5% and 24.8%, respectively (average, 25.2%). Those following treatment with hydroxyzine 30 mg were 64.4% and 70.7%, respectively (average, 67.6%). These results show that H1RO following treatment with hydroxyzine is substantially higher than that following treatment with cetirizine (Table 1 and Fig. 1). The differences in both the cetirizine groups to the hydroxyzine group were statistically significant (Discussion Fig. 1).

Disucussion

In the present study, we found that the baseline BP under the placebo condition showed a certain inter-individual variation (Table 1). This result suggests the use of a placebo-controlled study design could minimize the effect of inter-individual variation, although the H1RO of cetirizine 20 mg in this placebo-controlled study (mean value of frontal and cingulate cortices, 25.2%) was slightly different from that obtained in our previous study (mean value of frontal and cingulate cortices: 28.9%)[4].

In our previous healthy volunteer study (n=10), the plasma concentrations of hydroxyzine and cetirizine (a main metabolite) following oral administration (120 min post-administration) of hydroxyzine 30 mg was 20.0 +/- 9.3 ng/mL and 146.3 +/- 50.3 ng/mL, respectively, although these results were not presented in the paper[4]. In addition, the plasma cetirizine concentration following cetirizine treatment (20 mg) was 489.0 +/- 118.8 ng/mL. These pharmaco-kinetic data may suggest that a large proportion of hydroxyzine molecules rapidly distributed from the plasma into the tissue compartment and relatively

small part of hydroxyzine molecules is rapidly metabolized into cetirizine. And according to Simons and colleagues, the elimination half lives do not differ largely between hydroxyzine (29.3 +/- 10.1 h) and cetirizine (24.8 +/- 7.7 h)[7]. It seems that the subjective sedation is not associated with the plasma cetirizine concentration, but is associated with the brain distribution (penetration) of hydroxyzine measured as H1RO.

Interestingly, a significant correlation between H1RO and subjective sleepiness was observed following treatment with hydroxyzine 30 mg, but not following the treatment with cetirizine. This result suggests that subjective sleepiness is not reliable for evaluating the level of sedation particularly for mildly-sedative antihistamines. Thus, measurement of H1RO using PET seems to be promising as recommended by the Consensus Group on New Generation Antihistamines (CONGA). CONGA is responsible for summarizing the core measures regarding the evaluation of the sedative profiles of new generation antihistamines[8].

In conclusion, we examined the H1RO of cetirizine at different oral doses of 10 and 20 mg, and compared the results with those from the oral administration of hydroxyzine 30 mg. Cetirizine 10 mg occupied approximately 13% of available H1Rs in the frontal brain (frontal and cingulate cortices), while cetirizine 20 mg occupied approximately 25% of H1Rs, confirming that brain penetration of mildly-sedative antihistamines tends to be dose-dependent. In addition, it is noteworthy for users to know that oral administration of cetirizine 10 mg could be more safely used for the treatment of allergic disorders, while an increased dose (20 mg or more) could result in mild sedation[9].

References

1) Yanai K., Ryu J.H., Watanabe T., et al., Methods Find Exp Clin Pharmacol. Suppl. C (1995) 64.
2) Yanai K., Ryu J.H., Watanabe T., et al., Br J Pharmacol. **116** (1995) 1649.
3) Hindmarch I., Shamsi Z., Kimber S., Clin Exp Allergy. **32** (2002) 133.
4) Tashiro M., Sakurada Y., Iwabuchi K., et al., J Clin Pharmacol. **44** (2004) 890.
5) Logan J., Fowler J.S., Volkow N.D., et al., J Cereb Blood Flow Metab. **16** (1996) 834.
6) Suzuki A., Tashiro M., Kimura Y., et al., Ann Nucl Med. **19** (2005) 425.
7) Simons K., Simons E., Whomsley R., et al., Allergy. **63** (2008) 541.
8) Holgate S.T., Canonica G.W., Simons F.E., et al., Clin Exp Allergy. **33** (2006) 1305.
9) Tashiro M., Kato M., Miyake M., et al., Human Psychopharmacol. **24** (2009) 540.

Table 1. Binding potential and histamine H_1 receptor occupancy following administration of antihistamines and placebo (reproduced from the reference [9]).

Drug and Region	BP (S.E.M.)	BP_{Pla} (S.E.M.)	H_1RO [%] (S.E.M.)
Hydroxyzine (30 mg)	**BP_{HYD}**	**BP_{Pla}**	**H_1RO_{HYD}**
frontal	0.15 (0.06)	0.53 (0.07)	64.4 (9.1)
cingulate	0.24 (0.03)	0.67 (0.02)	70.7 (5.8)
Cetirizine (20 mg)	**BP_{CET20}**	**BP_{Pla}**	**H_1RO_{CET20}**
frontal	0.44 (0.09)	0.62 (0.11)	25.5 (9.5)
cingulate	0.50 (0.04)	0.66 (0.05)	24.8 (6.5)
Cetirizine (10 mg)	**BP_{CET10}**	**BP_{Pla}**	**H_1RO_{CET10}**
frontal	0.54 (0.04)	0.62 (0.05)	11.6 (3.3)
cingulate	0.68 (0.03)	0.78 (0.02)	13.6 (3.4)

*Abbreviations: BP=binding potential, H_1RO=histamine H_1 receptor occupancy, S.E.M.= standard error of the mean, HYD=hydroxyzine, CET=cetirizine

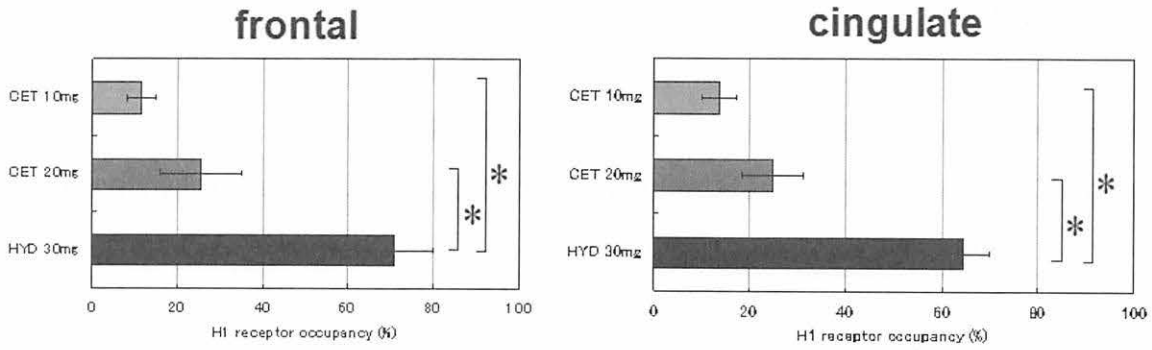

Figure 1. Histamine H1 receptor occupancy (H1RO) in the cingulate and frontal cortices. ROI measurements were performed in the anterior cingulate and frontal cortices following oral administration of cetirizine (10 and 20 mg) and hydroxyzine (30 mg). H1RO due to these antihistamines are shown, taking H1RO by those under the placebo condition as 0%. H1RO of hydroxyzine following administration was significantly higher than those of the other antihistamines. * $p < 0.001$, ANOVA followed by the Bonferroni test for multiple comparisons. Error bars represent inter-individual variability (S.E.M.). Abbreviations: CET10mg = cetirizine 10 mg, CET20mg = cetirizine 20 mg, HYD30mg = hydroxyzine 30mg. (modified from the reference [9]).

VIII. 2. Amyloid PET and Voxel-based Morphometry Analysis Using MRI in Mild Cognitive Impairment and Alzheimer's Disease

Waragai M.[1], Okamura N.[2], Furukawa K.[1], Tashiro M.[3], Watanuki S.[3], Furumoto S.[2,4], Funaki Y.[5], Kato M.[2], Iwata R.[5], Yanai K.[2], Kudo Y.[6], and Arai H.[1]

[1]*Department of Geriatrics and Gerontology, Division of Brain Sciences, Institute of Development, Aging and Cancer, Tohoku University,*
[2]*Department of Pharmacology, Tohoku University School of Medicine,*
[3]*Division of Cyclotron Nuclear Medicine, Cyclotron and Radioisotope Center, Tohoku University,*
[4]*Department of Nuclear Medicine and Radiology, Institute of Development, Aging and Cancer, Tohoku University,*
[5]*Division of Radiopharmaceutical Chemistry, Cyclotron and Radioisotope Center, Tohoku University,*
[6]*Innovation of New Biomedical Engineering Center, Tohoku University,*

Introduction

Currently, amyloid PET imaging using a tracer that binds to amyloid β (Aβ) fibrils can noninvasively and reliably assess Aβ deposition and be aaplied as a biomarker for AD[1)]. Pittburg Compound-B (PIB) has been the most commonly used tracer for the anyloid PET imaging. Our group has recently developed a novel PET tracer, 2-(2-[2-demethylaminothiazol-5-yl]ethenyl)-6-(2-[fluoro]ethoxy)benzoxazole (BF-227), and reported that this compound is able to finely detect Aβ deposition primarily in the posterior association area of AD patients[2,3)]. It might be speculated that BF-227 detects neuritic plaques containing dense amyloid fibrils preferentially, compared to PIB-PET, and provides unique and specific information about the Aβ pathology in AD patients[2,3)].

It should be important to detect Aβ deposition as early as possible in order to begin medication to prevent or treat cognitive decline before the symptoms of dementia become obvious because it is considered that deposition as well as aggregation of Aβ starts much earlier before patients indicate symptoms of dementia[2,3)].

On the other hand, it has been found that cognitive decline strongly correlates with cortical atrophy in AD supporting cortical degeneration as the primary basis for cognitive decline in AD[4)]. Thus, an increased rate of cerebral atrophy evaluated with MRI using voxel-based morphometry (VBM) is a diagnostic feature of AD that correlates with clinical stage/severity and is thought to represent the macroscopic consequences of neuronal

destruction[5]. However, it is still unclear the amounts of Aβ deposition in the brain directly correlate with progression and brain atrophy because recent studies suggested that amyloid deposition in the brain reaches a plateau by the early stage of AD. Moreover, clearance of amyloid plaques in patients with AD using immunisation with Aβ42 did not prevent progressive neurodegeneration[6]. n this study, we studied comparison of amyloid-imaging PET using novel β-amyloid prove [^{11}C]BF-227 and structural MRI analysis for the diagnosis and tracking the severity of AD.

Materials and Methods

Subjects

Patients recruited in the present study included 12 normal age-matched controls, 13 subjects with amnestic MCI, and 15 patients with AD. Diagnoses of probable AD were based on criteria from the National Institute of Neurological and Communicative Disorders and Stroke and the Alzheimer's Disease Related Disorders Association (NINCDS-ADRDA)[7]. The diagnosis of amnestic MCI was made according to the published criteria described previously[8]. The MCI subjects were divided into two groups, MCI converters (n=6) and MCI non-converters (n=7). The MCI converters were defined as patients who eventually developed AD within a mean follow-up of 27.0±7.9 months (range 14–30 months). The MCI non-converters were defined as having a transient memory loss or remaining cognitively stable through at least a 2-year follow-up (27.7±2.2 months; range 25–30 months). All subjects were screened using a questionnaire and medical history, and subjects with medical conditions potentially affecting the central nervous system were excluded. In addition, none of the subjects had asymptomatic cerebral infarction detected via T2-weighted MRI. The Committee on Clinical Investigation at Tohoku University School of Medicine and the Advisory Committee on Radioactive Substances at Tohoku University approved the study protocol.

MRI methods

All subjects underwent MRI with a 1.5 Tesla MR scanner (GE Signa Hispeed, Milwaukee, WI). A three-dimensional volumetric acquisition of a T1-weighted gradient echo sequence produced a gapless series of thin axial sections using a vascular TOF SPGR sequence (echo time/repetition time, 2.4/50 ms: flip angle, 45°; acquisition matrix, 256×256; 1 excitation; field of view, 22 cm; slice thickness, 2.0 mm). Cerebral atrophy

was evaluated by voxel-based morphometry (VBM) implemented in the Voxel-Based Specific Regional Analysis System for AD (VSRAD) software developed by Matsuda et al[9]. VSRAD software is an adjunctive diagnostic tool for early AD which can automatically analyze three dimensional T1-weighted MRI data as a series of segmentation, anatomical standardization and smoothing using SPM5, and Z-score analysis; Z-score = ([control mean]_[individual value])/(control S.D.) as previously reported by Minoshima et al. in a PET study [37]. The degree of the gray matter atrophy was calculated as ratio (%) of total area in which the Z score of the voxel is more than 2.0 to the whole brain.

PET procedure

Radiosynthesis of [^{11}C]BF-227 and the procedure used for BF-227-PET were performed as described previously[2]. BF-227 and its N-desmethylated derivative (a precursor of [^{11}C]BF-227) were custom-synthesized by Tanabe R&D Service Co. [^{11}C]BF-227 was synthesized from its precursor by N-methylation in dimethyl sulfoxide using [^{11}C]methyl triflate. The [^{11}C]BF-227 PET study was performed using a PET SET-2400W scanner (Shimadzu Inc., Japan). After an intravenous injection of 211-366 MBq [^{11}C]BF-227, dynamic PET images were obtained for 60 min with the subject's eyes closed. Standardized uptake value (SUV) images of [^{11}C]BF-227 were obtained by normalizing the tissue radioactivity concentration to the injected dose and body weight. ROIs were placed on individual axial MR images in the cerebellar hemisphere and the frontal, lateral temporal, parietal and posterior cingulate cortices. The ROI information was then copied onto the dynamic PET SUV images, and regional SUVs were sampled using Dr.View/LINUX software. The ratio of the regional to cerebellar SUV (SUVR) at 40-60 min post injection was calculated, and averaged SUVR values in the frontal, temporal, parietal and posterior cingulate cortices were considered representative of BF-227 retention in the neocortex (neocortical SUVR).

Statistical analysis

Statistical comparison of PET and MRI measurements in the four groups was performed via an analysis of variance followed by a Bonferroni multiple comparisons test with a significance level of $p<0.05$. Statistical comparisons of age and MMSE scores in the four groups were performed using a Kruskal-Wallis test followed by a Dunn's multiple comparison test with a significance level of $p<0.05$. Correlations between the MMSE score and BF-227 retention in the neocortex or the cerebral atrophy index were examined

using a non-parametric Spearman's rank correlation analysis. Correlations between the brain atrophy index and BF-227 retention were determined using Pearson's correlations. A linear model was applied to the data to obtain a correlation coefficient and *p* value. These analyses were performed using GraphPad Prism5 software (GraphPad, San Diego, CA).

Results

Representative images of [^{11}C]BF-227-PET and T1-weighted MRI in a normal control (70-year-old female, MMSE score 29), a MCI non-converter (76-year-old male, MMSE score 27), a MCI converter (85-year-old male, MMSE score 23), and an AD patient (62-year-old female, MMSE score 20) are shown in Figure 1.

We examined comparison of BF-227 SUVR in the neocortex (left) and and the parahippocampal ROI value from gray matter MR images processed by SPM5 the percent global atrophy (right). Significant inter-group difference between the MCI-converter and the MCI-nonconverter was observed in the frontal and the average neocortical SUVR assayed by BF227-PET, but not in the percent global atrophy or parahippocampal ROI value obtained by VBM-MRI (Fig. 2).

Next, we analyzed the correlations of MMSE scores with the BF-227 SUVR in the neocortex (left), the percent global atrophy (middle), the parahippocampal region of interest (ROI) value from gray matter images processed by SPM5 (right). We observed a significant correlation only between the percent global atrophy and the MMSE score (Spearman r=-0.459, p=0.036). In contrast, no significant correlation was observed between the parahippocampal ROI from SPM5 and the MMSE (Spearman r=0.181) or between the BF-227 SUVR in the neocortex and the MMSE (Spearman r=-0.200). Finally, no significant correlation was observed between the BF-227 SUVR and the percent global atrophy or parahippocampal atrophy in the analysis of all subjects (Fig. 3).

Discussion

In the present study, MCI converters were more clearly distinguished from MCI non-converters by BF-227 PET than by VBM-MRI. BF-227 PET achieved higher sensitivity and specificity in the discrimination between MCI converters and MCI non-converters than did VBM-MRI. Our results strongly suggest that amyloid imaging using BF-227 PET will be a useful tool to predict conversion from MCI to AD, as previously shown for PIB-PET[1]. However, cerebral gray matter loss as determined by VBM-MRI was better correlated with

the clinical severity of AD than BF-227 PET. Used together, BF-227 PET and VBM-MRI could be an effective method for the early diagnosis and severity tracking of AD.

We hope to explore the relationship between these imaging measurements and the impairment of episodic memory function in a future study. Additional longitudinal studies are also needed to confirm the findings we have obtained and to examine the time course of AD, including changes in the pre-symptomatic subjects, and to determine the relationship between amyloid deposition and brain atrophy as underlying factors in the pathogenesis of AD.

References

1) Nordberg A., Curr Opin Neurol. **20** (2007) 398.
2) Kudo Y., Okamura N., Furumoto S., et al., J Nucl Med. **48** (2007) 553.
3) Waragai M., Okamura N., Furukawa K.., et al., J Neurol Sci. **285** (2009) 100.
4) Mouton P.R., Martin L.J., Calhoun M.E., et al., Neurobiol Aging. **19** (1998) 371
5) Fox N.C., Crum W.R., Scahill R.I., et al., Lancet **358** (2001) 201.
6) Josephs K.A., Whitwell J.L., Ahmed Z., et al., Beta-amyloid burden is not associated with rates of brain atrophy. Ann Neurol **63** (2008) 204.
7) McKhann G., Drachman D., Folstein M., et al., Neurology **34** (1984) 939.
8) Petersen R.C., Smith G.E., Waring S.C., et al., Mild cognitive impairment: clinical characterization and outcome. Arch Neurol **56** (1999) 303.
9) Hirata Y., Matsuda H., Nemoto K., et al., Neurosci Lett **382** (2005) 269.

.

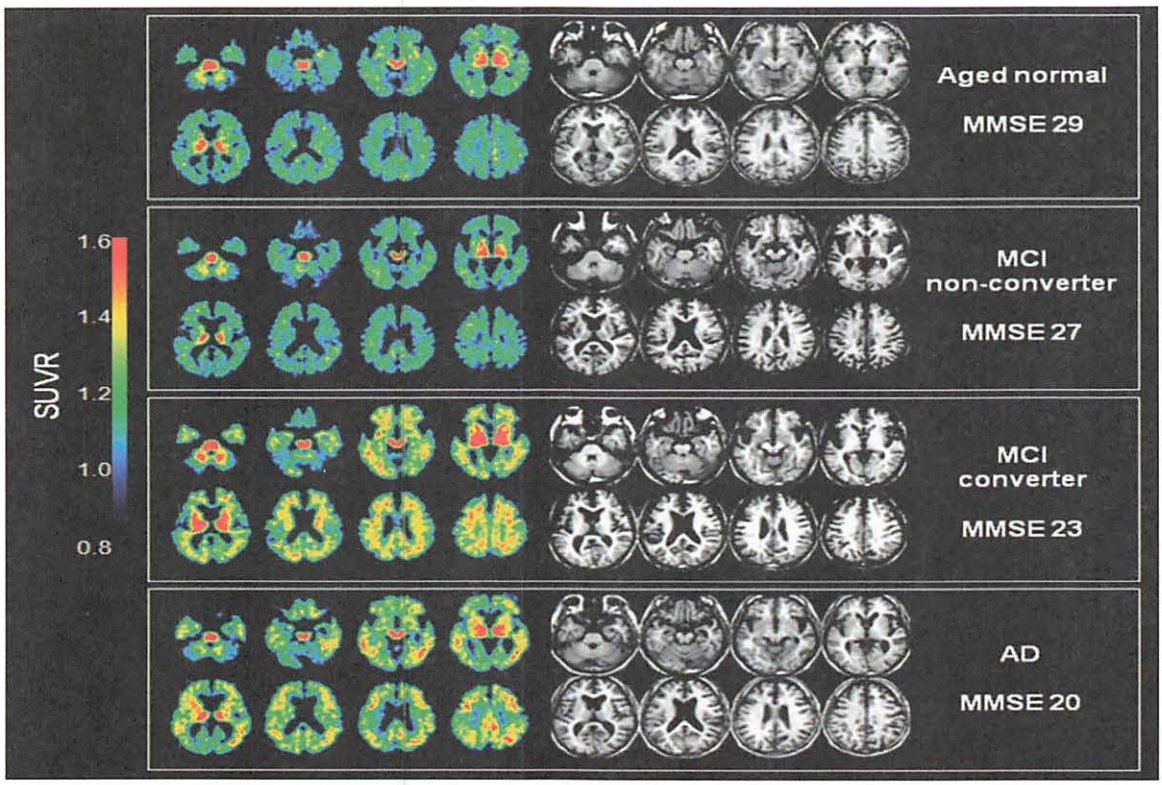

Figure 1. Representative images of [^{11}C]BF-227-PET SUVR between 20 and 40 min post-injection (left) and T1-weighted MRI (right) in a control subject, a MCI non-converter, a MCI converter and an AD subject. The degree of [^{11}C] BF-227 retention is shown by color intensity from yellow to red in the cortex.

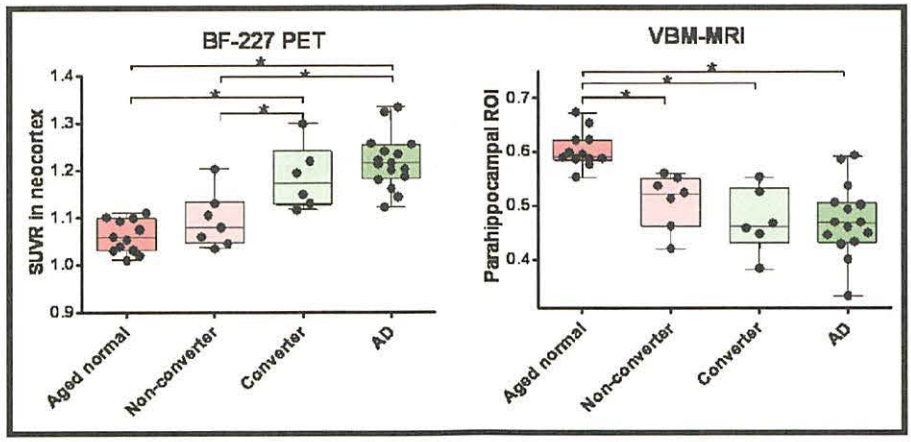

Figure 2. Statistical analysis showed that both of the BF-227 PET and the VBM-MRI could distinguish MCI and early AD from aged normal. Only BF-227 PET could statistically differentiate MCI converter from MCI non-converter.

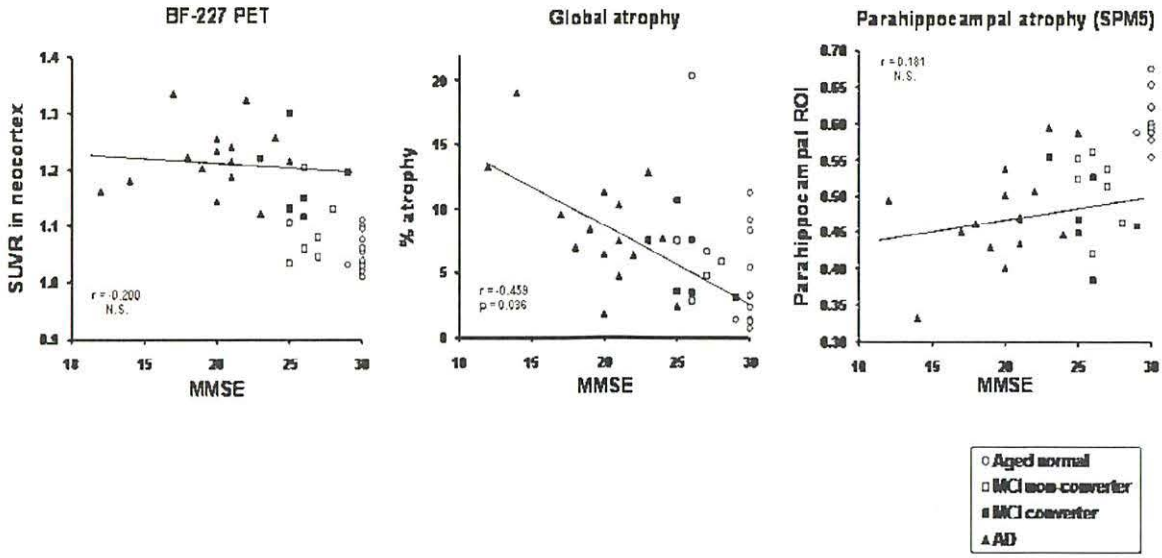

Figure 3. The correlations of MMSE scores with the BF-227 SUVR in the neocortex (right), the percent global atrophy (middle) and the parahippocampal region of interest (ROI) value from gray matter images processed by SPM5 (left).

VIII. 3. Evaluation of Cerebral Activity and Autonomic Function during Accompanying with Animal: a PET Study

Masud M. M.[1], Sugawara A.[1], yokoyama A.[2], Mizutani W.[3], Watanuki S.[1], Itoh M.[1], and Tashiro M.[1]

[1]Division of Cyclotron Nuclear Medicine, Cyclotron Radioisotope Center, Tohoku University
[2]Teikyo University of Science and Technology, Tokyo, Japan
[3]Japanese Animal Hospital Association, Tokyo, Japan

Introduction

Nowadays, partnership between human and animal has been well-established, relieving mental stress and anxiety for control our emotions in our busy life. Human-animal bond has been studied in terms of autonomic function and central brain activities. Previous investigators argued that heart rate and blood pressure of human subjects decreased when being together with pet dogs[1)], suggesting the presence of relaxing effects[1)]. Human-animal association possesses substantial impacts on moods and behaviors, which eventually brings psychological well-being. Previous findings suggest that human-animal association promotes psychological well-being in healthy people[2,3)]. Clinical effects of animal-assisted therapy (AAT) has also been studied beforehand. Barker et al showed that AAT reduced state of anxiety levels among hospitalized Schizophrenia patients[4)]. Furthermore, AAT provided vast effects on improvement of dementia level of geriatric patients[5)] and prevention of psychological disabilities of abused children[6)]. However, the mechanism of these physiological and psychological well-beings among healthy subjects and psychiatric patients has not been studied elaborately.

The aim of the present work was to investigate the effects of being together with accompanying dog on our mood, autonomic activity and regional brain activity. Three dimensional positron emission tomography (3D-PET) and 2-deoxy-2-[^{18}F]fluoroglucose ([^{18}F]FDG) were applied to evaluate static regional brain activities in certain static conditions, i.e. with and without accompanying dogs. Subjects' psychological condition and autonomic activity were assessed using Stress Response Scale (SRS-18) and heart rate

variability analysis (HRV).

Subjects and Methods

Fourteen healthy volunteers (men: 2; women: 12), those who are members of Japanese Animal Hospital Association, were assigned for this investigation. They had age range from 25 to 65 years old (mean ± S.D.: 43 ± 10.8 years old), without any psychological disorders. A written informed consent was taken from all subjects before start of the experiment. All the subjects were requested to take adequate rest and sleep during the night before the experiment day and they refrained from eating and drinking for at least 5 h prior to the start of the experiment. The study protocol was approved by the Clinical Committee for Radioisotope Studies of Tohoku University.

Study design

Each subject was studied twice as staying with accompanying animal (task) and without any company (control). The order of the conditions was counter-balanced. Subjects were requested to sit on chairs comfortably with eyes open in a dimly lit and quiet room. Then, two chest electrodes, Magnerode, TE-18 (Fukuda Denshi Co., LTD., Tokyo, Japan) were attached on subjects' chest, over manubrium sternum and apex (left 5^{th} intercostals space, about 1 cm medial to the mid-clavicular line) for evaluation of HRV. A Teflon catheter was inserted into the cutibal veins of right hands for administration of [^{18}F]FDG. Then the subjects were requested to stay with their accompanying dogs for 35 min, following intravenous injection of [^{18}F]FDG (74.5 MBq). ECG recordings for all subjects were performed following [^{18}F]FDG injections for 30 min to evaluate HRV. During ECG monitoring, subjects were requested to keep a relaxed-respiration. ECG recording was obtained by using polar 810i (Polar Electro Oy, Finland). Furthermore, subjects' psychological conditions were assessed by using Stress Response Scale (SRS-18) to rate their own stresses before PET scan was started. After 35 min of long uptake of [^{18}F]FDG, all the electrodes were detached and they were requested to micturate before the commencement of PET scan. Figure 1 shows the study design.

In another, the resting control condition referred to subjects remaining in a sitting posture in a dimly lit room for 35 min following [^{18}F]FDG injection (37.7 MBq). They were studied by maintaining similar study design as task condition without accompanying dogs.

PET scan protocol

For each subject, PET scans were conducted twice in a day with 2 hour separation for task (with dog) and resting (control) conditions and the order of the conditions were counterbalanced. In the PET scan procedure, the subjects were asked to lie down in the supine position on a PET table with eyes open following 40 min after [^{18}F]FDG injection. The PET room was kept dimmed and quiet and the scanning was done using PET apparatus (SET 2400 W, Shimadzu, Kyoto, Japan) with an intrinsic spatial resolution of 3.9 mm full width at half maximum (FWHM). The 3-D whole-brain emission scan lasted for 15 min from occipitomeatal line (OM line) to the vertex depending on the subjects' physique. Transmission scan (post-injection) which continued 10 min, was performed with a ^{68}Ge/^{68}Ga external rotating line source (370 MBqs at purchase) to correct the tissue attenuation of emission photons (Fig. 1).

Frequency-domain analysis of HRV

Frequency-domain analysis of HRV is an important method in evaluating sympathetic and parasympathetic activity of heart among resting controls and task condition (with dog). HRV refers to variation between two consecutive heartbeats, those are assessed from RR intervals. Usually, frequency of peak R wave is taken for evaluating autonomic activity. There are two spectral components mostly known in the HRV spectrum as follows: low frequency (LF: 0.04 to 0.15 Hz) and high frequency (HF: 0.15 to 0.4 Hz) components, accordingly[7]. For HRV analysis, the values of spectral components (LF and HF) are obtained for evaluation of autonomic function (sympathetic and parasympathetic activity). Here, LF corresponds to mostly autonomic sympathetic activity and HF corresponds to autonomic parasympathetic activity.

For analysis, we used HRV analytical software (University of Kuopio, Kuopio, Finland)[8]. In this analytical procedure, a 30 minute-long ECG record (control and task) was used. Consecutive heart beat intervals (R-R interval) of ECG recording were measured after determining peak QRS complex to obtain HRV spectral components (LF and HF). In another, heart rate (HR) was estimated from consecutive R-R intervals. Power spectral analysis of heart rate variability in frequency domain was performed to determine autonomic sympathetic and parasympathetic parameters (LF and HF) with fast fourier transformation technique (FFT). These LF and HF parameters were distinguished

from frequency bands[8]. The normalization values of LF and HF (nLF and nHF) were used for final elucidation of HRV data. Hence, normalized LF and HF (nLF and nHF) were determined according to following formulas (9): nLF = LF / (LF + HF) and nHF = HF / (LF + HF), respectively. Here, (LF + HF) is expressed as total power (TP).

[^{18}F]FDG-PET data analysis

The statistical parametric mapping (SPM 5) software[10,11] was used to identify regional glucose metabolic changes of PET brain images among control and task. First, the PET brain images were spatially normalized to reduce anatomical disparities between subjects. An [^{18}F]FDG brain template of Montreal Neurological Institute, McGill University, Canada[11] was used in this normalization procedure by applying affine and nonlinear transformations. Then, smoothing was performed with a 8-8-8 mm isotropic Gaussian filter kernel for compensation of errors in spatial normalization procedure. Voxel-based statistical analysis was performed on these smoothed images using paired t-test, based on the general linear model to obtain metabolic changes of brain activities between two conditions (control vs task). The statistical threshold for significance was set at $p < 0.001$ without corrections for multiple comparisons. The locations of relatively activated brain regions between two conditions were identified in the x, y and z standard coordinates[12].

Statistical analysis

Group comparisons of SRS-18 scores between control and task were made by using a non-parametric test (Wilcoxon signed-rank test), and significant differences were set at $P < 0.05$.

Results

Subjects' Psychological Stress Response Scale scores were shown in Fig. 2. SRS-18 scores were significantly lower ($p<0.05$) in the task condition (with dog) when compared with control (Fig. 2).

Figure 3 shows the data of autonomic activities (sympathetic and parasympathetic: nLF and nHF) among control and task (with dog). It was found relatively stable nLF and nHF between control and task (with dog), evaluating from FFT analysis (Fig. 3).

In another, brain PET image data analysis revealed the changes of regional brain

activations between control and task (with dog) ($p<0.001$) (Fig. 4). SPM results demonstrated the deactivated brain regions in the left middle frontal gyrus (BA, 8), right fusiform gyrus (BA, 20), left putamen and thalamus during task (with dog) to compare with control (Fig. 4); however, we did not find any activated brain areas at task (with dog).

Discussion

The present investigation evaluated the effects of being together with an accompanying dog on our mood, autonomic activity and regional brain activity by using SRS-18 scores, HRV and [^{18}F]FDG-3-D PET technique. Subjects' psychological condition such as SRS-18 scores were shown decreased ($p<0.05$) with accompanying dogs. The significantly reduced SRS-18 scores suggested that animal companionship can improve psychological condition from anxiety and stress. One study relating with changes of mood and physical health of animal pet (dog) owner showed that older people with pet dog owner had minor health problems and significant improvements in psychological well-being following after being a pet owner[13]. Recent findings suggest that human-animal bond may promote psychological well-being. Hence, it is suggested that animal-companionship inducing psychological well-being may improve social behavior. Previous study relating with dog contact postulated that human-dog association increased social behavior and decreased agitated behaviors[14]. This increase in social behavior may improve the quality of life (QOL).

Nowadays, the practice of animal companionship has been accomplished among population with psychiatric patients to improve psychological condition. For example, Barker and Dawson (1998) investigated the effects of animal companionship (pet dogs) on 230 hospitalized psychiatric patients and compared a single 30-minute animal companionship session with a 30-minute therapeutic recreation session[15]. They found that the patients who had animal companionship showed a significant decrease in anxieties with mood disorders, psychotic disorders and other disorders. In the present study, significantly lower SRS-18 scores ($p<0.05$) suggested that subject's stress and anxiety were relieved by the situation of staying with their dogs.

Recent findings revealed a relatively stable autonomic activities (nLF and nHF) between control and with dog. The heart function is mediated by autonomic nervous system. Hence, the rhythm of heart beat is controlled by autonomic sympathetic and parasympathetic nervous activities. Any variation in heart rate is referred to irregular

balance between sympathetic and parasympathetic components of autonomic nervous system functions. Frequency domain parameters of LF (mostly sympathetic nervous activity) and HF (parasympathetic nervous activity) suggest cardiovascular activity linking with physiological status[16,17].

It is acknowledged that dominant parasympathetic activity (nHF) represents relaxation effects; however, our results suggest relatively stable autonomic function, suggesting of synchronized sympathetic and parasympathetic activities. This might bring mild relaxation effects on subjects' mind with accompanying dogs. Inevitably, this stable autonomic activity suggests, human-animal interactions can persuade coolness and relaxation after harmonizing sympathetic and parasympathetic nerves activities of heart. Therefore, human-animal bond brings relaxation by reducing cardiovascular reactivity to stress and reliefs anxiety in the daily busy life.

As for the brain PET study, our results using SPM analysis (SPM 5) revealed the deactivated brain regions in the left middle frontal gyrus (BA, 8), right fusiform gyrus (BA, 20), left putamen and thalamus at task (with dog) when compared with control ($p<0.01$). However, we did not find any activated brain areas among subjects accompanying with dog. Since recent application of [^{18}F]FDG-3-D PET technique on human-animal bond research was established as the first imaging study, animal companionship-induced (with dog) regional brain activities were assessed to determine a coordination between mind and brain. Accompanying animal (with dog) might have a stress-relieving effect that was demonstrated by deactivated brain areas. Furthermore, these deactivated brain areas during accompanying with dog support relaxations of subjects' mind in psychological sense.

Conclusion

Present investigation evaluated the effects of being together with accompanying animal (with dog) on our mood, autonomic activity and regional brain responses. Results showed a significantly reduced psychological stress response scale (SRS-18) and some deactivated brain areas with accompanying animal, suggesting of psychological well-being and relaxations. Animal-assisted therapy (AAT) might have a potential application to certain programs for psychological rehabilitation and integrative health care facility. The brain mapping technique such as PET seems to be useful to examine the underlying brain mechanism of AAT in terms of regional brain responses.

Acknowledgments

The authors greatly acknowledge the enthusiastic support of Japanese Animal Hospital Association, Tokyo, Japan.

References

1) Vormbrock J.K., Grossberg J.M., J Behav Med, **11** (1988) 509.
2) Cole K.M., Gawlinski A., AACN Clin Issues, **11** (2000) 139.
3) Perkins J., Bartlett H., Travers C., Rand J., Australas J Ageing, **27** (2008) 177.
4) Barker S.B., Dawson K.S., Psychiatr Serv, **49** (1998) 797.
5) Zisselman M.H., Rovner B.W., Shmuely Y., Ferrie P., Am J Occup Ther, **50** (1996) 47.
6) Parish-Plass N., Clin Child Psychol Psychiatry, **13** (2008) 7.
7) Task force of the European society of cardiology and North American society of pacing and electrophysiology. Heart rate variability – standards of measurement, physiological interception, and clinical use. Circulation, **93** (1996) 1043.
8) Niskanen J.P., Tarvainen M.P., Ranta-Aho P.O., Karjalainen P.A., Comput Methods Programs Biomed, **76** (2004) 73.
9) Robert L.B., Sleep, **30** (2007) 913.
10) Friston K.J., Frith C.D., Liddle P.F., J Cereb Blood Flow Metab, **11** (1991) 690.
11) Friston K.J., Holmes A.P., Worsley K.J., Poline J.P., Frith C.D., Frackowiak R.S., Hum Brain Mapping, **2** (1995) 189.
12) Talairach J., Tournoux P., Co-planner Stero-taxic Atlas of the Human Brain. Rayport M (translator), Stuttgart: Theim, 1988.
13) Raina P., Waltner-Toews D., Bonnett B., Woodward C., Abernathy T., J Am Geriatr Soc, **47** (1999) 323.
14) Perkins J., Bartlett H., Travers C., Rand J., J Ageing, **27** (2008) 177.
15) Barker S.B., Dawson K.S., Psychiatr Serv, **49** (1998) 797.
16) Montano N., Porta A., Mallia ni A., Ann N Y Acad Sci, **940** (2001) 299.
17) Pumprla J., Howorka K., Groves D., Chester M., Nolan J., Int J Cardiol, **84** (2002) 1.

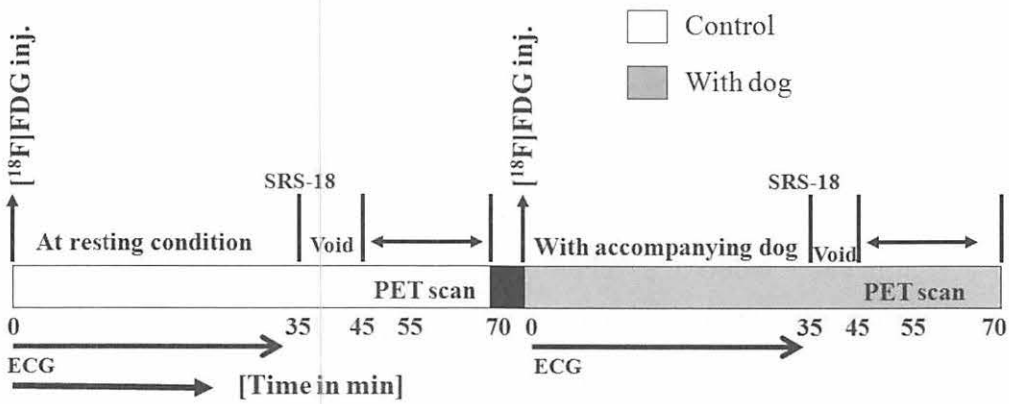

Figure 1. Schematic illustration of study design.

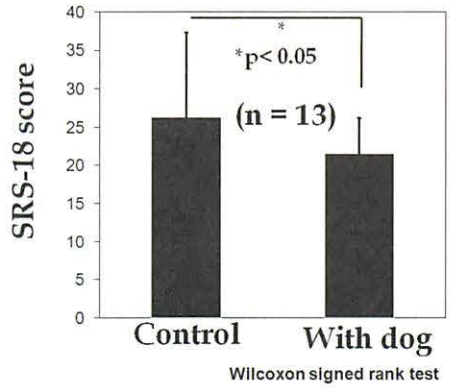

Figure 2. Measurements of psychological stress response scale score (SRS-18) between control and task (with dog). Subjects' SRS-18 scores were shown significantly reduced ($p<0.05$) during accompanying with dog compared with control..

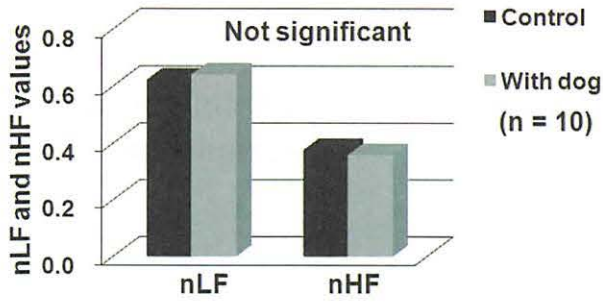

Figure 3. Measurements of HRV (heart rate variability) showing normalized units of low frequency and high frequency (nLF and nHF). HRV data demonstrated a relatively stable nLF and nHF between control and accompanying with dog.

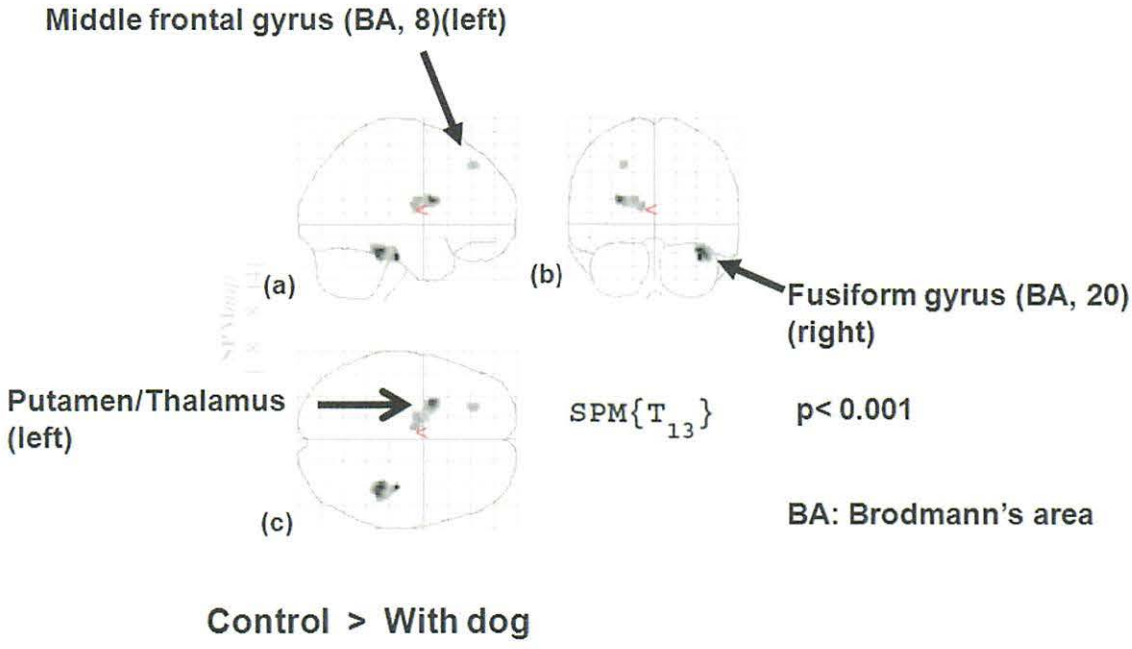

Figure 4. Reduction of regional brain activities with an accompanying animal (with dog).
Results of PET brain images demonstrated the deactivations ($p < 0.001$) in the left middle frontal gyrus (BA, 8) (a), right fusiform gyrus (BA, 20) (b) and subcortical structures (left putamen and thalamus) (c) during accompanying with dog compared with control. However, any activated brain areas were not found during accompanying with dog.

VIII. 4. Quantitative Analysis of Donepezil Binding to Acetylcholinesterase Using Positron Emission Tomography and [5-^{11}C-*methoxy*]Donepezil

Hiraoka K.[1], Okamura N.[2], Funaki Y.[3], Watanuki S.[4], Tashiro M.[4], Kato M.[3], Hayashi A.[1], Hosokai Y.[1], Yamasaki H.[1], Fujii T.[1], Mori E.[1], Yanai K.[2], and Watabe H.[5]

[1]*Dep. of Behavioral Neurology and Cognitive Neuroscience, Tohoku University Graduate School of Medicine*
[2]*Dep. of Pharmacology, Tohoku University Graduate School of Medicine*
[3]*Div. of Radiopharmaceutical Chemistry, CYRIC, Tohoku University*
[4]*Div. of Cyclotron Nuclear Medicine, CYRIC, Tohoku University*
[5]*Dep. of Investigative Radiology, National Cardiovascular Center Research Institute*

Backgrounds

The cholinergic system is one of the most crucial neurotransmitter systems in the brain, and it has very profound links with the manifestations of dementia[1,2]. The activity of choline acetyltransferase, the enzyme catalyzing acetylcholine synthesis, and of acetylcholinesterase (AChE), the enzyme degrading brain acetylcholine, are both reported to be decreased in the neocortex and the hippocampus of patients with Alzheimer's disease and Parkinson's disease with dementia[3,4], and this decreased activity correlates with the severity of cognitive impairment[5]. Significant loss of cholinergic neurons in the nucleus basalis of Meynert has been reported in the brains of patients with both diseases[6,7]. Based on these pathological findings, the rational use of reversible AChE inhibitors was proposed as means for potentiating cholinergic neurotransmission, with an aim to improve cognitive function. Currently, several AChE inhibitors are prescribed to improve the cognitive function of patients with dementia. Donepezil hydrochloride is an AChE inhibitor that has been proved to be effective in ameliorating the cognitive impairment of patients with Alzheimer's disease[8], and it is widely prescribed for the treatment of the disease.

Objective

The objective of this study was to establish kinetic analysis of [5-^{11}C-*methoxy*]donepezil ([^{11}C]donepezil), which was developed for the in-vivo visualization of donepezil binding to AChE using positron emission tomography (PET) (Fig. 1)[9].

Methods

Six healthy subjects took part in a dynamic study involving a 60-min PET scan after intravenous injection of [^{11}C]donepezil. The total distribution volume (tDV) of [^{11}C]donepezil was quantified by compartmental kinetic analysis and Logan graphical analysis[10]. A one-tissue compartment model (1TCM) and a two-tissue compartment model (2TCM) were applied in the kinetic analysis. Goodness of fit was assessed with χ^2 criterion and Akaike's Information Criterion[11].

Results

Compared with a 1TCM, goodness of fit was significantly improved by a 2TCM. The tDVs provided by Logan graphical analysis were slightly lower than those provided by a 2TCM (Fig. 2). The rank order of the mean tDV in 10 regions agreed with the AChE activity reported in a previous post-mortem study[12,13] (Fig. 3). Logan graphical analysis generated voxel-wise images of tDV, revealing the overall distribution pattern of AChE in individual brains (Fig. 4). Significant correlation was observed between tDVs calculated with and without metabolite correction for plasma time–activity curves, indicating that metabolite correction could be omitted.

Conclusions

This method enables quantitative analysis of AChE in the human brain, which is useful in various situations for patients with dementia. [^{11}C]donepezil-PET study can be exploited not only for the assessment of cholinergic dysfunction in patients, but also for the prediction of efficacy of treatment with AChE inhibitors. Moreover, by performing PET scans before and after treatment with AChE inhibitor, the AChE binding occupancy of orally administered AChE inhibitor can be measured, which facilitates the determination of clinical doses of AChE inhibitor.

References

1) Francis P. T., Palmer A. M., Snape M., and Wilcock G. K., J Neurol Neurosurg Psychiatry **66** (1999) 137.
2) Perry E., Walker M., Grace J., and Perry R., Trends Neurosci **22** (1999) 273.
3) Perry E. K., Curtis M., Dick D. J., Candy J. M., Atack J. R., Bloxham C. A., Blessed G., Fairbairn A., Tomlinson B. E., and Perry R. H., J Neurol Neurosurg Psychiatry **48** (1985) 413.
4) Davies P. and Maloney A. J., Lancet **2** (1976) 1403.
5) Perry E. K., Tomlinson B. E., Blessed G., Bergmann K., Gibson P. H., and Perry R. H., Br Med J **2** (1978) 1457.

6) Whitehouse P. J., Price D. L., Struble R. G., Clark A. W., Coyle J. T., and Delon M. R., Science **215** (1982) 1237.
7) Whitehouse P. J., Hedreen J. C., White C. L., 3rd, and Price D. L., Ann Neurol **13** (1983) 243.
8) Rogers S. L., Farlow M. R., Doody R. S., Mohs R., and Friedhoff L. T., Neurology **50** (1998) 136.
9) Funaki Y., Kato M., Iwata R., Sakurai E., Sakurai E., Tashiro M., Ido T., and Yanai K., J Pharmacol Sci **91** (2003) 105.
10) Logan J., Nucl Med Biol **27** (2000) 661.
11) Akaike H., IEEE Trans Automat Contr **AC19** (1974) 716.
12) Arai H., Kosaka K., Muramoto O., and Iizuka R., Rinsho Shinkeigaku **24** (1984) 1128.
13) Atack J. R., Perry E. K., Bonham J. R., Candy J. M., and Perry R. H., J Neurochem **47** (1986) 263.

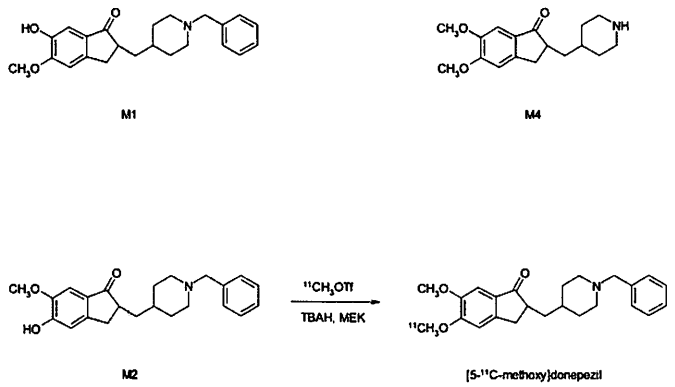

Figure 1. Chemical structures of [5-^{11}C-*methoxy*]donepezil and donepezil metabolites. [5-^{11}C-*methoxy*]donepezil is synthesized from 5'-O-demethylprecursor (M2).

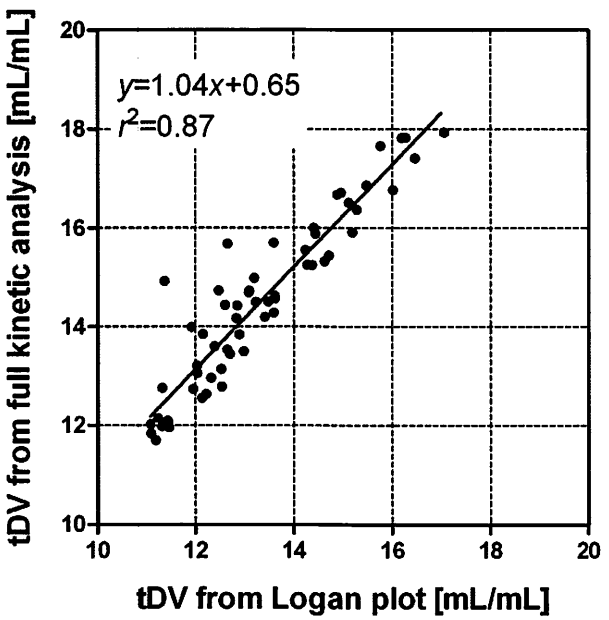

Figure 2. Total distribution volumes estimated by the two-tissue compartment model (2TCM) were compared with those estimated by Logan graphical analysis. All regions of interest (ROIs) obtained from all subjects are plotted.

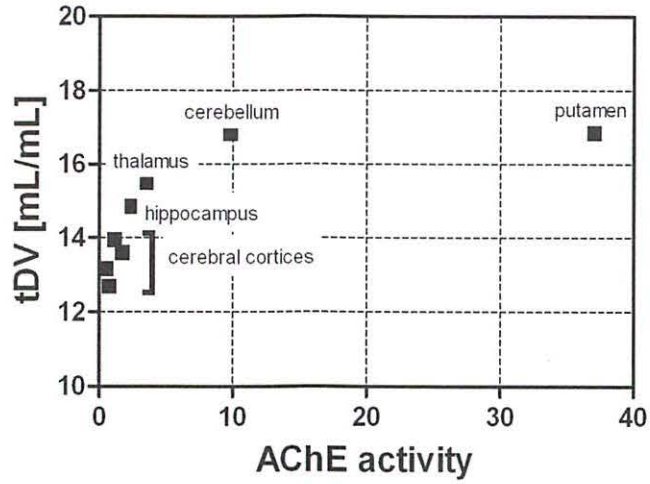

Figure 3. Mean estimated total distribution volume (tDV) values of cerebral regions and post-mortem acetylcholinesterase (AChE) values in human brain obtained from the literature[12,13]. Post-mortem AChE values are expressed as ratios to the mean AChE value of cerebral cortices.

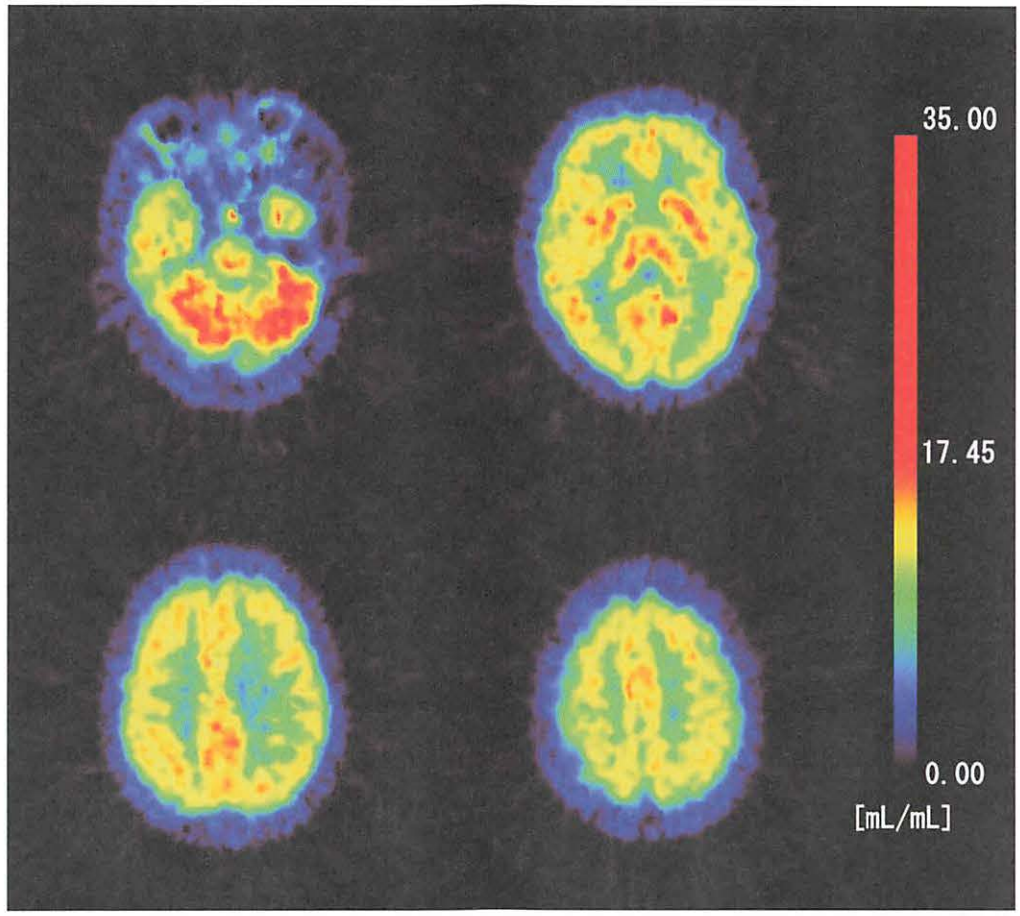

Figure 4. Image of total distribution volumes (tDVs) derived with a Logan plot. tDV values were large in the thalamus, basal ganglia, and cerebellar hemispheres, and small in the cortices.

VIII. 5. Function of the Shoulder Muscles during Arm Elevation: An Assessment Using Positron Emission Tomography

Omi R.[1], Sano H.[1], Ohnuma M.[1], Kishimoto KN.[1], Watanuki S.[2], Tashiro M.[2], and Itoi E.[1]

[1]Department of Orthopaedic Surgery, Tohoku University School of Medicine,
[2]Division of Cyclotron Nuclear Medicine, Cyclotron and Radioisotope Center, Tohoku University,

Introduction

Electromyography has been the standard method to assess the in vivo function of the muscles. However, its application to muscles located deep in the body such as the subscapularis is limited because of technical difficulties.

Positron emission tomography (PET) is a nuclear medicine tool for noninvasive quantification of regional blood flow and tissue glucose metabolism in vivo. 2-Deoxy-2-[^{18}F]fluoroglucose (FDG), as a glucose analog, is absorbed by tissues after intravenous injection, which is converted into FDG-6-phosphate by hexokinase. Radioactive ^{18}F is subjected to beta-decay, resulting in annihilation photon emissions, which are detected by PET scanner.

In the PET, the FDG accumulation in the muscle is used as a parameter of glucose uptake by the muscle, and accordingly, the muscle activity level. It is widely known that active muscle cells exhibit increased glucose uptake. Therefore, FDG PET has been used for the assessment of skeletal muscle activities[1-3]. However, the application of FDG PET to the shoulder muscles was only sparse.

Based on these backgrounds, we attempted to investigate the activities of the shoulder muscles with special interest on the rotator cuff muscles during arm elevation using FDG PET.

Methods

The experimental protocol of the present study was approved by the institutional ethics committee, and a signed consent form was obtained from each subject prior to the FDG PET examination.

Subjects

Six healthy volunteers without any histories of shoulder pain or trauma were examined using FDG PET in the present study. There were 4 males and 2 females and their average age was 42 (range; 28-65). Magnetic resonance imaging (MRI) was performed in all subjects to confirm that there were no pathologic conditions around the shoulder including rotator cuff tears. All the subjects refrained from eating and drinking for at least 3 hours before the examination, as well as from performing any kind of strenuous physical activity for at least 1 week prior to the experiment.

Experimental protocol

The FDG was injected intravenously via the cubital vein after 200 repetitions of arm elevation exercise (10 minutes) in the scapular plane with 0.25-kg weights (Steel Band; Tiger Medical Instruments, Osaka, Japan) fixed to the wrists. The mean dose and standard deviation of injected FDG was 86.0 ± 7.1 MBq for the exercise condition. After FDG injection, the subjects were asked to repeat the same exercise. The exercise was performed from 0 to 90 degrees of elevation in the scapular plane at a constant speed of 90 degrees/sec. In this study, we defined the scapular plane as a plane which inclines 30 degrees anteriorly from the coronal plane. For control data, PET scan was repeated for each subject on a separate day without any exercise. The mean dose of injected FDG for the control condition was 81.8 ± 22.7 MBq, giving no statistically significant difference of radiological doses in the two conditions.

PET examination

A set of emission scan in three-dimensional data acquisition mode was performed 50 minutes after injection of FDG from the base of the neck to the middle of the upper arm, using a PET scanner (SET-2400W; Shimadzu Inc., Kyoto, Japan).

Image analysis

To quantify the muscle activities, the volume of interests were established for each shoulder muscle using MR images. The subscapularis was divided into three portions (superior, middle and inferior). The standardized uptake value (SUV), which is considered as indication of muscle activities, was calculated in each muscle to quantify its activity. Statistical analysis was performed using the ANOVA and Tukey test.

Results

There were no abnormal artifactual accumulations in the PET images at rest. High FDG uptakes were observed in all the shoulder girdle muscles after exercise. Interestingly, one of the areas with the highest uptake was located in the superior one third of the subscapularis (Fig. 1).

The SUV increased significantly after exercise in the deltoid, supraspinatus and subscapularis muscles compared to those at rest. In comparison among the 3 divided portions of the subscapularis, the SUV of the superior one third was significantly greater than the rest of the muscle after exercise.

Discussion

As expected, the activities of the deltoid and supraspinatus increased after the arm elevation exercises. However, the activities of the subscapularis also increased significantly. The subscapularis is believed to be an internal rotator and adductor. Kuechle et al. showed that the subscapularis had a function as an elevator[4]. In most of the previous reports, however, the subscapularis muscle was considered as one muscle unit from the functional point of view. In the current study, we clearly demonstrated that there were two functionally different portions in the subscapularis muscle and the superior one third played an important role during arm elevation in the scapular plane.

References

1) Fujimoto T., Itoh M., Kumano H., Tashiro M., Ido T., Lancet **348** (1996) 226.
2) Tashiro M., Fujimoto T., Itoh M., et al., J Nucl Med. **40** (1999) 70.
3) Ohnuma M., Sugita T., Kokubun S., Yamaguchi K., Rikimaru H., J Orthop Sci. **11** (2006) 42.
4) Kuechle D.K., Newman S.R., Itoi E., Morrey B.F., An K.N., J Shoulder Elbow Surg. **6** (1997) 429.

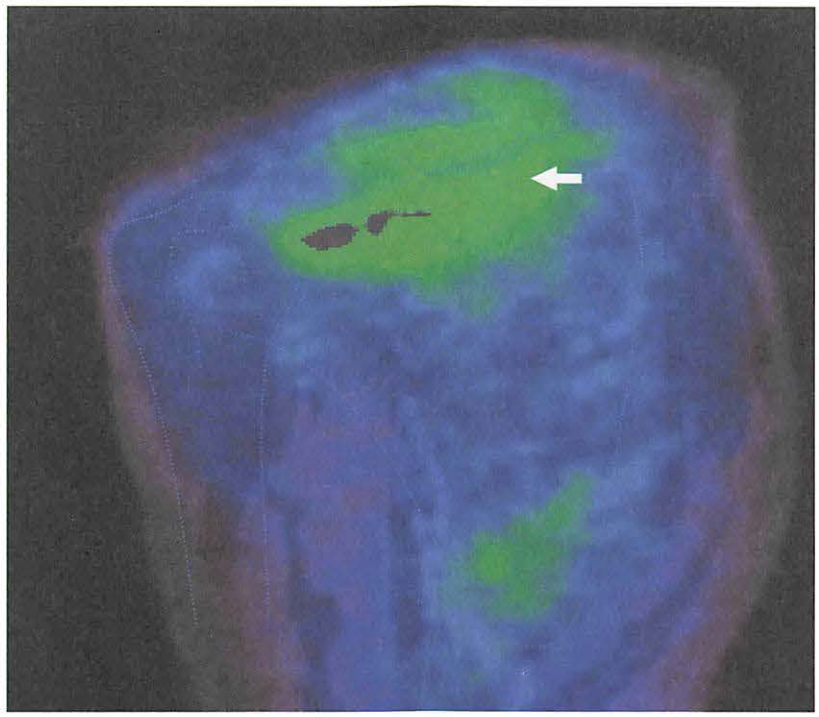

Figure 1. The oblique coronal fusion image of PET and MRI. High FDG uptake was observedin the superior one third of the subscapularis muscle.

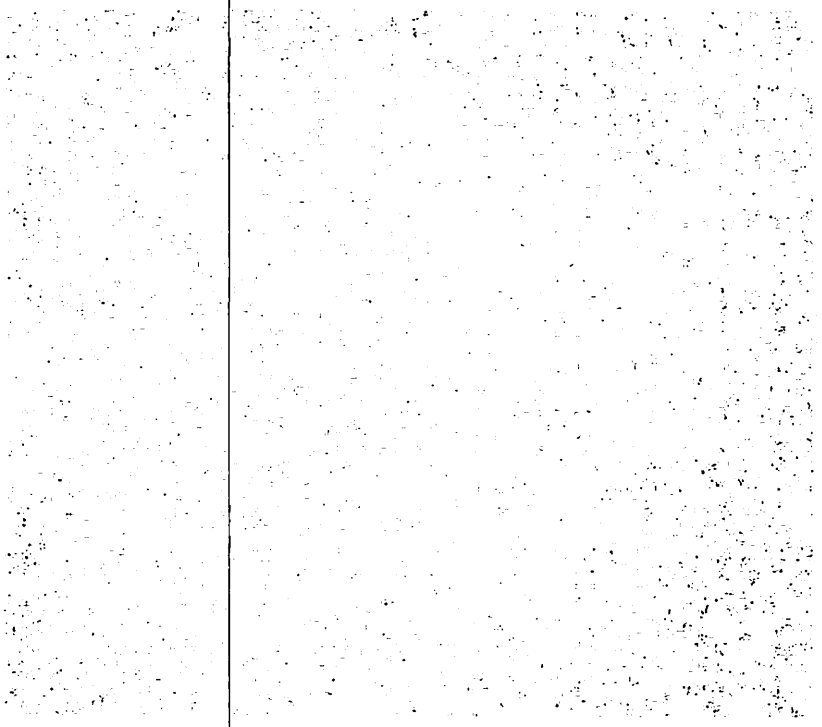

IX. RADIATION PROTECTION AND TRAINING OF SAFETY HANDLING

IX. 1. Radiation Protection and Management

Yuki H.[1], Miyata T.[1], Yamazaki H.[1], Baba M.[1], and Nakae H.[2]

[1]*Cyclotron and Radioisotope Center, Tohoku University*
[2]*Japan Radiation Protection Co., Ltd.*

(1) Overview

During the fiscal year of 2008, research and education in the center were conducted as active as usual.

The measurement of radioactivity concentration which was started along with the reorganization of national university in 2004 is continued periodically but the observed level was low enough generally. Devices and gas counters with automatic sample changer for radioactivity concentration measurement (samplers, α-β automatic counters) were routinely used without serious problems by several radiation facilities in Tohoku University.

(2) Unsealed radio nuclides used in CYRIC

The species and amounts of unsealed radio nuclides handled in CYRIC during the fiscal year of 2008 are summarized in Table 1. The table includes the isotopes produced by the cyclotron as well as those purchased from the Japan Radio Isotope Association or taken over from other radioisotope institutes.

(3) Radiation exposure dose of individual worker

The exposure doses of the workers in CYRIC during 2008 are given in Table 2. The doses were sufficiently lower than the legal dose limits.

(4) Radiation monitoring of the workplace

Radiation dose rates inside and outside of the controlled areas in CYRIC were monitored periodically and occasionally when needed. They were generally below the

legal dose limits although there are several "hot spots" in mSv/hr range like slits or beam stopper of the 930 cyclotron and so on. Surface contamination levels of the floors inside the controlled areas were also measured with a smear method and a survey meter method. They were under the legal regulation levels.

(5) Wastes management

The radioactive wastes were delivered to the Japan Radio Isotope Association twice in the fiscal year of 2008.

The concentration of radioisotopes in the air released from the stack after filtration was monitored with stack gas monitors. The values of concentration were well below the legal regulation levels. The radioactive water was stocked in the tanks at least for 3 days and then released to the sewerage after confirming that the concentration was lower than the legal regulation levels.

Radioactive organic scintillator waste was treated periodically by incinerator provided by Fuji-kogyo Co.Ltd.

Table 1. Unsealed radioisotopes used in each building of CYRIC during the fiscal year of 2008.

(a)Cyclotron Building (kBq)

Group1,2		Group 3		Group4	
		^{11}C	497,076,500.000	^{18}F	856,568,500.000
		^{124}I	280,000.000		
Total	0	Total	497,356,500.000	Total	856,568,500.000

(b) Radio-isotope Building (kBq)

Group 2		Group 3		Group4	
^{125}I	34,377.705	^{11}C	13,653,000.000	^{14}C	15,740.000
^{22}Na	7,648.700	^{124}I	1,810,169.248	^{18}F	71,787,400.000
		^{111}In	5,002.100	^{3}H	29,866.700
		^{32}P	1,086,927.509		
Total	42,026.405	Total	16,555,098.857	Total	71,833,006.700

(c) Research Building (kBq)

Group1,2		Group 3		Group 4	
		^{15}O	7,400,000.000	^{18}F	4,481,070.000
Total	0	Total	7,400,000.000	Total	4,481,070.000

Table 2. Occupational radiation exposures at CYRIC during the fiscal year of 2008.

Dose range (mSv)	Number of individuals
No measurable exposure	34
0.0 - 1.0	12
1.0 - 2.0	3
2.0 - 3.0	0
3.0 -	0
Total number of persons monitored	49

IX. 2. Beginners Training for Safe Handling of Radiation and Radioisotopes in Tohoku University

Yamazaki H., Baba M., Miyata T., and Yuki H.

Cyclotron and Radioisotope Center, Tohoku University

During 2008, the beginners training for safe handling of radiation and radioisotopes in Tohoku University was conducted in three courses as usual:

1) Radiation and Isotopes, 2) X-ray Machines and Electron Microscope, and 3) Synchrotron Radiation (SOR). The training was held twice a year, May and November, under the help for lectures and practice from various departments and research institutes of the university.

Lectures in English which were started in November of 2002 were continued for students and/or researchers who are not so familiar with Japanese language, by using PC projector and text of copies of view graphs (English class). The membership of the English class is almost constant as shown later.

The training for "Radiation and Radioisotopes" is for persons who use unshielded radioisotopes and accelerators, and has been conducted from 1977. The contents of lectures and practices are shown in Table 1. The order and content of the lecture was slightly modified from 2005 aiming at better understanding by trainees: the lecture on "the effect of radiation on human" was moved to the second to give stronger motivation for the training course and the following lectures. Along with the change, a new introductory lecture of "Introduction to radiation" was newly prepared as the first lecture to provide knowledge required to understand the lecture of "the effect of radiation on human". In the fiscal year of 2008, the training was performed for 514 persons (26 persons in the English class). The departments or institutes to which they belong are given in Table 2.

The training for "X-ray machines and electron microscopes" started at the end of 1983. The training is scheduled twice a year at the same time as that for "Radiation and Radioisotopes". In this course, only lectures are given with no practice. The contents of

the lectures and the distributions of trainees are shown in Table 3 and Table 4, respectively. The number of trainees was 396 (45 in the English class).

The training for the "Synchrotron Radiation" began at the end of 1995. The contents of the lectures are the same as those of the radiation and radioisotopes but no practice. In 2008, the number of trainees of the SOR course was 121 (11 in the English class).

Table 1. Contents of the lectures and practices for safe handling of radiation and radioisotopes in 2008.

Lectures (one day)	Hours
Introduction to radiation	0.5
Effects of radiation on human	1.0
Radiation physics and measurements	1.0
Chemistry of radioisotopes	1.0
Radiological protection ordinance including video	1.5
Safe handling of radioisotopes	1.5

Practices (one day)	Hours
Treatment of unsealed radioactive solution	4.0
Measurement of surface contamination and decontamination	1.0
Measurement of gamma-rays and beta-rays	2.0

Table 2. Distribution of trainees for "Radiation and Radioisotopes" in 2008.

Department	Staff	Student	Total	English class
CYRIC	1	9	10	3
Medicine	14	94	108	3
Dentistry	1	9	10	1
Pharmacy	0	40	40	1
Science	2	46	48	6
Engineering	8	126	134	6
Agriculture	4	62	66	0
Research Institutes	9	85	94	6
The others	3	1	4	0
Total	42	472	514	26

Table 3. Contents of the lectures for "X-ray machines and Electron microscopes" in 2008.
(same for both Japanese and English class)

Lectures (one day)	Hours
Safe handling of X-ray machines	1.5
Radiological protection ordinance	0.5
Video for safe handling of radiation and radioisotopes	0.5

Table 4. Distribution of trainees for "X-ray machines and Electron microscopes" in 2008.

Department	Staff	Student	Total	English class
Medicine	3	0	3	1
Dentistry	0	3	3	0
Pharmacy	1	8	9	0
Science	3	28	31	0
Engineering	19	182	201	9
Research Institutes	34	98	132	35
The others	5	12	17	0
Total	65	331	396	45

Table 5. Distribution of trainees for "Synchrotron radiation" in 2008.

Department	Staff	Student	Total	English Class
Dentistry	0	4	4	0
Pharmacy	0	0	0	1
Science	1	7	8	3
Engineering	3	39	42	0
Research Institutes	20	47	67	7
Total	24	97	121	11

X. PUBLICATIONS

X. PUBLICATIONS

[723] Decrease in glucose metabolism in frontal cortex associated with deterioration of microstructure of corpus callosum measured by diffusion tensor imaging in healthy elderly.
Kentaro Inoue, Hiroshi Ito, Shinya Uchida, Yasuyuki Taki, Shigeo Kinomura, Ichiro Tsuji Shigeru Sato, Kaoru Horie, Ryuta Kawashima, Masatoshi Ito, Hiroshi Fukuda.
Human Brain Mapping, **29** (2008) 375-384.

[724] Brain histamine H_1 receptor occupancy of orally administered antihistamines, bepotastine and diphenhydramine, measured by PET with ^{11}C-doxepin.
Manabu Tashiro, Xudong Duan, Motohisa Kato, Masayasu Miyake, Shoichi Watanuki, Yoichi Ishikawa, Yoshihito Funaki, Ren Iwata, Masatoshi Itoh, Kazuhiko Yanai.
Brithish Journal of Clinical Pharmacology, **65** (2008) 811-821.

[725] Discrete cortical regions associated with the musical beauty of major and minor chords.
Miho Suzuki, Nobuyuki Okamura, Yousuke Kawachi, Manabu Tashiro, Hiroshi Arao, Takayuki Hoshishiba, Jiro Gyoba, Kazuhiko Yanai.
Cognitive, Affective, & Behavioral Neuroscience ,**8** (2008) 126-131.

[726] Effects of a sedative antihistamine, D-chlorpheniramine, on regional cerebral perfusion and performance during simulated car driving.
Manabu Tashiro, Yumiko Sakurada, Hideki Mochizuki, Etsuo Horikawa, Masahiro Maruyama, Nobuyuki Okamura, Shoichi Watanuki, Hiroyuki Arai, Masatoshi Itoh, Kazuhiko Yanai.
Hum. Psychopharmacol Clin Exp **23** (2008) 139-150.

[727] Application of positron emission tomography to neuroimaging in sports sciences.
Manabu Tashiro, Masatoshi Itoh, Toshihiko Fujimoto, Md. Mehedi Masud, Shoichi Watanuki, Kazuhiko Yanai.
Methods, **45** (2008) 300-306.

[728] Effect of exercise intensities on free fatty acid uptake in whole-body organs measured with ^{123}I-BMIPP-SPECT.
Koji Kitada, Kazuo Kubota, Ryoichi Nagatomi, Masatoshi Itoh, Manabu Tashiro, Hiroshi Fukuda, Mehedi Masud, Toshihiko Fujimoto.
Eur. J. Appl. Physiol., **104** (2008) 769-775.

[729] Study of medium mass nuclei toward to the neutron drip line with RFIGISOL system.
Y. Miyashita, T. Wakui, N. Sato, A. Yamazaki, T. Endo, M. Fujita, A. Goto, S. Kinoshita, T. Koike, Y. Ma, Y. Miura, T. Miyake, T. Nagano, M. Ohguma, T. Sonoda, T. Suzuki, H. Tamura, E. Tanaka, M. Takeoka, W. Yamashita, M. Ukai, T. Shinozuka.

Nuclear Physics A, **805** (2008) 633-635.

[730] The RFIGISOL at Tohoku ISOL.
Y. Miyashita, T. Wakui, N. Sato, A. Yamazaki, T. Endo, M. Fujita, A. Goto, S. Kinoshita, T. Koike, Y. Ma, Y. Miura, T. Miyake, T. Nagano, M. Ohguma, T. Sonoda, T. Suzuki, H. Tamura, E. Tanaka, M. Takeoka, W. Yamashita, M. Ukai, T. Shinozuka.
Nucl. Instrum. Meth. Phys. Re. B, **266** (2008) 4498-4501.

[731] Medical applications of prticle-induced X-ray emission.
S. Harada, S. Ehara, K. Ishii, H. Yamazaki, S. Matsuyama, T. Sato, S. Oikawa, T. Kamiya, K. Arakawa, K. Sera, J. Ito.
Int. J. PIXE, **18** (2008) 101-110.

[732] μ-CT images of the egg of drosophila.
S. Okura, K. Ishii, S. Matsuyama, H. Yamazaki, A. Terakawa, Y. Kikuchi, M. Fujiwara, Y. Kawamura, S. Tsuboi, K. Yamanaka, M. Watanabe, M. Fujikawa.
Int. J. PIXE, **18** (2008) 167-171.

[733] Characterization of aerosol particles in a mechanical workshop environment.
S. Matsuyama, K. Ishii, H. Yamazaki, Y. Kikuchi, M. Fujiwara, Y. Kawamura, K. Yamanaka, M. Watanabe, S. Tsuboi, P. Pelicon, M. _itnik.
Int. J. PIXE, **18** (2008) 199-207.

[734] PIXE analysis of atmospheric aerosols from asian continent.
K. Yamanaka, K. Ishii, S. Matsuyama, A. Terakawa, Y. Kikuchi, Y. Kawamura, R. Oyama, T. Yamamoto, M. Watanabe, S. Tsuboi, S. Okura, M. Fujikawa, H. Yamazaki, K. Arao.
Int. J. PIXE, **18** (2008) 219-224.

[735] PIXE study on absorption of arsenate and arsenite by arsenic hyperaccumulating fern (Pteris vittata).
H. Yamazaki, K. Ishii, S. Matsuyama, Y. Kikuchi, Y. Takahashi, A. Terakawa, Y. Kawamura, K. Yamanaka, M. Watanabe, S. Tsuboi, K. Tashiro, T. Satoh, C. Inoue.
Int. J. PIXE, **18** (2008) 241-252.

[736] PIXE analysis of peanuts planted in japan and imported from abroad.
A. Terakawa, K. Ishii, J. Arikawa, Y. Kawamura, M. Fujikawa, S. Matsuyama, Y. Takahashi, H. Yamazaki, H. Sasaki, K. Maeda, K. Sera.
Int. J. PIXE, **18** (2008) 253-259.

[737] PIXE analysis of umeboshi (dried plum).
S. Tsuboi, K. Ishii, S. Matsuyama, A. Terakawa, Y. Kikuchi, M. Fujiwara, Y. Kawamura, M. Watanabe, K. Yamanaka, J. Arikawa, S. Okura, M. Fujikawa, H. Yamazaki.
Int. J. PIXE, **18** (2008) 267-271.

[738] Elemental PIXE analysis of oolong tea.
M. Watanabe, K. Ishii, S. Matsuyama, A. Terakawa, Y. Kikuchi, M. Fujiwara, Y. Kawamura, S. Tsuboi, K. Yamanaka, S. Okura, M. Fujiwara, H. Yamazaki.
Int. J. PIXE, **18** (2008) 273-277.

[739] Imaging assessment of local brain metabolic response to changing load during

exercise in humans.
Sabina Khondkar, Toshihiko Fujimoto, Manabu Tashiro, Masatoshi Itoh.
Current Medical Imaging Reviews, **14** (2008) 14-18.

[740] Proton therapy facilities at CYRIC, Tohoku University.
Atsuki Terakawa, Keizo Ishii, Toshiyuki Chiba, Takuya Miyashita, Tatsuya Yamamoto, Jun Arikawa, Takanori Togashi, Wataru Yamashita, Hisaki Akiyama, Hiroshi Koyata, Yuzo Fujita, Azusa Ishizaki, Taizo Honda, Yuuki Totsuka, Nobuhiko Ito, Tadashi Sano, Seiichi Wada.
16th Pacific Basin Nuclear Conference (16PBNC), Aomori, Japan, (Oct. 13-18, 2008) 1-6.

[741] Whole-body tumor imaging: *O*-[^{11}C]methyl-L-tyrosine/positron emission tomography.
K. Ishiwata, K. Kubota, T. Nariai, R. Iwata.
Cancer Imaging. Vol. 2 Instrumentation and applications, (2008) 175-179.

XI. MEMBERS OF COMMITTEE

XI. MEMBERS OF COMMITTEE (as of Jan. 1, 2009)

General

(Chairman)	Keizo	Ishii	(Graduate School of Engineering)
	Makoto	Watanabe	(Executive Vice President)
	Kazushige	Maeda	(Graduate School of Science)
	Kazuaki	Iwasa	(Graduate School of Science)
	Tetsuya	Ono	(Graduate School of Medicine)
	Keiichi	Sasaki	(Graduate School of Dentistry)
	Norimichi	Nakahata	(Graduate School of Pharmaceutical Sciences)
	Akira	Hasegawa	(Graduate School of Engineering)
	Minoru	Sato	(Graduate School of Agricultural Science)
	Kazuhiko	Sogawa	(Graduate School of Life Science)
	Atuki	Terakawa	(Graduate School of Biomedical Engineering)
	Isamu	Sato	(Institute for Materials Research)
	Hiroshi	Fukuda	(Institute for Development, Aging and Cancer)
	Tanetoshi	Koyama	(Institute of Multidisciplinary Research for Advanced Materials)
	Syoki	Takahashi	(University Hospital)
	Jirohta	Kasagi	(Laboratory of Nuclear Science)
	Ren	Iwata	(CYRIC)
	Hiromichi	Yamazaki	(CYRIC)
	Yasuhiro	Sakemi	(CYRIC)
	Etusyu	Kuraoka	(CYRIC)
	Tsutomu	Shinozuka	(CYRIC)
	Manabu	Tashiro	(CYRIC)
	Hirokazu	Tamura	(Graduate School of Science)
	Kazuhiko	Yanai	(Graduate School of Medicine)

	Tetsuya	Ono	(Radiation Safety Committee, Research Promotion Council)
(Observer)	Seiko	Sato	(Head of Administration Office, Graduate School of Information Science)

Cyclotron

(Chairman)	Yasuhiro	Sakemi	(CYRIC)
	Toshio	Kobayashi	(Graduate School of Science)
	Osamu	Hashimoto	(Graduate School of Science)
	Hideya	Onodera	(Graduate School of Science)
	Hirokazu	Tamura	(Graduate School of Science)
	Kazushige	Maeda	(Graduate School of Science)
	Yasushi	Kino	(Graduate School of Science)
	Keizo	Ishii	(Graduate School of Engineering)
	Akira	Hasegawa	(Graduate School of Engineering)
	Atuki	Terakawa	(Graduate School of Engineering)
	Isamu	Sato	(Institute for Materials Research)
	Anpo	Sai	(Institute of Multidisciplinary Research for Advanced Materials)
	Tsutomu	Otsuki	(Laboratory of Nuclear Science)
	Ren	Iwata	(CYRIC)
	Hiromichi	Yamazaki	(CYRIC)
	Etusyu	Kuraoka	(CYRIC)
	Tsutomu	Shinozuka	(CYRIC)
	Manabu	Tashito	(CYRIC)

Radiation Protection and Training of Safe Handling

(Chairman)	Hiromichi	Yamazaki	(CYRIC)
	Kazuaki	Iwasa	(Graduate School of Science)
	Yoshihiko	Uehara	(Graduate School of Medicine)
	Tetuya	Terasaki	(Graduate School of Pharmaceutical Sciences)

	Keizo	Ishii	(Graduate School of Engineering)
	Michio	Komai	(Graduate School of Agricultural Science)
	Kazuhiro	Sogawa	(Graduate School of Life Science)
	Tatuo	Shikama	(Institute for Materials Research)
	Katuyoshi	Hori	(Institute for Development, Aging and Cancer)
	Tomohiro	Kaneta	(University Hospital)
	Ren	Iwata	(CYRIC)
	Tsutomu	Shinozuka	(CYRIC)
	Etusyu	Kuraoka	(CYRIC)

Life Science

(Chairman)	Ren	Iwata	(CYRIC)
	Noriaki	Ohuchi	(Graduate School of Medicine)
	Shogo	Yamada	(Graduate School of Medicine)
	Syoki	Takahashi	(Graduate School of Medicine)
	Teiji	Tominaga	(Graduate School of Medicine)
	Masahiko	Yamamoto	(Graduate School of Medicine)
	Yukitsuka	Kudo	(Biomedical Engineering Research Organization)
	Keiichi	Sasaki	(Graduate School of Dentistry)
	Masayuki	Seki	(Graduate School Pharmaceutical Sciences)
	Keizo	Ishii	(Graduate School of Engineering)
	Kazuhiko	Nishitani	(Graduate School of Life Science)
	Hiroshi	Fukuda	(Institute for Development, Aging and Cancer)
	Nariyasu	Mano	(University Hospital)
	Yoshihiro	Takai	(College of Medical Sciences)
	Hiromichi	Yamazaki	(CYRIC)
	Manabu	Tashiro	(CYRIC)
	Yoshihito	Funaki	(CYRIC)

Prevention of Radiation Hazards

(Chairman)	Hiromichi	Yamazaki	(CYRIC)
	Naohito	Iwasa	(Graduate School of Science)
	Yasushi	Kino	(Graduate School of Science)
	Keizo	Ishii	(Graduate School of Engineering)
	Ren	Iwata	(CYRIC)
	Yasuhiro	Sakemi	(CYRIC)
	Tsutomu	Shinozuka	(CYRIC)
	Etusyu	Kuraoka	(CYRIC)
	Manabu	Tashiro	(CYRIC)
	Hideyuki	Yuki	(CYRIC)
	Katuo	Aizawa	(CYRIC)

Research Program

(Chairman)	Hiromichi	Yanazaki	(CYRIC)
	Toshio	Kobayashi	(Graduate School of Science)
	Hirokazu	Tamura	(Graduate School of Science)
	Kazushige	Maeda	(Graduate School of Science)
	Kazuhiko	Yanai	(Graduate School of Medicine)
	Shin	Fukushi	(Graduate School of Medicine)
	Akira	Takahashi	(Graduate School of Medicine)
	Akira	Hasegawa	(Graduate School of Engineering)
	Atuki	Terakawa	(Graduate School of Engineering)
	Isamu	Sato	(Institute for Materials Research)
	Hiroshi	Fukuda	(Institute for Development, Aging and Cancer)
	Syoki	Takahashi	(University Hospital)
	Jirohta	Kasagi	(Laboratory of Nuclear Science)
	Tsutomu	Otsuki	(Laboratory of Nuclear Science)
	Tsutomu	Sekine	(Center for the Advancement of Higher Education)

	Ren	Iwata	(CYRIC)
	Yasuhiro	Sakemi	(CYRIC)
	Etusyu	Kuraoka	(CYRIC)
	Tsutomu	Shinozuka	(CYRIC)
	Manabu	Tashiro	(CYRIC)
(Observer)	Masatoshi	Itoh	(CYRIC)
(Observer)	Takashi	Wakui	(CYRIC)

XII. STAFF

XII. STAFF (as of Jan. 1, 2009)

Director Keizo Ishii

Division of Accelerator

Osamu	Hashimoto[1)]
Tsutomu	Shinozuka
Takashi	Wakui
Kenji	Shimada
Shizuo	Chiba[7)]
Yasuaki	Ohmiya[7)]
Naoto	Takahashi[7)]
Shigenaga	Yokokawa[7)]
Jyunnya	Suzuki[7)]

Division of Instrumentations

Sakemi	Yasuhiro
Hirokazu	Tanura[1)]
Hikonojo	Orihara[5)]
Atuki	Terakawa[3)]
Masatoshi	Itoh
Sho-ichi	Watanuki
Hidetomo	Yoshida

Division of Radiopharmaceutical Chemistry

Ren	Iwata
Yukitsuka	Kudo[4)]
Yoshihito	Funaki
Yohichi	Ishikawa
Shozo	Furumoto[4)]

Division of Cyclotron Nuclear Medicine

Kazuhiko	Yanai[2)]
Masatoshi	Itoh[6)]
Keiichiro	Yamaguchi[5)]
Kohichiro	Kawashima[5)]
Manabu	Tashiro
Masayasu	Miyake
Mehedi	Masud
Kazuaki	Kumagai
Takehisa	Sasaki
Xuclong	Duan
Targino Rodrigues Dos Santos	
Takeshi	Ogura

Division of Radiation Protection and Safety Control

Hiromichi	Yamazaki
Etusyu	Kuraoka
Hideyuki	Yuki
Takashi	Nakamura[5)]
Mamoru	Baba[5)]
Takamoto	Miyata
Kazuhiro	Ootomo
Hirokazu	Nakae[8)]

Graduate Student and Researcher

Yu-ji	Miyashita	(Graduate School of Science)
Nozomi	Sato	(Graduate School of Science)
Naoya	Sugimoto	(Graduate School of Science)
Hiroyuki	Ouchi	(Graduate School of Science)
Ayaki	Sasaki	(Graduate School of Science)
Toshiya	Takahashi	(Graduate School of Science)
Ryo	Matsuo	(Graduate School of Science)
Tetuya	Nagano	(Graduate School of Science)
Sayo	Hoshino	(Graduate School of Science)

Yoshitaka	Aono	(Graduate School Pharmaceutical Sciences)
Eita	Sakai	(Graduate School Pharmaceutical Sciences)
Mari	Satoh	(Graduate School Pharmaceutical Sciences)
Wong	Rebecca	(Graduate School Pharmaceutical Sciences)
Akihiro	Sugawara	(Graduate School, Division of Medicine)
Katuhiko	Shibuya	(Graduate School, Division of Medicine)
Yutaro	Hashimoto	(Graduate School, Division of Medicine)
Takuji	Ohishi	(Graduate School of Engineering)
Mohammad	Nakhostin	(Graduate School of Engineering)
Akram	Mohammadi	(Graduate School of Engineering)
Toshio	Okuchi	(Graduate School of Engineering)
Yoichi	Yamaguchi	(Graduate School of Engineering)
Yasunori	Horiuchi	(Graduate School of Engineering)

Office Staff

Seiko	Sato
Aizawa	Katuo
Tomoya	Yonezawa
Satoshi	Arao
Yu-ko	Yamashita
Kyoko	Fujisawa
Fumiko	Mayama
Katuo	Ibuka
Kimiko	Abe
Shurikeiko	Fujimoto
Yumiko	Matsubara
Chihiro	Saeki
Asami	Sawada

1) Graduate School of Science
2) Graduate School of Medicine
3) Graduate School of Engineering
4) TUBERO
5) Visiting Professor
6) Specially-approved visiting professor
7) SUMI-JU Accelerator Service Ltd.
8) Japan Radiation Protection Co., Ltd.